Nonlinear ionic transport at the nanometric and Ångströmetric scales

Anthony R. Poggioli

Anthony R. Poggioli. Nonlinear ionic transport at the nanometric and Ångströmetric scales. Soft Condensed Matter [cond-mat.soft]. Université Paris sciences et lettres, 2019. English. NNT : 2019PSLEE031 . tel-02869126

HAL Id: tel-02869126
https://theses.hal.science/tel-02869126v1

Submitted on 15 Jun 2020

PSL
UNIVERSITÉ PARIS

THÈSE DE DOCTORAT
DE L'UNIVERSITÉ PSL

Préparée à l'École Normale Supérieure de Paris

Transport Ionique Non-Linéaire aux Échelles Nanométrique et Ångströmétrique

Soutenue par
Anthony R. Poggioli
Le 28 Novembre 2019

École doctorale n°564
Physique en Île de France

Spécialité
Physique de la Matière Molle et Nanoscience

Composition du jury :

Benjamin Rotenberg DR CNRS, PHENIX, Sorbonne Université	*Président du jury*
Manoel Manghi Maître de Conférence, HDR, IRSAMC Toulouse	*Rapporteur*
René van Roij Professeur, ITP, Université de Utrecht	*Rapporteur*
Elisabeth Charlaix Professeur, LiPhy, Université de Grenoble-Alpes	*Examinateur*
Emmanuel Trizac Professeur, LPTMS, Université de Paris-Sud	*Examinateur*
Alessandro Siria CR CNRS, LPENS, École Normale Supérieure	*Examinateur*
Lydéric Bocquet Directeur de l'IPGG, DR CNRS, LPENS, École Normale Supérieure	*Directeur de thèse*

ENS

Nonlinear Ionic Transport at the Nanometric and Ångströmetric Scales

Anthony R. Poggioli

2019

Supervised By:

Lydéric Bocquet

École Normale Supérieure
Paris Sciences et Lettres

Abstract

Nanofluidics research is motivated both by intrinsic interest in the novel transport phenomena observable only at the (sub-)nanometric scale, and by applications including energy generation, desalination, macromolecular analysis, and microscopy. Two key considerations in the development of such technologies are 1) the control of nonlinear ionic transport and 2) the characterization of electrostatic, frictional, and other interactions of solid-liquid interfaces with bulk electrolyte solutions. In this manuscript, I develop a coherent theory of ion-selectivity and nonlinear ionic transport in nanopores $\gtrsim 1$ nm in diameter, rationalizing previous experimental work and offering new routes in the development of desalination, energy generation, and other exotic functionalities. I then explore each of the above considerations separately. First, I explore the limits of continuum theory in rationalizing nonlinear coupled transport observed experimentally in ångströmetric channels, revealing the irrelevance of the Navier-Stokes description of the fluid dynamics at this scale and highlighting the role of the frictional characteristics of the confining material. Finally, I examine the surface-controlled modification of applied electric fields in scanning ion conductance microscopy, proposing a new approach for the imaging of surface charge that may substantially improve on the spatial resolution of current techniques.

Résumé

La recherche en nanofluidique est motivée à la fois par l'intérêt intrinsèque des nouveaux phénomènes de transport observables uniquement à cette échelle, mais aussi par les applications qui en résultent comme la production d'énergie, le dessalement, l'analyse macromoléculaire et la microscopie. Deux points clés pour le développement de telles technologies sont : 1) le contrôle du transport ionique non-linéaire et 2) la caractérisation des propriétés électrostatiques, frictionnelles et autres des interfaces solide-liquide avec des solutions électrolytiques. Dans ce manuscript, je m'intéresse à la sélectivité ionique ainsi qu'au transport non-linéaire des ions dans les nanopores. Je développe une théorie cohérente qui permet de rationaliser les travaux expérimentaux précédents et ouvre des nouvelles voies pour le dessalement et la génération d'énergie. J'explore ensuite chacun des

deux points clés cites précédemment. D'abord, j'étudie les limites de l'approche en milieu continu à travers l'exemple du couplage non-linéaire observé pour le transport dans des canaux qui font quelques ångström d'épaisseur. Dans ce cadre, je montre que l'équation de Navier-Stokes ne permet plus de décrire correctement la dynamique des fluides (à cette échelle), et je mets en évidence l'importance des propriétés de friction du matériau qui confine le liquide. Enfin, j'explore l'effet des propriétés de surface sur le champ électrique appliqué en Microscopie à conductance ionique à balayage (Scanning Ion Conductance Microscopy en anglais). Je propose une nouvelle approche pour l'imagerie de la charge de surface qui pourrait améliorer considérablement la résolution spatiale des techniques actuelles.

ACKNOWLEDGMENTS

I would like to thank Lydéric Bocquet for the opportunity to work in a dynamic and innovative group. I can only hope that my contribution has been commensurate with this opportunity. From Lydéric, I have tried to learn a creative approach to science that combines an eye for the most interesting features of any result with an ability to synthesize the insights of often disparate subjects into original topics of research. I am grateful for Lydéric's willingness to freely discuss both 'big' scientific questions and 'small' technical details with equal interest (and for his willingness to tell me when I've become too caught up in those small details). In working with Lydéric, I come away with the sense that his first and greatest interest is in *doing* science, an attitude which I share, appreciate, and hope to carry into my own scientific career.

I am also thankful to Alessandro Siria, for the opportunity to work in this group, for his good-naturedness, and for his insight not only in experimental science, but also in the more practical realities of living and working as a PhD student or scientist. I am also grateful to Antoine Niguès. I believe Antoine is one of the most gifted experimentalists I've had the opportunity to work with, and I admire his dedication to the idea that we are a team, and our outlook should not be one of competition, but of working together in pursuit of common goals.

I would also like to thank my collaborators–Laetitia Jubin, Timothée Mouterde, and Sara Dal Cengio, whose contributions to the work presented here cannot be overstated–and to all of the current and former members of the Micromégas team. Each of them has offered support within and beyond science, as well as humor and camaraderie. In particular, I am extremely grateful to Elisa Tamborini, Eleonora Secchi, and Benoit Laborie, who offered much of their time and support when I first arrived in the group, and who made the formidable task of adjusting to a new and challenging environment that much easier.

From this group has come two of my closest friends, Amin M'Barki and Christie Cherian. I prefer not to think of what the final year of my PhD would have been like without their friendship and immense support. They are family.

I would also like to gratefully acknowledge the opportunity provided by the European Commission in funding my PhD, and in particular the Nanotrans European Training Network, of which I am a part, for their continued support throughout my thesis. I would especially like to thank Jure Dobnikar, Benjamin Rotenberg, Marielore Sulpizi, and Daan Frenkel for their tireless work in coordinating the network and organizing meetings and training events, as well as all of the PIs, postdocs, and fellow PhD students who have become mentors, collaborators, and friends over the past three years. The opportunity to be part of this network was a unique gift for which I will forever be grateful.

Finally, I would like to extend my deepest gratitude to my family, and especially to my mother and father, Darlene and Robert, and my sisters Megan and Melissa. More than anything else, it is their unwavering love and support that has carried me through the most difficult times in my life. There is no one more important to me than they are, and there is nothing I could do without their support.

TABLE OF CONTENTS

LIST OF FIGURES

Figure Number Page

LIST OF TABLES

Chapter 1

INTRODUCTION

Nanofluidics, the study of fluid flow in conduits having minimum dimensions between one and several hundred nanometers, has existed as a discipline distinct from, *e.g.*, nanotechnology or membrane or colloid science, for over two decades (Eijkel & van den Berg, 2005; Schoch *et al.*, 2008; Bocquet & Charlaix, 2010). The justification for distinguishing nanofluidics from other related disciplines lies more in the exotic phenomena unique to these length scales than to its numerous technical applications. Theoretically, these novel phenomena are anticipated based on two criteria: 1) the strong interaction of the fluid with the solid-liquid interface owing to the relatively large surface-to-volume ratios typical of the nanoscale, and 2) the breakdown of the continuum description of the solute and solvent transport as molecular length scales are approached (Bocquet & Charlaix, 2010). Practially, however, there remain substantial difficulties in the ready and reproducible fabrication of devices with confinements approaching molecular scales ($\lesssim$ 1 nm). Furthermore, the continuum description of fluid transport has been found to be quite robust down to $1 - 2$ nm, with only slight modifications–chiefly, the relaxation of the no-slip condition (Bocquet & Charlaix, 2010). For these reasons, the majority of the nanofluidics literature is focused on exploring the novel transport phenomena induced by the interaction of the fluid with the confining boundary–typically, electrostatic interaction of a charged interface with a confined electrolyte solution subjected to external forcing.

In addition to the intrinsic interest in cataloging and rationalizing transport phenomena unique to the nanoscale, nanofluidic research is motivated by a variety of technical applications. Among them are the synthetic mimicry of exotic transport phenomena observed in nature, such as activation, ionic pumping, signal generation, and mechanosensitivity (Schasfoort *et al.*, 1999; Perozo *et al.*, 2002; Karnik *et al.*, 2005; Vásquez *et al.*, 2008; Kim *et al.*, 2009; Jiang & Stein, 2011; Pang *et al.*, 2011; Bonthuis & Golestanian, 2014; Chun & Chung, 2015; Fu *et al.*, 2017; Zhao *et al.*, 2017); applications to filtration (Bocquet & Charlaix, 2010; Picallo *et al.*, 2013), energy generation (van der Heyden *et al.*, 2006; Ren & Stein, 2008; Bocquet & Charlaix, 2010; Siria *et al.*, 2013; Rankin & Huang, 2016; Siria *et al.*, 2017), and other topics in membrane science; macro- and biomolecular detection (Misakian & Kasianowicz, 2003; Schiedt *et al.*, 2005; Vlassiouk *et al.*, 2009; Zhou *et al.*, 2011); and microscopy of soft substrates (Hansma *et al.*, 1989; Nitz *et al.*, 1998; Klenerman *et al.*, 2011; Sa *et al.*, 2013; McKelvey *et al.*, 2014; Dorwling-Carter *et al.*, 2018; Maddar *et al.*, 2019). Many of these applications hinge on inducing and controlling ion-selectivity and nonlinear transport, as well as on characterizing material-dependent solid-liquid interactions (*e.g.*, slippage) beyond generic electrostatic interactions. Additionally, both intrinsic interest and the potential for novel technical applications pushes researchers to probe beyond the regime of continuum nanofluidics, exploring for example extreme (sub-nanometric) confinement (Geim & Grigorieva, 2013; Radha *et al.*, 2016; Esfandiar *et al.*, 2017).

In this thesis, I address two related questions: 1) under what conditions, and by what mechanisms, may a nonlinear response of ionic current (and other fluxes) in an electrolyte solution be obtained in devices of (sub-)nanometric scale?, and 2) what is the role of surface charge in nanometrically-confined ionic transport? In particular, I consider the role of surface charge as characterized by the Dukhin number,

$$\mathrm{Du} \equiv \frac{\ell_{\mathrm{Du}}}{R} \equiv \frac{\kappa_{\mathrm{surf}}/\kappa_{\mathrm{bulk}}}{R} \equiv \frac{|\sigma|/ec}{R}, \tag{1.1}$$

where κ_{surf} is a surface conductivity characterizing charge transport in the vicinity of a solid-liquid interface, κ_{bulk} is a bulk conductivity characterizing charge transport far from any such interfaces, σ is the density of surface charge on the interface, c is the total ionic concentration, $\ell_{\mathrm{Du}} \equiv \kappa_{\mathrm{surf}}/\kappa_{\mathrm{bulk}} \equiv |\sigma|/ec$ is the Dukhin length, reaching values of $\mathcal{O}(100\,\mathrm{nm})$ for typical surface charge densities and ionic concentrations, and R is a typical length scale of the transport. In colloid science, R is the colloid radius, and in nanofluidics R is the minimum dimension (radius or half-width) of the nanometric conduit.

This dimensionless parameter was first introduced for, and is routinely applied in, the study of the electrokinetics of colloids (Delgado *et al.*, 2005; Posner, 2009). The applications to nanofluidics have been less frequent and more particular; see, for example, Bocquet & Charlaix (2010); Picallo *et al.* (2013), as well as recent publications citing the work presented in this thesis: Dal Cengio & Pagonabarraga (2019); Graf *et al.* (2019); Macha *et al.* (2019). Researchers in nanofluidics more frequently consider the ratio of the Debye length λ_D to the confinement scale R. The Debye length is defined as

$$\lambda_D \equiv \sqrt{\frac{k_B T \epsilon_r \epsilon_0}{e^2 c}}, \tag{1.2}$$

and it characterizes the thickness of the electrical diffuse layer (EDL) forming in electrolyte solutions in the vicinity of a charged solid-liquid interface. In particular, many authors have stated that the parameter λ_D/R controls both nonlinear transport and ionic selectivity (Woermann, 2003; Cervera *et al.*, 2006; Constantin & Siwy, 2007; Liu *et al.*, 2007; Vlassiouk *et al.*, 2008b; White & Bund, 2008; Perry *et al.*, 2010; Ai *et al.*, 2010; Nguyen *et al.*, 2010; Cheng & Guo, 2010; Kubeil & Bund, 2011; Lan *et al.*, 2011; Laohakunakorn & Keyser, 2015; Siria *et al.*, 2017), though this assertion has been challenged by numerical and experimental results (White *et al.*, 2006; White & Bund, 2008; Kovarik *et al.*, 2009; Kubeil & Bund, 2011; Lan *et al.*, 2011; Laohakunakorn & Keyser, 2015; He *et al.*, 2017; Lin *et al.*, 2018), including those presented in Chapters 2 and 3 of this manuscript.

1.1 Layout of the Thesis

Chapters 2 and 3 address both of the questions posed above simultaneously. In Chapter 2, I consider the role of the Dukhin number in nonlinear ionic transport in nanofluidic devices. I develop a theoretical framework within the context of Poisson-Nernst-Planck theory to treat the phenomenon of ionic current rectification (ICR) analytically. ICR is the nanofluidic analogue of the classical semiconductor diode, and it is the prototypical and most extensively studied example of nonlinear nanofluidic transport. My results indicate that the Dukhin number, rather than λ_D/R, is the principle parameter controlling both ionic selectivity and nonlinearity; in particular, it is found that both an asymmetry in Dukhin number and a maximum Du ~ 1 are necessary and sufficient conditions for rectification. These results both rationalize previous numerical and experimental work indicating that substantial rectification and selectivity is obtainable outside of the regime of Debye overlap, as well as suggest promising new avenues for improved efficiency of energy generation and desalination techniques.

In Chapter 3, I extend this theoretical framework to consider simultaneous electrical (voltage) and mechanical (pressure) forcing in the nonlinear (Du ~ 1) regime. It is found that the conductance of a conical nanopore subjected to an applied voltage shows a pronounced, gating-like sensitivity to mechanical forcing, returning to the ordinary linear response regime only when subjected to large pressures. This response is in contrast to the typical linear response scenario, and it is characteristic of a mechanical transistor-like response, in which ionic current is gated by an external mechanical forcing. These results are a step towards the synthetic realization of some of the exotic transport phenomena observed in nature, and the theoretical results are indeed corroborated by experimental results obtained in the group.

Chapters 4 and 5 break off, treating either the conditions for nonlinear transport (Ch. 4) or the role of the Dukhin length (Ch. 5) outside the context of nonlinear nanofluidic transport. In Chapter 4, I develop a theoretical framework to rationalize experiments conducted in the group measuring ionic current in ångströmetric channels subject to applied voltage and pressure. The experiments reveal a streaming (pressure-driven) conductance that is strongly dependent on both the applied voltage and the confining material–either hexagonal boron nitride (hBN) or graphite. At this scale, the continuum picture of a distinct EDL and bulk is no longer applicable, as only one or two layers of molecules are present. Furthermore, the ordinary continuum description (Navier-Stokes) of the solvent dynamics is inapplicable as well, as the concepts of a transverse viscosity or velocity gradient are no longer meaningful. I employ a phenomenological treatment of the frictional forces present in the system to develop a continuum approach that successfully reproduces the key qualitative results of the experiments, illustrating the important role of the different frictional characteristics of hBN and graphite.

In Chapter 5, I leave aside the question of nonlinear transport, instead focusing on the role of the Dukhin length in surface charge detection via scanning ion conductance microscopy (SICM). This work corroborates theoretically and numerically our hypothesis that isolated 'patches' of surface charge induce disturbances in applied electric fields that scale in spatial extent with the Dukhin length, and that these patches may therefore be imaged via SICM. This hypothesis is motivated by the work of Khair & Squires (2008), who first demonstrated theoretically the surface-controlled modification of applied electric fields, and of Lee *et al.* (2012), who demonstrated experimentally and numerically that the effective size of nanopores inferred from conductance measurements at low concentration scales with the Dukhin length rather than the physical pore size due to the discontinuity in surface charge at the ends of the nanopore. The results of Chapter 5 indicate that this effect may be used to infer relative surface charge density magnitude and the structure of isolated charged features, potentially improving upon the spatial resolution of current SICM-based surface charge detection by one-to-two orders-of-magnitude.

Finally, in Chapter 6, I offer some overall conclusions and perspectives from the thesis, as well as potential directions for future work.

Chapter 2

BEYOND THE TRADEOFF: DYNAMIC SELECTIVITY IN IONIC TRANSPORT AND CURRENT RECTIFICATION

Abstract In this Chapter, I derive one-dimensional equations for ionic transport in large-aspect-ratio ($L/R \gg 1$) nanopores in the limit of no Debye overlap ($\lambda_D/R \ll 1$). I solve these equations, along with the well known equations for ionic transport in the limit of strong Debye overlap ($\lambda_D/R \gg 1$), for the current-voltage relationship in so-called concentration diodes, in which ionic current rectification (ICR) is induced by an asymmetry in reservoir concentration. In line with recent experimental results, and in contrast to the typical theoretical understanding of ICR, I find that substantial rectification may be obtained when the maximum Dukhin number $\mathrm{Du} \equiv |\sigma|/ecR$ in the nanopore is of order one, irrespective of the value of λ_D/R. I show that this is because the Dukhin number, rather than Debye overlap, controls the selectivity of the nanopore. This result suggests the possibility of designing large-nanopore ($10-100$ nm), high-conductance membranes exhibiting significant ion-selectivity. Such membranes would have potentially dramatic implications for the efficiency of osmotic energy conversion and separation techniques. Numerical solutions for ICR induced by geometric and charge asymmetry are also presented, illustrating the universality of the underlying mechanism of dynamic selectivity, and limiting and linear response conductances are derived. The latter are potentially useful for the experimental determination of surface charge densities. The majority of this work is presented in 'Beyond the tradeoff: Dynamic selectivity in ion transport and current rectification' (Poggioli *et al.*, 2019, *J. Phys. Chem. B*, **123**, 1171–1185).

2.1 Introduction

The work presented in this thesis is principally motivated by a desire to understand under what conditions and via what mechanisms nonlinear ionic transport can be obtained in strongly confined systems. The prototypical (and simplest) example of such nonlinear transport is ionic current rectification (ICR), illustrated in Fig. 2.1a. In ICR ionic currents driven through nanopores by applied voltages of equal magnitude and opposite sign are found to be of unequal magnitude, in analogy to solid-state semiconductor diodes (Shockley, 1949; Bocquet & Charlaix, 2010). ICR has been extensively studied experimentally and via continuum simulations (*e.g.*, Ai *et al.*, 2010; Cervera *et al.*, 2006; Constantin & Siwy, 2007; Liu *et al.*, 2007; Nguyen *et al.*, 2010; Siwy & Fuliński, 2002; Wang *et al.*, 2007; Kubeil & Bund, 2011; Lan *et al.*, 2011; Laohakunakorn & Keyser, 2015; White & Bund, 2008; Kovarik *et al.*, 2009; Li *et al.*, 2013), though comparatively few studies have examined the phenomenon analytically (Picallo *et al.*, 2013; Siwy & Fuliński, 2002; Vlassiouk *et al.*, 2008b). Experimentally, it is found that ICR may be induced by unequal reservoir concentrations (Cheng & Guo, 2007), asymmetric geometries (Cervera *et al.*, 2006; Perry *et al.*, 2010; Siwy & Fuliński, 2002; Vlassiouk & Siwy, 2007; Kovarik *et al.*, 2009; White *et al.*, 2006), or asymmetric surface charge distributions (Karnik *et al.*, 2007; Nguyen *et al.*, 2010; Li *et al.*, 2013).

ICR is generally understood to be a consequence of the accumulation or depletion of ionic concentration induced by a gradient in ion selectivity along the length of a nanopore (Woermann, 2003). The key parameter controlling the local selectivity is accordingly understood to be the ratio of the local Debye length λ_D to the local nanopore radius R. The Debye length is defined as (Appendix A)

$$\lambda_D \equiv \sqrt{\frac{\epsilon_r \epsilon_0 k_B T}{e^2 \sum_j z_j^2 c_j}}, \tag{2.1}$$

where ϵ_r and ϵ_0 are, respectively, the relative dielectric permittivity of the solvent and the vacuum permittivity, k_B is the Boltzmann constant, T is the thermodynamic temperature, e is the elementary charge, z_j is the valence of the j^{th} ionic species, and c_j is the concentration of the j^{th} ionic species. As illustrated in Fig. 2.1b, this length scale characterizes the thickness of the diffuse layer of net ionic charge that forms in the vicinity of charged surfaces (Appendix A; Bocquet & Charlaix, 2010). As the diffuse layer must counterbalance the surface charge, a region of strong Debye layer overlap, $\lambda_D/R \gtrsim \mathcal{O}(1)$, should be highly selective to counterions, while a region of weak Debye overlap, $\lambda_D/R \ll 1$, should be essentially non-selective.

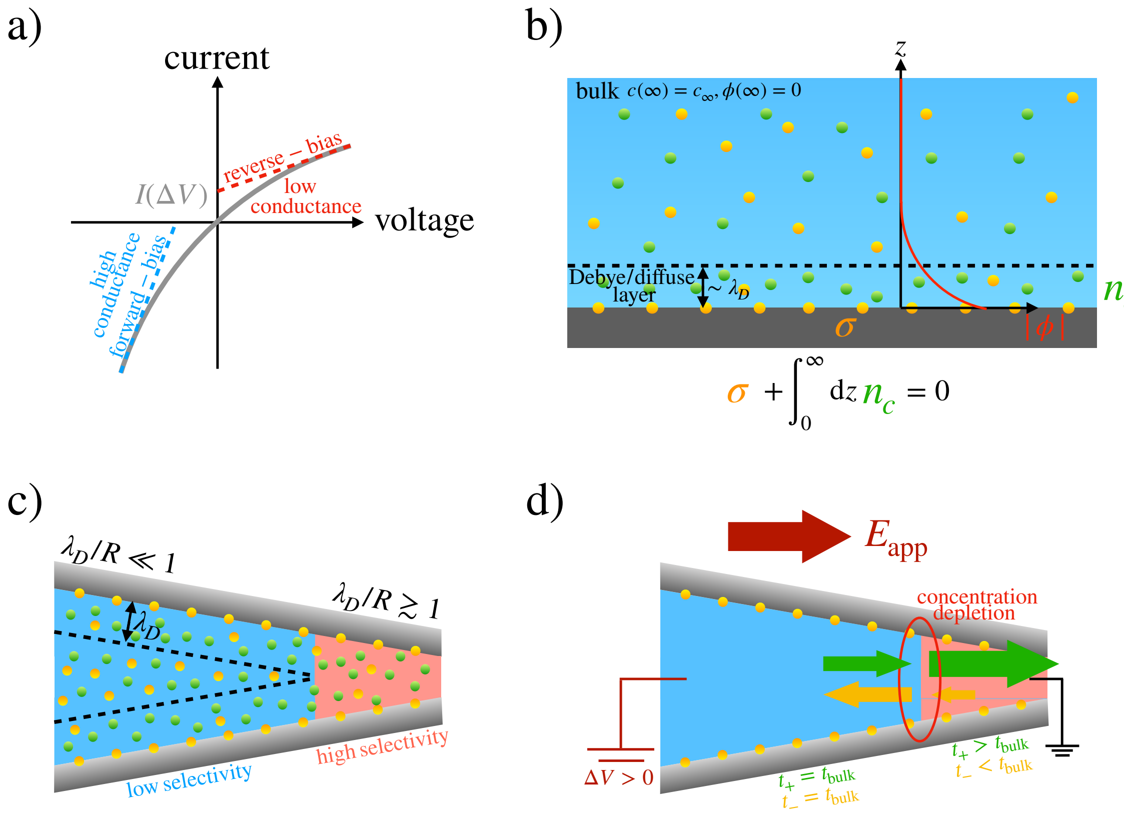

Figure 2.1: a) Sketch of a rectified current response. As illustrated here, a positive voltage bias results in a relatively lower conductance $G = \partial I/\partial \Delta V$ and hence corresponds to the reverse-bias state, while a negative voltage bias results in a relatively higher conductance and hence corresponds to the forward-bias state. b) Definition of the Debye length. In the vicinity of a charged solid-liquid interface, a diffuse layer forms in which the total and counterion concentrations are enhanced and the coion concentrations are suppressed. The characteristic thickness of this diffuse layer is given by the Debye length λ_D, as defined in Eq. 2.1 and discussed at length in Appendix A. The enhancement of counterion concentration and the suppression of coion concentration results in a net ionic charge density n_c, the integral of which must balance the surface charge density σ, a condition known as local electroneutrality. In addition to the modified ionic densities, the net ionic charge results in a deviation of the electrostatic potential ϕ from its value in the bulk. c) Sketch of the Debye layer in a conical nanopore with negative surface charge density. Here, the base radius is taken to be much larger than the Debye length, while the tip radius is taken to be smaller than the Debye length, resulting in a region of Debye overlap in the vicinity of the tip. Debye overlap is commonly understood to result in significant ion selectivity, while the absence of Debye overlap in the base of the nanopore is understood to result in essentially non-selective transport there. d) Illustration of ionic depletion in the vicinity of the conical nanopore tip under a positive voltage bias (that is, an applied field directed from base to tip). Near the tip, the high selectivity results in enhancement of the cation (counterion) transference t_+ and suppression of the anion (coion) transference t_-, while both the cation and anion transference take their bulk values in the essentially non-selective base. The result at steady state is a depletion of ionic concentration in the vicinity of the tip and a suppressed nanopore conductance corresponding to the reverse-bias state.

Debye overlap has significant consequences for ionic transport through the pore. In order to illustrate the underlying physical mechanisms, consider a conical nanopore with a uniform surface charge density, as discussed in Woermann (2003). When $\lambda_D/R \gtrsim \mathcal{O}(1)$ in the vicinity of the nanopore tip, continuity of the chemical potential between the tip and the connected reservoir results in the formation of a local Donnan equilibrium as discussed in Appendix A, and this region is highly selective to (positive) counterions (Fig. 2.1c). The tip is then a region of increased transference of cations and suppressed transference of anions. Thus, when an external electric field is directed from the (non-selective) base to the (highly selective) tip, both cations and anions pass from regions of relatively lower to relatively higher transference, and the result at steady state is a depletion of ionic concentration in the nanopore interior (Fig. 2.1d). The depletion of charge carriers results in a decrease of the local conductivity and corresponds to the low conductance (reverse-bias) diode state. On the other hand, if the direction of the applied field is inverted, both ionic species pass from regions of relatively high to relatively low transference, resulting in an accumulation of ionic concentration. This accumulation of charge carriers likewise results in a high conductance (forward-bias) state. Altogether, we anticipate that two criteria are prerequisite for the observation of nonlinear ionic transport generally, and ionic current rectification in particular: 1) a maximum value of $\lambda_D/R \gtrsim 1$ and 2) a gradient in λ_D/R, and hence in the local ionic selectivity, across the pore. The mechanism of concentration accumulation and depletion in ICR has been extensively corroborated numerically (Ai *et al.*, 2010; Vlassiouk *et al.*, 2008b; Cervera *et al.*, 2006; Constantin & Siwy, 2007; Liu *et al.*, 2007; Nguyen *et al.*, 2010; Cheng & Guo, 2010; Kubeil & Bund, 2011; Lan *et al.*, 2011; Laohakunakorn & Keyser, 2015; White & Bund, 2008) and experimentally (Perry *et al.*, 2010).

However, recent studies have indicated not only that the parameter λ_D/R fails to predict the occurrence or strength of rectification, but also that significant rectification may be obtained even when the Debye length is one-to-three orders of magnitude smaller than the minimum nanopore radius (Kovarik *et al.*, 2009; Kubeil & Bund, 2011; Lan *et al.*, 2011; Laohakunakorn & Keyser, 2015; White & Bund, 2008; White *et al.*, 2006; Jubin *et al.*, 2018; He *et al.*, 2017; Lin *et al.*, 2018). To my knowledge, no consistent alternative criterion has been proposed to predict the occurrence of ICR. Furthermore, while there have been many numerical simulations of ICR within the Poisson-Nernst-Planck (PNP) or Poisson-Nernst-Planck-Stokes (PNPS) framework, few studies have offered a detailed theoretical analysis of the phenomenon, and these studies are typically confined to quite specialized scenarios, (*e.g.*, Picallo *et al.*, 2013).

In this Chapter, I examine ionic transport and current rectification in the limits of no Debye overlap ($\lambda_D/R \ll 1$) and strong Debye overlap ($\lambda_D/R \gg 1$). I find that the nanopore selectivity is not determined by the relative value of the Debye length λ_D compared to the pore radius R, but rather by a dynamic criterion related to the relative magnitudes of the surface and bulk ionic conductances. This introduces the so-called Dukhin length ℓ_{Du}, defined as the ratio of the surface conductivity to the bulk conductivity in the nanopore (Bocquet & Charlaix, 2010). The Dukhin length can be adequatly rewritten in terms of the charge density on the pore surface, σ, as $\ell_{\mathrm{Du}} = (|\sigma|/e)/c$, with c the bulk salt concentration (Bocquet & Charlaix, 2010). A dimensionless Dukhin number is accordingly introduced as (Appendix A)

$$\mathrm{Du} \equiv \frac{\ell_{\mathrm{Du}}}{R} \equiv \frac{|\sigma|}{ecR}. \tag{2.2}$$

The Dukhin length approaches values of hundreds of nanometers for typical surface charges in the range of $10 - 100$ mC m^{-2} and concentrations in the range of $0.1 - 1$ mM, one-to-two orders of magnitude larger than the corresponding Debye lengths.

As I demonstrate below, substantial ionic selectivity may be obtained when the nanopore radius is comparable to the Dukhin length, *i.e.*, when $\mathrm{Du} \sim 1$. This is consistent with numerical results indicating substantial ion-selectivity may be obtained in highly charged pores with radii much larger than the Debye length (Vlassiouk *et al.*, 2008a), and it is in stark contrast to traditional ion-selective membranes, which typically have subnanometric pore sizes (Siria *et al.*, 2017). I term this mechanism dynamic selectivity, in contrast to the ‘thermodynamic’ picture of ionic selectivity based on Debye overlap and the formation of a Donnan equilibrium at the ends of the nanopore, (*e.g.*, Woermann, 2003; Plecis *et al.*, 2005; Bocquet & Charlaix, 2010). The possibility of obtaining significant selectivity for large ($10 - 100$ nm) pores may have significant implications for, *e.g.*, osmotic energy generation; I will discuss this point in more detail below.

Furthermore, I will show below that a gradient in the local Dukhin number along the length of the nanopore results in a repartitioning of the fraction of the ionic transport carried in the non-selective bulk and in the highly selective Debye layer. It is this repartitioning, rather than Debye overlap and the formation of a local Donnan equilibrium at one end of the nanopore, that results in ICR.

Though I am particularly interested in rationalizing those experimental (Lan *et al.*, 2011; Jubin *et al.*, 2018; Kovarik *et al.*, 2009; White *et al.*, 2006; He *et al.*, 2017; Lin *et al.*, 2018) and numerical (Kubeil & Bund, 2011; Laohakunakorn & Keyser, 2015; White & Bund, 2008; Jubin *et al.*, 2018; Vlassiouk *et al.*, 2008a) results indicating that substantial rectification and selectivity may be obtained in the absence of Debye overlap, I will examine ionic transport in both the limit of no overlap and strong overlap. This is done for completeness and to illustrate the similarity of the results for both rectification and selectivity at these opposing ends of parameter space, consistent with the assertion that the Dukhin number is the principal parameter controlling rectification and selectivity, with λ_D/R having only a secondary quantitative influence.

I will start by deriving one-dimensional transport equations from a radial integration of the axisymmetric PNP equations in the limit $\lambda_D/R \ll 1$ and $\mathrm{Du} \sim 1$ and comparing the form of these equations to the more well known one-dimensional transport equations valid in the limit of strong overlap ($\lambda_D/R \gg 1$) (*e.g.*, Bocquet & Charlaix, 2010; Picallo *et al.*, 2013). From these transport equations, I am able to derive simple implicit expressions for the current-voltage (IV) response in a concentration diode. To my knowledge, these solutions have not been presented previously in the literature. Additionally, I will give numerical solutions of these transport equations for a geometric diode (rectification induced by an asymmetric, continuously varying radius) and a charge diode (rectification induced by an asymmetric, continuously varying surface charge density distribution). These solutions will further illustrate the universality of the underlying mechanism of dynamic selectivity in ICR and the key role of the Dukhin number. Finally, I derive analytical expressions for general limiting and linear response conductances directly from the transport equations that will be useful in estimating, for example, surface charge densities from rectified IV curves.

2.2 1D Transport Equations

In this section, I derive one-dimensional transport equations for the electrostatic potential and total ionic concentration at the nanopore centerline from the axisymmetric PNP equations in the limit of no overlap $\lambda_D/R \ll 1$ and compare them to the well-known one-dimensional transport equations valid in the limit of strong overlap $\lambda_D/R \gg 1$. In both cases, the derivation relies on the geometric constraint $R_0/L_0 \ll 1$, where R_0 is a scale of the nanopore radius, and L_0 is a characteristic scale of variation of the nanopore geometry. Such a slowly varying approximation implies that a Poisson-Boltzmann (PB) equilibrium holds locally on each cross-section (Fair & Osterle, 1971; Rankin & Huang, 2016). The consequences of a local PB equilibrium are explored in detail in Appendix A, and I will make use of the results developed there in my derivation.

2.2.1 No Overlap ($\lambda_D/R \ll 1$)

I first focus on the limit that $\lambda_D/R \ll 1$ and Du $\gg \lambda_D/R$. The results obtained in this limit demonstrate that the Dukhin number is the principal parameter controlling selectivity and ICR, and that ICR may occur even in the absence of Debye overlap anywhere along the length of the nanopore, consistent with experimental observations. There is no Debye overlap in the center of the nanopore so that the electrolyte there is electroneutral, and we may partition the ionic concentrations and electrostatic potential as follows (Fair & Osterle, 1971):

$$c_\pm(x,r) = \frac{c_0(x)}{2} + \delta c_\pm(x,r), \quad \text{and} \tag{2.3}$$

$$\phi(x,r) = \phi_0(x) + \delta\phi(x,r), \tag{2.4}$$

where $c_0(x) \equiv c(x,0)$ is the value of the total ionic concentration $c \equiv c_+ + c_-$ at the nanopore centerline ($r = 0$), $\phi_0(x) \equiv \phi(x,0)$ is the electrostatic potential at the nanopore centerline, and $\delta c_\pm(x,r)$ and $\delta\phi(x,r)$ are the radial deviations in the ionic concentrations and electrostatic potential induced by the formation of a screening Debye layer in the vicinity of the nanopore wall. In Eq. 2.3, we have assumed a symmetric (z:z) salt. In what follows, we will assume a monovalent (1:1) salt in which the cation and anion have identical mobility and diffusion coefficients.

With this notation and these assumptions, the steady-state PNP equations reduce to

$$j_\pm = -D\left(\partial_x c_\pm \pm \frac{e}{k_BT} c_\pm \partial_x \phi\right), \tag{2.5}$$

$$\frac{d}{dx}\left(\int_0^R 2\pi r \mathrm{d}r j_\pm\right) \equiv \frac{dJ_\pm}{dx} = 0, \tag{2.6}$$

$$\epsilon_r\epsilon_0 \frac{\partial_r\left(r\partial_r\delta\phi\right)}{r} + n_c \approx \epsilon_r\epsilon_0\partial_Z^2\delta\phi + n_c = 0, \tag{2.7}$$

$$c = c_0 \cosh\left(\frac{e\delta\phi}{k_BT}\right), \quad \text{and} \tag{2.8}$$

$$n_c = -ec_0 \sinh\left(\frac{e\delta\phi}{k_BT}\right), \tag{2.9}$$

where D is the diffusion coefficient, and $n_c \equiv e(c_+ - c_-)$ is the ionic charge density. In Eq. 2.7 I have neglected the portion of the radial Laplacian induced by the curvature of the nanopore wall as it is suppressed by a factor $\lambda_D/R \ll 1$ relative to ∂_r^2, and I have introduced the coordinate $Z \equiv R - r$. Eq. 2.5 gives the Nernst-Planck parameterization of the ion number flux densities in the along-flow (x) direction; Eq. 2.6 is the cross-sectionally integrated continuity equation at steady state; Eq. 2.7 is the Poisson equation, retaining only the radial component of the electric field divergence in accordance with the slowly varying approximation; and Eqs. 2.8 and 2.9 are the distributions of the total ionic concentration and ionic charge density obtained from the Boltzmann distribution, applied on the assumption of a slowly varying geometry. Finally, I have neglected advection as it is found to have only a minor influence on ICR over most of parameter space (Ai *et al.*, 2010; Vlassiouk *et al.*, 2008a), and such an approach allows for tractable analytical derivations.

Before continuing, I introduce dimensionless rescaled variables, as listed in Table 2.1. I rescale the x-coordinate by the total nanopore length L, the surface charge σ by its maximum magnitude $|\sigma|_{\max}$, the nanopore radius by its minimum value $R_{\min}$, and the ionic concentrations by the average of the reservoir concentrations $\bar{c}$. I further recast Eqs. 2.5 and 2.6 in terms of the rescaled solute flux $J \equiv J_+ + J_- \equiv \int \mathrm{dA} j$ and ionic current $I \equiv J_+ - J_- \equiv \int \mathrm{dA} i$. With these modifications, the rescaled governing equations become

$$j = -\left(\partial_x c + n_c \partial_x \phi\right), \tag{2.10}$$

$$i = -\left(\partial_x n_c + c \partial_x \phi\right), \tag{2.11}$$

$$\frac{dJ}{dx} = \frac{dI}{dx} = 0, \tag{2.12}$$

$$\left(\frac{\lambda_D^{\mathrm{ref}}}{R_{\min}}\right)^2 \partial_Z^2 \delta\phi + n_c = 0, \tag{2.13}$$

$$c = c_0 \cosh(\delta\phi), \quad \text{and} \tag{2.14}$$

$$n_c = -c_0 \sinh(\delta\phi), \tag{2.15}$$

where I have introduced a reference Debye length $\lambda_D^{\mathrm{ref}} \equiv \sqrt{k_B T \epsilon_r \epsilon_0 / e^2 \bar{c}}$, defined in terms of the mean reservoir concentration $\bar{c}$.

quantity	variable	rescaled
position	x	$x \to Lx$
radius	R	$R \to R_{\min}R$
concentration	c	$c \to \bar{c}c$
ionic charge density	n_c	$n_c \to e\bar{c}n_c$
electrostatic potential	ϕ	$\phi \to (k_BT/e)\phi$
chemical potential	$\mu_\pm$	$\mu_\pm \to k_BT\mu_\pm$
flux density	$j_\pm$	$j_\pm \to (D\bar{c}/L)j_\pm$
surface charge	σ	$\sigma \to \lvert\sigma\rvert_{\max}\sigma$

Table 2.1: Independent and dependent variables and their rescaled dimensionless counterparts.

We differentiate Eq. 2.14 (2.15) with respect to x, insert the result into Eq. 2.10 (2.11), and integrate on the cross-section to obtain

$$\frac{J}{\pi R^2} = -\frac{dc_0}{dx} - \frac{\langle \delta c\rangle}{c_0}\frac{dc_0}{dx} - \frac{\langle n_c\rangle}{c_0}c_0\frac{d\phi_0}{dx}, \quad \text{and} \tag{2.16}$$

$$\frac{I}{\pi R^2} = -c_0\frac{d\phi_0}{dx} - \frac{\langle n_c\rangle}{c_0}\frac{dc_0}{dx} - \frac{\langle \delta c\rangle}{c_0}c_0\frac{d\phi_0}{dx}, \tag{2.17}$$

where $\langle\rangle \equiv A^{-1}\int \mathrm{dA}$ denotes a cross-sectional average. The integral of the charge density is set by the condition of local electroneutrality, a necessary consequence of a local PB equilibrium (Appendix A, Eq. A.41); the integral of δc may be evaluated using PB equilibrium theory (Appendix A, Eq. A.45) in the limit $\lambda_D/R \ll 1$. The condition of local electroneutrality requires that

$$\frac{\langle n_c\rangle}{c_0} = -2\mathrm{Du}_{\mathrm{ref}}\frac{\sigma}{Rc_0} \equiv -2\mathrm{Du}(x), \tag{2.18}$$

where $\mathrm{Du}_{\mathrm{ref}} \equiv |\sigma|_{\max}/e\bar{c}R_{\min}$ is a reference Dukhin number, and $\mathrm{Du}(x)$ is the local Dukhin number. Note that $\mathrm{Du}_{\mathrm{ref}}$ is defined to be always positive, but $\mathrm{Du}(x) \equiv \mathrm{S}|\mathrm{Du}(x)|$ carries the sign of the local surface charge density. In the preceding, $\mathrm{S} \equiv \mathrm{sign}(\sigma)$ is the sign of the surface charge. The integral of δc is evaluated on the assumption of a local PB equilibrium (Eqs. 2.13 through 2.15) in Appendix A (Eq. A.45). The result is

$$\frac{\langle \delta c\rangle}{c_0} = 4\frac{\lambda_D}{R_{\min}R}\left\{\sqrt{\left[\frac{\mathrm{Du}}{2(\lambda_D/R_{\min}R)}\right]^2 + 1} - 1\right\}, \tag{2.19}$$

where $\mathrm{Du}(x)$ is the local value of the Dukhin number, and $\lambda_D(x) \equiv \lambda_D^{\mathrm{ref}}/\sqrt{c_0(x)}$ is the local Debye length. Inserting Eqs. 2.18 and 2.19 into Eqs. 2.16 and 2.17, we obtain the one-dimensional transport equations valid in the limit $\lambda_D/R \ll 1$:

$$\frac{J}{\pi R^2} = -\left[\frac{dc_0}{dx} + 4\frac{\lambda_D}{R_{\min}R}\left\{\sqrt{\left[\frac{\mathrm{Du}}{2(\lambda_D/R_{\min}R)}\right]^2+1}-1\right\}\frac{dc_0}{dx} - 2\mathrm{Du}(x)c_0\frac{d\phi_0}{dx}\right], \quad \text{and} \tag{2.20}$$

$$\frac{I}{\pi R^2} = -\left[c_0\frac{d\phi_0}{dx} - 2\mathrm{Du}(x)\frac{dc_0}{dx} + 4\frac{\lambda_D}{R_{\min}R}\left\{\sqrt{\left[\frac{\mathrm{Du}}{2(\lambda_D/R_{\min}R)}\right]^2+1}-1\right\}c_0\frac{d\phi_0}{dx}\right], \tag{2.21}$$

where I and J are of course constant along the length of the nanopore (Eq. 2.12).

In the limit $(\lambda_D/R_{\min}R)/\mathrm{Du} \to 0$, the average deviation in the total ionic concentration (Eq. 2.19) reduces to

$$\frac{\langle \delta c\rangle}{c_0} = 2|\mathrm{Du}(x)|. \tag{2.22}$$

This limit is particularly relevant in rationalizing experimental observations of significant selectivity and rectification when the Debye length is much smaller than the scale of confinement but the Dukhin number is of order one. Furthermore, the resulting transport equations are analytically tractable in the case of a concentration diode. Inserting Eq. 2.22 into Eqs. 2.16 and 2.17 (or equivalently taking the limit of Eqs. 2.20 and 2.21 as $(\lambda_D/R_{\min}R)/\mathrm{Du} \to 0$), we obtain

$$\boxed{\frac{J}{\pi R^2} = -\left[\frac{dc_0}{dx} + 2|\mathrm{Du}(x)|\left(\frac{dc_0}{dx} - \mathrm{S}c_0\frac{d\phi_0}{dx}\right)\right], \quad \text{and}} \tag{2.23}$$

$$\boxed{\frac{I}{\pi R^2} = -\left[c_0\frac{d\phi_0}{dx} - \mathrm{S}2|\mathrm{Du}(x)|\left(\frac{dc_0}{dx} - \mathrm{S}c_0\frac{d\phi_0}{dx}\right)\right].} \tag{2.24}$$

Note that we have implicitly assumed in Eqs. 2.23 and 2.24 that the sign of the surface charge S does not change along the length of the nanopore. If the sign of the surface charge does change at one (or several) points along the length of the nanopore, Eqs. 2.23 and 2.24 may be applied in each region delineated by a discontinuity in $\mathrm{S}(x)$, matching c_0 and ϕ_0 at each discontinuity. (More about the proper boundary conditions for Eqs. 2.23 and 2.24 will be said below.)

It is useful to distinguish between those terms in Eqs. 2.23 and 2.24 that arise from transport outside of the Debye layer (bulk transport) and those arising from transport within the Debye layer (surface transport). In the equation for the solute flux (Eq. 2.23), the terms represent, from left to right, bulk diffusion, surface diffusion, and surface electrophoretic mass transport. In the equation for the ionic current (Eq. 2.24), the terms represent bulk electrophoretic current, surface charge diffusion, and surface electrophoretic current. We see that the local Dukhin number, which sets the cross-sectionally averaged ionic charge (Eq. 2.18), as well as the cross-sectionally averaged excess concentration when $\lambda_D/R_{\mathrm{min}}R \ll \mathrm{Du}$ (Eq. 2.22), determines the ratio of surface to bulk transport. Motivated by this observation, we quantify the ratio of the surface transport to the total transport by the following surface transport ratio (STR):

$$\mathrm{STR}(x) \equiv \frac{2|\mathrm{Du}(x)|}{1+2|\mathrm{Du}(x)|}. \tag{2.25}$$

We see immediately that the partitioning of the transport into surface and bulk components adjusts along the length of the nanopore and is controlled locally by the Dukhin number. In the case that there is a large asymmetry in Dukhin number on either end of the nanopore, this can result in a substantial repartitioning of the transport in the nanopore interior, the consequences of which will be explored in the following sections.

An illustrative form of Eqs. 2.23 and 2.24 is obtained by introducing the definition of the local Dukhin number, Eq. 2.18, and defining the coion and counterion fluxes $J_{\mathrm{co/count}} \equiv (J \pm \mathrm{S}I)/2$ and chemical potentials $\mu_{\mathrm{co/count}} \equiv \ln(c_0/2) \pm \mathrm{S}\phi$. Inserting these definitions into Eqs. 2.23 and 2.24, we obtain

$$\frac{J_{\mathrm{co}}}{\pi R^2} = -\frac{c_0}{2}\frac{d\mu_{\mathrm{co}}}{dx}, \quad \text{and} \tag{2.26}$$

$$\frac{J_{\mathrm{count}}}{\pi R^2} = -\left(\frac{c_0}{2} + 2\mathrm{Du}_{\mathrm{ref}}\frac{|\sigma|}{R}\right)\frac{d\mu_{\mathrm{count}}}{dx}. \tag{2.27}$$

In Eqs. 2.26 and 2.27, we recognize $c_0/2$ as the concentration of both coions and counterions at the nanopore centerline. Further, in Eq. 2.27, we recognize $2\mathrm{Du}_{\mathrm{ref}}|\sigma|/R$ as the additional concentration accumulated in the Debye layer (Eq. 2.22). The term $2\mathrm{Du}_{\mathrm{ref}}|\sigma|/R \times d\mu_{\mathrm{count}}/dx$ in Eq. 2.27 represents the entirety of the surface transport in the nanopore; this indicates that coions are perfectly excluded from the Debye layer in the limit $\lambda_D/R \ll \mathrm{Du}$ (R dimensioned).

2.2.2 Strong Overlap ($\lambda_D/R \gg 1$)

In the limit $\lambda_D/R \to \infty$, the profiles of ionic concentrations and electrostatic potential become radially uniform (Bocquet & Charlaix, 2010). This is shown explicitly in Appendix A, Sec. A.2.3.

In this case, the transport equations are, from Eqs. 2.10 and 2.11,

$$\frac{J}{\pi R^2} = -\left(\frac{dc}{dx} + n_c\frac{d\phi}{dx}\right), \quad \text{and} \tag{2.28}$$

$$\frac{I}{\pi R^2} = -\left(\frac{dn_c}{dx} + c\frac{d\phi}{dx}\right), \tag{2.29}$$

where c, n_c, and ϕ are the radially uniform total ionic concentration, ionic charge density, and electrostatic potential, respectively. As a consequence of the local PB equilibrium, the ionic charge density n_c must verify electroneutrality (Eqs. 2.18 and A.49): $n_c = -2\mathrm{Du}_{\mathrm{ref}}(\sigma/R) = -2\mathrm{Du}(x)c$. The transport equations (Eqs. 2.28 and 2.29) thus become

$$\boxed{\frac{J}{\pi R^2} = -\frac{dc}{dx} + 2\mathrm{Du}(x)c\frac{d\phi}{dx}, \quad \text{and}} \tag{2.30}$$

$$\boxed{\frac{I}{\pi R^2} = +2\frac{d}{dx}\left[\mathrm{Du}(x)c\right] - c\frac{d\phi}{dx}.} \tag{2.31}$$

I will employ Eqs. 2.23 (2.30) and 2.24 (2.31) below to develop an implicit analytical solution for the current-voltage (IV) relationship in a concentration diode and numerical solutions for the IV relationships in geometric and charge diodes in the limit of no (strong) overlap.

2.2.3 Boundary Conditions

Before solving Eqs. 2.23 and 2.24 or Eqs. 2.28 and 2.29, we must take care to ensure that we are imposing appropriate boundary conditions at the nanopore ends. This is a nontrivial question because the rapid variation in local Dukhin number (from a nonzero value in the nanopore interior to zero in the reservoir) that occurs on either end of the nanopore means that the slowly varying approximation we have used to impose a local PB equilibrium breaks down (Picallo *et al.*, 2013). In one-dimensional PNP-based models of nanopore ionic transport, this is typically taken into account by imposing continuity of the chemical potential $\mu_\pm = \ln c_\pm \pm \phi$ across the junction and local electroneutrality on either side (Cervera *et al.*, 2006; Constantin & Siwy, 2007; Vlassiouk *et al.*, 2008b; Bocquet & Charlaix, 2010; Picallo *et al.*, 2013). This is justified as follows: The rapid variation in local geometry and surface charge and consequently in the local Dukhin number results in localized deviations from equilibrium and electroneutrality and rapid variations in electrostatic potential and ionic concentrations. The scale of this adjustment region is given by the Debye length. (See Shockley (1949) for an extensive discussion of this point in the equivalent context of semiconductor physics.) Thus, in the limit $\lambda_D/L \to 0$, the adjustment region may be treated as a point discontinuity in the ionic concentrations and electrostatic potential. However, as the ionic flux densities $j_\pm = -c_\pm \partial_x \mu_\pm$ are proportional to the gradient of the chemical potential, the discontinuities in ionic concentration and electrostatic potential must be such that continuity of chemical potential is maintained, ensuring finite ionic fluxes. Outside of this adjustment region, the ions again locally equilibrate, and thus local electroneutrality is imposed on either side of the junction.

No Overlap ($\lambda_D/R \ll 1$)

In the limit of no overlap ($\lambda_D/R \ll 1$), the profiles of electrostatic potential and ionic concentrations are radially nonuniform, and we must ensure that the chemical potentials just inside the ends of the nanopore are equal to the uniform reservoir values everywhere on the cross-section. However, as we have already assumed a radially uniform chemical potential in locally applying a PB equilibrium, this condition is satisfied by equating the chemical potential in the connecting reservoir to the value on the nanopore centerline. Furthermore, as the ionic charge vanishes at the nanopore centerline, imposition of electroneutrality there amounts to imposing $(c_+^0)_{\ell/r} = (c_-^0)_{\ell/r} = c_0^{\ell/r}/2$, where '$\ell/r$' indicates the value just inside the left/right end of the nanopore. Chemical continuity across the junction thus requires $\ln(c_{L/R}/2) \pm V_{\text{res}}^{L/R} = \ln(c_0^{\ell/r}/2) \pm \phi_0^{\ell/r}$, where $c_{L/R}$ and $V_{\text{res}}^{L/R}$ are, respectively, the total ionic concentration and electrostatic potential imposed in the left/right reservoir. This condition is satisfied by (Fair & Osterle, 1971; Rankin & Huang, 2016)

$$\boxed{c_0^{\ell/r} = c_{L/R}, \quad \text{and}} \tag{2.32}$$

$$\boxed{\phi_0^{\ell/r} = V_{L/R}.} \tag{2.33}$$

We note that this condition still results in finite discontinuities in the ionic concentrations and electrostatic potential within the Debye layer.

Strong Overlap ($\lambda_D/R \gg 1$)

In the opposing limit of strong overlap ($\lambda_D/R \gg 1$), the profiles of ionic concentration and electrostatic potential are radially uniform, and the ionic charge density is therefore uniform and nonvanishing everywhere on the cross-section. The conditions of chemical continuity and local electroneutrality applied between the reservoir and nanopore interior are the same conditions imposed when considering the formation of a Donnan equilibrium, and we may directly transcribe the results derived in Appendix A, Sec. A.3 (Eqs. A.58 and A.59):

$$\boxed{c_{\ell/r} = c_{L/R}\sqrt{1+(2\mathrm{Du}_{L/R})^2}, \quad \text{and}} \tag{2.34}$$

$$\boxed{\phi_{\ell/r} = V_{\text{res}}^{L/R} + \mathrm{S}\frac{1}{2}\ln\left(\frac{\sqrt{1+(2\mathrm{Du}_{L/R})^2}+2\mathrm{Du}_{L/R}}{\sqrt{1+(2\mathrm{Du}_{L/R})^2}-2\mathrm{Du}_{L/R}}\right),} \tag{2.35}$$

with the 'reservoir' Dukhin numbers $\mathrm{Du}_{L/R}$ defined as

$$\boxed{\mathrm{Du}_{L/R} \equiv \frac{|\sigma|_{\ell/r}}{ec_{L/R}R_{\ell/r}},} \tag{2.36}$$

where $|\sigma|_{\ell/r}$ and $R_{\ell/r}$ are, respectively, the surface charge magnitude and nanopore radius at the left/right end of the nanopore.

We note that Eqs. 2.34 and 2.35 describe the formation of a local Donnan equilibrium at either end of the nanopore, and the second term on the RHS of Eq. 2.35 proportional to the sign of the surface charge corresponds to the Donnan potential at equilibrium.

2.3 Dynamic Selectivity

As noted above, in the slowly varying limit ($R_0/L_0 \ll 1$) considered here, the ionic concentration profiles on the cross-section deviate negligibly from those predicted by PB equilibrium theory. We may therefore apply this equilibrium theory to determine how the ionic selectivity on the cross-section is influenced by Debye overlap (λ_D/R) and the Dukhin number. Using Eqs. 2.18 and 2.19, we determine the cross-sectionally averaged total concentration, $\langle c\rangle = \langle \delta c\rangle + c_0$, and the cross-sectionally averaged co- and counterion concentrations, $\langle c_{\text{co/count}}\rangle = (\langle c\rangle \pm \mathrm{S}\langle n_c\rangle)/2$:

$$\frac{\langle c\rangle}{c_0} = 1 + 4\frac{\lambda_D}{R_{\min}R}\left\{\sqrt{\left[\frac{\mathrm{Du(x)}}{2(\lambda_D/R_{\min}R)}\right]^2+1}-1\right\}, \quad \text{and} \tag{2.37}$$

$$\frac{\langle c_{\text{co/count}}\rangle}{c_0} = \frac{1}{2} + 2\frac{\lambda_D}{R_{\min}R}\left\{\sqrt{\left[\frac{\mathrm{Du(x)}}{2(\lambda_D/R_{\min}R)}\right]^2+1}-1\right\} \mp |\mathrm{Du}(x)|. \tag{2.38}$$

We take the ratio $\langle c_{\text{count}}\rangle/\langle c\rangle$ as a metric of selectivity:

$$\boxed{\frac{\langle c_{\text{count}}\rangle}{\langle c\rangle} = \frac{\frac{1}{2} + 2\frac{\lambda_D}{R_{\text{min}}R}\left\{\sqrt{\left[\frac{\text{Du(x)}}{2(\lambda_D/R_{\text{min}}R)}\right]^2+1}-1\right\} + |\text{Du}(x)|}{4\frac{\lambda_D}{R_{\text{min}}R}\left\{\sqrt{\left[\frac{\text{Du(x)}}{2(\lambda_D/R_{\text{min}}R)}\right]^2+1}-1\right\}+1}.} \tag{2.39}$$

This result is plotted in Fig. 2.2 against Du for several values of $\lambda_D/R_{\text{min}}R$. Its value ranges between 1/2, indicating the total average concentration is equally partitioned between coions and counterions, and the nanopore is locally non-selective, and unity, indicating that the entirety of the average concentration is due to counterions, and the nanopore is perfectly selective. We find that, in the range $0 < \lambda_D/R < 2(10^{-1})$, the nanopore selectivity is strongly influenced by the local Dukhin number in the range $10^{-1} < \text{Du} < 10^{1}$ (Fig. 2.2). In comparison, the influence of λ_D/R on selectivity for this range of λ_D/R is substantially less pronounced.

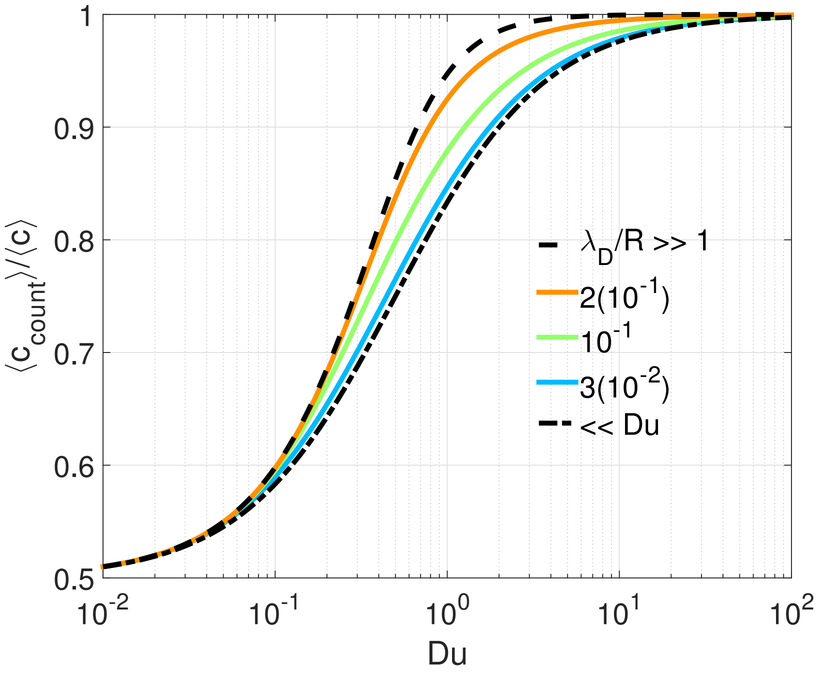

Figure 2.2: The ratio of the cross-sectionally averaged counterion concentration to the cross-sectionally averaged total concentration, a metric of the nanopore selectivity, as a function of Dukhin number. The lines are colored according to λ_D/R, as indicated in the legend. The dashed (dot-dashed) line indicates the curve obtained in the limit $\lambda_D/R \to \infty$ ($\to 0$).

2.3.1 From Equilibrium to Dynamic Selectivity

An upper limit on the selectivity induced by Debye overlap may be obtained by considering the selectivity of the nanopore entrance/exit in the limit $\lambda_D/R \to \infty$. In this case, a Donnan equilibrium forms at the nanopore tips, and we may calculate the ratio of the counterion concentration to the total concentration according to Eqs. A.57 and A.58:

$$\boxed{\frac{c_{\text{count}}}{c} = \frac{1}{2}\frac{\sqrt{1+(2|\text{Du}|)^2}+2|\text{Du}|}{\sqrt{1+(2|\text{Du}|)^2}}.} \tag{2.40}$$

This upper limit exceeds the selectivity obtained above for $\lambda_D/R = 2(10^{-1})$ only slightly (Fig. 2.2), indicating that the nanopore selectivity rapidly saturates for values of $\lambda_D/R \gtrsim 1/5$.

A lower limit, valid when $\lambda_D/R \ll \text{Du}$, is obtained from Eq. 2.39. In this case, we find

$$\boxed{\frac{\langle c_{\text{count}}\rangle}{\langle c\rangle} = \frac{1}{2}\left(1+\frac{2|\text{Du}|}{1+2|\text{Du}|}\right) \equiv \frac{1}{2}\left(1+\text{STR}\right),} \tag{2.41}$$

where in the second equality I have made use of Eq. 2.25. Eq. 2.41 shows the deep connection between transport and selectivity and can be made more intuitive as follows. As shown above, the Debye layer in this limit is perfectly selective, so that the ratio of counterion concentration to total concentration is unity. As always, the bulk is perfectly non-selective, so that the ratio there is 1/2. As the STR is the ratio of surface transport to total transport, the ratio of bulk-to-total transport is 1− STR, and we may estimate the total selectivity on the cross-section based on the partitioning of the ionic transport as

$$\underbrace{\frac{1}{2}\times(1-\text{STR})}_{\text{bulk}} + \underbrace{1\times\text{STR}}_{\text{surface}} = \frac{1}{2}\left(1+\text{STR}\right).$$

We thus recover the result given in Eq. 2.41. This result illustrates that it is the selectivity in the bulk and surface weighted by the dynamic partitioning of the ionic transport that controls local selectivity.

Together, the upper and lower limits on selectivity (Eqs. 2.40 and 2.41, respectively), define an envelope of selectivity variation with λ_D/R (Fig. 2.2). The conclusion of these results is apparent: the principal parameter controlling nanopore selectivity is not λ_D/R but the local Dukhin number. This result may be understood as follows: when λ_D/R is small, the local Dukhin number controls the fraction of the transport in the Debye layer (Eq. 2.25). It also controls the selectivity of the Debye layer, which we show explicilty by calculating $\langle \delta c_{\text{count}} \rangle / \langle c \rangle$ from Eqs. 2.37 and 2.38:

$$\frac{\langle \delta c_{\text{count}} \rangle}{\langle c \rangle} = \frac{2\frac{\lambda_D}{R_{\text{min}} R}\left\{\sqrt{\left[\frac{\text{Du(x)}}{2(\lambda_D/R_{\text{min}}R)}\right]^2 + 1} - 1\right\} + |\text{Du}(x)|}{4\frac{\lambda_D}{R_{\text{min}} R}\left\{\sqrt{\left[\frac{\text{Du(x)}}{2(\lambda_D/R_{\text{min}}R)}\right]^2 + 1} - 1\right\} + 1} \xrightarrow[\frac{\lambda_D/R_{\text{min}}R}{\text{Du}} \to 0]{} \text{STR}(x), \tag{2.42}$$

where in the second expression on the RHS I have taken the limit $(\lambda_D/R_{\text{min}}R)/\text{Du} \to 0$. A large value of Du means that the majority of the ionic flux is carried within the Debye layer, and that this region is highly selective. Thus, even though the unselective bulk region takes up the majority of the cross-section, the majority of the transport must pass through the highly selective but relatively small Debye layer. As this process is controlled by the local Dukhin number and the local partitioning of ionic currents, both of which adjust dynamically, I refer to it as dynamic selectivity.

On the other hand, when λ_D/R is large, a significant surface charge (as quantified by the Dukhin number) must still be present to draw counterions into (and exclude coions from) the nanopore and thus render the nanopore highly selective. This is indicated in the Donnan result for the selectivity (Eq. 2.40). All together, the result is the dominance of the local Dukhin number in determining the local nanopore selectivity (Fig. 2.2).

These results suggest that a nanopore may exhibit significant selectivity when the pore size is comparable to the Dukhin length. As noted above, the Dukhin length reaches hundreds of nanometers for typical ionic concentrations ($0.1 - 1$ mM) and surface charge densities ($10 - 100$ mC m^{-2}). This is in strong contrast to traditional ion-selective membranes, which have typically subnanometric pore sizes (Siria *et al.*, 2017), and indeed to the typical picture of ion-selectivity as occurring only in the presence of strong Debye overlap ($\lambda_D/R \gg 1$) (Bocquet & Charlaix, 2010).

I explore this idea in Sec. 2.6 below by examining the ion selectivity in large nanopores ($\lambda_D/R \ll 1$) under an applied concentration difference and voltage in a uniform nanopore, and under an applied voltage in a conical nanopore.

2.4 Analytical Solutions for the Concentration Diode

In this section, I illustrate the principal role of the Dukhin number in ICR by developing implicit expressions for the IV relationships in concentration diodes in the regime of no overlap ($\lambda_D/R \ll 1$) using Eqs. 2.23 and 2.24 subject to boundary conditions 2.32 and 2.33, and in the regime of strong overlap ($\lambda_D/R \gg 1$) using Eqs. 2.30 and 2.31 subject to boundary conditions 2.34 and 2.35. I will show that the IV curves are structurally similar in both limits, showing strong rectification irrespective of whether there is overlap nowhere along the nanopore or strong overlap everywhere along the nanopore. This provides strong evidence that 1) $\lambda_D/R \sim 1$ somewhere along the nanopore is not a necessary condition for the observation of ICR, and 2) a gradient in the value of λ_D/R along the length of the nanopore, from a value $\lambda_D/R \ll 1$ to a value $\lambda_D/R \sim 1$ is likewise unnecessary to induce rectification. Instead, we will find 1) that a maximum Du ~ 1 is a (rough) criterion for maximum rectification, and 2) that ICR is driven by an asymmetry in Dukhin number across the nanopore.

As the rectification is fundamentally a consequence of the mechanism of dynamic selectivity outlined above, there is no fundamental mechanistic difference between ionic diodes induced by asymmetric geometry, differences in reservoir concentration, or (continuous) asymmetric surface charge profiles induced by, *e.g.*, differences in reservoir pH. I focus here on the concentration diode because I am able to derive illustrative analytical solutions.

2.4.1 Fluxes Across a Concentration Diode

I consider here the uniform nanopore configuration shown schematically in the inset of Fig. 2.3a: a nanopore of uniform radius and uniform (negative) surface charge density connects two reservoirs of unequal concentration, with the concentration in the left reservoir c_L exceeding that in the right reservoir c_R. A voltage ΔV is applied in the left reservoir while the right reservoir is held at ground. The local Dukhin number along the length of the nanopore is given by

$$\mathrm{Du}(x) = -\frac{\mathrm{Du_{ref}}}{c}, \tag{2.43}$$

where the reference Dukhin number $\mathrm{Du_{ref}} \equiv |\sigma|/e\bar{c}R$ is defined in terms of the magnitude of the uniform surface charge density, the average of the two reservoir concentrations, and the uniform nanopore radius. I have omitted the subscript zero on the concentration, and I will continue to omit the subscript in what follows, recalling that the indicated total ionic concentrations and electrostatic potentials are centerline values when we are in the no overlap regime, and the uniform values over the entire cross-section when we are in the strong overlap regime.

Note that, because the surface charge density and nanopore radius do not vary along the length of the nanopore, the variation in the local Dukhin number is determined entirely by the variation in the local concentration. In addition to the reference Dukhin number, I introduce the reservoir Dukhin numbers in accordance with Eq. 2.36 as $\mathrm{Du}_L \equiv \mathrm{Du}_{\mathrm{ref}}/c_L$ and $\mathrm{Du}_R \equiv \mathrm{Du}_{\mathrm{ref}}/c_R$, respectively. The ratio of Dukhin numbers $\mathrm{Du}_R/\mathrm{Du}_L = c_L/c_R \geq 1$ is then simply the ratio of reservoir concentrations. With these definitions, we can express the reference Dukhin number as

$$\mathrm{Du}_{\mathrm{ref}} = \frac{2}{\mathrm{Du}_L^{-1} + \mathrm{Du}_R^{-1}}. \tag{2.44}$$

I will formulate the results below in terms of the maximum Dukhin number in the system, Du_R, corresponding to the minimum reservoir concentration, and the concentration ratio $\mathrm{Du}_R/\mathrm{Du}_L = c_L/c_R$. Note that, while I do not impose particular values for the reservoir concentrations in this rescaled, dimensionless model, the concentration ratios considered here are consistent with the range of concentrations considered experimentally, typically between 0.1 mM and 1 M.

No Overlap ($\lambda_D/R \ll 1$)

With the local Dukhin number given in Eq. 2.43, Eqs. 2.23 and 2.24 become

$$\frac{J}{\pi} = -\left[\frac{dc}{dx} + 2\mathrm{Du}_{\mathrm{ref}}\left(\frac{d\mathrm{ln}c}{dx} + \frac{d\phi}{dx}\right)\right], \quad \text{and} \tag{2.45}$$

$$\frac{I}{\pi} = -\left[c\frac{d\phi}{dx} + 2\mathrm{Du}_{\mathrm{ref}}\left(\frac{d\mathrm{ln}c}{dx} + \frac{d\phi}{dx}\right)\right]. \tag{2.46}$$

With the boundary conditions given in Eqs. 2.32 and 2.33, we can directly integrate Eq. 2.45 for the solute flux:

$$\boxed{\left(\frac{\mathrm{Du}_R}{\mathrm{Du}_L} + 1\right)\frac{J}{2\pi} = \left(\frac{\mathrm{Du}_R}{\mathrm{Du}_L} - 1\right) + 2\mathrm{Du}_R\left[\ln\left(\frac{\mathrm{Du}_R}{\mathrm{Du}_L}\right) + \Delta V\right],} \tag{2.47}$$

where I have used Eq. 2.44 and the definitions of Du_L and Du_R to rewrite the result in terms of the maximum Dukhin number Du_R and the ratio $\mathrm{Du}_R/\mathrm{Du}_L = c_L/c_R$.

Using Eq. 2.45, we solve for $cd\phi/dx$ in terms of J and dc/dx, insert the result into Eq. 2.46, and integrate. The result can be combined with Eq. 2.47 to obtain

$$\boxed{\ln\left(\frac{\mathrm{Du}_R}{\mathrm{Du}_L}\right) + \Delta V = \left(1 + \frac{I}{J}\right) \ln\left[\frac{\frac{\mathrm{Du}_R}{\mathrm{Du}_L} + 2\mathrm{Du}_R\left(1 - \frac{I}{J}\right)}{1 + 2\mathrm{Du}_R\left(1 - \frac{I}{J}\right)}\right].} \tag{2.48}$$

Eq. 2.48 may be used to determine the applied voltage as a function of the ratio I/J for given values of Du_R and $\mathrm{Du}_R/\mathrm{Du}_L$, and the result can be combined with Eq. 2.47 to determine the solute flux and ionic current as a function of applied voltage. IV curves obtained using Eqs. 2.47 and 2.48 are plotted in Fig. 2.3 for a fixed value of $\mathrm{Du}_R = 1$ and several values of $\mathrm{Du}_R/\mathrm{Du}_L \equiv c_L/c_R \geq 1$.

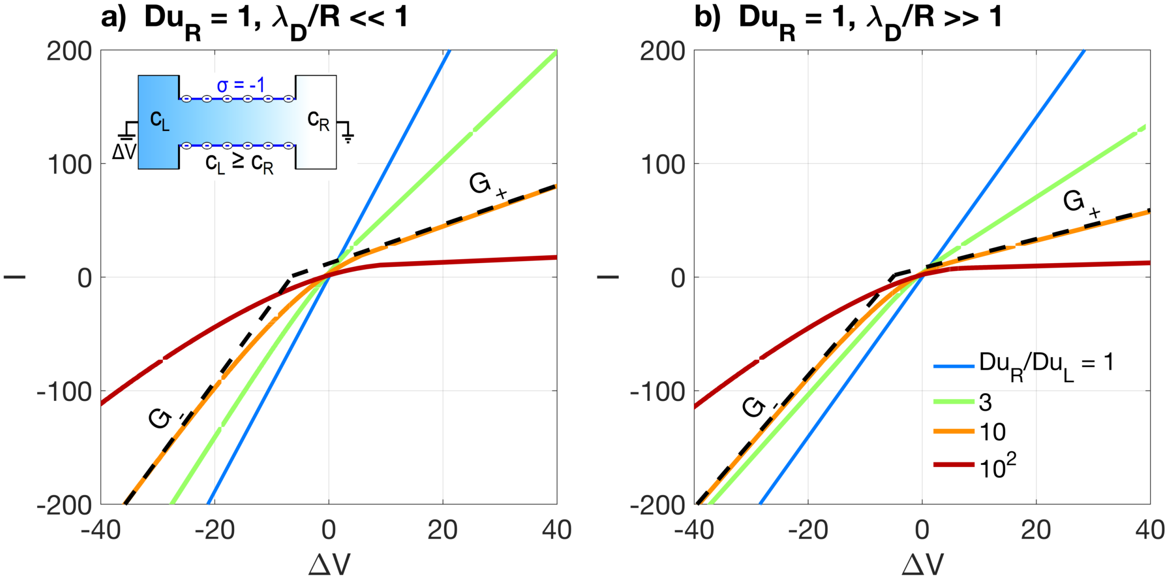

Figure 2.3: Current-voltage (IV) relationship in the concentration diode. a) IV curves obtained from Eqs. 2.47 and 2.48 in the limit of no Debye overlap ($\lambda_D/R \ll 1$). b) IV curves obtained from Eqs. 2.51 through 2.53 in the limit of strong overlap ($\lambda_D/R \gg 1$). All curves are calculated for $\mathrm{Du}_R = 1$, and they are colored according to $\mathrm{Du}_R/\mathrm{Du}_L = c_L/c_R$ as indicated in the legend in panel b. In both panels, the dashed black lines indicate the limiting conductances G_+ and G_-, obtained in the limits $\Delta V \to \pm\infty$, and calculated according to Eqs. 2.60 and 2.62 in panel a, and Eqs. 2.66 and 2.68 in panel b, for $\mathrm{Du}_R/\mathrm{Du}_L = 10$. The inset in panel a shows a sketch of the geometry considered here.

Strong Overlap ($\lambda_D/R \gg 1$)

We insert the local Dukhin number (Eq. 2.43) into the transport equations valid in the limit $\lambda_D/R \ll 1$, Eqs. 2.30 and 2.31, to obtain

$$\frac{J}{\pi} = -\frac{dc}{dx} - 2\mathrm{Du}_{\mathrm{ref}}\frac{d\phi}{dx}, \quad \text{and} \tag{2.49}$$

$$\frac{I}{\pi} = -c\frac{d\phi}{dx}. \tag{2.50}$$

Again, we may immediately integrate Eq. 2.49, applying the boundary conditions given in Eqs. 2.32 and 2.33, to obtain

$$\boxed{\left(\frac{\mathrm{Du}_R}{\mathrm{Du}_L}+1\right)\frac{J}{2\pi} = \left[\sqrt{\left(\frac{\mathrm{Du}_R}{\mathrm{Du}_L}\right)^2 + (2\mathrm{Du}_R)^2} - \sqrt{1+(2\mathrm{Du}_R)^2}\right] + 2\mathrm{Du}_R\left(\Delta V_D + \Delta V\right),} \tag{2.51}$$

where I have defined

$$\boxed{\begin{aligned}\Delta V_D &\equiv V_D^{\ell} - V_D^{r} \\ &\equiv \frac{1}{2}\ln\left\{\frac{\left[\sqrt{(\mathrm{Du}_R/\mathrm{Du}_L)^2+(2\mathrm{Du}_R)^2} - 2\mathrm{Du}_R\right]\left[\sqrt{1+(2\mathrm{Du}_R)^2}+2\mathrm{Du}_R\right]}{\left[\sqrt{(\mathrm{Du}_R/\mathrm{Du}_L)^2+(2\mathrm{Du}_R)^2} + 2\mathrm{Du}_R\right]\left[\sqrt{1+(2\mathrm{Du}_R)^2}-2\mathrm{Du}_R\right]}\right\},\end{aligned}} \tag{2.52}$$

the difference between the Donnan potentials on either end of the nanopore.

Again proceeding as in the case of strong overlap, we solve Eq. 2.49 for $cd\phi/dx$, insert the result into Eq. 2.50, and then substitute Eq. 2.51 into the result to obtain

$$\boxed{\Delta V_D + \Delta V = \frac{I}{J}\ln\left[\frac{\sqrt{(\mathrm{Du}_R/\mathrm{Du}_L)^2+(2\mathrm{Du}_R)^2} - 2\mathrm{Du}_R(I/J)}{\sqrt{1+(2\mathrm{Du}_R)^2} - 2\mathrm{Du}_R(I/J)}\right].} \tag{2.53}$$

I plot IV curves obtained from Eqs. 2.51 through 2.53 in Fig. 2.3b. We note immediately the similarity between the IV curves obtained in the limits of no overlap ($\lambda_D/R \ll 1$, Fig. 2.3a) and strong overlap ($\lambda_D/R \gg 1$, Fig. 2.3b). These results illustrate that Debye overlap has only a secondary quantitative influence on the degree of rectification, and that the main parameter controlling rectification is the Dukhin number.

2.4.2 Limiting Conductances

In this section, I examine the behavior of the IV curves shown in Fig. 2.3 in more detail by deriving expressions for voltage-independent limiting conductances in several different scenarios. I examine the regimes of no overlap ($\lambda_D/R \ll 1$) and strong overlap ($\lambda_D/R \gg 1$) in turn.

No Overlap ($\lambda_D/R \ll 1$)

As anticipated, as $\mathrm{Du}_R/\mathrm{Du}_L = c_L/c_R \to 1$, representing equal reservoir concentrations, the IV curve becomes progressively more linear, and in the limit of no overlap the conductance approaches a limiting value representing the sum of the bulk and surface electrophoretic contributions (Bocquet & Charlaix, 2010; Siria *et al.*, 2013):

$$G = G_{\text{bulk}} + G_{\text{surf}}, \quad \text{with} \tag{2.54}$$

$$G_{\text{bulk}} \equiv \pi, \quad \text{and} \tag{2.55}$$

$$G_{\text{surf}} \equiv 2\pi \mathrm{Du}_{\text{ref}}. \tag{2.56}$$

This result is obtained by solving Eqs. 2.45 and 2.46 with $dc/dx = 0$ and $c \equiv 1$. In dimensioned terms, these conductances are given by (Siria *et al.*, 2013)

$$G_{\text{bulk}} = \frac{\pi R^2}{L} \frac{e^2 D}{k_B T} c_{\text{res}}, \quad \text{and} \tag{2.57}$$

$$G_{\text{surf}} = \frac{2\pi R}{L} \frac{eD}{k_B T} |\sigma|, \tag{2.58}$$

where $c_{\text{res}} \equiv c_L \equiv c_R$ is the concentration in both reservoirs. This limiting conductance is indicated by the blue curve in Fig. 2.3a.

As a concentration difference is applied ($\mathrm{Du}_R/\mathrm{Du}_L > 1$) and increased, the IV curves become progressively more rectified. This is due to the asymmetry in selectivity between the left and right ends of the nanopore. The Dukhin number at the right end is held fixed at one, resulting in substantial selectivity for positive coions at that end (Fig. 2.2). On the other hand, as the Dukhin number on the left end is decreased via an increasing reservoir concentration c_L, the counterion selectivity at this end rapidly decreases, approaching the non-selective limit for values of $\mathrm{Du}_R/\mathrm{Du}_L > 10$ (Fig. 2.2).

I next examine the limiting currents and differential conductances $G \equiv \partial I/\partial \Delta V$ when Du_R and $\mathrm{Du}_R/\mathrm{Du}_L$ are held fixed and $\Delta V \to \pm\infty$, denoted $I_\pm$ and $G_\pm$, respectively. From Eq. 2.48, we see that the logarithm on the right-hand side must diverge as the voltage diverges for a fixed concentration ratio $\mathrm{Du}_R/\mathrm{Du}_L$. In the limit $|\Delta V| \to \infty$, the ionic current and solute flux will be in the same direction for the negative surface charge density assumed here, such that the coefficient of the logarithm $1 + I/J > 0$. Thus, when $\Delta V \to +\infty$, the argument of the logarithm must diverge. This requires that $I/J \to 1 + (2\mathrm{Du}_R)^{-1} \equiv \mathrm{STR}_R^{-1}$, where STR_R is the surface transport ratio at the right end of the nanopore (Eq. 2.25). Combined with Eq. 2.47, this gives for the current and conductance when $\Delta V \to +\infty$

$$\left(\frac{2\pi\mathrm{Du}_{\mathrm{ref}}}{\mathrm{STR}_R}\right)^{-1} I_+ = \frac{1}{2\mathrm{Du}_R}\left(\frac{\mathrm{Du}_R}{\mathrm{Du}_L} - 1\right) + \ln\left(\frac{\mathrm{Du}_R}{\mathrm{Du}_L}\right) + \Delta V, \quad \text{and} \tag{2.59}$$

$$G_+ = \frac{G_{\mathrm{surf}}}{\mathrm{STR}_R} \equiv 2\pi\mathrm{Du}_{\mathrm{ref}}\frac{1+2\mathrm{Du}_R}{2\mathrm{Du}_R}. \tag{2.60}$$

Likewise, as $\Delta V \to -\infty$, Eq. 2.48 indicates that the argument of the logarithm must vanish, and thus $I/J \to \mathrm{STR}_L^{-1}$. By the same procedure we find

$$\left(\frac{2\pi\mathrm{Du}_{\mathrm{ref}}}{\mathrm{STR}_L}\right)^{-1} I_- = \frac{1}{2\mathrm{Du}_R}\left(\frac{\mathrm{Du}_R}{\mathrm{Du}_L} - 1\right) + \ln\left(\frac{\mathrm{Du}_R}{\mathrm{Du}_L}\right) + \Delta V, \quad \text{and} \tag{2.61}$$

$$G_- = \frac{G_{\mathrm{surf}}}{\mathrm{STR}_L} \equiv 2\pi\mathrm{Du}_{\mathrm{ref}}\frac{1+2\mathrm{Du}_L}{2\mathrm{Du}_L}. \tag{2.62}$$

The limiting conductances are indicated by the dashed black lines in Fig. 2.3a for $\mathrm{Du}_R = 1$ and $\mathrm{Du}_R/\mathrm{Du}_L = 10$.

As Du_R becomes smaller for a fixed value of the ratio $\mathrm{Du}_R/\mathrm{Du}_L$, the asymmetry in nanopore selectivity between either end of the nanopore becomes weaker (Fig. 2.2), and consequently the voltage magnitude that leads to significant concentration accumulation or depletion becomes larger. This means that, for an experimentally feasible range of applied voltages, the IV curve linearizes as Du_R is decreased. From Eq. 2.48, we see that as $\mathrm{Du}_R \to 0$ for a fixed value of $\mathrm{Du}_R/\mathrm{Du}_L$, $I/J \to \Delta V/\ln(\mathrm{Du}_R/\mathrm{Du}_L)$. This is true so long as the numerator and denominator of the logarithm are $\gg 0$, which, from our discussion above, requires that the voltage magnitude not be too large. We find from this limit and Eq. 2.47 a limiting conductance

$$G \to \frac{2\left(\frac{\mathrm{Du}_R}{\mathrm{Du}_L} - 1\right)}{\left(\frac{\mathrm{Du}_R}{\mathrm{Du}_L} + 1\right)\ln\left(\frac{\mathrm{Du}_R}{\mathrm{Du}_L}\right)} G_{\mathrm{bulk}}, \tag{2.63}$$

valid for fixed $\mathrm{Du}_R/\mathrm{Du}_L$ when $\mathrm{Du}_R \ll 1$. Note that the prefactor in Eq. 2.63 approaches unity and $G \to G_{\mathrm{bulk}}$ in the limit $\mathrm{Du}_R/\mathrm{Du}_L \to 1$, as it must.

Finally, I examine the limit $\mathrm{Du}_R \to \infty$ for fixed $\mathrm{Du}_R/\mathrm{Du}_L$. In this case, the entire nanopore becomes perfectly selective for counterions (Fig. 2.2), and the IV curve again linearizes. Unlike in the case that $\mathrm{Du}_R \ll 1$, however, I find that the IV curve is linear irrespective of the magnitude

	$\lambda_D/R \ll 1$	$\lambda_D/R \gg 1$
condition	G	
$c_{\mathrm{max}}/c_{\mathrm{min}} = 1$	$G_{\mathrm{bulk}} + G_{\mathrm{surf}}$	$\sqrt{G_{\mathrm{bulk}}^2 + G_{\mathrm{surf}}^2}$
$\mathrm{Du}_{\mathrm{max}} \ll 1$	$\frac{2(c_{\mathrm{max}}/c_{\mathrm{min}}-1)}{(c_{\mathrm{max}}/c_{\mathrm{min}}+1)\ln(c_{\mathrm{max}}/c_{\mathrm{min}})} \times G_{\mathrm{bulk}}$	$\frac{2(c_{\mathrm{max}}/c_{\mathrm{min}}-1)}{(c_{\mathrm{max}}/c_{\mathrm{min}}+1)\ln(c_{\mathrm{max}}/c_{\mathrm{min}})} \times G_{\mathrm{bulk}}$
$\mathrm{Du}_{\mathrm{max}} \to \infty$	G_{surf}	G_{surf}
$\lvert\Delta V\rvert \to \infty$	$G_{\mathrm{min}} = \frac{1+2\mathrm{Du}_{\mathrm{max}}}{2\mathrm{Du}_{\mathrm{max}}} \times G_{\mathrm{surf}}$	$G_{\mathrm{min}} = \frac{\sqrt{1+(2\mathrm{Du}_{\mathrm{max}})^2}}{2\mathrm{Du}_{\mathrm{max}}} \times G_{\mathrm{surf}}$
	$G_{\mathrm{max}} = \frac{1+2\mathrm{Du}_{\mathrm{min}}}{2\mathrm{Du}_{\mathrm{min}}} \times G_{\mathrm{surf}}$	$G_{\mathrm{max}} = \frac{\sqrt{1+(2\mathrm{Du}_{\mathrm{min}})^2}}{2\mathrm{Du}_{\mathrm{min}}} \times G_{\mathrm{surf}}$

Table 2.2: Limiting conductances for the concentration diode and the conditions under which they obtain in the limits of no overlap ($\lambda_D/R \ll 1$) and strong overlap ($\lambda_D/R \gg 1$). The results are written generically in terms of the maximum and minimum reservoir concentrations, c_{max} and c_{min}, respectively, and the corresponding maximum and minimum Dukhin numbers, $\mathrm{Du}_{\mathrm{max}} \equiv |\sigma|/ec_{\mathrm{min}}R$ and $\mathrm{Du}_{\mathrm{min}} \equiv |\sigma|/ec_{\mathrm{max}}R$, imposed on either end of the nanopore. G_{max} and G_{min} are, respectively, the maximum and minimum conductances obtained as $|\Delta V| \to \infty$. (See Eqs. 2.60, 2.62 and 2.75, 2.76 for the case of no overlap, and Eqs. 2.66, 2.68 and 2.83, 2.84 for the case of strong overlap.) The bulk (G_{bulk}) and surface (G_{surf}) electrophoretic condutances are given in Eqs. 2.55/2.57 and 2.56/2.58, respectively. Note that, in the case of strong overlap ($\lambda_D/R \gg 1$), the partitioning between 'surface' and 'bulk' transport is not strictly meaningful, as there is no distinct surface layer; however, the terms G_{surf} and G_{bulk} retain the same form they have in the no overlap ($\lambda_D/R \ll 1$) limit.

of the applied voltage for large Du_R. From Eq. 2.25, we note that, as $\mathrm{Du} \to \infty$, $\mathrm{STR} \to 1$. Thus, as $\mathrm{Du}_R \to \infty$ for fixed $\mathrm{Du}_R/\mathrm{Du}_L$, $\mathrm{STR}_L \to \mathrm{STR}_R \to 1$, and, from Eqs. 2.60 and 2.62, we find $G_+ \to G_- \to G_{\mathrm{surf}}$. In this case, the conductance is dominated by the (concentration-independent) surface contribution.

Each of the limiting conductances discussed above, and the conditions under which they obtain, are listed in Table 2.2.

Strong Overlap ($\lambda_D/R \gg 1$)

I now derive the conductances in the corresponding limits in the strong overlap regime. I begin with the limit that $\mathrm{Du}_R/\mathrm{Du}_L = c_L/c_R = 1$, *i.e.*, that the reservoir concentrations are equal and the IV curve is therefore linear. Solving Eqs. 2.49 and 2.50 with $dc/dx = 0$ and $c = \sqrt{1 + (2\mathrm{Du}_{\mathrm{ref}})^2}$

(see Eq. 2.34 with $c_L = c_R = 1$ and $\mathrm{Du}_L = \mathrm{Du}_R = \mathrm{Du}_{\mathrm{ref}}$), we find

$$G = \sqrt{G_{\mathrm{bulk}}^2 + G_{\mathrm{surf}}^2}, \tag{2.64}$$

with G_{bulk} and G_{surf} as given in Eqs. 2.55/2.57 and 2.56/2.58. The result given in Eq. 2.64 is indicated by the blue curve in Fig. 2.3b. Note that in the regime of strong overlap there is no distinct surface layer and the conductance is not meaningfully partitioned into a bulk and a surface term. In this case, what is referred to as surface transport is better understood as that portion of the transport due to the excess counterion concentration induced by the surface charge. However, for consistency I will continue to use the definitions of G_{surf} and G_{bulk} in what follows.

Next, I examine the case that the magnitude of the applied voltage diverges. We see from Eq. 2.53 that, as $\Delta V \to +\infty$, the denominator of the logarithm must tend to zero. This requires that $I/J \to \sqrt{1 + (2\mathrm{Du}_R)^2}/2\mathrm{Du}_R$. With Eq. 2.51 we find for the current and conductance in this limit

$$\frac{I_+}{2\pi \mathrm{Du}_{\mathrm{ref}}} = \frac{\sqrt{1+(2\mathrm{Du}_R)^2}}{2\mathrm{Du}_R}\left\{\left[\frac{\sqrt{1+(2\mathrm{Du}_L)^2}}{2\mathrm{Du}_L} - \frac{\sqrt{1+(2\mathrm{Du}_R)^2}}{2\mathrm{Du}_R}\right] + \Delta V_D + \Delta V\right\}, \quad \text{and} \tag{2.65}$$

$$G_+ = \frac{\sqrt{1+(2\mathrm{Du}_R)^2}}{2\mathrm{Du}_R} G_{\mathrm{surf}}, \tag{2.66}$$

where I have used the definition of G_{surf} given in Eq. 2.56.

Likewise, when $\Delta V \to -\infty$, we find from Eq. 2.53 that $I/J \to \sqrt{1 + (2\mathrm{Du}_L)^2}/2\mathrm{Du}_L$. Thus, from Eq. 2.51, we have

$$\frac{I_-}{2\pi \mathrm{Du}_{\mathrm{ref}}} = \frac{\sqrt{1+(2\mathrm{Du}_L)^2}}{2\mathrm{Du}_L}\left\{\left[\frac{\sqrt{1+(2\mathrm{Du}_L)^2}}{2\mathrm{Du}_L} - \frac{\sqrt{1+(2\mathrm{Du}_R)^2}}{2\mathrm{Du}_R}\right] + \Delta V_D + \Delta V\right\}, \quad \text{and} \tag{2.67}$$

$$G_- = \frac{\sqrt{1+(2\mathrm{Du}_L)^2}}{2\mathrm{Du}_L} G_{\mathrm{surf}}. \tag{2.68}$$

The limiting conductances are indicated by the dashed black lines in Fig. 2.3b for $\mathrm{Du}_R = 1$ and $\mathrm{Du}_R/\mathrm{Du}_L = 10$.

From Eqs. 2.52 and 2.53, we find that to lowest order in Du_R as $\mathrm{Du}_R \to 0$ with fixed $\mathrm{Du}_R/\mathrm{Du}_L$, $I/J = \Delta V/\ln(\mathrm{Du}_R/\mathrm{Du}_L)$. This is identical to the result obtained above for $\lambda_D/R \ll 1$, and the conductance in this limit is likewise given by Eq. 2.63. Likewise, for $\mathrm{Du}_R \to \infty$ and fixed $\mathrm{Du}_R/\mathrm{Du}_L$, G_+ and G_- both saturate to G_{surf}, as in the no overlap limit. These limiting conductances are indicated along with the corresponding results for $\lambda_D/R \ll 1$ in Table 2.2.

2.4.3 Rectification Ratio

I am now in a position to discuss the rectification ratio, defined as

$$\text{rectification ratio} \equiv \frac{|I(-|\Delta V|) - I(\Delta V = 0)|}{|I(+|\Delta V|) - I(\Delta V = 0)|}. \tag{2.69}$$

I plot this ratio in Fig. 2.4 as a function of Du_R for fixed concentration ratios $\mathrm{Du}_R/\mathrm{Du}_L = c_L/c_R$ and in the limits of no overlap ($\lambda_D/R \ll 1$, Fig. 2.4a) and strong overlap ($\lambda_D/R \gg 1$, Fig. 2.2b). In general, the rectification ratio is a function of the voltage magnitude $|\Delta V|$; for definiteness, I take $|\Delta V| = 20$, which corresponds to a dimensioned applied voltage of approximately 500 mV. We note from Fig. 2.4 that the rectification ratio is generally larger in the case of extreme overlap, though it is of the same order in either case.

In both limits, the rectification ratios display a peak for a finite value of Du_R (Fig. 2.4). This peak is nearly coincident for a given value of $\mathrm{Du}_R/\mathrm{Du}_L$ in the limits of no overlap ($\lambda_D/R \ll 1$, Fig. 2.4a) and extreme overlap ($\lambda_D/R \gg 1$, Fig. 2.4b). In both limits, the peak grows and is shifted to higher values of Du_R as $\mathrm{Du}_R/\mathrm{Du}_L = c_L/c_R$ is increased. The value of Du_R corresponding to the peak rectification ratio $\mathrm{Du}_R^{\mathrm{peak}}$ is of order one over much of the parameter space ($0.2 < \mathrm{Du}_R^{\mathrm{peak}} < 2$ for $3 \leq \mathrm{Du}_R/\mathrm{Du}_L \leq 10^2$).

The fact that the rectification ratio shows a peak at a finite value of Du_R can be understood as follows: By taking the ratio of the limiting conductances valid when $|\Delta V| \to \infty$ (Eqs. 2.60 and 2.62 in the case of no overlap, or Eqs. 2.66 and 2.68 in the case of strong overlap), we see that there is an upper limit on the maximum rectification. In the case of no overlap, it is given by

$$\text{rectification ratio} \xrightarrow[|\Delta V|\to\infty]{} \frac{\mathrm{STR}_R}{\mathrm{STR}_L} = \frac{\frac{\mathrm{Du}_R}{\mathrm{Du}_L} + 2\mathrm{Du}_R}{1 + 2\mathrm{Du}_R} \xrightarrow[\mathrm{Du}_R\to 0]{} \frac{\mathrm{Du}_R}{\mathrm{Du}_L}, \tag{2.70}$$

where in the limit on the RHS we have taken $\mathrm{Du}_R \to 0$ with the concentration ratio $\mathrm{Du}_R/\mathrm{Du}_L$ fixed; this corresponds to the maximum of the theoretical rectification curve and indicates that this theoretical maximum is set by the concentration ratio. Likewise, in the limit of strong overlap, we take the ratio of the conductances given in Eqs. 2.66 and 2.68 to find

$$\text{rectification ratio} \xrightarrow[|\Delta V|\to\infty]{} \sqrt{\frac{\left(\frac{\mathrm{Du}_R}{\mathrm{Du}_L}\right)^2 + (2\mathrm{Du}_R)^2}{1 + (2\mathrm{Du}_R)^2}} \xrightarrow[\mathrm{Du}_R\to 0]{} \frac{\mathrm{Du}_R}{\mathrm{Du}_L}, \tag{2.71}$$

where again we take the limit that $\mathrm{Du}_R \to 0$ with $\mathrm{Du}_R/\mathrm{Du}_L$ fixed to find that the theoretical maximum rectification is also given by the concentration ratio in the limit of strong overlap.

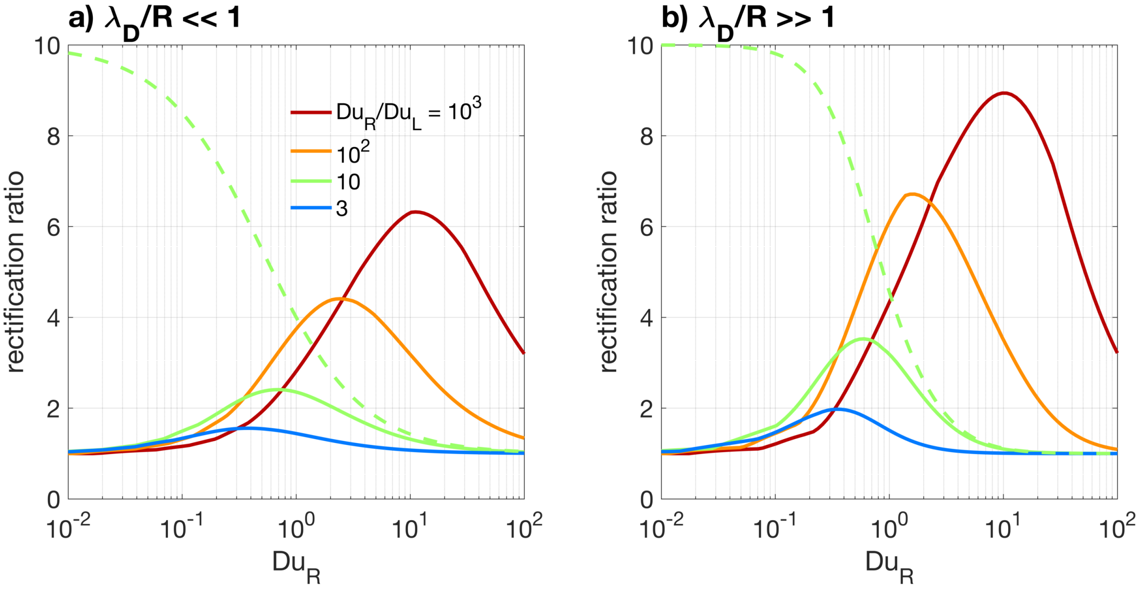

Figure 2.4: Rectification ratio as a function of maximum Dukhin number Du_R. a) Rectification ratio in the limit of no overlap ($\lambda_D/R \ll 1$), calculated from Eqs. 2.47 and 2.48. b) Rectification ratio in the limit of strong overlap ($\lambda_D/R \gg 1$), calculated according to Eqs. 2.51 and 2.53. In both panels, the curves are evaluated at $|\Delta V| = 20$ ($\approx 500\,\mathrm{mV}$) and colored according to $\mathrm{Du}_R/\mathrm{Du}_L = c_L/c_R$ as indicated in the legend. The dashed lines in panels a and b indicate the theoretical maximum rectification ratios for no overlap (panel a, Eq. 2.70) and strong overlap (panel b, Eq. 2.71), valid in the limit $|\Delta V| \rightarrow \infty$, for $\mathrm{Du}_R/\mathrm{Du}_L = 10$.

However, in the case that $\mathrm{Du}_R \ll 1$, the local Dukhin number is everywhere much smaller than one, and the nanopore is therefore only weakly selective for counterions (Fig. 2.2). It thus takes very large voltages to engender significant ion accumulation or depletion, voltages much larger than the practical upper limit in nanofluidic experiments (~ 1 V), and the IV curve is effectively linearized.

On the other hand, when $\mathrm{Du}_R \rightarrow \infty$ (with $\mathrm{Du}_R/\mathrm{Du}_L$ fixed), $G_+ \rightarrow G_- \rightarrow G_{\mathrm{surf}}$ in both the no overlap and strong overlap regimes. (See the discussion in the preceding section and Eqs. 2.60/2.66 and 2.62/2.68 for the case of no overlap / strong overlap.) This indicates that the IV curve is strictly linear in this limit, irrespective of the voltage magnitude. This is because the local Dukhin number is everywhere much larger than one and the entirety of the ionic transport is carried by counterions. There is therefore no gradient in ion selectivity along the length of the nanopore. In this case, the conductance is given by the (concentration-independent) surface conductance (Eq. 2.58). Thus, the location of $\mathrm{Du}_R^{\max}$ represents a compromise between the non-selective ($\mathrm{Du}_R \rightarrow 0$)

and perfectly selective ($\text{Du}_R \rightarrow \infty$) limits.

The occurrence of a maximum rectification ratio for a finite value of Du_R and a fixed value of the ratio Du_R/Du_L is exactly analogous to the common observation of a maximum rectification ratio for a finite concentration or surface charge density and a fixed geometry in conical diodes, (*e.g.*, Ai *et al.*, 2010; Cervera *et al.*, 2006; Vlassiouk *et al.*, 2009; Zhou *et al.*, 2011). In that case, the ratio of Dukhin numbers is fixed by the ratio of base and tip radii, while the variation of concentration or surface charge results in a variation of the maximum Dukhin number occuring at the tip of the conical nanopore. As in the concentration diode, the location of the maximum is determined by a compromise between the non-selective (high concentration or low surface charge) and perfectly selective (low concentration or high surface charge) limits. I will discuss the role of dynamic selectivity in diodes induced by asymmetric geometry (and surface charge density distributions) below.

2.5 Dynamic Selectivity and Limiting Conductances in Generic Diodes

2.5.1 Rectification in Generic Diodes

From our understanding of the role of the Dukhin number in controlling local selectivity we conclude that ICR is generically a consequence of inequality of the Dukhin numbers imposed on either end of a nanopore, irrespective of whether that asymmetry is induced by a difference in reservoir concentrations, an asymmetric geometry, or an asymmetric surface charge density distribution (or any combination thereof). This is corroborated by the results shown in Fig. 2.5, where I compare an IV curve obtained from the above solution for a concentration diode (Figs. 2.5a and d, Eqs. 2.47 and 2.48) to numerical solutions of the transport equations for the IV curve in a geometric (Figs. 2.5b and e) and a charge diode (Figs. 2.5c and f). These solutions are obtained from Eqs. 2.23 and 2.24 subject to boundary conditions 2.32 and 2.33. Here and in the rest of this Chapter, I will focus primarily on results obtained in the limit of no overlap ($\lambda_D/R \ll 1$). The results obtained in the strong overlap regime ($\lambda_D/R \gg 1$) are qualitatively similar.

In order to illustrate rectification induced by an asymmetric geometry, I assume a linear variation in the nanopore radius from the maximum radius (minimum Dukhin number) on the left to the minimum radius (maximum Dukhin number) on the right. The surface charge density

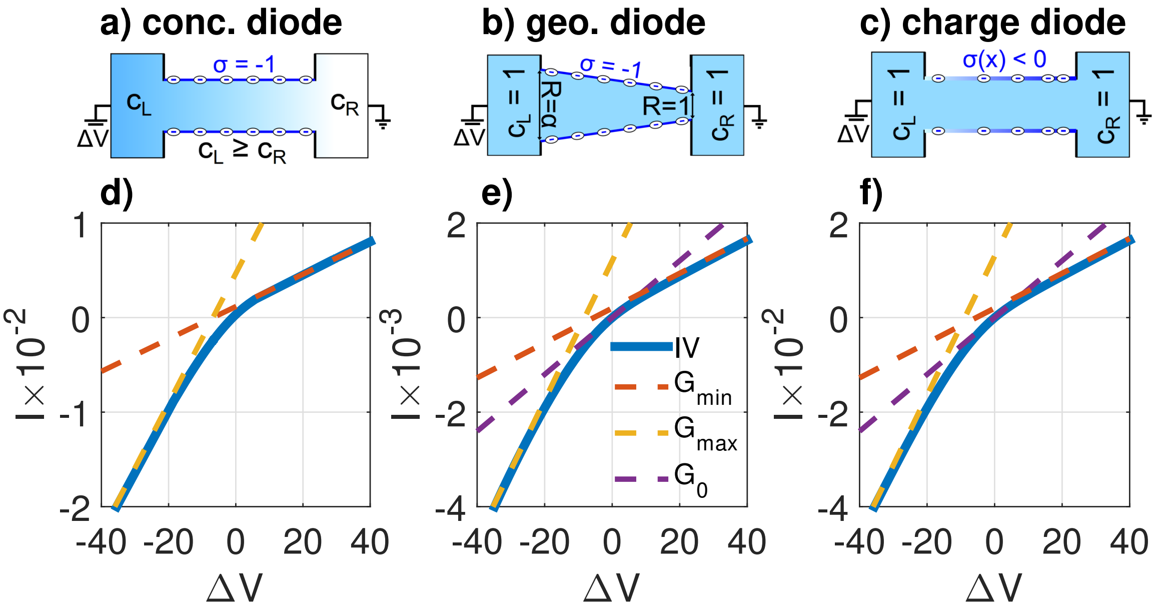

Figure 2.5: a-c) Schematics of diodes induced by a) unequal reservoir concentrations, b) asymmetric geometry, and c) asymmetric surface charge distribution. d-f) IV curves obtained for $\mathrm{Du}_R = 1$ and $\mathrm{Du}_L = 0.1$ for d) the concentration diode shown in a, e) the geometric diode shown in b, and f) the charge diode shown in c. In panels d-f, the dashed yellow and red lines show the maximum and minimum conductances obtained when $|\Delta V| \to \infty$ and calculated according to Eqs. 2.75 and 2.76, respectively. In panels e and f, the dashed purple line indicates the linear response conductance valid in the vicinity of $\Delta V = 0$ for the charge and geometric diodes and calculated according to Eq. 2.89. The IV curves shown in panels d-f are calculated in the limit of no overlap ($\lambda_D/R \ll 1$).

is taken to be fixed and negative, and the reservoir concentrations are taken to be equal. This configuration is shown schematically in Fig. 2.5b. Likewise, I illustrate rectification induced by a continuous, asymmetric surface charge profile by imposing a negative surface charge density whose magnitude varies linearly from a minimum density (minimum Dukhin number) on the left to a maximum density (maximum Dukhin number) on the right. In this case, I impose a constant nanopore radius and equal reservoir concentrations. This configuration is shown schematically in Fig. 2.5c. In all three cases, I take $\mathrm{Du}_L = 0.1$ and $\mathrm{Du}_R = 1$. We immediately see from Figs. 2.5d through f that the qualitative structure of the rectified IV curve is essentially the same over a given range of voltage ($-40 \leq \Delta V \leq +40$ here). Indeed, in each case the rectification ratio (Eq. 2.69) is ~ 3 for $|\Delta V| = 40$. The qualitative similarity of the IV curves obtained in these three different configurations illustrates the primary role of the Dukhin number in rectification and the equivalence of the underlying mechanism of dynamic selectivity in each case.

2.5.2 General Expressions for the Limiting Conductances and Selectivities When $|\Delta V| \to \infty$

In this section, I show that the above expressions obtained for the limiting conductances when $|\Delta V| \to \infty$ (Eqs. 2.60 and 2.62 in the case of no overlap, and Eqs. 2.66 and 2.68 in the case of strong overlap) obtained for the concentration diode are particular examples of general expressions relating the minimum (maximum) Dukhin number imposed at one end of the nanopore to the maximum (minimum) conductance obtained for large imposed voltages. I also derive expressions for the limiting ion-selectivities when $|\Delta V| \to \infty$ in the more interesting case of large nanopores ($\lambda_D/R \gg 1$). For the geometric and charge diodes, these correspond to the minimum and maximum selectivities obtainable by varying the applied voltage. These expressions are valid for concentration, geometric, and charge diodes (or any combination thereof), as illustrated in Fig. 2.5 for the limiting conductances. In the course of this discussion, I illustrate general features of the evolution of the Dukhin number profile in the nanopore interior as a function of applied voltage, further illustrating the principal role of dynamic selectivity in the accumulation or depletion of concentration in the nanopore interior and hence in ICR.

The general expressions for limiting conductances in generic diodes, along with those derived below for the linear response near $\Delta V = 0$ in geometric and charge diodes, will allow observations of rectified IV curves to be related to, for example, the surface charge density. The surface charge density is difficult to estimate directly and is often estimated by observing the saturation of the conductance at the surface-dominated value for low concentrations, (*e.g.*, Stein *et al.*, 2004; Karnik *et al.*, 2005; Secchi *et al.*, 2016b). However, the inference of surface charge from conductance measurements typically relies on a linear response, in which case the relation between surface charge and the saturating conductance at low concentration is known analytically, (*e.g.*, Stein *et al.*, 2004; Bocquet & Charlaix, 2010; Siria *et al.*, 2013). It is not clear *a priori* how this framework may be extended to, *e.g.*, conical nanopores, where ICR is inherent to the IV response below a certain concentration. To my knowledge, general analytical results for the relationship between surface charge and conductance do not exist in the literature for rectified IV curves, except in certain specialized scenarios, (*e.g.*, Picallo *et al.*, 2013).

I will focus primarily on the no overlap limit ($\lambda_D/R \ll 1$), as the occurrence of selectivity generally and ICR in particular in large nanopores is more novel and potentially relevant for applications to energy harvesting and separation techniques (as discussed in Sec. 2.6 below). However, I will also develop the expressions for the limiting conductances in the strong overlap regime ($\lambda_D/R \gg 1$) for completeness.

No Overlap ($\lambda_D/R \ll 1$)

As $|\Delta V| \to \infty$, the solute flux (Eq. 2.23) will be dominated by the surface electrophoretic mass transport, $J/\pi R^2 \sim \mathrm{S}2|\mathrm{Du}|c d\phi/dx = \mathrm{S}2\mathrm{Du}_{\mathrm{ref}}(|\sigma|/R)d\phi/dx$. Integrating in x, we find

$$J = -\mathrm{S}\left(\int_L \frac{\mathrm{dx}}{2\pi R|\sigma|}\right)^{-1} \mathrm{Du}_{\mathrm{ref}}\Delta V. \tag{2.72}$$

In order to obtain a condition on the flux ratio I/J that holds in the limit $|\Delta V| \to \infty$, we solve Eqs. 2.23 and 2.24 for the concentration gradient dc/dx in terms of I/J, the local Dukhin number, and the (divergent) solute flux:

$$\frac{dc}{dx} = -\mathrm{S}\frac{\frac{I}{J} + \mathrm{S}\left(1 + \frac{1}{2|\mathrm{Du}|}\right)}{2 + \frac{1}{2|\mathrm{Du}|}}\frac{J}{\pi R^2}. \tag{2.73}$$

On physical grounds, the concentration gradient cannot diverge everywhere in the nanopore interior, even in the limit that $|\Delta V| \to \infty$. Accordingly, the prefactor in Eq. 2.73 must vanish as the solute flux diverges. This requires that $I/J \to -\mathrm{S}(1 + 1/2|\mathrm{Du}|) \equiv -\mathrm{S}/\mathrm{STR}$, where in the second equality I have made use of Eq. 2.25. As the ratio I/J is spatially uniform at steady state, this condition requires the Dukhin number in the nanopore interior to approach a uniform value, which I will designate Du_u. Likewise, I designate the corresponding surface transport ratio $\mathrm{STR}_u \equiv 2\mathrm{Du}_u/(1 + 2\mathrm{Du}_u)$. With this result for the flux ratio I/J and Eq. 2.72 we find for the current

$$I = \left(\int_L \frac{\mathrm{dx}}{2\pi R|\sigma|}\right)^{-1} \frac{\mathrm{Du}_{\mathrm{ref}}}{\mathrm{STR}_u}\Delta V. \tag{2.74}$$

The mechanism of concentration accumulation/depletion is driven by the gradient in Dukhin number induced by the asymmetry between the maximum ($\mathrm{Du}_{\max}$) and minimum ($\mathrm{Du}_{\min}$) Dukhin numbers imposed on either end of the nanopore. Thus, for very strong applied voltages, the accumulation (depletion) will cease when the concentration everywhere is such that the uniform Dukhin number in the interior is equal to $\mathrm{Du}_u = \mathrm{Du}_{\min}$ ($\mathrm{Du}_{\max}$). At one end of the nanopore, the concentration gradient then must diverge to match the divergence in the solute flux (Eq. 2.72) while allowing the Dukhin number to deviate from its uniform interior value and adjust to the appropriate boundary condition.

This mechanism is illustrated in Fig. 2.6: In Figs. 2.6a through c, I show the profiles of centerline concentration as a function of the applied voltage for the concentration (Fig. 2.6a), geometric (Fig. 2.6b), and charge (Fig. 2.6c) diodes shown schematically in Figs. 2.5a through c, respectively. In the case of the concentration diode, Eq. 2.73 may be integrated to obtain an implicit expression for the concentration profile, while for the geometric and charge diodes it is necessary to solve the transport equations (Eqs. 2.23 and 2.24) numerically to obtain the concentration profiles. As for the IV curves shown in Figs. 2.5d through f, the profiles are calculated for $\mathrm{Du}_L = 0.1$ and $\mathrm{Du}_R = 1$. The qualitative structure of the concentration profiles is quite different in the three configurations considered; however, in each case, there is increasing depletion (accumulation) of concentration in the nanopore interior for increasing magnitude positive (negative) voltage. Note that the sign of the voltage resulting in accumulation/depletion would be inverted for a positive surface charge, rather than the negative surface charge considered here.

However, in Figs. 2.6d through f, we see that the evolution of the local Dukhin number profiles $|\mathrm{Du}(x)|$ with applied voltage are strikingly similar in the three configurations, even though the concentration profiles are quite different. In each case, an increasing magnitude positive (negative) voltage results in a growing region in the nanopore interior where $|\mathrm{Du}| \approx \mathrm{Du}_{\mathrm{max}} = \mathrm{Du}_R$ ($|\mathrm{Du}| \approx \mathrm{Du}_{\mathrm{min}} = \mathrm{Du}_L$). Fig. 2.6 illustrates the key role of the local Dukhin number in controlling the accumulation/depletion of concentration in the nanopore and hence in ICR. It also illustrates that, in the extreme limit that $|\Delta V| \to \infty$, the Dukhin number will approach a uniform value equal to the maximum or minimum Dukhin number imposed at one end of the nanopore. (Whether it approaches $\mathrm{Du}_{\mathrm{max}}$ or $\mathrm{Du}_{\mathrm{min}}$ depends on the sign of the applied voltage and the surface charge density.) Thus, denoting the maximum and minimum limiting conductances as G_{max} and G_{min}, respectively, we find from Eq. 2.74

$$\boxed{G_{\mathrm{max}} = \frac{G_{\mathrm{surf}}}{\mathrm{STR}_{\mathrm{min}}} \equiv G_{\mathrm{surf}} \frac{1 + 2\mathrm{Du}_{\mathrm{min}}}{2\mathrm{Du}_{\mathrm{min}}}, \quad \text{and}} \tag{2.75}$$

$$\boxed{G_{\mathrm{min}} = \frac{G_{\mathrm{surf}}}{\mathrm{STR}_{\mathrm{max}}} \equiv G_{\mathrm{surf}} \frac{1 + 2\mathrm{Du}_{\mathrm{max}}}{2\mathrm{Du}_{\mathrm{max}}}.} \tag{2.76}$$

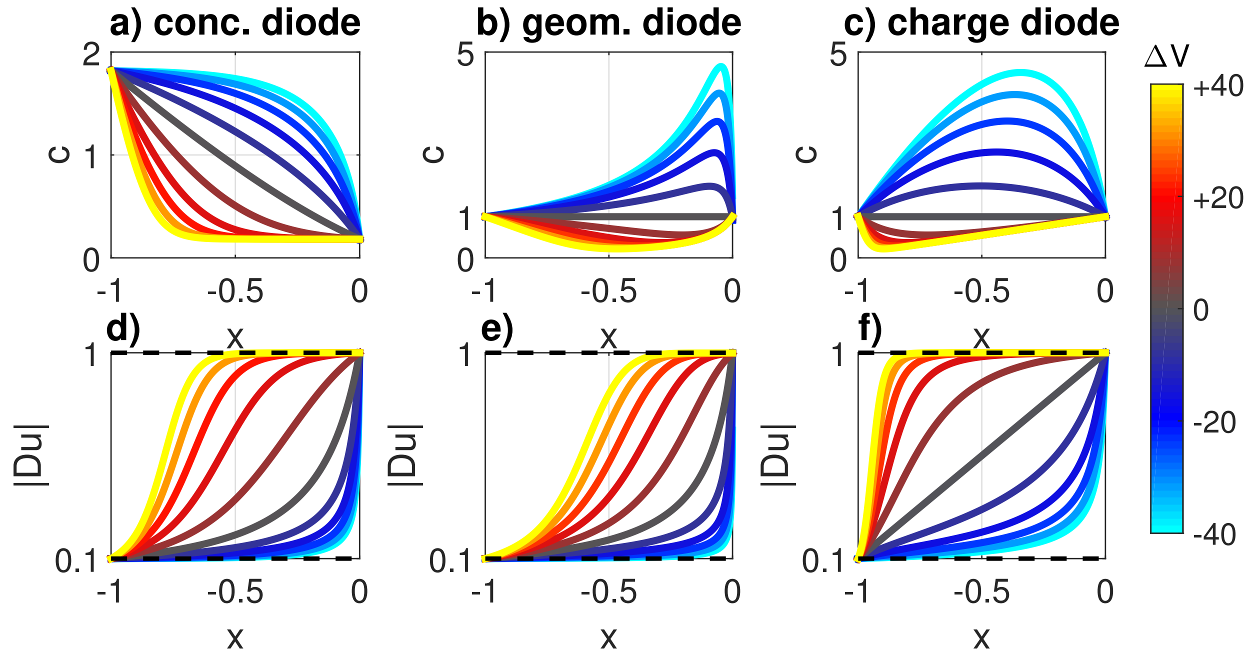

Figure 2.6: a-c) Profiles of centerline total ionic concentration along the length of the a) concentration diode shown schematically in Fig. 2.5a, b) the geometric diode (Fig. 2.5b), and c) the charge diode (Fig. 2.5c). d-f) The corresponding profiles of local Dukhin number for the concentration (d), geometric (e), and charge (f) diodes. The dashed black lines in d-f indicate the minimum and maximum imposed Dukhin numbers at either end of the nanopore, $\mathrm{Du}_L = 0.1$ and $\mathrm{Du}_R = 1$, respectively. In all panels, the curves are colored according to the applied voltage, as indicated in the colorbar on the right. All curves are obtained in the limit of no overlap ($\lambda_D/R \ll 1$).

In these equations, G_{surf} is the surface conductance obtained when $\mathrm{Du}_{\mathrm{ref}} \to \infty$ and only the surface terms in Eq. 2.21 are relevant (Frament & Dwyer, 2012):

$$\boxed{G_{\mathrm{surf}} = \left(\int_L \frac{\mathrm{dx}}{2\pi R|\sigma|}\right)^{-1} \mathrm{Du}_{\mathrm{ref}} \xrightarrow{\mathrm{dim.}} \frac{eD}{k_B T}\left(\int_L \frac{\mathrm{dx}}{2\pi R|\sigma|}\right)^{-1},} \tag{2.77}$$

where I have redimensionalized in the second line. This expression reduces to that given in Eqs. 2.56 and 2.58 in the case of a nanopore of uniform radius and surface charge density. The limiting conductances predicted using Eqs. 2.75 and 2.76 are shown in Figs. 2.5d through f (dashed yellow and red lines).

We note that, by setting $|\sigma| \equiv R \equiv 1$ and identifying $\mathrm{Du}_{\mathrm{min}} = \mathrm{Du}_L$ and $\mathrm{Du}_{\mathrm{max}} = \mathrm{Du}_R$, we recover Eqs. 2.60 and 2.62 from Eqs. 2.76 and 2.75, respectively.

Figs. 2.6d through f show that the Dukhin number has not fully approached a uniform value everywhere in the nanopore interior even for $|\Delta V| = +40$; however, Figs. 2.5d through f indicate that the differential conductance is roughly equal to its limiting value for $|\Delta V| \gtrsim 10 - 20$ ($\sim 250 - 500$ mV). Note, however, that the voltage necessary to reach the limiting conductance depends on both the maximum Dukhin number in the system $\mathrm{Du}_{\mathrm{max}}$ and the asymmetry in Dukhin numbers, quantified by the ratio $\mathrm{Du}_{\mathrm{max}}/\mathrm{Du}_{\mathrm{min}}$. (See Fig. 2.4 and related discussion.) Thus, we note that care must be taken in applying Eqs. 2.75 and 2.76 to experimental IV curves. This difficulty can be avoided by instead fitting the surface charge to the linear response conductance G_0 obtained in the vicinity of $\Delta V = 0$; we will obtain an analytical expression for G_0 in the following section.

Using the asymptotic expressions for the solute flux (Eq. 2.72) and ionic current (Eqs. 2.74 through 2.77) we can calculate the co-/counterion fluxes $J_{\mathrm{co/count}} = (J \pm \mathrm{S}I)/2$ and derive expressions for the counterion selectivities $\mathcal{S}_{\mathrm{count}} \equiv |J_{\mathrm{count}}|/(|J_{\mathrm{co}}| + |J_{\mathrm{count}}|)$ in the limits $\Delta V \to \pm\infty$. The results are

$$\boxed{\mathcal{S}_{\mathrm{count}}^{\mathrm{max}} = \frac{1 + 4\mathrm{Du}_{\mathrm{max}}}{2 + 4\mathrm{Du}_{\mathrm{max}}} \quad (\mathrm{reverse-bias});} \tag{2.78}$$

$$\boxed{\mathcal{S}_{\mathrm{count}}^{\mathrm{min}} = \frac{1 + 4\mathrm{Du}_{\mathrm{min}}}{2 + 4\mathrm{Du}_{\mathrm{min}}} \quad (\mathrm{forward-bias}).} \tag{2.79}$$

We see that the ion-selectivity is maximized in the reverse-bias (low conductance) configuration and reaches a value of $\sim 83\%$ for $\mathrm{Du}_{\mathrm{max}} = 1$. The coion selectivity is of course given by the relation $\mathcal{S}_{\mathrm{co}} + \mathcal{S}_{\mathrm{count}} = 1$. Note that the counterion selectivity will fall between 1/2 and 1, while the coion selectivity will fall between 0 and 1/2.

Strong Overlap ($\lambda_D/R \gg 1$)

I now derive the corresponding general expressions for the maximum and minimum conductances in the limit of strong overlap ($\lambda_D/R \gg 1$). From Eq. 2.30, we see that $J/\pi R^2 \sim \mathrm{S}2|\mathrm{Du}|c\,d\phi/dx = \mathrm{S}2|\mathrm{Du}_{\mathrm{ref}}|(|\sigma|/R)d\phi/dx$ as $|\Delta V| \to \infty$, as in the no overlap limit. Thus, the solute flux is again given by Eq. 2.72.

Following a similar procedure as we did in the no overlap case, we solve Eqs. 2.30 and 2.31 for the concentration gradient dc/dx in terms of the flux ratio I/J and the solute flux J. We find

$$\frac{dc}{dx} = 4\mathrm{Du}_{\mathrm{ref}}|\mathrm{Du}|\frac{d}{dx}\left(\frac{|\sigma|}{R}\right) - \left(1 + \mathrm{S}2|\mathrm{Du}|\frac{I}{J}\right)\frac{J}{\pi R^2}. \tag{2.80}$$

The first term on the RHS is bounded for all applied voltages. Thus, to ensure a finite concentration gradient as $|\Delta V|$, and hence J, diverges, the prefactor of the second term on the RHS must vanish as $|\Delta V| \to \infty$. This requires that $I/J \to -\mathrm{S}/2\mathrm{Du}_u$, where Du_u is again a uniform Dukhin number in the nanopore interior. We thus find for the asymptotic ionic current

$$I = \frac{G_{\text{surf}}}{2\mathrm{Du}_u}\Delta V, \tag{2.81}$$

where G_{surf} is the surface conductance given in Eq. 2.77. However, in this case, owing to the Donnan concentrations that bulid up at either end of the nanopore (see Eq. 2.34), the uniform interior Dukhin number is not simply one of the imposed values ($\mathrm{Du}_{L/R}$, Eq. 2.36) at the ends of the nanopore. Instead, it is given by one of the interior Dukhin numbers defined by

$$\mathrm{Du}_{\ell/r} \equiv \frac{|\sigma|_{\ell/r}}{ec_{\ell/r}R_{\ell/r}} = \frac{\mathrm{Du}_{L/R}}{\sqrt{1+(2\mathrm{Du}_{L/R})^2}}, \tag{2.82}$$

where I have made use of Eq. 2.34 in the second equality.

Thus, from Eqs. 2.81 and 2.82, we find for the limiting conductances

$$\boxed{G_{\max} = G_{\text{surf}}\frac{\sqrt{1+(2\mathrm{Du}_{\min})^2}}{2\mathrm{Du}_{\min}}, \quad \text{and}} \tag{2.83}$$

$$\boxed{G_{\min} = G_{\text{surf}}\frac{\sqrt{1+(2\mathrm{Du}_{\max})^2}}{2\mathrm{Du}_{\max}}.} \tag{2.84}$$

These results confirm those for the special case of the concentration diode given in Eqs. 2.66 and 2.68.

2.5.3 Conductance in the Vicinity of $\Delta V = 0$

As noted above, it can be difficult to apply the limiting conductances derived in the previous section to experimental results, as the linearization of the IV curve depends on the magnitude of the applied voltage and the imposed Dukhin numbers. I will therefore derive here a general expression for the linear response conductance valid in the vicinity of $\Delta V = 0$. This expression is valid for rectification induced by an asymmetry in geometry or surface charge density (though not concentration for reasons that will be discussed below), and it may be used to infer information about the surface charge density from rectified experimental IV curves. I will focus only on the limit of no overlap ($\lambda_D/R \ll 1$) because this is the more experimentally relevant regime and because the linear response conductance in the presence of strong overlap ($\lambda_D/R \gg 1$) is no longer analytically tractable due to the nontrivial, spatially inhomogeneous Donnan equilibrium in a pore of nonuniform geometry and/or surface charge density.

In the case of the concentration diode, the imposed concentration difference means that there is a difference in chemical potentials between the reservoirs for at least one of the ionic species irrespective of the applied voltage, and there is thus no clear state about which to linearize. However, for the geometric and charge diodes equilibrium obtains when $\Delta V = 0$, and we can linearize about this equilibrium to obtain an expression for the differential conductance $G_0 \equiv \partial I/\partial \Delta V|_{\Delta V=0}$ in the vicinity of $\Delta V = 0$. The equilibrium state is characterized by $\Delta V = 0 \implies J_{\text{co}} = J_{\text{count}} = 0$ and the (centerline) concentration, electrostatic potential, and chemical potential profiles $c \equiv 1$, $\phi \equiv 0$, and $\mu_{\text{co}} \equiv \mu_{\text{count}} \equiv -\ln 2$, respectively. We introduce a perturbative forcing δV ($|\delta V| \ll 1$), which induces fluxes δJ_{co} and δJ_{count}. The applied voltage perturbs the concentration and electrostatic potential profiles such that $c \to 1 + c'$ and $\phi \to 0 + \phi'$, with $c' = 0$ on either end of the nanopore and ϕ' varying between δV on the left and 0 on the right end of the nanopore. The chemical potentials become $\mu_{\text{co/count}} \to -\ln 2 + c' \pm \mathrm{S}\phi'$, from which we define $\mu'_{\text{co/count}} \equiv c' \pm \mathrm{S}\phi'$.

We linearize Eqs. 2.26 and 2.27 to find

$$\frac{\delta J_{\text{co}}}{\pi R^2} = -\frac{1}{2}\frac{d\mu'_{\text{co}}}{dx}, \quad \text{and} \tag{2.85}$$

$$\frac{\delta J_{\text{count}}}{\pi R^2} = -\left(\frac{1}{2} + 2\mathrm{Du}_{\text{ref}}\frac{|\sigma|}{R}\right)\frac{d\mu'_{\text{count}}}{dx}. \tag{2.86}$$

Integration of Eqs. 2.85 and 2.86 along the length of the nanopore gives

$$\delta J_{\text{co}} = +\mathrm{S}\frac{1}{2}\left(\int_L \frac{\mathrm{dx}}{\pi R^2}\right)^{-1}\delta V, \quad \text{and} \tag{2.87}$$

$$\delta J_{\text{count}} = -\mathrm{S}\frac{1}{2}\left[\int_L \frac{\mathrm{dx}}{\pi R^2\left(1 + 4\mathrm{Du}_{\text{ref}}|\sigma|/R\right)}\right]^{-1}\delta V. \tag{2.88}$$

From these results we may calculate the conductance at $\Delta V = 0$ as $G_0 \equiv \delta I/\delta V \equiv \mathrm{S}(\delta J_{\text{co}} - \delta J_{\text{count}})/\delta V$. We find

$$\boxed{G_0 = \underbrace{\left(2\int_L \frac{\mathrm{dx}}{\pi R^2}\right)^{-1}}_{G_0^{\text{bulk}}} + \underbrace{\left[2\int_L \frac{\mathrm{dx}}{\pi R^2(1 + 4\mathrm{Du}_{\text{ref}}|\sigma|/R)}\right]^{-1}}_{G_0^{\text{surf}}},} \tag{2.89}$$

where I have partitioned the result into bulk and surface contributions. The conductances predicted from Eq. 2.89 are shown in Fig. 2.5 for a diode induced by a linear variation in i) nanopore radius (Fig. 2.5e) and ii) surface charge density (Fig. 2.5f).

For the sake of illustration, I derive an explicit expression for G_0 in a conical nanopore with a linearly varying radius and uniform surface charge density. Many studies have looked at ICR in such nanopores, (*e.g.*, Ai *et al.*, 2010; Cervera *et al.*, 2006; Constantin & Siwy, 2007; Kovarik *et al.*, 2009; Lan *et al.*, 2011; Laohakunakorn & Keyser, 2015; Liu *et al.*, 2007; Vlassiouk & Siwy, 2007; White & Bund, 2008; Woermann, 2003; Siwy & Fuliński, 2002), and our result will be useful in relating rectified IV curves to surface charge densities in conical nanopores.

I take the radius to vary linearly between a maximum at the base of the conical nanopore, R_{base}, and a minimum at the tip, R_{tip}. This gives for the magnitude of the radial slope $|dR/dx| = \alpha - 1$ (in rescaled variables), where $\alpha \equiv R_{\text{base}}/R_{\text{tip}}$. We insert this into Eq. 2.89, along with the condition that the surface charge density is uniform $|\sigma| = 1$, and evaluate the integrals to find

$$G_0^{\text{bulk}} = \pi\frac{\alpha}{2}, \quad \text{and} \tag{2.90}$$

$$G_0^{\text{surf}} = \frac{\alpha - 1}{\ln\left(\frac{1+4\text{Du}_{\text{tip}}}{1+4\text{Du}_{\text{tip}}/\alpha}\right)} 2\pi\text{Du}_{\text{tip}}. \tag{2.91}$$

In the above, I have recognized that $\text{Du}_{\text{ref}} = \text{Du}_{\text{tip}} \equiv |\sigma|/ec_{\text{res}}R_{\text{tip}}$, the Dukhin number defined in terms of the uniform surface charge density magnitude, reservoir concentration, and tip radius. Redimensioning Eqs. 2.90 and 2.91, we find

$$G_0^{\text{bulk}} = \frac{\pi R_{\text{base}} R_{\text{tip}}}{2L} \frac{e^2 D}{k_B T} c_{\text{res}}, \quad \text{and} \tag{2.92}$$

$$G_0^{\text{surf}} = \frac{\alpha - 1}{\ln\left(\frac{1+4\text{Du}_{\text{tip}}}{1+4\text{Du}_{\text{tip}}/\alpha}\right)} \frac{2\pi R_{\text{tip}}}{L} \frac{eD}{k_B T} |\sigma|. \tag{2.93}$$

Note that, in the limit of a uniform nanopore $\alpha \to 1$, the sum of Eqs. 2.90 (2.92) and 2.91 (2.93) agrees with the sum of Eqs. 2.55 (2.57) and 2.56 (2.58), as it must.

We find that the dependence of the surface conductance on the surface charge (through the terms proportional to Du_{tip} appearing in the logarithm) is more complicated than a linear proportionality, indicating that the results for the conductance in a conical nanopore reported in Frament & Dwyer (2012), for example, cannot be naïvely applied to the linear response conductance obtained for $|\Delta V| \ll k_B T/e$ (in dimensioned terms). The conductance derived in Frament & Dwyer

(2012) indicates a linear proportionality between the surface conductance and the magnitude of the surface charge density, and we obtain the expression for the surface conductance given therein from Eq. 2.93 only in the limit that $4\mathrm{Du}_{\mathrm{tip}} \gg \alpha$.

2.6 Dynamic Selectivity and Transport in Large Nanopores

In this section, I consider the implications of the mechanism of dynamic selectivity detailed in Sec. 2.3 for transport in large nanopores–*i.e.*, nanopores having radii much larger than the Debye length ($\lambda_D/R \ll 1$). I will make use of the results derived in Sec. 2.5.2 for the limiting conductances and selectivities in the no overlap regime.

I first consider a nanopore of uniform negative surface charge density σ and constant radius R connecting a left reservoir of concentration c_L and applied voltage ΔV to a grounded right reservoir of concentration $c_R \leq c_L$ (Fig. 2.7, inset). This is the same configuration considered in developing an analytical solution for ICR in the conical diode in Sec. 2.4 above.

From Eqs. 2.47 and 2.48, I calculate the cation (counterion) selectivity $\mathcal{S}_+ \equiv |J_+|/(|J_+| + |J_-|)$ as a function of the maximum imposed Dukhin number Du_R and for fixed values of the concentration ratio $\mathrm{Du}_R/\mathrm{Du}_L = c_L/c_R$ (Fig. 2.7). We see that for moderate concentration ratios ($c_L/c_R \leq 10$), a maximum Dukhin number Du_R of order one results in selectivities of $\sim 70-80\%$.

In the inset of Fig. 2.7 I show the cation selectivity as a function of applied voltage ΔV, again colored according to concentration ratio c_L/c_R, and at a fixed $\mathrm{Du}_R = 1$. Recall that the voltage is applied in the high concentration reservoir; this corresponds to the reverse-bias (low conductance / maximum selectivity) state of the concentration diode. Under an applied voltage, the anion flux is reduced and eventually shut down as the anion chemical potential differential $\Delta\mu_- = \ln(c_L/c_R) - \Delta V$ decreases and vanishes. This results in a rapid increase in the cation selectivity as small voltages are applied in the high concentration reservoir and a peak cation selectivity of 100% when $\Delta V = \ln(c_L/c_R)$ and $J_- = 0$. We see in the inset of Fig. 2.7 that the cation selectivity saturates at a value that is independent of c_L/c_R as ΔV is increased above $\ln(c_L/c_R)$ and anions begin to flow from the right to the left reservoir. This saturation value is given by Eq. 2.78, and for $\mathrm{Du}_R = 1$ we find that the saturation value of the cation selectivity is $\sim 83\%$. These results suggest that the nanopore selectivity may be tuned with the application of small external applied voltages.

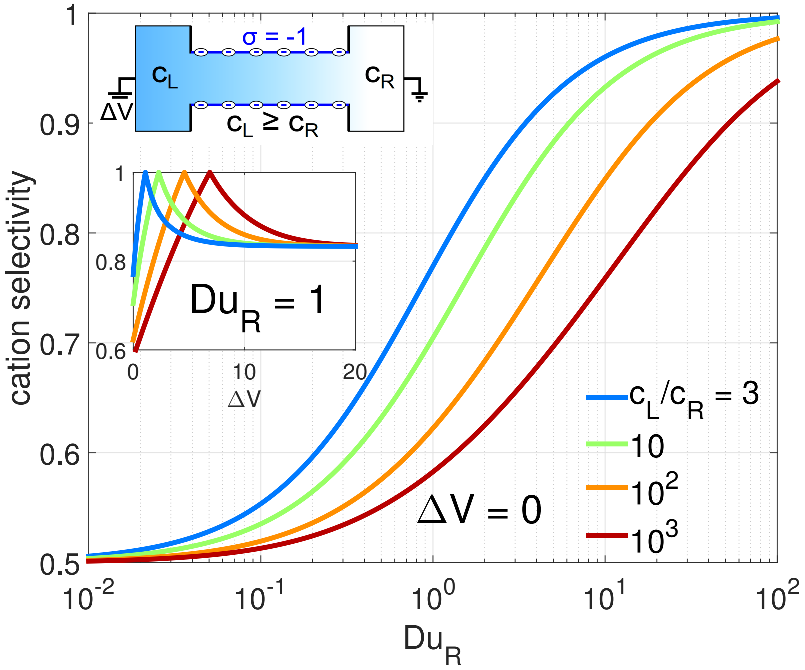

Figure 2.7: Cation selectivity for the diffusive flux in the absence of an applied voltage ($\Delta V = 0$) as a function of the maximum imposed Dukhin number Du_R. The curves are colored according to the corresponding value of c_L/c_R, as indicated in the legend. The fluxes are calculated for a nanopore of uniform negative surface charge density and constant radius, as indicated in the schematic in the upper left. The inset shows the selectivity as a function of applied voltage for a fixed value of $\mathrm{Du}_R = 1$. The curves are colored according to c_L/c_R, as in the main panel.

While the zero-voltage selectivity is not as optimal as traditional ion-selective membranes, which have counterion selectivity ratios $\sim 99\%$, this tradeoff is more than made up for by pore diameters that are of the order of the Dukhin length and thus one-to-two orders-of-magnitude larger.

Let us consider two prototypical situations in which such effects could be usefully harnessed. Reverse electrodialysis (RED) is one of a few proposed techniques for the conversion of the osmotic energy associated with the salinity contrast between fresh and saltwater to electrical energy. This technique depends on ion-selective diffusive fluxes of the type discussed above and shown in Fig. 2.7 across stacks of alternating cation- and anion-selective membranes. The principal limiting factor in commercialization of this process is the low conversion efficiency engendered by the high membrane resistance due to the subnanometric pores in typical ion-selective membranes (Siria *et al.*, 2017). My results suggest that this problem may be circumvented by using large-pore

(10 − 100 nm) membranes with pore diameters and surface charges tailored to the operating concentrations such that a maximum Dukhin number of order one is achieved.

Another phenomenon of interest is traditional electrodialysis (ED), in which an electric field is applied across stacks of cation- and anion-selective membranes in order to separate ions from brackish source water. In this case, what is of interest is the selectivity of the ionic flux induced by an applied voltage in the absence of a concentration differential. To this end, I first consider as a benchmark the performance (in terms of both selectivity and conductance) of a uniform nanopore–*i.e.*, a nanopore with constant (negative) surface charge density and radius; I then compare this to the performance of a conical nanopore having the same length, surface charge density, and tip radius R_{tip}. That is, I hold the tip Dukhin number $\text{Du}_{\text{tip}} \equiv |\sigma|/ecR_{\text{tip}}$ fixed while increasing the ratio of base and tip radii $\alpha \equiv R_{\text{base}}/R_{\text{tip}}$ above unity. The scenario under consideration is sketched in an inset in Fig. 2.8. The goal in increasing the opening angle is to improve the conductance compared to the uniform nanopore without a great cost to the nanopore selectivity.

In the case of a uniform nanopore, the conductance and selectivity are voltage independent and given by Eq. 2.54 and either of Eqs. 2.78 and 2.79 (with $\text{Du}_{\text{max}} \equiv \text{Du}_{\text{min}} \equiv \text{Du}_{\text{tip}}$), respectively. This is indicated by the blue curves in Figs. 2.8a, showing the cation selectivity as a function of voltage, and 2.8b, showing the apparent conductance $G_{\text{app}} \equiv I/\Delta V$ normalized by the uniform nanopore conductance.

The influence of introducing a conical structure (i.e., increasing $\alpha \equiv R_{\text{base}}/R_{\text{tip}}$ above one) on the cation selectivity is shown in Fig. 2.8a. In the vicinity of $\Delta V = 0$, the selectivity drops as α is increased, decreasing from the theoretical limit of $\sim 83\%$ (Eq. 2.78) to $\sim 74\%$ as α is increased from 1 to 10; however, as ΔV is increased, the selectivity again rapidly approaches the theoretical limit for large positive voltages. We see in Fig. 2.8a that a voltage as small as ~ 1 V ($\Delta V = 40$) is enough to achieve a selectivity very nearly identical to the uniform nanopore selectivity.

I plot in Fig. 2.8b the influence of increasing $\alpha \equiv R_{\text{base}}/R_{\text{tip}}$ on the apparent conductance. We see that the limiting apparent conductance for large positive applied voltages is substantially increased as α is increased. Increasing α to 3 is enough to approximately double the conductance, while $\alpha = 10$ results in a conductance that is more than four times larger than the uniform pore conductance. We can derive the relationship between the limiting conductance in the reverse-bias state G_{min} and the uniform conductance G_{uni} by first performing the integration in Eq. 2.77

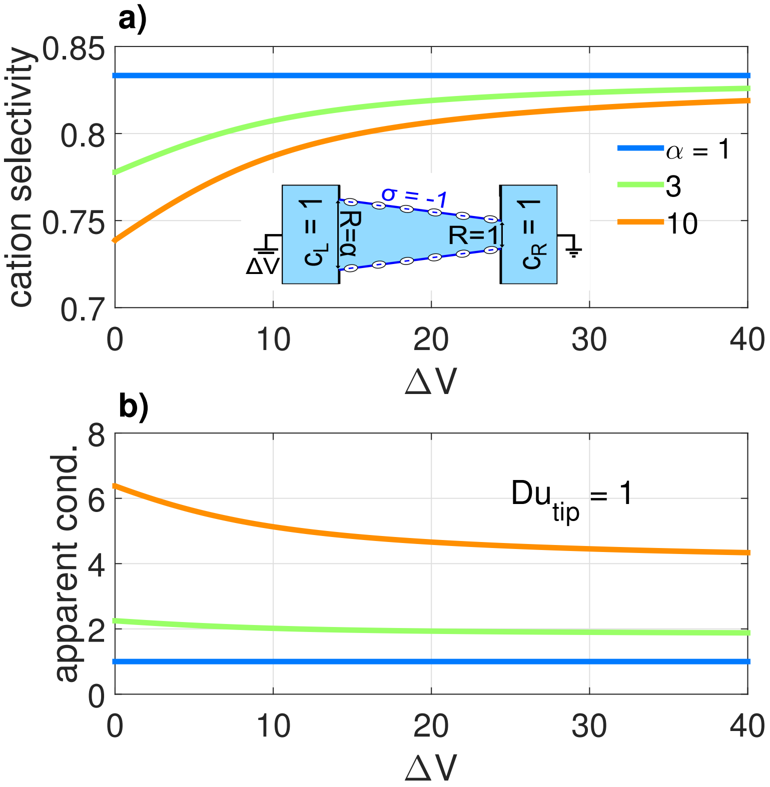

Figure 2.8: a) Cation selectivity in a conical nanopore as a function of applied voltage and colored according to the ratio of base and tip radii $\alpha \equiv R_{\mathrm{base}}/R_{\mathrm{tip}} \geq 1$, as indicated in the legend. b) Apparent conductance $G_{\mathrm{app}} \equiv I/\Delta V$ normalized by the conductance of a uniform ($\alpha = 1$) nanopore (Eqs. 2.54 through 2.56) as a function of ΔV and colored according to $\alpha \equiv R_{\mathrm{base}}/R_{\mathrm{tip}}$, as in a. The inset in panel a shows a schematic representation of the geometry considered here. All curves are calculated with a Dukhin number at the tip $\mathrm{Du}_{\mathrm{tip}} = 1$.

with $|\sigma| = 1$ and imposing a linear variation in the radius to find $G_{\mathrm{surf}} = 2\pi \mathrm{Du}_{\mathrm{tip}}(\alpha - 1)/\ln\alpha$. We then combine this result with Eq. 2.76, recognizing that $2\pi\mathrm{Du}_{\mathrm{tip}} \times (1 + 2\mathrm{Du}_{\mathrm{tip}})/2\mathrm{Du}_{\mathrm{tip}} = \pi + 2\pi\mathrm{Du}_{\mathrm{tip}} \equiv G_{\mathrm{uni}}$, the uniform reference nanopore conductance (Eqs. 2.54 through 2.56), to find

$$\frac{G_{\mathrm{min}}}{G_{\mathrm{uni}}} = \frac{\alpha - 1}{\ln\alpha}. \tag{2.94}$$

The results for a conical nanopore shown in Fig. 2.8 and given in Eqs. 2.78 and 2.94 indicate that 1) substantial selectivity may be achieved in large (*i.e.*, high conductance) uniform radius nanopores if the surface charge and pore radius is tailored to the operating concentrations such that $\mathrm{Du}_{\mathrm{tip}} \sim 1$ and 2) the conductance may be even further enhanced by introducing a conical shape to the nanopore while holding the tip radius fixed. Together, these results suggest that, *e.g.*, desalination processes based on ED may be made substantially more efficient by using high

peak rect. ratio	λ_D/R_{tip}	Du_{tip}	reference
10	$6(10^{-4})$	1.3	He *et al.* (2017)
15	0.014	0.38	Lin *et al.* (2018)
4.6	0.046	0.41	Cervera *et al.* (2006)
2.4	0.082	1.3	Jubin *et al.* (2018)
6.5	0.17	4.8	Kovarik *et al.* (2009)
5.2	0.33	2.9	Cervera *et al.* (2006)
1.9	0.61	1.0	White & Bund (2008)

Table 2.3: Maximum rectification ratios in conical nanopores for fixed Dukhin ratios ($\text{Du}_{\text{max}}/\text{Du}_{\text{min}} = R_{\text{base}}/R_{\text{tip}}$) along with corresponding values of λ_D/R_{tip} and Du_{tip}, as estimated from the literature. Note that the peak rectification ratios cannot be directly compared as they are not all calculated at the same reference voltage magnitude. (The reference voltage magnitudes range between 400 mV and 2 V.)

surface charge, large, conical nanopores.

2.7 Discussion

2.7.1 A Reanalysis of ICR Data in the Literature

These results suggest that inequality of the Dukhin numbers imposed on either end of a nanopore is the only criterion for the occurrence of ICR. Further, they suggest that Du ~ 1 is a (rough) criterion for the maximization of rectification. To this end, I have reinterpreted data for conical nanopores in the literature in terms of the (maximal) tip Dukhin number (Table 2.3). We see that substantial rectification may be obtained even when the minimum radius is two-to-three orders-of-magnitude larger than the Debye length, but that peak rectification consistently corresponds to Du ~ 1, consistent with our theoretical description of dynamic selectivity and its role in ICR in the limit of no overlap ($\lambda_D/R \ll 1$).

In selecting experimental and numerical data from the literature, I searched for any rectification data that was obtained by imposing a *continuous* variation in concentration, geometry, and/or surface charge. Immediately, this excludes data obtained in charge diodes containing a discontinuity in the magnitude and/or sign of the surface charge, (*e.g.*, Li *et al.*, 2013; Nguyen *et al.*, 2010; Karnik *et al.*, 2007). The important distinction between diodes containing discontinuities in the local Dukhin number or the sign of the local surface charge and those considered here will be discussed in the following section. I additionally searched for rectification ratios (either directly reported or inferred from reported IV curves) that displayed a local maximum as the maximum Dukhin number was varied (via variations either in reservoir concentration or surface charge density) while the Dukhin ratio was held fixed. In the end, all of the data that fit these criteria were found to come from conical nanopores.

2.7.2 A Note on the Distinction Between Intrinsic and Extrinsic Diodes

Briefly, I note that we have been concerned here with ICR induced by continuous variations in the local Dukhin number and in the presence of surface charge of a single sign. This is in contrast to both classical bipolar diodes, containing regions of both positive and negative surface charge, (*e.g.*, Picallo *et al.*, 2013; Nguyen *et al.*, 2010; Constantin & Siwy, 2007; Vlassiouk & Siwy, 2007), and unipolar diodes, (*e.g.*, Karnik *et al.*, 2007; Wang *et al.*, 2007; Li *et al.*, 2013), containing regions of zero and nonzero surface charge. I term the latter intrinsic diodes, as in this case the zone of depletion or accumulation is localized to the intrinsic discontinuity in either the local Dukhin number or the sign of the surface charge. I term the type of diodes considered here extrinsic diodes, in contrast to the previous terminology and in recognition of the fact that, in this case, the rectification is due to an imposed inequality in the Dukhin numbers on either end of the nanopore, rather than an intrinsic discontinuity.

Intrinsic diodes are typically found to exhibit much stronger rectification (Li *et al.*, 2013; Vlassiouk & Siwy, 2007) due to the presence of a localized intrinsic accumulation/depletion zone. Picallo *et al.* (2013) showed analytically that, in the limit of high surface charge ($\mathrm{Du} \to \infty$), bipolar diodes exhibit ideal Shockley behavior, typical of classical p-n junction semiconductor diodes (Shockley, 1949). In this case, the current is described by $I = I_{\mathrm{sat}}\left[1 - \exp\left(-e\Delta V/k_B T\right)\right]$, where I_{sat} is the finite saturation current obtained for large positive (reverse-biased) voltages. This is in strong contrast to the behavior of extrinsic diodes as detailed above, in which two finite limiting conductances are observed for large positive or negative voltages, and it is further notable because it illustrates that rectification in intrinsic diodes is maximized as $\mathrm{Du} \to \infty$, rather than being washed out.

2.8 Conclusions and Perspectives

We may summarize the main results of this Chapter as follows:

- The principal parameter controlling selectivity in nanopores is the Dukhin number $\mathrm{Du} \equiv |\sigma|/ecR$, rather than the ratio of the Debye length to the confinement scale λ_D/R.

- In the case that $\lambda_D/R \ll 1$, the Dukhin number controls the nanopore selectivity via a dynamic repartitioning of the ionic transport along the length of the nanopore between the non-selective bulk and the highly selective surface layer, a mechanism we term dynamic selectivity.

- An asymmetry in Du, rather than in λ_D/R, is the only necessary condition for ICR, and a maximum $\mathrm{Du} \sim 1$, rather than a maximum $\lambda_D/R \gtrsim 1$, is the only criterion for the maximization of rectification. This rationalizes many experimental studies showing that ICR may be obtained in pores with radii up to three orders-of-magnitude larger than the Debye length, and that rectification is maximized when the surface charge density magnitude $|\sigma|$ or reservoir concentration c is adjusted such that $\mathrm{Du} \sim 1$.

- Substantial ion selectivity may be obtained in pores with radii comparable to the Dukhin, rather than Debye, length. This is a much less stringent design criterion, as typical Dukhin lengths ($10 - 100$ nm) are one-to-two orders-of-magnitude larger than corresponding Debye lengths ($1 - 10$ nm).

Crucially, the last point suggests the possibility of designing large, conical pore ion-selective membranes. The tip radius and surface charge density of such membrane nanopores can be tailored to the operating concentrations in order to obtain significant ion-selectivity ($80 - 90\%$) while achieving orders-of-magnitude larger conductances than those obtained in traditional (subnanometric) ion-selective membranes. The implications for the design of much more efficient osmotic energy conversion (RED) and desalination/filtration (ED) devices is profound, as the key limiting factor in commercialization of such technologies is the poor efficiency due to low membrane conductance.

Chapter 3

DRAMATIC PRESSURE-SENSITIVE ION CONDUCTION IN CONICAL NANOPORES: TOWARDS A MECHANICAL IONIC TRANSISTOR

Abstract In the previous Chapter, I examined ionic selectivity and transport in nanofluidic devices theoretically, recovering a diode-like behavior analogous to that observed in doped semiconductor devices. However, nanofluidics offers an additional degree-of-freedom compared to solid state devices–namely, the solvent flow and the associated advective ion transport. In this Chapter, I theoretically examine ionic transport in confinement under coupled mechanical (pressure) and voltage forcing by extending the effective one-dimensional framework developed in the previous Chapter to include the solvent flux, solute advection, and pressure. Before doing this, however, I present the results of experiments performed in the group examining ion conduction in conical nanopores under coupled pressure and voltage forcing in the regime wherein there is no Debye overlap ($\lambda_D/R \ll 1$), but the Dukhin number is of order one ($\mathrm{Du} \sim 1$). From the results of the previous Chapter, we anticipate a nonlinear response, and indeed we find that the pressure-response of the ionic current in the presence of an applied voltage is nonlinear and highly sensitive to very small pressures, similar to a mechanical transistor-like effect. In addition to the inclusion of solvent flow, I extend the theoretical framework to allow for perturbative deviations from local electroneutrality and hence the formation of so-called spatially charged zones (SCZs), wherein the sum of the surface charge and the radially integrated ionic charge density is nonzero. SCZ-formation is known to be fundamental to the current response of doped semiconductor devices (Shockley, 1949), and I show here that the formation and deformation of an SCZ mediates the coupled, highly nonlinear pressure-voltage response. The one-dimensional transport equations are numerically integrated in an asymmetric domain similar to the experimental geometry, and the results are compared favorably with the experimental observations. This theoretical framework allows me to obtain a functional relationship between the conductance and the ionic concentration at low pressure, rationalizing the observed nonlinearity in the pressure-response, and to recover

the electrical and streaming conductances at high pressures. The content of this Chapter is presented in ‘Dramatic pressure-sensitive ion conduction in conical nanopores’ (Jubin *et al.*, 2018, *Proc. Natl. Acad. Sci. U.S.A.*, **115**, 4063–4068).

3.1 Introduction

In Chapter 2, we began our theoretical consideration of nonlinear ionic transport in strong confinement with a detailed treatment of ionic current rectification (ICR), the simplest and most ubiquitous example of nonlinear transport in nanofluidics. We found that the main parameter controlling both nanopore selectivity and the occurrence of nonlinear transport is the Dukhin number, $\mathrm{Du} \equiv |\sigma|/ecR$, and that Debye overlap, indicated by a value of the ratio of the local Debye length to the local nanopore radius $\lambda_D/R > 1$, is of secondary importance. Indeed, high selectivity and ICR occur equally well in pores with strong Debye overlap *everywhere* ($\lambda_D/R \gg 1$) and no Debye overlap *anywhere* ($\lambda_D/R \ll 1$). My aim in this Chapter will be to extend the framework of Chapter 2 in order to examine more exotic nonlinear transport processes under coupled mechanical (pressure) and voltage forcing.

We are interested in examining transport under coupled pressure-voltage forcing for two reasons. In the first place, while ICR in particular and the Poisson-Nernst-Planck (PNP) framework generally are analogous to the theory of electron/hole transport in semiconductor devices (Bocquet & Charlaix, 2010), pressure forcing, solvent flow, and advection are absent from PNP and collectively represent an additional degree-of-freedom unique to nanofluidics. For this reason, understanding the influence of this additional degree-of-freedom on ionic transport in strong confinement is of intrinsic interest.

More broadly, when examining the variety of ionic transporters found in nature, one observes a wealth of exotic transport processes including voltage gating, activation, and mechanosensitivity (Bonthuis & Golestanian, 2014; Perozo *et al.*, 2002; Vásquez *et al.*, 2008; Tybrandt, 2017; Coste *et al.*, 2012; Wu *et al.*, 2017) that are unobtainable in the laboratory. In particular, the ability to tune the ionic conduction by an external stimulus remains challenging to achieve artificially. The nanofluidic equivalent of the transistor, as pioneered by Schasfoort *et al.* (1999) and Karnik & Castelino (2006), still poses many difficulties for efficient implementation in nanofluidic circuitry. More generally, the non-linear response of ionic transport in nanopores to coupled forcings and forcings other than applied electric fields, and its relation to the nanopore geometry, remains poorly understood. While ICR has been extensively characterized in the literature, the extension to driving forces other than the electric forcing remains largely unexplored up to now. Of particular interest in this context is the response of the ionic current to mechanical forcing beyond the linear response regime. The ability to tune the conduction by such an external stimulus would open up the possibility of designing advanced fluidic circuitry, such as the hypothetical memristor response (Chua, 2013). However, the low Reynolds number hydrodynamics governing nanometric fluid transport are essentially time-reversible and resolutely linear in pressure forcing, suggesting the *a priori* impossibility of a non-linear mechanical response. Accordingly, the ionic response to mechanical driving is usually described in terms of a streaming current that is linear in pressure drop and verifies the Onsager symmetry relations (Bocquet & Charlaix, 2010).

I will begin this Chapter by presenting the results of experiments conducted in the group examining the ionic current response of a conical, glass nanopipette under coupled pressure and voltage forcing. These experiments are conducted in the limit of no overlap ($\lambda_D/R \ll 1$) and finite Dukhin number ($\mathrm{Du} \gg \lambda_D/R$), and in addition to the anticipated ICR in the absence of applied pressure, we find that the response of the streaming current to pressure is strongly nonlinear in the presence of an applied voltage, and that the ionic conductance is likewise highly sensitive to, and thus tunable by, applied pressure. Even more striking is the fact that this behavior is observed for small imposed pressure drops, while the classical linear response is recovered at large imposed pressure drops, at odds with the expected linear response scenario.

I then derive one-dimensional transport equations valid in the no overlap, finite Dukhin number regime, extending the approach developed in the previous chapter. I include the additional influence of solvent flow and advective ionic transport, as well as perturbative deviations from local electroneutrality. In order to rationalize the experimental results, I numerically integrate the one-dimensional transport equations in an asymmetric domain similar to the experimental geometry. While the transport equations I develop here are more general than those considered in Chapter 2, the price is that they are in general analytically insoluble. However, I am able to obtain analytical results for the conductance at low pressure, the current at high pressure, and a general relationship between the deformation of the spatially charged zone (SCZ) and the response of the ionic current to coupled pressure-voltage forcing valid at all pressures and voltages.

3.2 Motivating Experiments

Experiments were conducted in the group on conical glass nanocapillaries, which constitute easily fabricated and readily reproducible physical models of a single conical nanopore. The radial profiles of the nanocapillaries were characterized via scanning electron microscopy (SEM). The interior radius varied between 250 μm on the upstream end and 165 ± 15 nm at the tip over a length of approximately 3 mm, corresponding to a half angle of approximately 5°. (See Fig. 3.1b.) During the experiments, ionic current was measured as a function of applied voltage ($-400 < \Delta V < +400$ mV) and pressure ($0 < \Delta P < 1500$ mbar) at a fixed molarity of potassium chloride (KCl), as illustrated in Fig. 3.1a.

The results of experiments conducted at a molarity $[\mathrm{KCl}] = 10^{-3}\,\mathrm{M}$ and natural pH ≈ 6 are shown in Figs. 3.1c and d. At this concentration and pH, the surface charge of glass is approximately $10 - 20$ mC m^{-2} (Iler, 1979; Behrens & Grier, 2001; Laohakunakorn & Keyser, 2015), corresponding to a nominal maximum Dukhin number occurring at the tip of the nanopipette of $\mathrm{Du}_{\mathrm{tip}} \approx 0.3 - 0.6$. As the maximum Dukhin number is of order one, we anticipate substantial rectification of the current-voltage (IV) curve in the absence of applied pressure, and indeed this is what we observe (Fig. 3.1c), in agreement with the results of Chapter 2 and previous observations (White & Bund, 2008; Lan *et al.*, 2011; Laohakunakorn & Keyser, 2015). Conversely, for $\Delta V = 0$, the pressure-driven response behaves as expected and a streaming current is generated, linear in ΔP (Figs. 3.1c, inset and 3.1d). This streaming current originates from the pressure-induced advection of ions within the Debye screening layer that forms in the vicinity of solid-liquid interfaces (Schoch *et al.*, 2008). It is given by the Smoluchowski result (Appendix B), which, in a conical nanopore with linearly varying radius of slope α_1, takes the form $I_{\mathrm{stm}} = \pi R_{\mathrm{tip}} \alpha_1 \mu_{\mathrm{EO}} \times \Delta P$, where R_{tip} is the minimum radius occurring at the tip of the nanopipette, and $\mu_{\mathrm{EO}} \equiv (\epsilon/\eta)(-\zeta)$ is the signed, dimensioned EO mobility (Appendix B, Eq. B.23). This is obtained by retaining only the streaming current term $\mathrm{S}|\mu_{\mathrm{EO}}| dP_0/dx$ in Eq. 3.25 and integrating along the length of the nanopipette. In this expression for the EO mobility, ζ is the so-called zeta potential, a generalization of the wall potential appearing in Eq. B.23 that accounts for a nonzero hydrodynamic slip length at the solid-liquid interface. Quantitatively, the streaming conductance $\mathrm{S}_{\mathrm{stm}} \equiv I_{\mathrm{stm}}/\Delta P$ obtained at zero applied voltage is $\mathrm{S}_{\mathrm{stm}}^{\mathrm{exp}} = 0.153\,\mathrm{nA\ bar}^{-1}$, corresponding to a zeta potential of

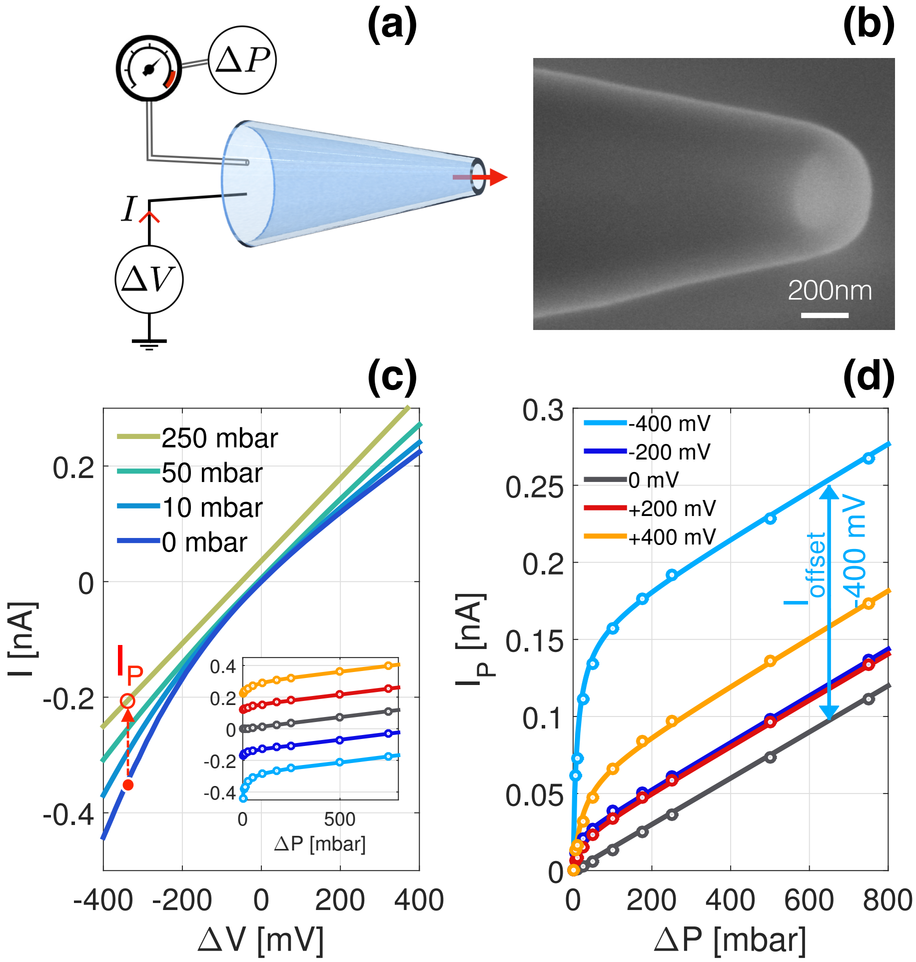

Figure 3.1: Experimental setup with single conical glass nanopipette and experimental response of the ionic current I to applied voltage ΔV and pressure ΔP. a.) Sketch. b.) SEM image. c.) Current-voltage curves for increasing values of ΔP, as indicated in the legend. d.) Additional current induced by applied pressure, I_P, as a function of ΔP for several different values of ΔV, as indicated in the legend. The arrow in panel c indicates I_{offset}, the offset in I_P compared to the linear response obtained for $\Delta V = 0$, for $-400\,\text{mV}$, and the inset shows the total ionic current as a function of ΔP for the values of ΔV indicated in the legend in panel d. The experimental data are fit according to Eq. (3.1) (solid lines). All measurements correspond to a molarity $[\text{KCl}] = 10^{-3}\,\text{M}$, pH $\simeq 6$, and a nominal tip radius of $R_0 = 165 \pm 15\,\text{nm}$.

$\zeta \simeq -42$ mV in agreement with the literature (Iler, 1979).

The behavior for combined finite ΔV and ΔP differs dramatically from the behavior observed when only one forcing is nonzero. As shown in Fig. 3.1c, the IV response changes qualitatively for increasing applied pressures, linearizing for pressures $\gtrsim$ 200 mbar. Similarly, for a given applied voltage drop ΔV, the current-pressure (IP) response is dramatically nonlinear for small pressures $\Delta P \lesssim 50\,\mathrm{mbar}$. As shown in Fig. 3.1d, this non-linearity is particularly apparent if we examine the additional current induced by pressure, $I_P \equiv I(\Delta P, \Delta V) - I(\Delta P = 0, \Delta V)$, as a function of ΔP for fixed values of ΔV. As shown in Fig. 3.1d, for any voltage drop the pressure dependence of I_P is well described by a simple expression of the form:

$$I_P(\Delta P) = S_{\mathrm{stm}}\Delta P + I_{\mathrm{offset}}\frac{a_1\,\Delta P^{1/2} + a_2\,\Delta P}{1 + a_1\,\Delta P^{1/2} + a_2\,\Delta P}, \tag{3.1}$$

where the fitting coefficients $\{a_i\}$ and I_{offset} are functions of the voltage drop ΔV. This highlights a small pressure response of the current that scales as $I_P \sim \Delta P^{1/2}$, while the linear regime $I_P \sim \Delta P$ is recovered for large pressure. The square-root dependence of the ionic current on pressure as $\Delta P \to 0$ suggests that the response is non-analytic at $\Delta P = 0$, within the accuracy of the experiments. This response is at odds with a more naïve analysis, which would suggest that the pressure-induced response at small ΔP should take the form of a Taylor expansion in odd powers of ΔP, $I_P \simeq b_1\Delta P + b_3\Delta P^3 + \ldots$, where the coefficients of the expansion may themselves be expressed as (even) analytic expansions in ΔV. As highlighted by Fig. 3.1d, the response to mechano-electric driving forces is highly non-linear and far stronger than such considerations would suggest.

Surprisingly, while the pressure response observed here is highly non-linear for small ΔP (and any finite ΔV), the limiting slope of the IP curves obtained for large ΔP is independent of voltage and equal to the slope obtained when $\Delta V = 0$ (Fig. 3.1d). In this large ΔP regime, the IP response is again characterized by a linear relationship, but now with a voltage-dependent offset current (Eq. 3.1). The offset current represents a substantial enhancement of the streaming current that would be obtained in the ordinary linear response regime; this can be seen by comparing the linear IP curves corresponding to $\Delta V = 0$ and $-400\,\mathrm{mV}$ (Fig. 3.1d).

Finally, I again emphasize this drastically non-linear behavior is obtained when no Debye-layer overlap occurs in the nanocapillary; the Debye layer here is ~ 10 nm thick, an order of magnitude smaller than the minimum nanocapillary radius, $R_{\mathrm{tip}} = 165 \pm 15$ nm.

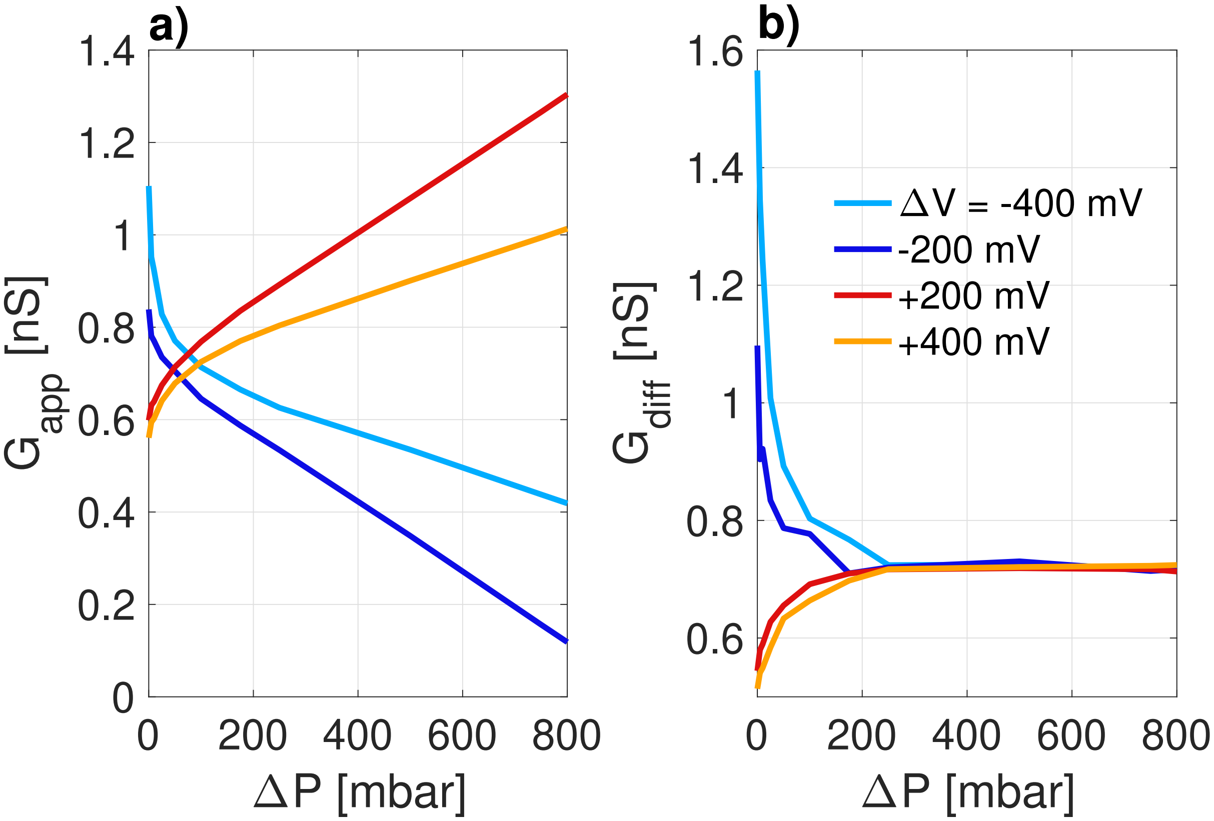

Figure 3.2: Experimental a) apparent and b) differential conductance as a function of applied pressure for several different values of applied voltage, as indicated in the legend in panel b.

Altogether, these results are best described in terms of a pressure-dependent ionic conductance. I report in Figs. 3.2a and b, respectively, both the apparent conductance $G_{\text{app}} \equiv I/\Delta V$ and the differential conductance $G_{\text{diff}} \equiv \partial_{\Delta V} I$. Both quantities highlight a strong sensitivity of the conductance to pressure for small applied pressures. Depending on the applied voltage, the conductance increases or decreases with ΔP, with variations of up to 100% for a change of pressure as small as 100 mbar. The result is an ionic conduction that is dramatically dependent on external mechanical conditions, behavior that is similar to mechanical gating observed in natural ionic transporters, and which constitutes a mechanical transistor-like effect.

3.3 1D Advective-Electrodiffusive Transport Equations

As noted above, our starting point in Chapter 2 was the Poisson-Nernst-Planck (PNP) system of equations. In applying these equations, I assumed that advective ionic transport was negligible in comparison to diffusive and electrophoretic transport. When the only applied forcing is a voltage differential, this amounts to neglecting the quantitative influence of the electro-osmotic flow, a good assumption over much of parameter space (Ai *et al.*, 2010; Vlassiouk *et al.*, 2008a). However, as I am interested here in the ionic transport under coupled voltage and pressure forcing, it will be necessary to account for the solvent flow, pressure, and advective ionic transport explicitly. Thus, in addition to the PNP equations, modified by the inclusion of advective terms in the Nernst-Planck parameterization of the ionic fluxes, we must also include the Stokes equations, statements of solvent mass and momentum conservation valid at the low Reynolds numbers typical of nanofluidic experiments. Together, these comprise the so-called Poisson-Nernst-Planck-Stokes (PNPS) framework. By extending the procedure applied in the previous Chapter for a large-aspect-ratio nanopore in the regime of no Debye overlap ($\lambda_D/R \ll 1$) and finite Dukhin number ($\mathrm{Du} \gg \lambda_D/R$), we will derive effective one-dimensional transport equations for the ionic and solvent fluxes.

The full axisymmetric PNPS equations are

$$j_\pm^x = -D\left(\partial_x c_\pm \pm \frac{e}{k_B T} c_\pm \partial_x \phi\right) + u_x c_\pm, \tag{3.2}$$

$$j_\pm^r = -D\left(\partial_r c_\pm \pm \frac{e}{k_B T} c_\pm \partial_r \phi\right) + u_r c_\pm, \tag{3.3}$$

$$\partial_x j_\pm^x + \frac{\partial_r (r j_\pm^r)}{r} = 0, \tag{3.4}$$

$$0 = -\partial_x P + n_c(-\partial_x \phi) + \eta\left[\partial_x^2 u_x + \frac{\partial_r (r \partial_r u_x)}{r}\right], \tag{3.5}$$

$$0 = -\partial_r P + n_c(-\partial_r \phi) + \eta\left[\partial_x^2 u_r + \frac{\partial_r (r \partial_r u_r)}{r} - \frac{u_r}{r^2}\right], \tag{3.6}$$

$$\partial_x u_x + \frac{\partial_r (r u_r)}{r} = 0, \quad \text{and} \tag{3.7}$$

$$\epsilon_r \epsilon_0 \left[\partial_x^2 \phi + \frac{\partial_r (r \partial_r \phi)}{r}\right] + n_c = 0. \tag{3.8}$$

In the above, $j_\pm^x$ (u_x) and $j_\pm^r$ (u_r) are, respectively, the ion number flux densities (hydrodynamic velocities) along the nanopore axis (x-direction) and in the radial direction, η is the dynamic viscosity of water, and P is the mechanical pressure. All other symbols take their usual meaning (see Chapter 2). As in Chapter 2, I have assumed that the diffusion coefficients for the two species are identical.

Eqs. 3.2 and 3.3 give the Nernst-Planck parameterization of the longitudinal and radial ionic fluxes, respectively, modified by the inclusion of an advective flux; Eq. 3.4 is a statement of local conservation of ion number; Eqs. 3.5 and 3.6 are, respectively, the longitudinal and radial solvent momentum conservation equations neglecting advective acceleration, consistent with the low Reynolds numbers typical of nanofluidic experiments; Eq. 3.7 is a statement of local conservation of solvent volume; and Eq. 3.8 is the Poisson equation.

I partition the ionic charge $n_c \equiv e\,(c_+ - c_-)$ into a component satisfying a local Poisson-Boltzmann (PB) equilibrium, $n_c^{\mathrm{PB}}(x,r)$, and a deviation from local equilibrium, $\delta n_c(x)$, which *a priori* needn't be confined to the Debye layer and is thus assumed to be radially uniform. PB theory requires local electroneutrality when summing over the contributions of the ions and surface to the total charge (Appendix A), so that the local equilibrium charge density must satisfy $\langle n_c^{\mathrm{PB}} \rangle + 2\sigma/R = 0$, where the angled brackets indicate a cross-sectional average, σ is the surface charge density at the solid-liquid interface, and R is the local radius. Thus, $\delta n_c(x) \equiv \langle n_c \rangle + 2\sigma/R$ represents the density of net spatial charge at a location x along the nanopore. I assume that the net spatial charge is small compared to the surface charge, *i.e.*, that $|\delta n_c| \ll |\langle n_c^{\mathrm{PB}} \rangle| = 2|\sigma|/R$. In particular, this implies that, within the Debye layer where the equilibrium ionic charge is significant, $n_c \approx n_c^{\mathrm{PB}}$, whereas outside of the Debye layer (in the bulk), $n_c \approx \delta n_c$. I further assume that $|\langle \delta n_c \rangle|/e \ll c$ such that we may neglect the perturbation to the total ionic concentration induced by the net spatial charge. These assumptions will be validated in the numerical results presented below.

Eqs. 3.2 through 3.8 are dramatically simplified if we apply the assumptions of scale separation ($R/L \ll 1$) and no Debye overlap ($\lambda_D/R \ll 1$). The former assumption allows us to locally neglect longitudinal gradients, except in the forcing terms $\partial_x \phi$ and $\partial_x P$, and the radial velocity and ionic fluxes. The latter assumption allows us to partition the ionic concentrations as $c_\pm(x,r) = c_0(x)/2 + \delta c_\pm(x,r)$ and the electrostatic potential as $\phi(x,r) = \phi_0(x) + \delta\phi(x,r)$, where $c_0(x) \equiv c(x, r=0)$ and $\phi_0(x) \equiv \phi(x, r=0)$ are the centerline total ionic concentration and electrostatic potential, respectively, and $\delta c_\pm(x,r)$ and $\delta\phi(x,r)$ are, respectively, the radial deviations in the ionic concentrations and electrostatic potential induced by the Debye layer. (See Chapter 2, Eqs. 2.3 and 2.4 and Appendix A.)

Before writing down the simplified PNPS equations obtained with the above assumptions, I

variable	notation	rescaled
position	x	$x \to Lx$
radius	R	$R \to R_{\min} R$
concentration	c	$c \to \overline{c} c$
ionic charge density	n_c	$n_c \to e\overline{c} n_c$
electrostatic potential	ϕ	$\phi \to (k_B T/e)\phi$
chemical potential	$\mu_\pm$	$\mu_\pm \to k_B T \mu_\pm$
flux density	$j_\pm$	$j_\pm \to (D\overline{c}/L) j_\pm$
surface charge	σ	$\sigma \to \lvert\sigma\rvert_{\max} \sigma$
hydrodynamic velocity	u	$u \to (D/L) u$
pressure	P	$P \to k_B T \overline{c} P$
electro-osmotic mobility	μ_{EO}	$\mu_{\mathrm{EO}} \to \mu_{\mathrm{EO}}/\mu_{\mathrm{EP}}$
diffusio-osmotic mobility	μ_{DO}	$\mu_{\mathrm{DO}} \to \mu_{\mathrm{DO}}/D$

Table 3.1: Model variables and their rescaled dimensionless counterparts.

rescale the model variables according to Table 3.1. In addition to the rescalings introduced in the preceding Chapter, I rescale the velocity by D/L and the pressure by $k_B T \overline{c}$. In the preceding, L is a scale of longitudinal variation in the geometry, and $\overline{c}$ is the average of the two imposed reservoir concentrations. Note that these scales are taken for convenience, and the rescaled terms are not necessarily of order one. I further rescale the electro-osmotic (EO) mobility μ_{EO} by the electrophoretic mobility $\mu_{\mathrm{EP}} \equiv eD/k_B T$ and the diffusio-osmotic (DO) mobility μ_{DO} by the diffusion coefficient D. Rewriting the ionic flux densities (Eq. 3.2) in terms of the total ion number and charge flux densities, $j \equiv j_+^x + j_-^x$ and $i \equiv e(j_+^x - j_-^x)$, respectively, we find after rescaling

$$j = -\left(\partial_x c + n_c^{\mathrm{PB}} \partial_x \phi\right) - \delta n_c \frac{d\phi_0}{dx} + u_x c_0 + u_x \delta c, \tag{3.9}$$

$$i = -\left(\partial_x n_c^{\mathrm{PB}} + c\partial_x \phi\right) - \frac{d\delta n_c}{dx} + u_x \delta n_c + u_x n_c^{\mathrm{PB}}, \tag{3.10}$$

$$0 = -\partial_x P + n_c \left(-\frac{d\phi_0}{dx}\right) + n_c^{\mathrm{PB}} \left(-\partial_x \delta\phi\right) + \frac{1}{\mathrm{Pe}_{\mathrm{osm}}} \frac{\partial_r (r \partial_r u_x)}{r}, \tag{3.11}$$

$$0 = -\partial_r P + n_c^{\mathrm{PB}} \left(-\partial_r \delta\phi\right), \tag{3.12}$$

$$\left(\frac{\lambda_D^{\mathrm{ref}}}{R_{\mathrm{min}}}\right)^2 \frac{\partial_r\left(r\partial_r\delta\phi\right)}{r} + n_c^{\mathrm{PB}} = 0, \tag{3.13}$$

$$\delta c = c_0\left(\cosh\delta\phi - 1\right), \quad \text{and} \tag{3.14}$$

$$n_c^{\mathrm{PB}} = -c_0 \sinh\delta\phi., \tag{3.15}$$

where I have introduced a reference Debye length $\lambda_D^{\mathrm{ref}} \equiv (\epsilon_r\epsilon_0 k_B T/e^2\overline{c})^{1/2}$, defined in terms of the average of the reservoir concentrations $\overline{c}$, and an osmotic Péclet number, defined as

$$\boxed{\mathrm{Pe}_{\mathrm{osm}} \equiv \frac{(R_{\mathrm{min}}^2/\eta)(k_B T\overline{c}/L)\times L}{D} \equiv \frac{R_{\mathrm{min}}^2 k_B T\overline{c}}{\eta D}.} \tag{3.16}$$

The term $(R_{\mathrm{min}}^2/\eta)(k_B T\overline{c}/L)$ is the product of a scale of the Hagen-Poiseuille hydraulic conductivity $k_{\mathrm{HP}} = R^2(8\eta)^{-1}$ (Appendix B) and a scale of an osmotic pressure gradient $d\Pi_{\mathrm{osm}}/dx = k_B T dc/dx$, and it therefore gives the scale of an osmotic velocity $\mathcal{U}_{\mathrm{osm}}$. For this reason, we may interpret the above parameter as an osmotic Péclet number $\mathrm{Pe}_{\mathrm{osm}} = \mathcal{U}_{\mathrm{osm}}L/D$.

In Eqs. 3.9, 3.11, and 3.12 I have made use of the fact that $\delta\phi$ is substantially different from zero only within the Debye layer to make the approximation $n_c\nabla\delta\phi \approx n_c^{\mathrm{PB}}\nabla\delta\phi$, and in Eq. 3.13 to make the approximation $n_c \approx n_c^{\mathrm{PB}}$. Note that Eqs. 3.13 through 3.15 describe the local PB quasi-equilibrium holding in the radial direction at each point x along the nanopore.

3.3.1 Radially Integrated Continuity Equations

Radial integration of Eqs. 3.4 and 3.7 give

$$\boxed{\frac{dJ}{dx} = \frac{dI}{dx} = \frac{dQ}{dx} = 0,} \tag{3.17}$$

where $J \equiv \int_A \mathrm{d}Aj$ and $I \equiv \int_A \mathrm{d}Ai$ are the total ion number and ion charge fluxes, respectively, and $Q \equiv \int_A \mathrm{d}Au_x$ is the total volumetric solvent flux.

Eq. 3.8 may likewise be radially integrated, subject to the Guassian boundary condition $\hat{\boldsymbol{n}}\cdot\mathbf{E}(x, r = R) = +\sigma/\epsilon_r\epsilon_0$ (in dimensioned variables), where $\hat{\boldsymbol{n}}$ is the unit normal vector pointing out of the solid boundary into the fluid (Appendix A). After rescaling, the result is

$$\boxed{\left(\frac{\lambda_D^{\mathrm{ref}}}{L}\right)^2 \frac{1}{\pi R^2}\frac{d}{dx}\left[\pi R^2\left(-\frac{d\phi_0}{dx}\right)\right] = \delta n_c.} \tag{3.18}$$

3.3.2 Centerline Momentum Equation

Combining the Boltzmann distribution obtained in Eqs. 3.14 and 3.15 with the radial momentum balance, Eq. 3.12, and integrating gives an osmotic pressure balance in the radial direction (Ajdari & Bocquet, 2006):

$$P(x,r) = P_0(x) + \delta c(x,r), \tag{3.19}$$

where $P_0(x) \equiv P(x, r=0)$ is the pressure at the nanopore centerline. Inserting Eq. 3.19 into Eq. 3.11 gives

$$\left(\frac{dP_0}{dx} + \delta n_c \frac{d\phi_0}{dx}\right) + \left(n_c^{\mathrm{PB}} \frac{d\phi_0}{dx}\right) + \left(\delta c \frac{d\ln c_0}{dx}\right) = \frac{1}{\mathrm{Pe}_{\mathrm{osm}}} \frac{\partial_r \left(r \partial_r u_x\right)}{r}, \tag{3.20}$$

where, on the LHS, I have segregated the forcing terms into, from left to right, the pressure gradient and electric body force associated with the net spatial charge, which together induce a quadratic Hagen-Poiseuille flow, and the electro-osmotic and diffusio-osmotic driving forces, which both induce plug-like flows.

3.3.3 Radial Integration of the Ionic Fluxes and Momentum Equation

We note that the first terms in parentheses on the RHS of Eqs. 3.9 and 3.10 are identical to the simplified Nernst-Planck equations considered in Chapter 2 (Eqs. 2.10 and 2.11), and hence we may directly transcribe the results for the radial integration of these terms obtained in Chapter 2 (Eqs. 2.23 and 2.24). Furthermore, the second terms on the RHS of Eqs. 3.9 and 3.10 are radially uniform, and the third terms depend on r only through the hydrodynamic velocity $u_x(x,r)$. Hence, we may immediately write

$$\frac{J}{\pi R^2} = -\left[\frac{dc_0}{dx} + \frac{2\mathrm{Du}_{\mathrm{ref}}|\sigma|}{R} \frac{d\mu_{\mathrm{count}}}{dx}\right] - \delta n_c \frac{d\phi_0}{dx} + \frac{Q}{\pi R^2} c_0 + \langle u_x \delta c \rangle, \quad \text{and} \tag{3.21}$$

$$\frac{I}{\pi R^2} = -\left[c_0 \frac{d\phi_0}{dx} - \mathrm{S}2 \frac{2\mathrm{Du}_{\mathrm{ref}}|\sigma|}{R} \frac{d\mu_{\mathrm{count}}}{dx}\right] - \frac{d\delta n_c}{dx} + \frac{Q}{\pi R^2} \delta n_c + \langle u_x n_c^{\mathrm{PB}} \rangle, \tag{3.22}$$

where we recall that $\mathrm{S} \equiv \mathrm{sign}(\sigma)$ is the sign of the surface charge density, and the counterion chemical potential is given by

$$\boxed{\mu_{\mathrm{count}} = \ln\left(\frac{c_0}{2}\right) - \mathrm{S}\phi_0.} \tag{3.23}$$

In order to determine the volumetric solvent flux Q and to evaluate the final terms on the RHS of Eqs. 3.21 and 3.22, we must first radially integrate the centerline momentum equation, Eq.

3.20, for the velocity profile $u_x(x, r)$. The current and ion number fluxes are then calculated by integrating the resulting flow profiles multiplied by the ionic concentrations over the cross-section. This procedure is described in detail in Appendix B. With the results given there, we find for our final system of one-dimensional transport equations

$$\boxed{\frac{J}{\pi R^2} = -\left(\frac{dc_0}{dx} + \delta n_c \frac{d\phi_0}{dx}\right) - \frac{2\mathrm{Du}_{\mathrm{ref}}|\sigma|}{R}\left(1+\kappa\right)\frac{d\mu_{\mathrm{count}}}{dx} - \mu_{\mathrm{DO}}\left(\frac{dP_0}{dx} + \delta n_c \frac{d\phi_0}{dx}\right) + \frac{Q}{\pi R^2}c_0,} \tag{3.24}$$

$$\boxed{\frac{I}{\pi R^2} = -\left(\frac{d\delta n_c}{dx} + c_0 \frac{d\phi_0}{dx}\right) + \mathrm{S}\frac{2\mathrm{Du}_{\mathrm{ref}}|\sigma|}{R}\left(1+\kappa\right)\frac{d\mu_{\mathrm{count}}}{dx} + \mathrm{S}|\mu_{\mathrm{EO}}|\left(\frac{dP_0}{dx} + \delta n_c \frac{d\phi_0}{dx}\right) + \frac{Q}{\pi R^2}\delta n_c,} \tag{3.25}$$

$$\boxed{\frac{Q}{\pi R^2} = -\mathcal{L}(R)\left(\frac{dP_0}{dx} + \delta n_c \frac{d\phi_0}{dx}\right) - \mu_{\mathrm{DO}}\frac{d\mathrm{ln} c_0}{dx} + \mathrm{S}|\mu_{\mathrm{EO}}|\frac{d\phi_0}{dx},} \tag{3.26}$$

$$\boxed{\frac{dJ}{dx} = \frac{dI}{dx} = \frac{dQ}{dx} = 0, \quad \text{and}} \tag{3.27}$$

$$\boxed{\left(\frac{\lambda_D^{\mathrm{ref}}}{L}\right)^2 \frac{1}{\pi R^2}\frac{d}{dx}\left[\pi R^2\left(-\frac{d\phi_0}{dx}\right)\right] = \delta n_c.} \tag{3.28}$$

In the above, in addition to the normalized DO and EO mobility coefficients, μ_{DO} and $|\mu_{\mathrm{EO}}|$, respectively, I have introduced the Hagen-Poiseuille hydraulic conductivity $\mathcal{L}(R)$, defined as

$$\boxed{\mathcal{L}(R) \equiv \frac{\mathrm{Pe}_{\mathrm{osm}} R^2}{8},} \tag{3.29}$$

and κ, the ratio of the electro-/diffusio-osmotic (acvective) ion flux to the electrophoretic/diffusive flux, defined as

$$\boxed{\kappa \equiv 2\frac{\epsilon_r \epsilon_0}{\eta D}\left(\frac{k_B T}{e}\right)^2 \approx 0.45. \quad (\mathrm{KCl\,in\,water,\ 293\,K}).} \tag{3.30}$$

From left to right, the terms on the RHS of Eqs. 3.24 and 3.25 represent the sum of bulk diffusion and electrophoresis, the sum of surface electro-diffusion and electro-/diffusio-osmotic transport, surface transport induced by the Hagen-Poiseuille (pressure-driven) flow (the streaming fluxes), and bulk advection.

I note that the advective term $Q\delta n_c$ appearing in Eq. 3.25, when combined with Eq. 3.26, results in a term that is quadratic in δn_c. For both consistency with our assumption of small deviations from electroneutrality and numerical stability, it is necessary to neglect this term. This is done in the theoretical results presented below.

3.3.4 A Note on the Radial Integration Procedure

Before examining the experimental results obtained in conical glass nanopores, I note the contrasting procedures available for reducing the 'effective dimensionality' of the PNP equations (*i.e.*, the electro-diffusive terms in Eqs. 3.2) from a two-dimesional axisymmetric system to a quasi-one dimensional system. In deriving the above transport equations (Eqs. 3.24 through 3.28), as well as the simplified transport equations presented in Chapter 2 for the case that advection is negligible (Eqs. 2.23 and 2.24), I have made use of the local Boltzmann equilibrium expressions for the total ionic concentration and ionic charge distributions, inserting them into the local Nernst-Planck parameterizations for the ionic fluxes to obtain equations that are linear in the centerline gradients with transport coefficients that depend on the local ionic concentration or charge density (Eqs. 2.16 and 2.17). I am then able to apply the results of PB equilibrium theory to calculate the average of the total ionic concentration and ionic charge density on the cross-section in the limit of no overlap (Appendix A), and thus to obtain radial integrations of the transport equations that are exact in the limits $R/L \to 0$ and $\lambda_D/R \to 0$.

This procedure is in contrast to at least two other integration procedures applied in the literature: 1) the Fick-Jacobs approach (Malgaretti *et al.*, 2015, 2016) and 2) the 'naïve' averaging approach (Cervera *et al.*, 2006; Constantin & Siwy, 2007; Vlassiouk *et al.*, 2008b; Picallo *et al.*, 2013), in which the one-dimensional transport equations valid in the limit of strong overlap (Eqs. 2.28 and 2.29) are assumed to remain approximately valid in the absence of overlap, with the cross-sectionally averaged ionic concentrations and electrostatic potential replacing the radially uniform values appearing in the strong-overlap equations. The Fick-Jacobs approach is applied specifically to rectification in conical channels in Dal Cengio & Pagonabarraga (2019). This approach relies on the introduction of a complicated 'effective free energy' that is defined implicitly in terms of unknown model variables, and this effective free energy accounts for the entropic influence of confinement. As in the approach applied here and in Chapter 2, the Fick-Jacobs approach relies only on a separation of longitudinal and transverse scales ($R/L \ll 1$), and the transport equations so obtained take particularly simple forms in the limits of no overlap ($\lambda_D/R \ll 1$) and strong overlap ($\lambda_D/R \gg 1$). Indeed, it can be shown that the equations obtained via the Fick-Jacobs approach are precisely identical to those obtained here and in Chapter 2. The advantage of my approach is that it is conceptually more straightforward, avoiding the introduction of an 'effective free energy'.

The latter 'naïve' procedure was applied in the treatment of the electro-diffusive terms in the published version of this work (Jubin *et al.*, 2018). In addition to a separation of longitudinal and transverse scales ($R/L \ll 1$), this approach assumes that the average of the product of model variables (or their gradients) is roughly equivalent to the product of their averages, a less rigorous assumption. (See Cervera *et al.* (2006) and the Supporting Information of Jubin *et al.* (2018).) Here, for the sake of consistency, I have applied the more rigorous methodology originally employed to treat ICR in Chapter 2 and the published version of that work (Poggioli *et al.*, 2019). While either procedure gives results that are qualitatively identical and in complete qualitative agreement with the experiments described below, the more rigorously obtained equations applied here give more quantitatively accurate results than those applied in Jubin *et al.* (2018).

3.4 Theoretical Results

I now examine numerical solutions to the one-dimensional transport equations, Eqs. 3.24 through 3.28, in a simplified geometry characteristic of the conical nanopipettes examined experimentally in Section 3.2. I consider two regions of constant radial slope: $dR/dx = -\alpha_1$ in the interior of the nanopipette and $dR/dx = +\alpha_2$ in the downstream reservoir; the radial profile is taken to vary continuously between these two limiting regions. The imposed radial profile is given by

$$R(x) = \frac{1 - [(x/\ell) + k_1]}{1 - e^{2[(x/\ell)+k_1]}} + \frac{1 + \alpha_{\text{res}}\,[(x/\ell) + k_1]}{1 - e^{-2[(x/\ell)+k_1]}} + k_2, \tag{3.31}$$

where ℓ is a transition length, rescaled by the reference length L (Table 3.1), and k_1 and k_2 are constants chosen such that the minimum radius $R(0) = 1$ occurs at $x = 0$. Note that I have taken $L = R_{\text{tip}}/\alpha_1$ so that $|dR/dx| = 1$ in the nanopipette interior in rescaled variables, and $dR/dx = \alpha_{\text{res}} \equiv \alpha_2/\alpha_1$ in the downstream reservoir. The model geometry and transition length are illustrated in the inset of Fig. 3.3. I take $\alpha_1 = 0.1$, a typical radial slope estimated from SEM profiles, and $\alpha_2 = 10$.

The boundary conditions are imposed in the reservoirs at $x = \pm\infty$. The applied voltage and pressure are imposed in the upstream reservoir, $\phi(-\infty) = \Delta V$ and $P(-\infty) = \Delta P$, while the downstream reservoir is held at ground and reference pressure, $\phi(+\infty) = P(+\infty) = 0$. The reservoir concentrations are fixed and equal, $c(\pm\infty) = 1$, and the reservoirs are electroneutral,

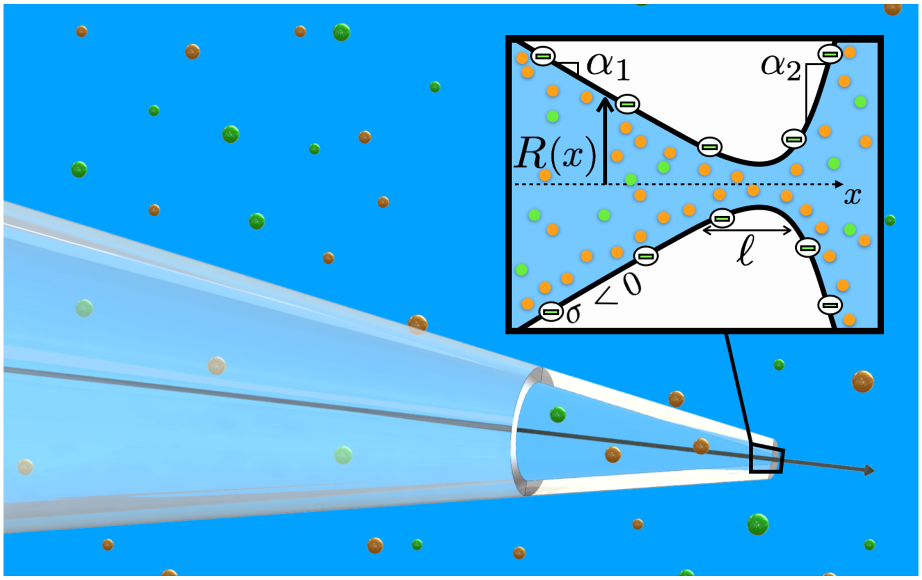

Figure 3.3: A sketch of the geometry of the glass nanocapillary. The inset shows a zoom-in of the model geometry in the vicinity of the tip. The radius is taken to vary between two regions of linear variation over a length scale ℓ as indicated, and these regions are characterized by (unrescaled) radial slopes $\alpha_1 = 0.1$ in the interior and $\alpha_2 = 10$ in the exterior.

$\delta n_c(\pm\infty) = 0$. Note that here and throughout the rest of the Chapter I will drop the subscript zero, taking care to recall that the quantities indicated are centerline values.

The values of all of the dimensionless parameters appearing in Eqs. 3.24 through 3.28 and governing the solution were estimated for the experiments presented above: $\mathrm{Du}_{\mathrm{tip}} \simeq 0.5$, $\lambda_D^{\mathrm{ref}}/L = \alpha_1 \lambda_D^{\mathrm{ref}}/R_{\mathrm{tip}} \simeq 0.0058$, $|\mu_{\mathrm{EO}}| \simeq 0.37$, $\mu_{\mathrm{DO}} \simeq 0.075$, $\mathrm{Pe}_{\mathrm{osm}} \simeq 66.4$. Additionally, I (arbitrarily) take a rescaled transition length of $\ell = 0.1$. These parameters are used in all of the numerical calculations presented below.

The numerical results for the response of the current to applied voltage and pressure are reported in Fig. 3.4, and the results for the conductance are reported in Fig. 3.5. Crucially, this theoretical framework reproduces all of the essential qualitative features of the experiments. Comparing the experimental results – Figs. 3.1c-d and 3.2 – to the theoretical predictions – Figs. 3.4 and 3.5 – we see that we successfully recover a strong, non-linear dependence of the ionic conduction on pressure (Figs. 3.2c and d) resulting in a highly sensitive response of the pressure-induced current I_P to pressure (Fig. 3.4b). Furthermore, we note that the theoretical results are quantitatively consistent with the experimental results; indeed, given the minimal assumptions made in deriving Eqs. 3.24 through 3.28, and the fact that they are all satisfied in the experiments reported above, we expect these one-dimensional results to be essentially as accurate as a full three-dimensional simulation within the full PNPS framework.

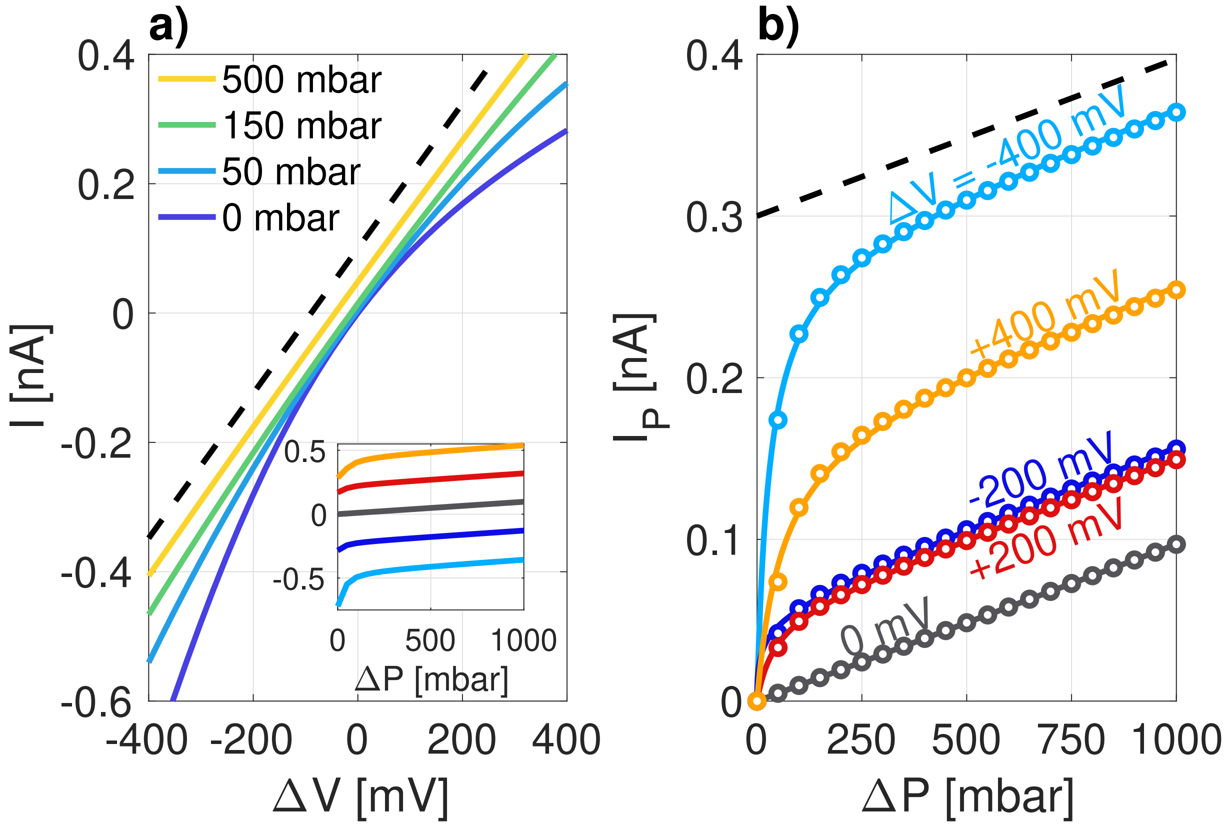

Figure 3.4: Model-derived response of the ionic current I to applied voltage ΔV and pressure ΔP in a conical geometry (Fig. 3.3). a.) Current-voltage curves for increasing values of ΔP, as indicated in the legend. b.) Additional current induced by applied pressure, I_P, as a function of ΔP for several different values of ΔV. The inset in panel a shows the current as a function of ΔP for several different values of ΔV, colored according to the labels in panel b. In panel b, the model predictions are fit according to Eq. 3.1, similar to Fig. 3.1 for the experimental data. The slope of the dashed black line in panel a indicates the value of G_0, and that in panel b indicates the value of $\mathrm{S}_{\mathrm{stm}}$ (Eq. 3.49).

The prediction for the pressure-dependence of the current I_P shown in Fig. 3.4b is successfully described by Eq. 3.1, in full agreement with the experimental results shown in Fig. 3.1d. This demonstrates that the experimental behavior $I_P \sim \Delta P^{1/2}$ measured for low pressure-drop is fully recovered by the model, indicating a strong sensitivity to applied pressure for small pressures. Finally, the theoretical IV curves are observed to linearize as pressure is increased, in accordance

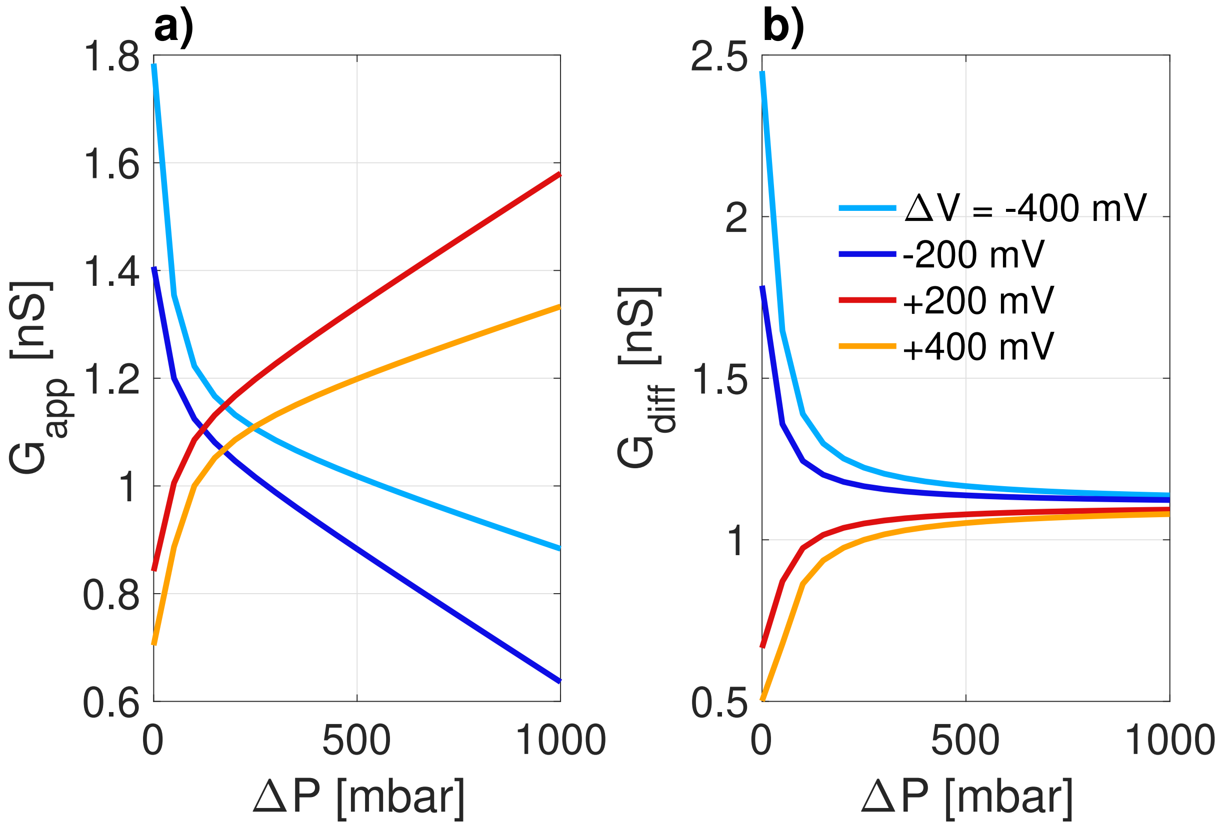

Figure 3.5: Model-derived a) apparent and b) differential conductance as a function of applied pressure for several different values of applied voltage, as indicated in the legend in panel b.

with the experimental observations shown in Fig. 3.1c, with the conductance for all voltages approaching the conductance at zero voltage drop, $\Delta V = 0$ (Fig. 3.4a). The apparent offset in the linear streaming current for large applied pressures is asymmetric in applied voltage, growing much more quickly for negative than for positive values of ΔV, in full agreement with its experimental counterpart.

3.5 Discussion: Deformation of the SCZ

I now show that this nontrivial behavior originates in the sensitivity of the SCZ to the balance between electrical and mechanical forcing. I first note that there is a direct analytical relationship between the formation and deformation of an SCZ and the coupled, nonlinear voltage-pressure response. Beginning with the Poisson equation, Eq. 3.28, we integrate once to obtain

$$\mathcal{F}_D(x) = \mathcal{F}_D(-\infty) + \delta q(x), \tag{3.32}$$

where $\mathcal{F}_D \equiv \epsilon\pi R^2(-d\phi/dx)$ is the electric displacement flux, $\epsilon \equiv (\lambda_D^{\text{ref}}/L)^2 = (\alpha_1\lambda_D^{\text{ref}}/R_{\text{tip}})^2$ is the rescaled permittivity, and I have introduced the cumulative charge

$$\delta q(x) \equiv \int_{-\infty}^{x} \mathrm{d}x' \pi R^2 \delta n_c(x'). \tag{3.33}$$

We integrate this result across the model domain, applying the appropriate boundary conditions at $x = \pm\infty$ for the electrostatic potential ϕ, to obtain

$$\mathcal{F}_D(-\infty) = G_{\text{bulk}} \left[\epsilon \Delta V - \int_{-\infty}^{+\infty} \frac{\mathrm{d}x}{\pi R^2} \delta q\right], \tag{3.34}$$

where I have introduced the bulk conductance G_{bulk}, defined as

$$G_{\text{bulk}} \equiv \left(\int_{-\infty}^{+\infty} \frac{\mathrm{d}x}{\pi R^2}\right)^{-1}. \tag{3.35}$$

We may relate this result to the ionic current by examining the limiting behavior of each of the terms from left to right on the RHS of Eq. 3.25 as $x \to -\infty$. As $\mathcal{F}_D(-\infty)$ tends to a constant value as $x \to -\infty$ (Eq. 3.34), we find from the Poisson equation, Eq. 3.28, that δn_c must vanish faster than $1/R^2$, and therefore $\pi R^2 d\delta n_c/dx \to 0$. From Eq. 3.34, we find that the bulk electrophoretic current $I_{\text{EP}}^{\text{bulk}} \equiv \pi R^2 c d\phi/dx$ tends to a nonzero constant as $x \to -\infty$, given by $I_{\text{EP}}^{\text{bulk}}(-\infty) = \mathcal{F}_D(-\infty)/\epsilon$. From Eq. 3.26, we see that $d\mu_{\text{count}}/dx$ must vanish no slower than $1/R^2$ as $x \to -\infty$, and hence the term proportional to $d\mu_{\text{count}}/dx$ on the RHS of Eq. 3.25 must vanish. And finally, as the volumetric solvent flux Q is a constant and $\pi R^2 d\phi/dx$ tends to a constant, the last and second-to-last terms must vanish as δn_c. We thus have

$$I = I_{\text{EP}}^{\text{bulk}}(-\infty), \tag{3.36}$$

i.e., the ionic current is carried entirely by the bulk electrophoretic current far in the nanopipette interior. Combining this with the above-noted relationship between $I_{\text{EP}}^{\text{bulk}}(-\infty)$ and $\mathcal{F}_D(-\infty)$ and Eq. 3.34, we find

$$\boxed{I = G_{\text{bulk}} \left[\Delta V - \frac{1}{\epsilon} \int_{-\infty}^{+\infty} \frac{\mathrm{d}x}{\pi R^2} \delta q(x)\right].} \tag{3.37}$$

This result explicitly confirms that the nonlinear response results from the deformation of the SCZ under coupled pressure-voltage forcing. From the model results, we learn that for small imposed pressures, the current is dominated locally by the bulk and surface electrophoretic currents along with the EO current.

On the other hand, for large ΔP, the linearization of the IP response is found to correspond to an increase in importance of the local streaming current, such that the current is dominated by the local electrophoretic, EO, and streaming current responses. I discuss each of these two regimes in turn.

Low Pressure Regime

In this regime, the striking result is the dramatic sensitivity of the conductance to applied pressure. As suggested by Eq. 3.1, the current I_P exhibits an apparent square-root dependence on pressure drop in this regime, so that the model predicts $G \sim \Delta P^{1/2}$.

The conductance in this regime may be estimated by retaining only the electro-phoretic and EO terms in the expression for the ionic current (Eq. 3.25):

$$I \approx I_{\mathrm{EP}}^{\mathrm{bulk}} + I_{\mathrm{EP}}^{\mathrm{surf}} + I_{\mathrm{EO}} = -\pi R^2 c \frac{d\phi}{dx} - 2\pi R \mathrm{Du}_{\mathrm{tip}} (1+\kappa) \frac{d\phi}{dx}. \tag{3.38}$$

Integrating in x, we find for the apparent conductance $G \equiv I/\Delta V$:

$$\boxed{G^{-1} = \int_{-\infty}^{+\infty} \frac{\mathrm{dx}}{\pi R^2 \left[c + \frac{2\mathrm{Du}_{\mathrm{tip}}(1+\kappa)}{R} \right]},} \tag{3.39}$$

where the (non-linear) pressure dependence is hidden in the concentration profile $c(x; \Delta P, \Delta V)$. The above result for the apparent conductance (Eq. 3.39) shows that for small imposed pressure, the variation in the apparent conductance with pressure drop, $G(\Delta P)$, may be understood in terms of the pressure-induced variations in the concentration profile $c(\Delta P)$ relative to equilibrium. Concentration profiles are plotted in Figs. 3.6a and b. These profiles exhibit a strong sensitivity to applied pressure when $\Delta P \lesssim 150$ mbar, with the concentration everywhere relaxing to the reservoir value as the linearizing pressure $\Delta P_{\mathrm{lin}} \approx 200$ mbar is approached.

The equivalence of Eq. 3.39 and the more general Eq. 3.37 in describing the current response at low ΔP implies a direct relationship between the net spatial charge δn_c and the concentration field. This is illustrated in Fig. 3.6, where I have also plotted profiles of the cumulative charge in the nanopore (Eq. 3.33). The structural similarity between the cumulative charge and the excess concentration relative to the reservoir value $\delta c \equiv c - 1$ is immediately apparent.

This suggests a back-of-the-envelope argument to account for the square-root variation of the conductance with pressure, $G \sim \Delta P^{1/2}$, highlighted in Eq. 3.1. Under a pressure drop, one may

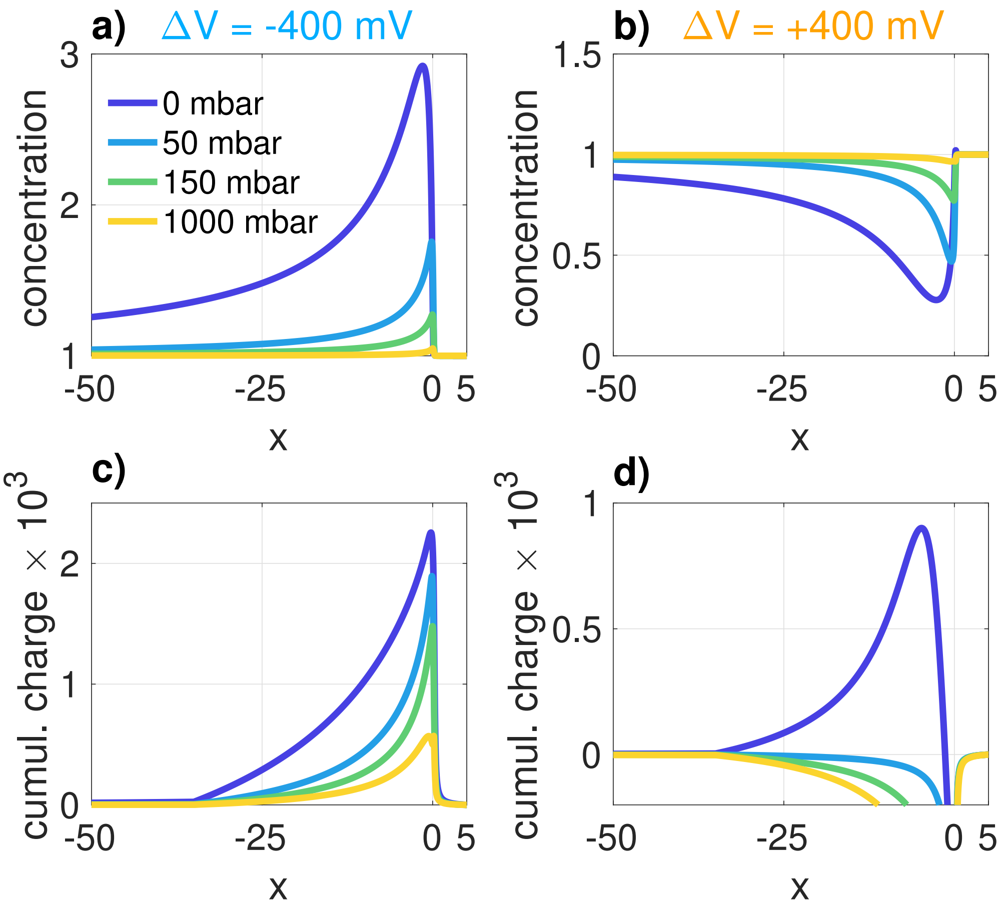

Figure 3.6: Model-derived profiles of local concentration (panels a and b) and cumulative charge (panels c and d) for $\Delta V = -400$ mV (a, c) and $\Delta V = +400$ mV (b, d). The profiles are colored according to increasing values of ΔP, as indicated in the legend in panel a.

anticipate a simple mechanical balance for the SCZ between the electrostatic and pressure forces. This typically takes the form $\delta q \times E_{\text{app}} \sim R_{\text{tip}}^2 \Delta P$, where δq is the cumulative charge in the SCZ, and E_{app} is variation in the induced electric field under an applied pressure. Equivalently, one may interpret the force balance in terms of a balance between the Maxwell stress and the applied pressure: $\epsilon E_{\text{app}}^2/2 \sim \Delta P$. The equivalence of these perspectives requires that the cumulative charge in the SCZ be proportional to the induced electric field, $\delta q \sim E_{\text{app}}$, in agreement with the Poisson equation, Eq. 3.28. Solving for δq yields $\delta q \sim \pm\sqrt{\Delta P}$. Furthermore, as noted above, the variation in the concentration field is found to scale with the cumulative charge. We thus have $\delta c \sim \delta q \sim \pm\sqrt{\Delta P}$. From Eq. 3.39, this variation in the concentration leads to a modification of the conductance that scales as $\delta G(\Delta P) \sim \pm\sqrt{\Delta P}$ for small imposed pressures.

While this scaling is established *a posteriori*, it revovers the apparent square-root correction to the conductance in the applied pressure, in full agreement with the corresponding variation observed in the experiments and theory (Figs. 3.2 and 3.5). It also suggests that the origin of the square-root dependence is in the contribution to the mechanical balance on the SCZ of the Maxwell stress tensor, and its quadratic dependence on the electric field. Interestingly, this dependence is expressed for the present conical geometry, but disappears for cylindrical geometries with constant radius.

High Pressure Regime

In this regime, the current response is linear in applied voltage and pressure (Figs. 3.1 and 3.4). This puzzling behavior can be rationalized analytically by noting from the numerical results that 1) the current is dominated by the electro-phoretic, EO, and streaming contributions, 2) the concentration is homogenized and equal to the reservoir concentration $c \equiv 1$, and 3) the volumetric solvent flux is dominated by the (pressure-driven) Hagen-Poiseuille (HP) contribution. From the third point, we find for the solvent flux and pressure gradient

$$Q = \frac{\mathrm{Pe}_{\mathrm{osm}}}{8} \left(\int_{-\infty}^{+\infty} \frac{\mathrm{d}x}{\pi R^4} \right)^{-1} \Delta P, \quad \text{and} \tag{3.40}$$

$$-\frac{dP}{dx} = \left(\int_{-\infty}^{+\infty} \frac{\mathrm{d}x}{R^4} \right)^{-1} \frac{\Delta P}{R^4}, \tag{3.41}$$

respectively. Inserting this result into the expression for the local streaming current $I_{\mathrm{stm}} = -\pi R^2 |\mu_{\mathrm{EO}}| (dP/dx)$, we obtain

$$I_{\mathrm{stm}} = \left(\int_{-\infty}^{+\infty} \frac{\mathrm{d}x}{\pi R^4} \right)^{-1} |\mu_{\mathrm{EO}}| \frac{\Delta P}{R^2}. \tag{3.42}$$

Eq. 3.32 may be rewritten as

$$I_{\mathrm{EP}}^{\mathrm{bulk}}(x) = I + \frac{1}{\epsilon} \delta q(x), \tag{3.43}$$

where I have applied Eq. 3.36 and noted that $c \equiv 1$ and therefore $I_{\mathrm{EP}}^{\mathrm{bulk}}(x) = \pi R^2 (-d\phi/dx) = \mathcal{F}_D(x)/\epsilon$ in the high-pressure limit. The total ionic current in this limit is given approximately by the sum of the bulk and surface electrophoretic, EO, and streaming currents:

$$I = -\pi R^2 \left[1 + \frac{2\mathrm{Du}_{\mathrm{tip}}(1+\kappa)}{R} \right] \frac{d\phi}{dx} + I_{\mathrm{stm}} = \left[1 + \frac{2\mathrm{Du}_{\mathrm{tip}}(1+\kappa)}{R} \right] I_{\mathrm{EP}}^{\mathrm{bulk}} + I_{\mathrm{stm}}. \tag{3.44}$$

We solve this equation for $I_{\mathrm{EP}}^{\mathrm{bulk}}$ and insert the result into Eq. 3.43 to find

$$\frac{I - I_{\mathrm{stm}}}{1 + \frac{2\mathrm{Du}_{\mathrm{tip}}(1+\kappa)}{R}} = I + \frac{1}{\epsilon}\delta q. \tag{3.45}$$

We rearrange this equation, divide by πR^2, insert Eq. 3.42 for the streaming current, and integrate in x to obtain

$$I\left(G_0^{-1} - G_{\mathrm{bulk}}^{-1}\right) = \gamma|\mu_{\mathrm{EO}}|\Delta P + \frac{1}{\epsilon}\int_{-\infty}^{+\infty}\frac{\mathrm{d}x}{\pi R^2}\delta q, \tag{3.46}$$

where γ is an order-one constant defined as

$$\gamma \equiv \left(\int_{-\infty}^{+\infty}\frac{\mathrm{d}x}{\pi R^4}\right)^{-1}\int_{-\infty}^{+\infty}\frac{\mathrm{d}x}{\pi R^4}\left[1 + \frac{2\mathrm{Du}_{\mathrm{tip}}(1+\kappa)}{R}\right]^{-1}, \tag{3.47}$$

and I have introduced the linear-response conductance

$$G_0^{-1} = \int_{-\infty}^{+\infty}\frac{\mathrm{d}x}{\pi R^2}\left[1 + \frac{2\mathrm{Du}_{\mathrm{tip}}(1+\kappa)}{R}\right]^{-1}, \tag{3.48}$$

valid at high ΔP and in the vicinity of $\Delta V = 0$ (Fig. 3.4c). Finally, we combine Eq. 3.46 with Eq. 3.37 to obtain

$$\boxed{I = G_0\Delta V + \mathrm{S}_{\mathrm{stm}}\Delta P,} \tag{3.49}$$

where $\mathrm{S}_{\mathrm{stm}} \equiv \gamma G_0|\mu_{\mathrm{EO}}|$.

This result, though formally clear, is striking in several aspects. First, in this regime, the current is shown to be linear in both voltage drop ΔV and pressure drop ΔP, in full agreement with the experimental results. Furthermore, the conductance and streaming current take their *linear response values*, *i.e.*, those calculated at vanishing voltage and pressure drop. Indeed, with the exception of small corrections induced by the inclusion of the surface electrophoretic and EO contribution, the streaming conductance $\mathrm{S}_{\mathrm{stm}} \equiv \gamma G_0|\mu_{\mathrm{EO}}| \approx G_{\mathrm{bulk}}|\mu_{\mathrm{EO}}|$ takes the value obtained by assuming that the streaming current alone drives the local current response at high pressure everywhere in the nanopore.

3.6 Conclusions and Perspectives

The key results of this Chapter may be summarized as follows:

- As in the case of ICR (Chapter 2), nonlinear ionic transport occurs when the maximum Dukhin number in an asymmetric nanofluidic device is of order-one, irrespective of the value of λ_D/R.

- The ionic conductance in a conical nanopore may be sensitively tuned by applied pressures. In the present experiments and theoretical results, we demonstrate increases/decreases in conductance of up to 100% under slight variations in the applied pressure.

- The highly nonlinear response to coupled mechanical and electrical forcing is mediated by the formation and deformation of an SCZ. This deformation results in an apparent square-root dependence of the ionic current response on ΔP at low pressure.

The possibility to mechanically tune conduction mimics a mechanical transistor functionality, with the pressure opening or closing conductance channels. In organisms, the mechano-sensitive response of dedicated pores is of crucial importance in preventing fatal osmotic shocks by activating channels under hydrostatic or diffusio-osmotic forces (Bonthuis & Golestanian, 2014; Perozo *et al.*, 2002; Vásquez *et al.*, 2008). Here the response to pressure is of a different type, as the pressure is found to tune rather than open or close the electric conduction channels.

I conclude by noting that such a mechano-sensitive behavior may also find applications in the context of membrane science, where the possibility to activate or inhibit the electric conduction by small pressure stimuli could be of interest for various applications. For example, in the context of osmotic (blue) energy, the maximum achievable power is proportional to the electric resistance of the membrane (Siria *et al.*, 2017), and the present non-linear couplings may allow for mechanical tunability of the extracted power.

Chapter 4

MOLECULAR STREAMING AND ITS VOLTAGE CONTROL IN ÅNGSTRÖM-SCALE CHANNELS

Abstract As in the preceding Chapter, I present here experimental results and corresponding theory demonstrating nonlinear pressure-voltage coupling in ionic transport. However, the origin of the coupling detailed in this Chapter is distinct from that examined in Chapter 3. In the preceding Chapter I discussed nonlinear, coupled transport in large ($10-100$ nm) pores induced by surface charge effects; here, the channels examined are of molecular scales (7 Å) and the surface charge is negligibly small when the coupling is maximized. The channels are manufactured from hexagonal boron nitride and graphene via the process of van der Waals assembly detailed previously (Geim & Grigorieva, 2013; Radha *et al.*, 2016; Esfandiar *et al.*, 2017), and ionic current is measured experimentally under applied pressure and voltage, revealing a transistor-like electrohydrodynamic effect. An applied bias of a fraction of a volt increases the measured pressure-driven ionic transport (characterized by streaming mobilities) by up to 20 times. This gating effect is observed in both graphite and hexagonal boron nitride channels but exhibits marked material-dependent differences. I use a modified continuum framework accounting for the material-dependent frictional interaction of water molecules, ions, and the confining surfaces to explain the differences observed between channels made of graphene and hexagonal boron nitride. This work is presented in 'Molecular streaming and its voltage control in ångström-scale channels' (Mouterde *et al.*, 2019, *Nature*, **567**, 87–90).

4.1 Introduction

Over the past decade, the ability to reduce the dimensions of fluidic devices to the nanometer scale–by using nanotubes (Fornasiero *et al.*, 2008; Siria *et al.*, 2013; Secchi *et al.*, 2016b,a; Tunuguntla *et al.*, 2017) or nanopores (Garaj *et al.*, 2010; Joshi *et al.*, 2014; Jain *et al.*, 2015; Feng *et al.*, 2016; Hong *et al.*, 2017; Abraham *et al.*, 2017), for example–has led to the discovery of unexpected water- and ion-transport phenomena (Eijkel & van den Berg, 2005; Schoch *et al.*, 2008; Howorka & Siwy, 2009). More recently, van der Waals assembly of two-dimensional materials (Geim & Grigorieva, 2013) has allowed researchers to create artificial channels with ångström-scale precision (Radha *et al.*, 2016). Such channels push fluid confinement to the molecular scale, where the limits of the continuum transport theory applied in preceding Chapters are challenged (Bocquet & Charlaix, 2010). Water films on this scale can rearrange into one or two layers with strongly suppressed dielectric permittivity (Schlaich *et al.*, 2016; Fumagalli *et al.*, 2018) or form a room temperature ice phase (Algara-Siller *et al.*, 2015). Ionic motion in such confined channels is affected by direct interactions between the channel walls and the hydration shells of the ions (Esfandiar *et al.*, 2017), and water transport becomes strongly dependent on the channel wall material (Tocci *et al.*, 2014).

In this Chapter, I will first present experiments conducted in the group examining ionic transport in such devices. The ionic current is measured as a function of applied pressure and voltage, again finding nontrivial and highly nonlinear couplings between the mechanical and electrical forcing, as in Chapter 3. However, the origin of this coupling must be much different in this case for two reasons. In the first place, previous conductance measurements performed on ångström-scale devices fabricated in the same manner as the devices examined here have demonstrated that the surface charges in hexagonal boron nitride (hBN) and graphite channels are three-to-four orders-of-magnitude smaller than those measured in boron nitride and carbon nanotubes (BNNTs and CNTs, respectively) (Esfandiar *et al.*, 2017). Though at the lowest concentrations considered experimentally the extreme confinement does lead to a Dukhin number of order one in the more highly charged graphite channels (though not in hBN), surface charge effects cannot be at the origin of the nonlinear coupling found here because the coupling persists and is enhanced as the concentration is increased (see Figs. 4.4d and e and 4.5b and c). This is true even though, as the concentration is increased, the Dukhin number is decreased to values of order $10^{-4} - 10^{-3}$.

Secondly, we found in Chapters 2 and 3 that a necessary condition for nonlinear transport in larger ($10 - 100$ nm) pores and channels is an asymmetry in the Dukhin numbers imposed on either end of the pore–typically induced either by an asymmetry in channel geometry or in reservoir conditions (total ionic concentration or pH). However, no such asymmetry is present here (though an asymmetry in the geometry of the reservoirs does have an important impact on our measurements, as will be discussed below). Thus, the origin of the nonlinear pressure-voltage couplings must be quite different from the mechanisms at play in larger pores and channels.

After presenting these experimental results, I will detail my efforts to rationalize these observations theoretically on the basis of what I term an ‘extended Poisson-Nernst-Planck (PNP) framework’. In particular, as only one or two adjacent layers of water molecules are present in the channels, the Stokes description of the water transport is inapplicable here. Furthermore, the ionic velocities must be modified by the interaction of the ions with the confining walls. In order to account for these effects, I consider a force balance on the individual ions and on a control volume containing both water molecules and ions, considering three phenomenological forces: the frictional interactions between ions and the wall, between water molecules and the wall, and between the ions and water molecules. The description is still fundamentally hydrodynamic, as I consider only mean quantities and neglect fluctuations. I selected this approach in order to derive qualitative insight into the experimental results without resorting to more complex and costly methods (*e.g.*, *ab initio* molecular dynamics simulation) by using an approach that retains the relative simplicity of the continuum description while still accounting for the more dramatic effects of extreme confinement. Indeed, we will see below that the model developed here does reproduce many of the qualitative features of the experiments.

4.2 Experiments

Our devices were fabricated following previously reported procedures (Radha *et al.*, 2016; Esfandiar *et al.*, 2017). In brief, a free-standing silicon nitride (SiN) membrane of around 500 nm in thickness provided mechanical support and served to separate the two reservoirs connected by the channels. On the membrane, a rectangular hole of approximately 3 μm × 26 μm was defined by lithography and plasma etching. The channels were made by van der Waals assembly of three layers–bottom, spacer, and top–of two-dimensional crystals of either graphite or hBN. First, a bottom layer of around 10-to-50-nm-thick graphite or hBN was transferred onto the hole in the SiN membrane and etched from the back side, which projected the hole into the bottom layer. Following this, pre-patterned bilayer graphene spacers (about 6.8 Å thick) in the form of parallel ribbons about 130 nm wide and separated also by about 130 nm were transferred onto the bottom crystal and aligned perpendicular to the long axis of the rectangular hole. Finally, a thick (about $100 - 150$ nm) top crystal of graphite or hBN was transferred onto the spacers covering the hole (Fig. 4.1). The lateral extent of the top crystal defined the length of the channels. The end result

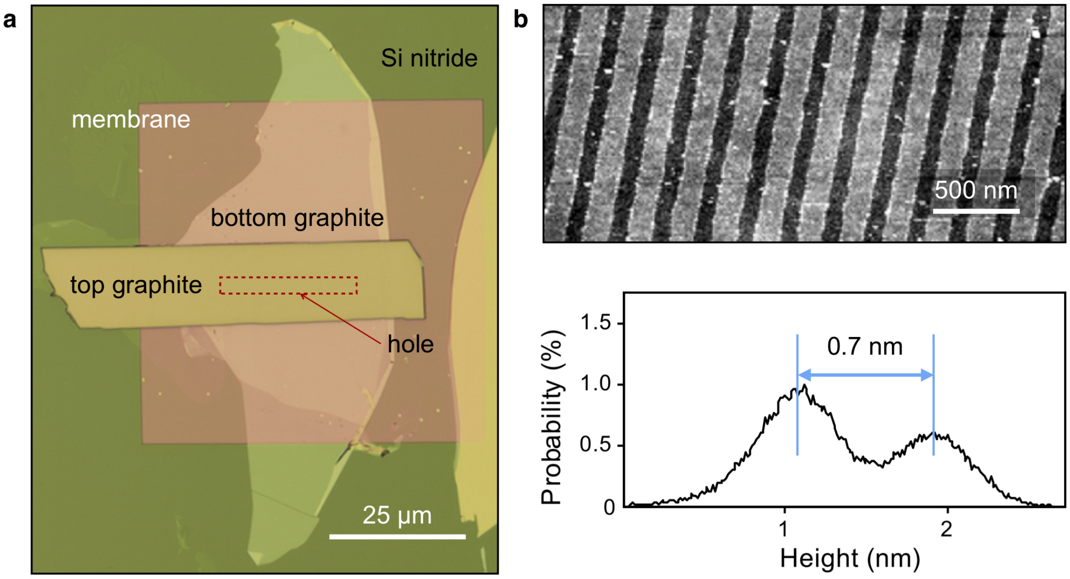

Figure 4.1: Ångström-scale channel devices. a) Optical image of a device with ångström channels. The light pink square is the silicon nitride membrane, which has a rectangular hole shown by the red dotted line. Covering the hole, the bottom graphite layer, spacer, and top graphite layer are placed. Bottom and top graphite are visible in the image in light and bright yellow colors, respectively. b) Atomic force microscopy (AFM) image of the bilayer graphene spacer lines on the device. The histogram of the heights (below the AFM image) shows that the spacer is about 0.7 ± 0.1 nm thick.

was devices with $N = 200$ channels of micrometric length L, height $h_0 = 6.8$ Å, and nominal width $w = 130$ nm.

The channels connected two macroscopic reservoirs filled with KCl solution of concentration c and containing chlorinated Ag/AgCl electrodes for voltage imposition and electrical current measurement. As previously reported (Esfandiar *et al.*, 2017), the net current I at high salt concentration is typically of the order of a few picoamps per channel for applied voltages of a few tens of millivolts and varies linearly with voltage and concentration as expected for this ultra-confined system with small surface charge. The experiments presented here are focused on the ionic current driven by the pressure drop ΔP and the effect of the additional potential difference ΔV applied along the channel. For this, ΔV was imposed in the lower reservoir connected directly to the hole in the Si/SiN substrate via a patch-clamp amplifier with a current resolution of 0.1 pA, while the upper reservoir connected to the channels was held at ground (Fig. 4.2). We applied the pressure in both directions across the channel and found no influence on the reported results

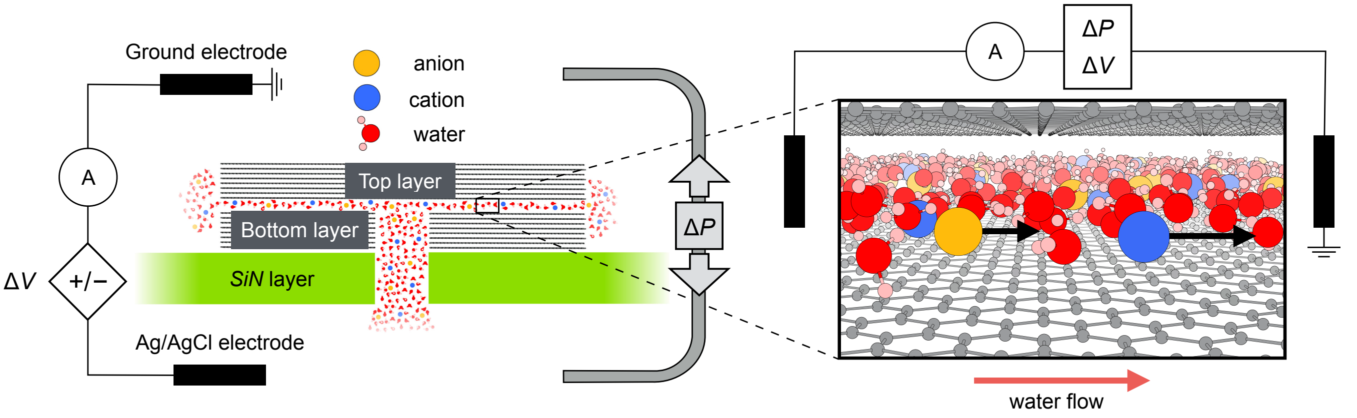

Figure 4.2: Experimental setup for pressure- and voltage-driven current. Schematic: ångström channels (fabricated on a Si/SiN wafer) separate two reservoirs containing KCl solutions. The entry and exit of the channel are on either side of the wafer. We set the voltage ΔV and the pressure ΔP along the channels and monitored the resulting current I. Right panel: illustration of ions moving in water under strong confinement (only one layer of top and bottom graphite walls is shown for clarity). Positive streaming currents indicate that potassium ions move faster than chloride ions inside the channel.

(see Appendix C, Fig. C.2). Note that, consistent with the applied voltage, pressure applied from the bottom side in Fig. 4.2 is denoted as positive. Control experiments used similar devices but without channels and yielded no current upon application of ΔP or ΔV, confirming that our devices were structurally stable and, for example, did not delaminate under pressure (see Appendix C, Fig. C.1).

This setup (Fig. 4.2) allows us to measure the pressure driven component of the ionic current, referred to as the streaming current $I_{\text{str}} \equiv I(\Delta P, \Delta V) - I(0, \Delta V)$. Figure 4.3 illustrates the behavior in the absence of applied bias ($\Delta V = 0$), with Fig. 4.3a showing the time response of I_{str} when stepping ΔP up to 125 mbar in 25 mbar increments. Each step lasts 20 s, and the delay between successive steps is likewise 20 s. After an initial overshoot, I_{str} rapidly reaches a steady state and, once the pressure is released, quickly returns to zero. The measured current is positive for positive applied pressures. This is consistent with a pressure-driven flow that gradually increases with pressure gradient and conveys a net positive charge owing to the suppression of the potassium mobility under strong confinement (Esfandiar *et al.*, 2017, right panel of Fig. 4.2). However, the theoretical results presented below suggest that the origins of the current response

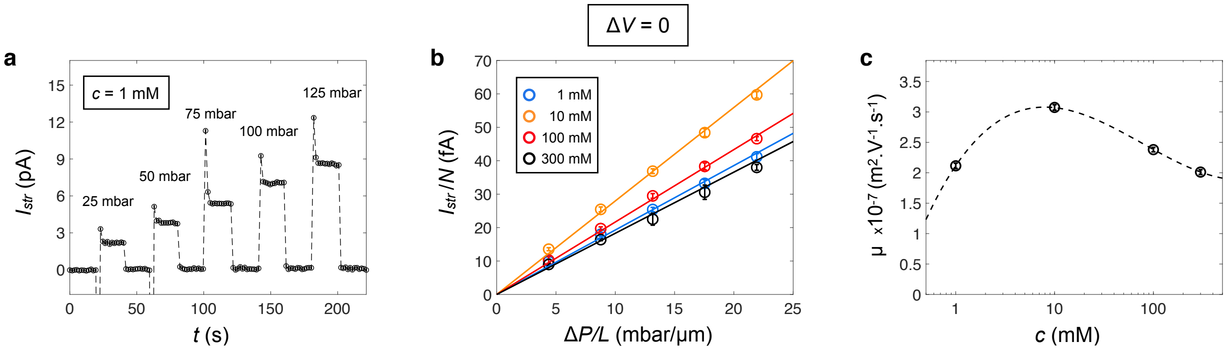

Figure 4.3: Pressure-driven current without applying bias. a) I_{stm} as a function of time for graphite channels, $c = 1$ mM; $L = 5.7 \pm 0.1$ μm. Current overshoots once the pressure is applied, and we consider only the steady-state regime in this study. b) Streaming current per channel, I_{stm}/N, as a function of the pressure gradient $\Delta P/L$ for channels in panel a, and with different KCl concentrations c. For each c, the line corresponds to the best linear fit. c) Electro-osmotic mobility μ as a function of the KCl concentration (linear-logarithmic coordinates; dashed line is a guide to the eye). Error bars represent a) error in the currents measured during temporal evolution (± 0.1 pA), b) standard error, and c) uncertainty in the fit value. Three devices were measured and showed the same behavior.

may be more complicated than this simplified picture.

For concentrations between 1 and 300 mM (the range examined experimentally), the steady-state current reached after each pressure increment (Fig. 4.3a) increases linearly with the pressure gradient (Fig. 4.3b). From the measured slopes, we calculate the streaming mobility $\mu \equiv I_{\text{str}}/(NA\Delta P/L)$, where $A = wh_0$ is the channel cross-sectional area. The streaming mobility weakly depends on salt concentration, varying by less than 50% if the concentration is increased by a factor of 300 (Fig. 4.3c). However, the absolute value of μ is surprisingly high; it is of the order of 10^{-7} m^2 V^{-1} s^{-}1, which is in the range of the bulk potassium electrophoretic mobility $\mu_{K^+} = 7.6 \times 10^{-8}$ m^2 V^{-1} s^{-1} and an order of magnitude larger than streaming mobilities reported in the literature. (For example, the streaming mobility for SiO$_2$ channels is about $0.1\mu_{K^+}$.)

In order to facilitate a direct comparison between the mobilities observed here and those typically encountered in the literature, we consider the measured streaming mobility in terms of the corresponding zeta potential, which has the dimension of an electrostatic potential. The zeta potential takes the place of the wall potential in the expression for the electro-osmotic mobility

(Appendix B, Eq. B.23) when the slip length is nonzero. We emphasize, however, that the Smoluchowski formulae (Appendix B, Eqs. B.23 and B.24) for the electro-osmotic velocity, and, indeed, the physical concept of electro-osmosis itself, is fully irrelevant in a channel with height much smaller than the Debye length, let alone in the channels examined here, which are too small to allow the formation of a diffuse screening layer at all. The calculation of the zeta potential serves only to highlight the dramatic disagreement between the mobilities measured here and those that would be predicted via continuum theory that is valid in conduits of much greater dimension. Using bulk water properties (viscosity $\eta = 1$ mPa s and relative permittivity $\epsilon_r \approx 80.1$) gives us an apparent zeta potential, $\zeta = -\mu\eta/\epsilon_r\epsilon_0$, of roughly -0.4 V, at least ten times the typical values in the literature (Siria *et al.*, 2013; Sze *et al.*, 2003; Geismann *et al.*, 2007) which are of the order of $k_BT/e \approx 25$ mV. Recent studies of confined water indicate that its out-of-plane relative permittivity can be markedly suppressed (Fumagalli *et al.*, 2018) to $\epsilon_{\text{conf}} \approx 2$ whereas η remains close to the bulk value (Radha *et al.*, 2016), which would translate into an even larger apparent ζ of -16 V. However, as noted above, such a large apparent zeta potential does not reflect an anomalously high surface potential on graphite but instead the high streaming mobility arising from the unusually fast transport of water, and hence hydrated ions, at molecular distances from the channel surfaces.

Figure 4.4 shows pressure-driven streaming currents measured under different applied voltage biases, allowing us to explore how the pressure-induced current couples to electric forces at these molecular scales. Figure 4.4a shows the time response of I_{str} when applying pressure and voltage simultaneously, revealing a considerable coupling between them. In particular, we see that I_{str} is increased by more than 100% for $\Delta V = 50$ mV compared to its value when $\Delta V = 0$. As illustrated in Fig. 4.4b, the effects of ΔP and ΔV do not simply add; although the current always remains proportional to the pressure gradient, irrespective of the applied bias, the slope of this linear dependence–the streaming mobility $\mu(\Delta V)$–varies with ΔV according to $I_{\text{str}} = \mu(\Delta V) \times A \times N \times \Delta P/L$. The dependence of the streaming current on voltage indicates an unexpected interplay between mechanical and electric driving forces. To disentangle these effects further, we plot in Fig. 4.4d mobilities measured in graphite channels and normalized by μ_{K^+} as a function of applied voltage and concentration.

We also compare the streaming effects in graphite channels with those of similar channels

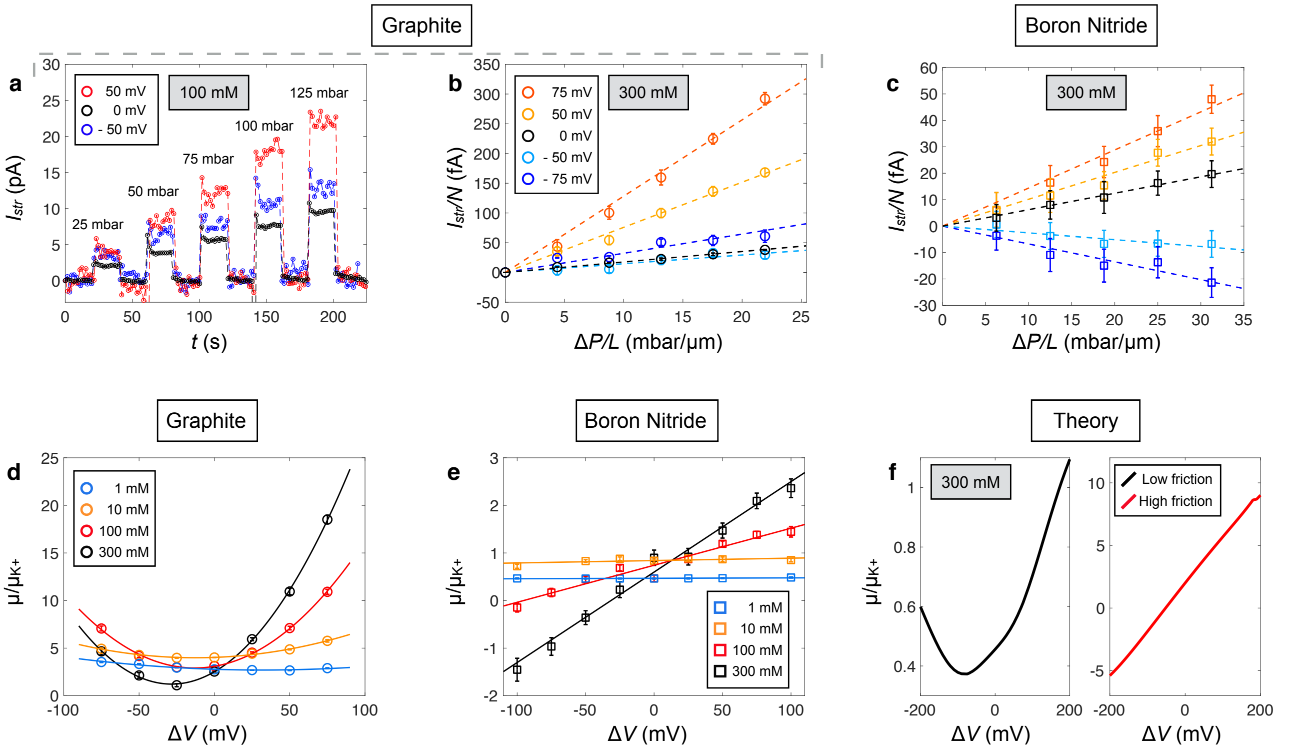

Figure 4.4: Streaming current for different biases and channel materials. a) Pressure-driven I_{stm} for a graphite device at different ΔV. $L = 5.7 \pm 0.1$ μm; KCl concentration, 100 mM. The pressure applied for 20 s intervals is gradually increased to 125 mbar in 25 mbar steps. b) Streaming current per channel for the same device as a function of $\Delta P/L$ (bias ΔV ranges from -75 to $+75$ mV; color coded). c) Streaming current for similar devices but with hBN walls; same experiments and color coding as in a and b. d) Streaming mobility (normalized by the K^+ electrophoretic mobility) as a function of ΔV for different KCl concentration for the graphite devices. Curves are the quadratic fits. e) Same as in panel d but with hBN channels. Linear fits; $L = 16 \pm 0.1$ μm. f) Extended PNP prediction for the streaming mobility using different friction coefficients between the water, ions and well, with a factor of 100 between low and high friction. Low friction reproduces the quadratic gating observed for graphite in panel d, while high friction leads to the linear gating observed for hBN in panel e. In panels a through c, error bars represent measurement uncertainty, and in d and e, uncertainty in the fit value.

made from hBN. In terms of crystal structure and atomic flatness, hBN is an analogue of graphite (Keerthi *et al.*, 2018). However, unlike graphite, hBN is electrically insulating. Our hBN devices were fabricated using the same procedures as before and had the same parameters including h_0, and their behavior was similar to that of graphite devices in that I_{str} varied linearly in ΔP (see Figs. 4.4c, C.2, and C.3) with a slope (streaming mobility μ) that varies as a function of the applied bias. However, the dependence of the steaming mobility on the applied voltage $\mu(\Delta V)$ differs greatly between the two materials: μ shows a quadratic response to electric bias for graphite (Fig. 4.4d), whereas it is essentially linear over the entire measurement range for hBN (Fig. 4.4e). The data can be described for graphite by

$$\mu(\Delta V) = \mu_0 \left[1 + \alpha \left(\frac{\Delta V - V_{\mathrm{min}}}{V_{\mathrm{ref}}}\right)^2\right], \tag{4.1}$$

and for hBN by

$$\mu(\Delta V) = \mu_0 \left(1 + \beta \frac{\Delta V}{V_{\mathrm{ref}}}\right), \tag{4.2}$$

where $V_{\mathrm{ref}} = k_B T/e \approx 25$ mV is the thermal voltage, μ_0 is a mobility, and α and β are dimensionless parameters accounting for the voltage response. Typically, V_{min} is found to be of the order of V_{ref}, and to decrease with concentration. The voltage susceptibility α increases linearly with concentration (Figs. 4.5a and b), reaching a value close to unity for a high concentration of 300 mM. The characteristic mobility μ_0 is typically of the order of μ_{K^+} for both systems. However, similar to α in graphite, the bias susceptibility β for hBN increases linearly with c (Fig. 4.5c). Owing to the linear voltage coupling, the sign of the streaming current for hBN can be inverted for negative biases (Fig. C.3). For both materials, the sensitivity of I_{str} to voltage bias is very large, in contrast to other known control or gating mechanisms (Schasfoort *et al.*, 1999; Kim *et al.*, 2009; Jiang & Stein, 2011; Karnik *et al.*, 2005; Pang *et al.*, 2011). For graphite channels, a relatively small voltage ($\Delta V \approx 75$ mV) yields streaming mobilities that are up to about 20 times as large as the bulk potassium mobility, taken as a reference. This corresponds to zeta potentials of up to 2 V assuming bulk water properties, and about 100 V if the relative permittivity appropriate to water in confinement ϵ_{conf} is used. Although the effect is still large for hBN, it is substantially smaller than that in graphite channels. This observation echoes the smaller slip length for water on hBN as compared to graphite (Secchi *et al.*, 2016a; Tocci *et al.*, 2014; Xie *et al.*, 2018).

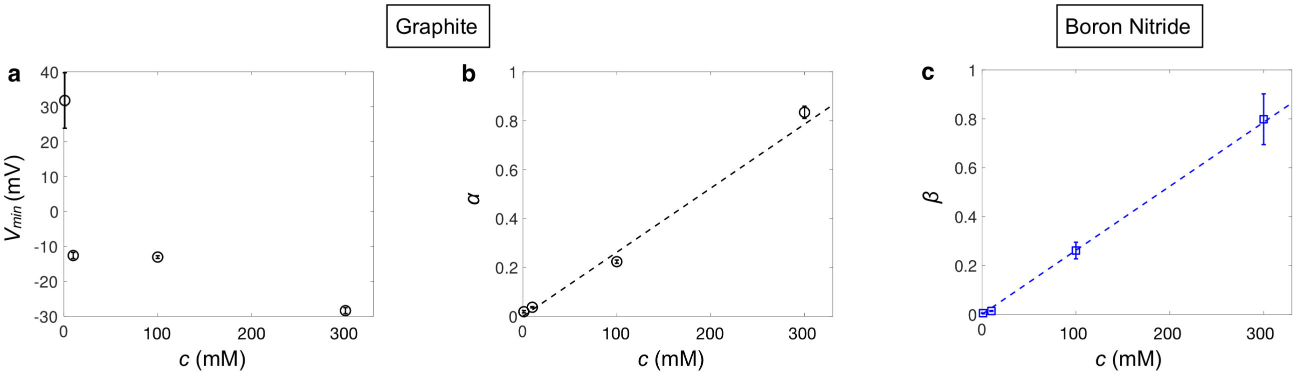

Figure 4.5: Concentration dependence of the fit parameters of the gate-controlled mobility. We report the fitting parameters of the voltage-gated streaming current. a, b) The quadratic dependence of the gated streaming current observed in graphite channels (Fig. 4.4d) and described by Eq. 4.1: a) V_{min} plotted as a function of the concentration; b) α as a function of the concentration. c) We report the fitting parameter β as a function of the concentration for hBN channels; β describes the linear dependence of the streaming current observed for hBN channels (Fig. 4.4e) as given by Eq. 4.2. The dashed lines in panels b and c are linear fits.

4.3 Theory

Taken together, our findings indicate that the applied bias voltage acts as a gate for pressure-driven streaming currents. Although it is tempting to rationalize this behavior in terms of capacitive gating, as is assumed, for example, in the description of flowFET-type devices, the fluidic analogues of field-effect-transistors (Schasfoort *et al.*, 1999), such an explanation fails to capture key experimental observations such as the stark difference in the voltage dependencies of the gated streaming mobilities in graphite and hBN. Any explanation based on the capacitive gating mechanism also neglects the electrohydrodynamic coupling between ion and water transport under ångström-scale confinement, which is usually described in terms of the Poisson-Nernst-Planck-Stokes (PNPS) framework commonly used to describe ionic transport in biological or artificial channels (see Chapter 3). However, similar to the capacitive gating model, the unmodified PNPS framework is also unable to account for all our observations, in particular the qualitatively different bias dependence of μ seen for graphite and hBN as summarized in Eqs. 4.1 and 4.2. We attribute this to the strong confinement encountered in our devices, which renders the Stokes equation irrelevant when describing flow within the water/ion layer, owing to the strong and direct interactions of the moving ions and water molecules with the confining walls. I therefore develop in this section a modified continuum description that does not incorporate the Stokes equation, instead relying on a first-principles, phenomenological force balance to describe the frictional interaction of the ions and water molecules with the confining walls.

4.3.1 Governing equations

At scales greater than about 1 nm, the influence of water motion on the ionic fluxes is accounted for by (1) appending the Stokes equation for the solvent velocity to the typical PNP description of the ionic transport and (2) including an ionic drift velocity set by the balance of forces between the electric force on the individual ion and the frictional force between the ion and water in the Nernst-Planck parameterization of the solute fluxes. Both assumptions are inapplicable here owing to the extreme confinement scale of the channels considered, which approaches the diameter of the water molecules and hydrated ions themselves. In particular, application of the Stokes equation to predict the hydrodynamic velocity relies on the assumption of a spatially homogeneous and isotropic scalar viscosity, an assumption that cannot be valid when a single layer of water molecules is present. *A priori*, we would expect strong interaction between the ions and walls, and the water molecules and walls. The former supposition is supported by the results of Esfandiar *et al.* (2017), where the chloride mobility in both graphite and hBN devices of the type examined here was observed to be reduced by approximately 65% compared with bulk. The latter is supported by the present results when combined with the simple, first-principles, phenomenological model detailed below.

In order to develop an alternative description of the water transport and ionic drift more appropriate to the extreme confinement considered here, I consider the force balances on the individual ions and on a control volume of infinitesimal length along the channel containing both ions and water molecules. I include three phenomenological forces: the frictional interactions of (1) water with walls, (2) ions with walls, and (3) ions with water. I emphasize that this is the simplest possible coherent approach to capture the modification in the qualitative behavior of the ion dynamics owing to the extreme confinement. Quantifying the friction to achieve a more quantitatively accurate treatment would probably necessitate more in-depth modeling (such as *ab initio* molecular dynamics).

Including the ion-wall interaction, a force balance on an individual ion gives:

$$0 = \pm e\left(-\frac{d\phi}{dx}\right) - \xi_{\pm}\left(v_{\pm} - v_w\right) - \lambda_{\pm} v_{\pm}, \tag{4.3}$$

where $v_{\pm}$ is the velocity of the positive or negative ion species, v_w is the water velocity, and ϕ is the electrostatic potential. From left to right, the terms represent (1) the electric body force on the positive or negative ion, (2) the frictional force of the water on the ion, parameterized by friction coefficients $\xi_{\pm}$ for the cation and anion species, and (3) the frictional force of the wall on the ions, parameterized by friction coefficients $\lambda_{\pm}$. Note that I have assumed that all of the ions interact appreciably with the walls, a reasonable assumption here given the extreme confinement. We solve Eq. 4.3 for the ion velocities $v_{\pm}$ to obtain:

$$v_{\pm} = \pm\mu_{\pm}\left(-\frac{d\phi}{dx}\right) + \alpha_{\pm} v_w. \tag{4.4}$$

I have introduced the ionic mobilities $\mu_{\pm} \equiv e/\left(\xi_{\pm} + \lambda_{\pm}\right)$ and the normalized water-ion friction coefficients $\alpha_{\pm} \equiv \xi_{\pm}/\left(\xi_{\pm} + \lambda_{\pm}\right)$. The former parameters are constrained by the experimental results of Esfandiar *et al.* (2017); the latter parameters characterize how effectively the drag of the water flow is able to overcome frictional resistance on the ions from the wall and engender ionic transport. We note that the definition of $\alpha_{\pm}$ may be rearranged to give $\lambda_{\pm}/\xi_{\pm} = \left(1 - \alpha_{\pm}\right)/\alpha_{\pm}$. This indicates that values of $\alpha_{\pm} \ll 1$ corresponds to stronger ion-wall than ion-water friction, whereas values of $\alpha_{\pm}$ approaching unity indicate relatively weaker ion-wall than ion-water interaction.

From the above definitions, we see that the sums of the ion-water and ion-wall friction coefficients are constrained by the experimentally measured mobilities reported in Esfandiar *et al.* (2017), $\xi_{\pm} + \lambda_{\pm} = e^{-1}\mu_{\pm}$, while the relative importance of the ion-wall and ion-water interactions, characterized by the ratios $\lambda_{\pm}/\xi_{\pm} = \left(1 - \alpha_{\pm}\right)/\alpha_{\pm}$, is not.

I next consider the force balance on a control volume of width and height equal to the channel width w and height h_0, respectively, and of infinitesimal length δx in the along-channel direction. The total volume of the control volume is then $\delta V \equiv wh_0\delta x$. The total electric body force is given by $e\left(\rho_+ - \rho_-\right) \times \left(-d\phi/dx\right) \times \delta V$, and the net pressure force is given by $wh_0 \times \left(-dP/dx\right) \times \delta x$. In the preceding, $\rho_{\pm}$ are the ionic densities (per unit volume) at the position x coincident with the center of the control volume, and P is the pressure. Note that this notation is in contrast with that used in the preceding Chapters, where $c_{\pm}$ denoted the ionic concentrations, and is chosen to agree with the notation adopted in the published version of this work (Mouterde *et al.*, 2019). The total frictional force due to ion-wall interactions is $-\left(\rho_+\lambda_+v_+ + \rho_-\lambda_-v_-\right)\delta V$. Finally, I introduce a coefficient λ_0 characterizing the frictional interaction of water molecules with the walls such that $-\lambda_0 v_w$ is the force per unit wall area acting on the water molecules, and $-\lambda_0 v_w \times w\delta x$ is the total frictional force on the control volume due to water-wall interaction. The force balance on the control volume thus gives:

$$0 = e(\rho_+ - \rho_-)\left(-\frac{d\phi}{dx}\right)\delta V + \left(-\frac{dP}{dx}\right)\delta V - \left(\rho_+\lambda_+v_+ + \rho_-\lambda_-v_-\right)\delta V - \frac{\lambda_0}{h_0}v_w\delta V. \tag{4.5}$$

Before solving the above for the water velocity v_w, we use Eq. 4.4 and the definitions of $\mu_\pm$ and $\alpha_\pm$ to rewrite the total ion-wall friction force per unit volume δV, $\rho_+\lambda_+v_+ + \rho_-\lambda_-v_-$, as

$$\begin{aligned} &\rho_+\lambda_+v_+ + \rho_-\lambda_-v_- = \\ &\qquad e\left(\rho_+ - \rho_-\right)\left(-\frac{d\phi}{dx}\right) - e\left(\alpha_+\rho_+ - \alpha_-\rho_-\right)\left(-\frac{d\phi}{dx}\right) + \left(\kappa_+\rho_+ + \kappa_-\rho_-\right)v_w, \end{aligned} \tag{4.6}$$

where I have defined $\kappa_\pm \equiv e\alpha_\pm\left(1-\alpha_\pm\right)/\mu_\pm$ and made use of the identities $\lambda_\pm\mu_\pm \equiv e\left(1-\alpha_\pm\right)$ and $\lambda_\pm\alpha_\pm \equiv \kappa_\pm$. We insert this result into equation 4.5 and solve for v_w to obtain:

$$v_w = K_{\text{app}}\left(\rho_+, \rho_-\right)\left[\left(-\frac{dP}{dx}\right) + e\left(\alpha_+\rho_+ - \alpha_-\rho_-\right)\left(-\frac{d\phi}{dx}\right)\right], \tag{4.7}$$

where $K_{\text{app}}\left(\rho_+, \rho_-\right)$ is a concentration-dependent apparent hydraulic conductance, given by

$$K_{\text{app}}\left(\rho_+, \rho_-\right) \equiv \frac{1}{\frac{\lambda_0}{h} + \kappa_+\rho_+ + \kappa_-\rho_-}. \tag{4.8}$$

To better interpret the significance of the parameter $\alpha_\pm$ and the non-intuitive form in which the electric field appears in Eq. 4.7, I use the above results to calculate the difference of the electric force $f_e^\pm$ and the ion-wall friction force $f_{\text{ion-wall}}^\pm$ on a given ionic species:

$$f_e^\pm - f_{\text{ion-wall}}^\pm = \pm e\alpha_\pm\rho_\pm\left(-\frac{d\phi}{dx}\right) - \kappa_\pm\rho_\pm v_w. \tag{4.9}$$

Let us examine two extreme limits: When $\alpha_\pm = 0$, $\xi_\pm/\lambda_\pm = 0$, indicating that only ion-wall (rather than ion-water) friction is relevant. Further, from the above definition, $\kappa_\pm \propto \alpha_\pm\left(1-\alpha_\pm\right) = 0$, and the net (electric less ion-wall friction) force vanishes. Thus, in this case, all of the electric force on the given ionic species in the control volume is balanced by the strong ion-wall interaction such that the given ionic species does not communicate any electric force to the water molecules. (See Eq. 4.7 with α_+ and/or α_- set to zero.)

On the other hand, when $\alpha_\pm = 1$, $\lambda_\pm/\xi_\pm = 0$, indicating that only ion-water friction is relevant, and all of the electric force on the ions is communicated to the water molecules such that $f_e^\pm - f_{\text{ion-wall}}^\pm = \pm e\rho_\pm \left(-d\phi/dx\right)$. (Again, $\kappa_\pm \propto \alpha_\pm \left(1 - \alpha_\pm\right) = 0$.)

I emphasize that the behavior described in Eqs. 4.7 and 4.8 is in strong contrast to what is observed for conduits with confinement scales (radius or height) greater than about 1 nm, in which the Hagen-Poiseuille equation holds (Bocquet & Charlaix, 2010). In this case, we would have a concentration-independent conductance $K_{\text{HP}} = h_0/\lambda_0$ and a net electric driving force equal to the total electric driving force $e\left(\rho_+ - \rho_-\right)\left(-d\phi/dx\right)$. K_{HP} is recovered in the high water friction limit, $\lambda_0/h \gg \kappa_+\rho_+ + \kappa_-\rho_-$, and both K_{HP} and the total electric driving force are recovered outside of confinement where $\alpha_\pm = 1$ (equivalent to no ion-wall friction: $\lambda_\pm = 0$).

It is necessary to use Eqs. 4.7 and 4.8 instead of Hagen-Poiseuille to capture the full range of qualitative behavior observed in the experimental $\mu(\Delta V)$ curves. This emphasizes the importance of the two-dimensionality of the flow, resulting in a strong frictional interaction between the channel walls, water, and ions.

We insert Eq. 4.7 into the general Nernst-Planck parameterization for the ionic fluxes, $j_\pm = D_\pm\left(-d\rho_\pm/dx\right) + v_\pm\rho_\pm$, to obtain

$$j_\pm = \mu_\pm\left[\frac{k_BT}{e}\left(-\frac{d\rho_\pm}{dx}\right) \pm \rho_\pm\left(-\frac{d\phi}{dx}\right)\right] + \alpha_\pm v_w \rho_\pm, \tag{4.10}$$

where $D_\pm$ are the cation/anion diffusion coefficients, and we have made use of the Einstein relation, $D_\pm = k_BT\mu_\pm/e$.

At steady state, the conservation equations become

$$\frac{d\left(hv_w\right)}{dx} = \frac{d\left(hj_\pm\right)}{dx} = 0. \tag{4.11}$$

Finally, the electrostatic potential ϕ is related to the total charge density $e\left(\rho_+ - \rho_-\right)$ via the Poisson equation:

$$\frac{d}{dx}\left[\epsilon_r\epsilon_0 h\left(-\frac{d\phi}{dx}\right)\right] = he\left(\rho_+ - \rho_-\right). \tag{4.12}$$

4.3.2 Model Geometry and Boundary Conditions

As I am mainly interested in capturing the qualitative features of the ionic current response, I adopt a simplified one-dimensional geometry. The model geometry adopted here is sketched in

Fig. 4.6. A channel of uniform height $h_0 = 7$ Å and length $L = 5$ μm connects two reservoirs of divergent geometry. It is necessary to include the reservoirs in some capacity in our calculations to capture the entrance/exit effects associated with the discontinuous change in ionic mobility as the ions enter/exit the channel. The rate of divergence of the reservoir heights is asymmetric, qualitatively mimicking the asymmetry of the experimental reservoirs (Fig. 4.2). The height profile $h(x)$ is given by:

$$\frac{h(x)}{h_0} = \begin{cases} \Gamma_\ell \left(\frac{x}{L} + \frac{1}{2} \right)^2 + 1, & x < -\frac{L}{2} \\ 1, & x \in \left[-\frac{L}{2}, +\frac{L}{2} \right] \\ \Gamma_r \left(\frac{x}{L} - \frac{1}{2} \right)^2 + 1, & x > +\frac{L}{2}. \end{cases} \tag{4.13}$$

The parameters Γ_ℓ and Γ_r are the rates of divergence of the reservoir geometries; the larger Γ is, the more abrupt the transition to the open reservoir. I take $\Gamma_\ell = 5$ and $\Gamma_r = 20$. Although the magnitudes of Γ_ℓ and Γ_r influence the quantitative predictions of the model, the qualitative behavior of the mobilities is similar so long as $\Gamma_\ell < \Gamma_r$. I present a more extensive discussion of the sensitivity of the model predictions to the relative and absolute magnitudes of Γ_ℓ and Γ_r in Appendix C.

The reservoir conditions are imposed at $x = \pm\infty$. In the left reservoir, we apply a voltage and pressure:

$$\phi(x = -\infty) = \Delta V, \quad \text{and} \tag{4.14}$$

$$P(x = -\infty) = \Delta P. \tag{4.15}$$

In the right reservoir, the voltage and pressures are held fixed at reference values arbitrarily set to zero:

$$\phi(x = +\infty) = P(x = +\infty) = 0. \tag{4.16}$$

The total ionic density in both reservoirs is held fixed at the imposed reservoir concentration ρ_{res}, and both reservoirs are assumed to be electroneutral such that

$$\rho_{\pm}(x = \pm\infty) = \frac{\rho_{\text{res}}}{2}. \tag{4.17}$$

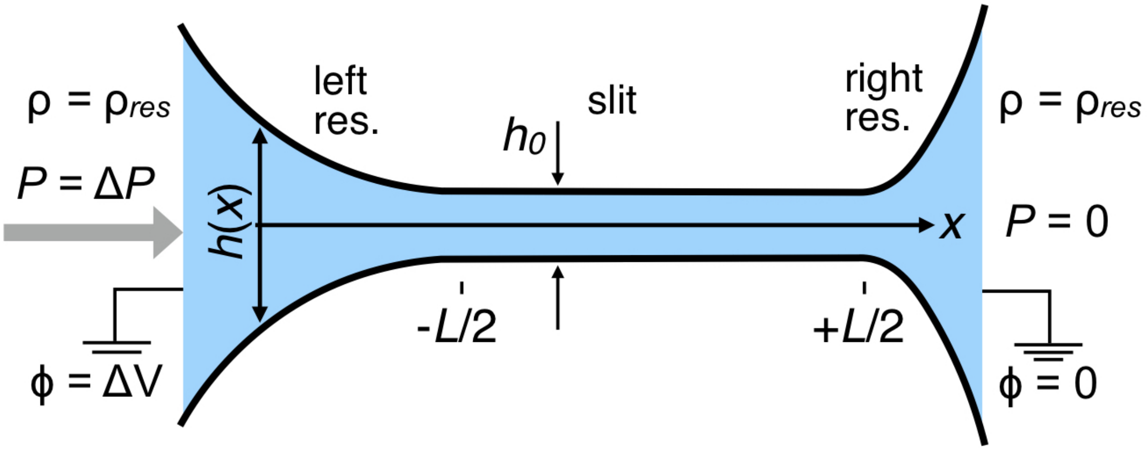

Figure 4.6: Sketch of the model geometry. A channel of uniform height $h_0 = 7$ Å and length $L = 5$ μm connects two asymmetric, divergent reservoirs of variable height $h(x)$. The asymmetry in the rate of divergence of the reservoir heights qualitatively mimics the asymmetry of the experimental geometry. A voltage $\phi = \Delta V$ and pressure $P = \Delta P$ are applied in the left reservoir (at $x = -\infty$); the voltage and pressure are held fixed at $\phi = 0$, $P = 0$ in the right reservoir ($x = +\infty$). The total ionic concentration in both reservoirs is held fixed at $\rho = \rho_{\text{res}}$.

4.3.3 Variation of Ion Mobilities $\mu_\pm$ and Normalized Water-Ion Friction Coefficients $\alpha_\pm$

I impose the following profiles for the ionic mobilities:

$$\mu_\pm = \left(\mu_\pm^{\text{bulk}} - \mu_\pm^{\text{conf}}\right)\left[1 - \frac{\tanh\left(\frac{x+\frac{L}{2}}{\lambda_{\text{adj}}}\right) - \tanh\left(\frac{x-\frac{L}{2}}{\lambda_{\text{adj}}}\right)}{2}\right] + \mu_\pm^{\text{conf}}, \tag{4.18}$$

where $\mu_\pm^{\text{bulk}}$ and $\mu_\pm^{\text{conf}}$ are, respectively, the ionic mobilities in bulk (the reservoirs) and in confinement (the channels), and λ_{adj} is an adjustment length, which I take to be 0.3 nm, smaller than any other length scale in the system. To qualitatively account for the reduction in chloride mobility, I take $\mu_\pm^{\text{conf}} = 0.5\mu_\pm^{\text{bulk}}$. Similarly, I impose for the normalized water-ion friction coefficients

$$\alpha_\pm = \left(1 - \alpha_\pm^{\text{conf}}\right)\left[1 - \frac{\tanh\left(\frac{x+\frac{L}{2}}{\lambda_{\text{adj}}}\right) - \tanh\left(\frac{x-\frac{L}{2}}{\lambda_{\text{adj}}}\right)}{2}\right] + \alpha_\pm^{\text{conf}}. \tag{4.19}$$

4.3.4 Results

Calculations were performed using the finite element method. Figs. 4.7a-c show the results of the above model for low water-wall ($\lambda_0/h_0 = 10^{11}$ kg m^{-3} s^{-1}) and water-ion ($\alpha_+ = 1 \iff \lambda_+/\xi_+ = 0$; $\alpha_- = 0.7 \iff \lambda_-/\xi_- \approx 0.43$) friction, and Figs. 4.7d-f, the results for high water-wall ($\lambda_0/h_0 =$

10^{13} kg m^{-3} s^{-1}) and water-ion ($\alpha_+ = \alpha_- = 0.01 \iff \lambda_+/\xi_+ = \lambda_-/\xi_- = 99$) friction. We first note that in both cases we reproduce the linear dependence of the streaming current on the pressure gradient for both zero and non-zero applied voltages (Figs. 4.7b and e), in agreement with the experiments (Figs. 4.4b and c).

We observe in the low-friction configuration (Figs. 4.7a-c) a streaming mobility that depends quadratically on the applied voltage with a minimum mobility occurring for $\Delta V = V_{\text{min}} < 0$ (Fig. 4.7c). This qualitative behavior is in agreement with the experimental results obtained for graphite (Fig. 4.4d). Likewise, the high-friction results (Figs. 4.7d-f) reproduce the linear dependence of the streaming mobility on ΔV (Fig. 4.7f) that is observed experimentally in hBN (Fig. 4.4e). The frictional characteristics of these results are consistent with the typically much lower friction (larger slip lengths) observed on graphite than in hBN (Secchi *et al.*, 2016a; Tocci *et al.*, 2014; Xie *et al.*, 2018). We note that, in addition to taking low to moderate values of $\lambda_\pm/\xi_\pm \approx 0 - 1$, it is necessary to take $\alpha_+ > \alpha_-$ to recover the qualitative behavior of graphite. On the other hand, it is necessary to take $\alpha_+ \approx \alpha_- \lesssim 0.1$ to recover the qualitative behavior of hBN. This suggests that frictional interaction of the wall with the ions is weaker generally in graphite, and that it is stronger for chloride than potassium, while in hBN the frictional interaction of the ions with the wall is fairly strong for both species.

The numerical results presented here for the low-friction (graphite-like) configuration indicate that $\mu(\Delta V = 0)$ is independent of concentration, roughly consistent with the minimal variation observed in the experiments (Fig. 4.3c). However, the linear dependence of the mobility on concentration for non-zero applied voltages (Figs. 4.4d and e) is not observed in the model (Fig. 4.7c). Conversely, at higher friction (Figs. 4.7d–f), $\mu(\Delta V = 0)$ varies strongly with the concentration, as well as the gated mobility (Fig. 4.7f). This suggests the possibility that the concentration, applied voltage, and friction are coupled in ways not accounted for in our simple model.

The model results depend crucially on the difference in water flow characteristics between the two materials through the concentration-dependent conductance given in Eq. 4.8. However, the nature of this dependence is intricate. The model results indicate that, in addition to the advective current engendered by the applied pressure, the streaming current characteristics depend crucially on the modification of the electrophoretic current $I_{\text{EP}} \propto \rho E$ via the modification of the

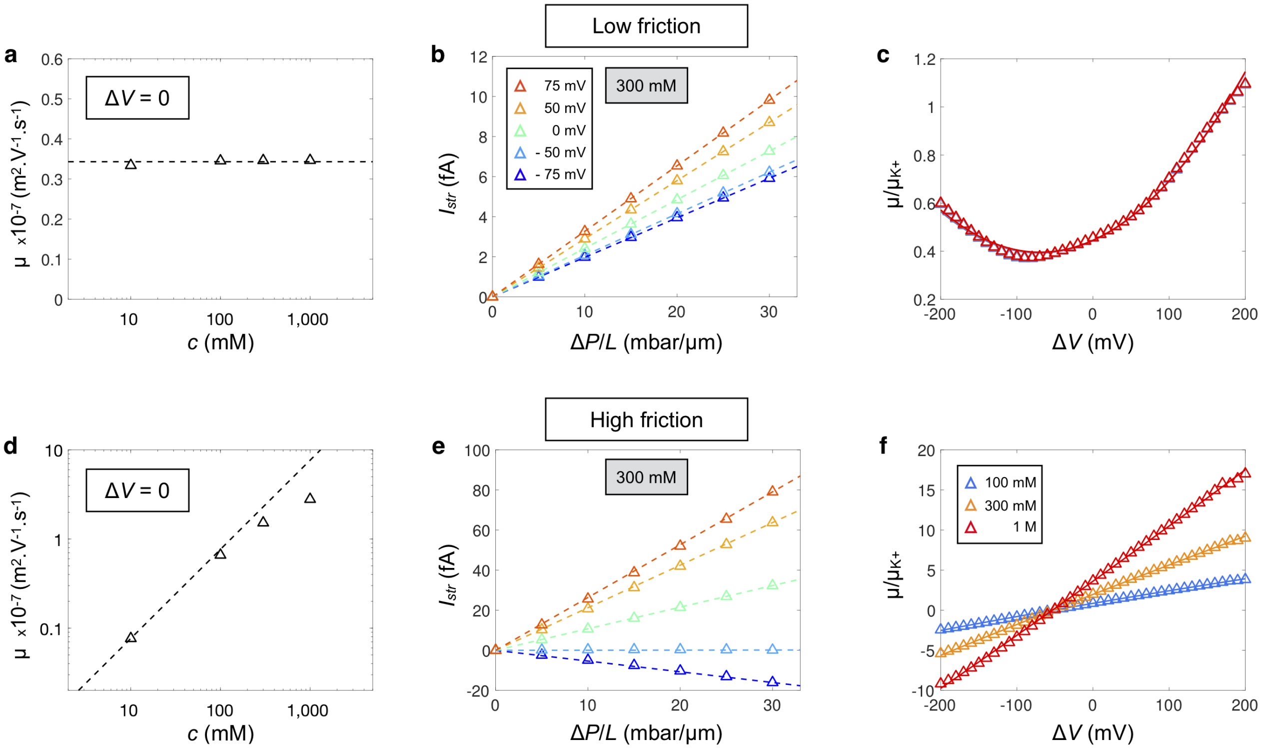

Figure 4.7: Prediction of the streaming current from extended Poisson-Nernst-Planck modeling. a) Mobility without applied voltage as a function of KCl concentration in linear-logarithmic coordinates for low water-wall friction and $\alpha_+ > \alpha_-$. b) Streaming current per channel I_{str} for 300 mM as a function of the pressure gradient $\Delta P/L$ for ΔV varying from -75 (blue data) to $+75$ mV (red data). For each voltage, the dashed line corresponds to the linear fit of the data made to extract the mobility. c) Streaming mobility μ normalized by the K^+ electrophoretic mobility μ_{K^+} and plotted as a function of the applied voltage for KCl concentration varying from 100 mM (blue data) to 1 M (red data). d-f) Same is in panels a-c but with high water-wall friction and $\alpha_+ = \alpha_-$. Parameters: a-c) $\lambda_0/h_0 = 10^{11}$ kg m^{-3} s^{-1}, $\alpha_+ = 1$, $\alpha_- = 0.7$; d-f) $\lambda_0/h_0 = 10^{13}$ kg m^{-3} s$^-$$-1$, $\alpha_+ = 0.01$, $\alpha_- = 0.01$. Dashed lines in panels a and d are guides to the eye corresponding to a constant value of μ and a linear variation with concentration, respectively.

concentration and electrostatic fields (figure not shown) by coupled voltage and pressure effects. An example of the influence of voltage on the evolution of the concentration fields in the presence of a fixed applied pressure gradient $\Delta P/L = 30$ mbar μm^{-1} and a reservoir molarity [KCl] $= 300$ mM is shown in Figs. 4.8c and d. We see that both the applied pressure and voltage modify the concentration profile across the channel (and induce charge separation, not shown). The modification of the concentration profile due to pressure is much stronger in hBN (Figs. 4.8a and c), and it is also much more sensitive to applied pressure and voltage in hBN than in graphite. This latter characteristic is consistent with the smaller streaming mobilities observed in the graphite-like configuration observed in our numerical results (Figs. 4.7c and f). Additionally, we see that the evolution of the concentrations under coupled pressure-voltage forcing is different in the two materials. It is this difference, and the corresponding difference in the response of the advective and electrophoretic currents, that determines the difference between the two material behaviors.

There are several aspects of the observations in graphite that I am not able to reproduce: (1) the non-monotonicity of the dependence of $\mu(\Delta V = 0)$ on concentration, (2) the linear dependence of the mobility on concentration when a voltage is applied, and (3) the magnitude of the mobilities measured at high concentration under an applied voltage. Indeed, the model consistently predicts mobilities in the quadratic (graphite-like) regime that are smaller than those observed in the linear (hBN-like) regime (Figs. 4.7c and f). This is not an issue of the voltage range examined, as the mobilities are found to saturate or even reduce at much higher voltages. Likewise, there is much that I have not included in this model: in particular, steric effects and ionic correlations generally, as well as the 'granular' nature of water, which might be important at this length scale. Nonetheless, the model does reproduce much of the key qualitative behavior, and its success depends on the strong differences in the frictional characteristics of hBN and graphite, and further on the incorporation of the retarding influence of the ions on the water transport, an effect that is exclusively two-dimensional. Thus, these results illustrate the two-dimensional character of the flow and the limit of the continuum description of matter.

Ultimately, we conclude that the different material responses observed in Fig. 4.4 for channels made from hBN and graphite can be traced back to the difference of molecular friction of water and ions on these two materials. This is in agreement with expectations for the friction of water on these two materials (Secchi *et al.*, 2016a; Tocci *et al.*, 2014; Xie *et al.*, 2018). A remarkable

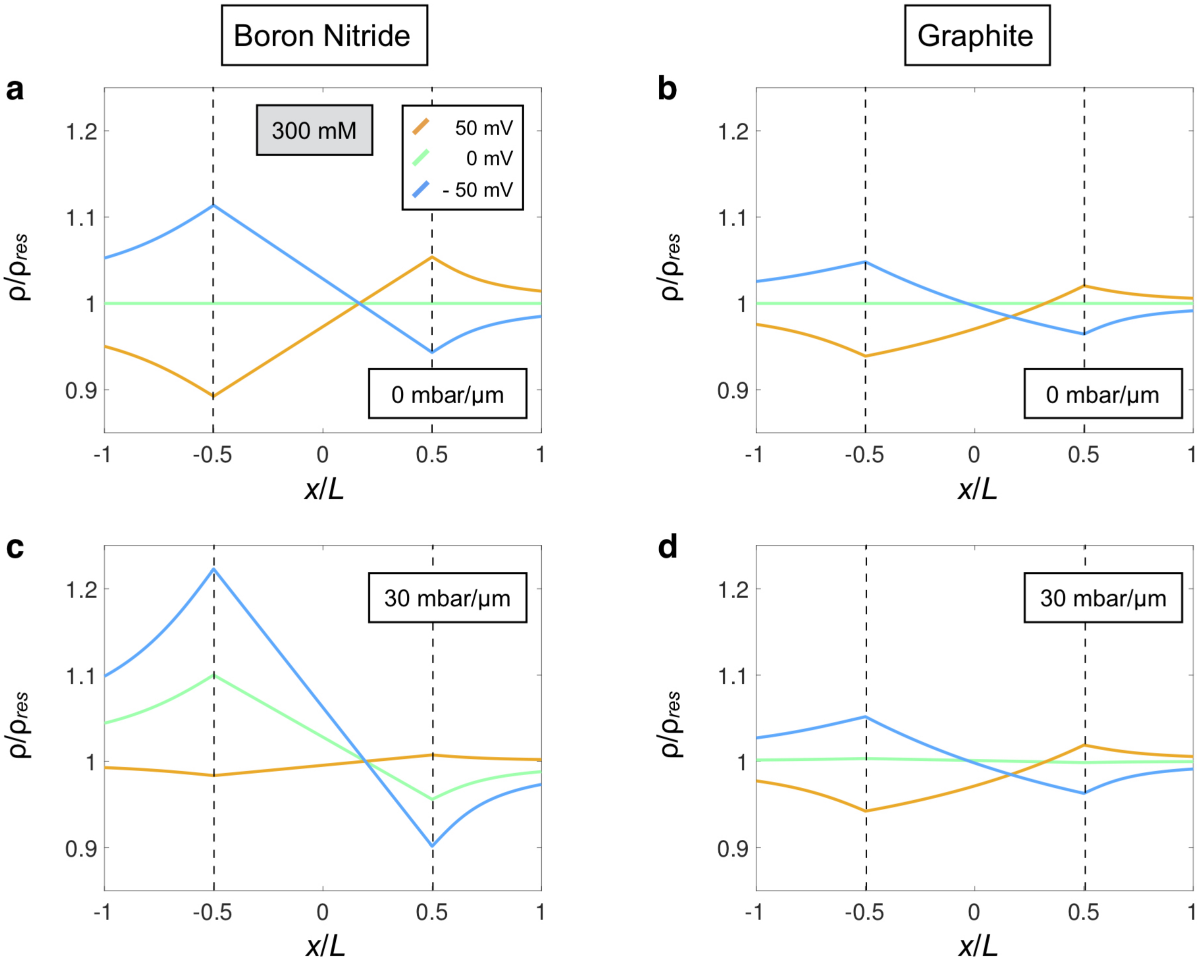

Figure 4.8: Total ionic concentration profiles from extended Poisson-Nernst-Planck modeling. a-d) Total ionic concentration profiles as a function of the normalized position x/L along the channel without (panels a and b) and with (panels c and d) applied pressure for $c = 300$ mM. The dashed vertical lines segregate the channel interior, $x/L \in (-0.5, +0.5)$, from the left ($x/L < -0.5$) and right ($x/L > +0.5$) reservoirs. The curves are colored according to the applied voltage from -50 (blue) to $+50$ mV (orange). a) The high-friction (hBN-like) configuration with $\Delta P/L = 0$. b) The low-friction (graphite-like) behavior with $\Delta P/L = 0$. c) The high-friction (hBN-like) configuration with $\Delta P/L = 30$ mbar μm^{-1}. d) The low-friction (graphite-like) behavior with $\Delta P/L = 30$ mbar μm^{-1}.

feature of this framework is that the observed nonlinear bias response thus has its roots in the fundamental nature of interactions between confining walls, water molecules and ions. For instance, the minimum mobility seen in Fig. 4.4d arises from the slight asymmetry in device geometry which is at the origin of different frictions (induced by the confinement) and modifies locally the transport rates of ions on each side. Although the simple model reproduced our experimental results qualitatively (Fig. 4.7), it cannot account for the large amplitude of the bias voltage effect seen with graphite channels. Better agreement will require more comprehensive evaluation of the effects of strong confinement (including the suppressed dielectric constant), which are expected to modify not only water and ion dynamics but also the adsorption of the ions (Takasaki *et al.*, 2017). Furthermore, the metallicity of graphite can substantially modify ionic interactions and thereby ion concentrations. I anticipate that extending *ab initio* molecular simulations of water friction (Tocci *et al.*, 2014), to include the effect of ions, will provide further insight beyond the simple picture proposed here.

4.4 Conclusions and Perspectives

Our experimental system allows us to probe purely two-dimensional flow of water and ions, a configuration very different from the one-dimensional transport through nanotubes. Thanks to the lateral extension of the ångström channels, streaming currents under molecular confinement become measurable. Hence, such devices are an interesting platform in which to mimic the behavior of biological channels in terms of stimuli responsive behavior such as voltage gating, where ions are driven through ångström-scale confinement by coupled osmotic pressure and electric forcing. This is of relevance for gaining new insights into the electromechanical coupling at the root of the mechanosensitivity observed in recently discovered biological ionic channels (Coste *et al.*, 2012) (TRAAK, TREK, PIEZO). Furthermore, the observed friction-based electric gating opens a new route to achieve flow-control under extreme confinement where small voltages induce strong responses, which would constitute an important step towards building nanofluidic circuits responding to external stimuli.

Chapter 5

DUKHIN LENGTH AND SURFACE CHARGE DETECTION IN SCANNING ION CONDUCTANCE MICROSCOPY

Abstract In this Chapter, I use a combination of analytical techniques and finite element modeling to examine the modification induced by isolated surface charge features to the signal obtained via scanning ion conductance microscopy (SICM). Our hypothesis, that isolated surface charge patches may be detected at sufficiently large Dukhin length using SICM, is based on the mechanism of surface-controlled modification of an applied electric field first proposed by Khair & Squires (2008). Indeed, the theoretical results presented here show a substantial signal that is detectable using current SICM techniques and that scales with the Dukhin number as hypothesized. The results also indicate that the lower limit on the spatial resolution of this technique is set by the inner radius of the scanning ion conductance microscope. Altogether, the results suggest that this technique may be applied to SICM measurements using nanotubes inserted into nanopipettes (Secchi *et al.*, 2016a,b), potentially improving the spatial resolution of current SICM-based surface charge measurements by one-to-two orders-of-magnitude. This work was conducted with Sara Dal Cengio of the University of Barcelona.

5.1 Introduction

In this Chapter I focus on the applications of the mechanism proposed by Khair & Squires (2008) for the surface-controlled modification of an applied electric field to the detection of surface charge via scanning ion conductance microscopy (SICM). The relevant details of the Khair & Squires (2008) mechanism are given in Appendix D, and the configuration these authors consider is sketched in Fig. 5.1. Briefly, they consider an electrolyte solution above and in contact with a planar solid-liquid interface occupying the $x-z$ plane. The electrolyte is subjected to an applied electric field $\mathbf{E}_\infty = E_\infty \hat{\boldsymbol{x}}$ running parallel to the interface and perpendicular to a surface charge discontinuity along the line $x = 0$. This discontinuity separates a region of zero surface charge ($x < 0$) from a region of nonzero surface charge ($x > 0$) (Fig. 5.1). The authors consider the case that the spatial extent of the perturbation to the applied field induced by the surface charge discontinuity, the so-called 'healing length' ℓ_H, is large compared to the Debye length λ_D. This allows them to model the enhanced conductivity in the diffuse layer as a discontinuous surface conductivity $\kappa_s(x) = \kappa_s^0 \Theta(x)$, where κ_s^0 is the uniform nonzero value for $x > 0$, and $\Theta(x)$ is the Heaviside theta function. Furthermore, as they do not resolve the details of the diffuse layer, they take the bulk conductivity κ_b to be a constant. Continuity of charge applied along the solid-liquid interface, balancing the in-plane divergence of current with that entering or leaving the surface, gives the following boundary condition:

$$\partial_y \phi|_{y=0} + \ell_{\mathrm{Du}} \partial_x \left[K_{\lambda \ell_{\mathrm{Du}}}(x) \partial_x \phi|_{y=0} \right] = 0, \tag{5.1}$$

where ϕ is the electrostatic potential, and $\ell_{\mathrm{Du}} \equiv \kappa_s^0/\kappa_b$ is the Dukhin length, defined dynamically in terms of the surface and bulk conductivities. It is shown in Appendix A that this definition is equivalent to the equilibrium definition in terms of the surface charge density, $\ell_{\mathrm{Du}} \equiv |\sigma|/ec$, provided Poisson-Boltzmann equilibrium theory is sufficient to describe the structure of the diffuse layer. The function $K_{\lambda \ell_{\mathrm{Du}}}(x) \equiv \kappa_s(x)/\kappa_s^0$ is the normalized surface charge distribution. I generalize the theoretical distribution given above, $\kappa_s(x)/\kappa_s^0 = \Theta(x)$, to allow for a finite transition length $\lambda \ell_{\mathrm{Du}}$; in this case, $\kappa_s^0 \equiv \kappa_s(x \to \infty)$ is defined to be the maximum, asymptotic value of the surface conductivity far from the 'discontinuity' at $x = 0$.

Eq. 5.1 may be obtained by integrating the steady state charge continuity equation $\nabla \cdot \boldsymbol{i} = 0$ in the direction normal to the solid-liquid interface over a distance h from the interface larger than the diffuse layer thickness but much smaller than the healing length, $\lambda_D < h \ll \ell_H$. Alternatively, it may be obtained by summing the fluxes entering and exiting the infinitesimal control volume sketched in Fig. 5.1 and setting the result to zero.

The problem statement is completed by imposing continuity of charge in the bulk, $\nabla \cdot \boldsymbol{i} = \kappa_b \nabla \cdot \mathbf{E} = 0 \Longrightarrow \nabla \cdot \mathbf{E} = 0$, and continuity with the applied electric field $\mathbf{E}_\infty = E_\infty \hat{\boldsymbol{x}}$ far from the discontinuity at $x = 0$. After rescaling the spatial coordinate by the Dukhin length, $\mathbf{r} \to \ell_{\mathrm{Du}} \mathbf{r}$, the electric field by the magnitude of the applied field, $\mathbf{E} \to E_\infty \mathbf{E}$, and hence the electrostatic potential as $\phi \to \ell_{\mathrm{Du}} E_\infty \phi$, Khair & Squires (2008) obtain the following set of equations:

$$\nabla^2 \phi = 0, \tag{5.2}$$

$$\phi \xrightarrow[r \to \infty]{} -x, \quad \text{and} \tag{5.3}$$

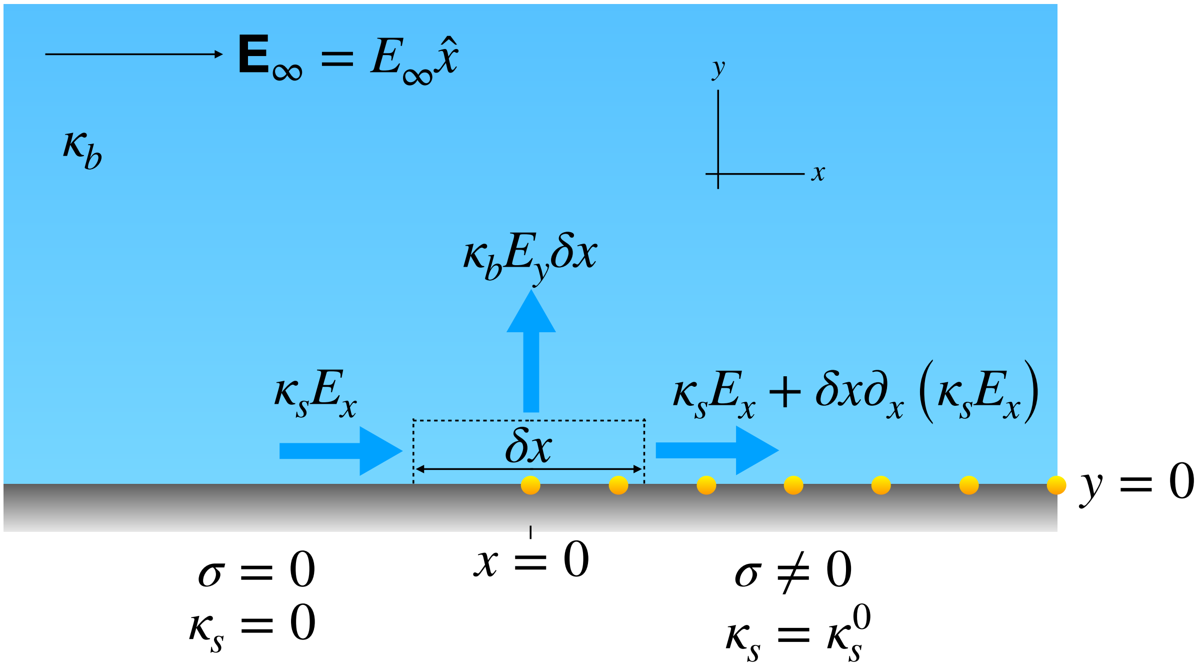

Figure 5.1: Schematic showing the configuration considered in Khair & Squires (2008). An electrolyte is in contact with a solid substrate, forming a solid-liquid interface on the $x-z$ plane. There is a discontinuity in the surface charge density, and hence in the surface conductivity, along the line $x = 0$, with zero surface charge for $x < 0$ and nonzero surface charge for $x > 0$, and an external field $\mathbf{E}_\infty = E_\infty \hat{\boldsymbol{x}}$ is applied along the interface. The blue arrows indicate currents entering and leaving a control volume of infinitesimal length δx and height h much smaller than the healing (Dukhin) length ℓ_{Du} and larger than the characteristic extent of the diffuse layer, the Debye length λ_D: $\lambda_D < h \ll \ell_{\mathrm{Du}}$.

$$\partial_y \phi|_{y=0} + \partial_x \left[K_\lambda(x) \partial_x \phi|_{y=0}\right] = 0, \tag{5.4}$$

where, in Eq. 5.3, $r \equiv \sqrt{x^2+y^2}$, is the radial distance from the surface charge discontinuity. Modeling the diffuse layer with a surface conductance and assuming a constant bulk conductivity allows the authors to neglect the solute dynamics entirely. From Eqs. 5.2 through 5.4, we see that the problem has been reduced to an effective sourceless electrostatics problem with an exotic boundary condition (Eq. 5.4). Furthermore, comparison of Eq. 5.4 to the Gaussian boundary condition $\mathbf{E}\cdot\hat{\boldsymbol{n}} = \sigma/\epsilon$, allows us to interpret this exotic boundary condition in terms of an effective surface charge density that is functionally dependent on the electrostatic potential, $\sigma_{\mathrm{eff}}[\phi] = \partial_x \left[K_\lambda(x) \partial_x \phi|_{y=0}\right]$.

Numerical solutions to these equations are presented in Appendix D, Fig. D.2. However, the relevant result is apparent from Eqs. 5.2 through 5.4 directly, where we see that the two privileged length scales appearing in the problem are the transition length λ and unity (*i.e.*, the Dukhin length in dimensioned terms). In the limit $\lambda \to 0$–that is, in the limit that that transition length is vanishingly small compared to the Dukhin length–unity is the only privileged length scale, and we conclude that the healing length in this case is given by the Dukhin length. Thus, the requirement that the healing length be much larger than the Debye length reduces to the condition $\ell_{\mathrm{Du}}/\lambda_D \gg 1$. The result that the apparent size of surface charge discontinuities in bulk scales with the Dukhin length motivates the central hypothesis of this work: surface charge discontinuities generally, and surface charge 'patches' with extents much smaller than the Dukhin length in particular, may be detected experimentally by measuring the deformation of an applied field/current within a distance ℓ_{Du} of a substrate. This hypothesis is corroborated by the results of Lee *et al.* (2012), who demonstrate that the apparent size of nanopores at low salt concentrations as inferred from conductance measurements is given by the Dukhin length, rather than the physical pore size, due to the discontinuity in surface charge at the ends of the pore.

One candidate for experimental detection of surface charge based on this hypothesis is scanning ion conductance microscopy (SICM) (Hansma *et al.*, 1989). The basic SICM setup is sketched in Fig. 5.2: a substrate is submerged in an electrolyte solution, acquiring a surface charge σ, and a pipette of nanometric interior tip radius R_{tip}, tip thickness τ, interior base radius R_{base}, and length L_P is held at some distance H above the substrate. An electric field is generated between an electrode inserted into the base of the pipette far from the substrate and held at a fixed voltage ΔV and a ground electrode inserted into the bulk solution far from the point of measurement. This electric field drives a current through the pipette and across the substrate. As the separation distance H decreases, the increased access resistance between the pipette tip and substrate results in a decrease in the magnitude of the current (Nitz *et al.*, 1998). In the absence of surface charge effects, the geometric dependence of the current can be used to infer the separation distance H and hence the surface topography. The semi-analytical results of Nitz *et al.* (1998) show that the conductance $G \equiv I/\Delta V$ is related to the tip and separation geometry via

$$G(H) = G_P \left[1 + \frac{\ell_{\mathrm{geo}}(R_{\mathrm{tip}}, R_{\mathrm{base}}, \tau, L_P)}{H} \right]^{-1}, \tag{5.5}$$

where ℓ_{geo} is an effective geometric length scale depending on the details of the pipette geometry, and G_P is the pipette conductance in bulk, measured when the pipette is far from the substrate.

In the model of Nitz *et al.* (1998), the geometric length scale is given by $\ell_{\mathrm{geo}} = 3/2 \cdot \ln(1 + \tau/R_{\mathrm{tip}}) \cdot R_{\mathrm{base}} \cdot R_{\mathrm{tip}}/L_P$.

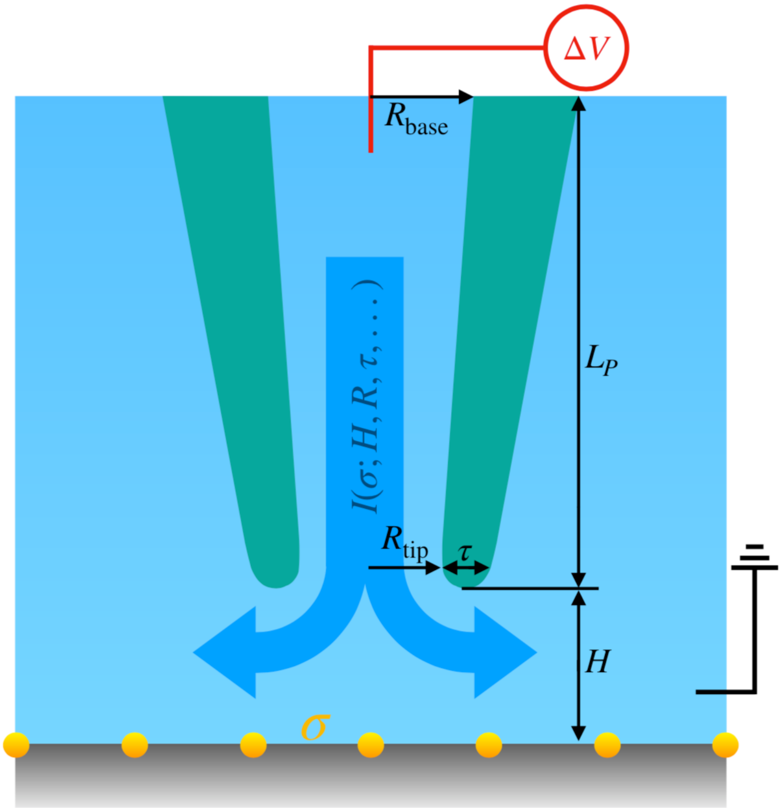

Figure 5.2: Schematic of the typical configuration of a scanning ion conductance microscope (SICM). A substrate is submerged in electrolyte solution, acquiring a surface charge σ. A typically nanometric pipette of interior tip radius R_{tip}, tip thickness τ, interior base radius R_{base}, and length L_P is held at a height H above the substrate, and a voltage is applied via an electrode in the base of the pipette far from the substrate. A second electrode is held at ground in the bulk solution far from the measurement point, and the resulting ionic current through the pipette is measured. The current is in general a function both of the surface charge and the details of the geometry including the separation distance H, allowing information about the substrate topography and surface charge to be extracted.

Typically, SICM measurements are conducted at high ionic concentrations so that both the diffuse layer thickness $\lambda_D \propto c^{-1/2}$ and the Dukhin length $\ell_{\mathrm{Du}} \propto c^{-1}$ are small compared to the separation distance and tip radius, and surface charge effects may therefore be neglected (Klenerman *et al.*, 2011; McKelvey *et al.*, 2014). However, some recent work (*e.g.*, McKelvey *et al.*, 2014; Dorwling-Carter *et al.*, 2018; Maddar *et al.*, 2019) has focused on detecting surface charge via surface-induced rectification (SIR) (Sa *et al.*, 2013). These measurements are performed at lower ionic concentrations, such that the Debye and/or Dukhin length becomes comparable to the separation distance H. In this case, the access conductance (and typically also the pipette conductance) is modified by the presence of surface charge and the resulting surface currents, generally leading to a rectified ionic current response. (See Chapter 2.) The modification of the current response by the surface charge as the pipette tip approaches the substrate may then be used to extract the sign and magnitude of the surface charge density via comparison to finite element method (FEM) simulation (McKelvey *et al.*, 2014). This technique is able to resolve charged features of the order of 1 μm or larger in size (McKelvey *et al.*, 2014; Dorwling-Carter *et al.*, 2018; Maddar *et al.*, 2019).

In this Chapter, I explore theoretically and numerically a fundamentally different technique for surface charge detection based on the Khair & Squires (2008) mechanism described above. As noted previously, this mechanism and the results of Lee *et al.* (2012) suggest the possibility of resolving sharply defined surface charge features with extents much smaller than the Dukhin length, potentially improving upon the accuracy of SICM charge mapping based on SIR. In what follows, I combine FEM simulation with semi-analytical scaling in order to determine the dependence of the current response on surface charge, separation distance, and size of the surface charge feature. As three-dimensional modeling of this problem has proven to be computationally intensive owing principally to the implicit, discontinuous, second-order boundary condition (Eq. 5.4), I will focus instead on results obtained with two-dimensional axisymmetric and translationally invariant models.

5.2 Theory and Finite Element Modeling

In this section, I combine FEM-based numerical modeling with semi-analytical scalings derived via a Green's function approach similar to that applied in Appendix D to the problem of Khair & Squires (2008). Much of the work is focused on modeling the additional current produced by an isolated, circular patch of surface charge and understanding how this additional current scales with parameters such as the separation distance H, patch radius R_{patch}, and Dukhin number Du. These basic questions are readily answered using a two-dimensional axisymmetric model in which the pipette approaches along the axis passing through the center of the charged patch and running perpendicular to the substrate. However, in order to understand the lateral structure of the current response, I will also consider a two-dimensional translationally invariant configuration featuring a semi-infinite charged strip. Both of these cases are treated in turn below.

5.2.1 Two-Dimensional Axisymmetric Model

The axisymmetric model configuration is sketched in Fig. 5.3. For simplicity, the interior pipette radius R and pipette thickness τ are taken to be constant. The pipette is held fixed at a distance H above the center of an isolated charged patch of radius R_{patch} located on an otherwise neutral substrate. The origin of the cylindrical coordinate system is taken to be the center of the patch, with the z coordinate extending upward from the substrate along the centerline of the pipette. In what follows, I rescale the spatial coordinates by the interior pipette radius R and the potential by the thermal voltage k_BT/e. All other geometric length scales (H, R_{patch}, τ, L_P) are then understood to be in units of the interior radius. The boundary condition given in Eq. 5.1 thus becomes

$$\boxed{\partial_z\phi|_{z=0} = -\mathrm{Du}\frac{\partial_r\left[rK(R_{\text{patch}}-r)\partial_r\phi|_{z=0}\right]}{r} \equiv -\sigma_{\text{eff}}[\phi](r),} \tag{5.6}$$

where I've defined the Dukhin number in terms of the interior pipette radius as

$$\boxed{\mathrm{Du} \equiv \frac{\ell_{\mathrm{Du}}}{R},} \tag{5.7}$$

and $K(R_{\text{patch}}-r)$ is a smoothed numerical approximation to $\Theta(R_{\text{patch}}-r)$; the dependence on the transition length λ is suppressed, as it will always be much smaller than the Dukhin length in what follows.

The boundary conditions imposed in the model are illustrated in Fig. 5.3. The boundary condition of Khair & Squires (2008) (Eq. 5.6) is applied at the bottom boundary (the solid-liquid interface), and a fixed voltage ΔV is applied on the exterior boundary at the base of the pipette, far from the substrate. All other external boundaries are held at ground. The walls of the pipette are assumed to be uncharged, and so a vanishing normal field, $\nabla\phi\cdot\hat{\boldsymbol{n}} = 0$, is imposed there. As before, steady state charge conservation requires in the bulk

$$\boxed{\nabla^2\phi = 0.} \tag{5.8}$$

Eq. 5.8, along with the boundary condition given in Eq. 5.6 and the remaining boundary conditions illustrated in Fig. 5.3 and described above, constitutes the effective electrostatics problem to be solved numerically.

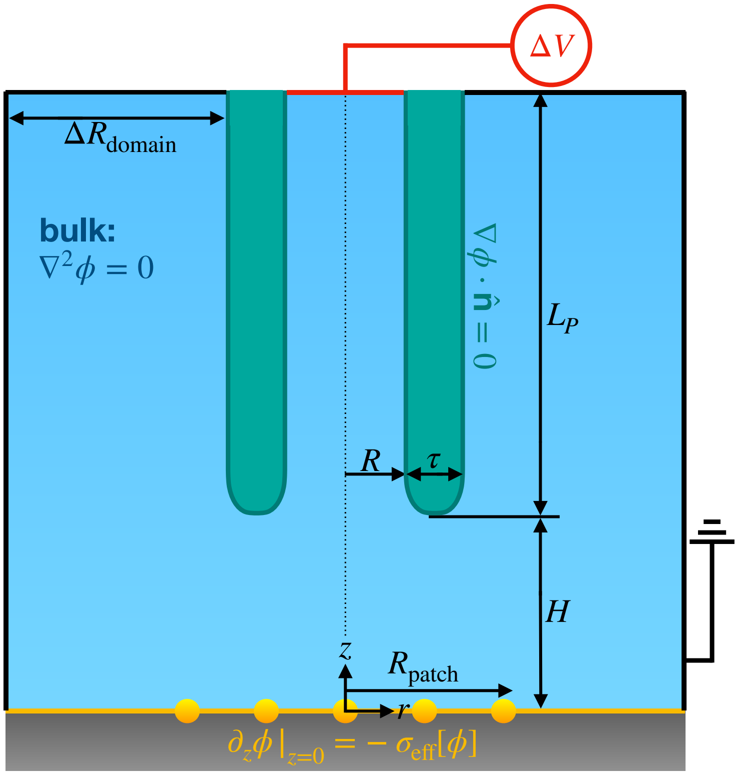

Figure 5.3: Schematic of the two-dimensional axisymmetric model configuration. A pipette of uniform thickness τ, constant interior radius R, and length L_P is held a distance H above an otherwise uncharged substrate containing an isolated patch of surface charge of radius R_{patch}. The radial coordinate is measured in the plane of the solid-liquid interface from the center of the charged patch, and the z coordinate is measured vertically from the substrate into the pipette along the pipette axis, indicated by the thin dotted vertical line. The total radial extent of the domain is $R + \tau + \Delta R_{\text{domain}}$, and the total vertical extent is $H + L_P$. The model boundary conditions are indicated in the schematic.

I begin by examining the current response in the absence of a charged patch. Fig. 5.4 shows the numerically calculated conductance, in units of $R\kappa_b$, as a function of the separation distance for $\tau = 0.1$, $L_P = 10$, and $\Delta R_{\text{domain}} = 10$. The numerical data are compared with a best fit of the scaling proposed by Nitz *et al.* (1998) (Eq. 5.5). We see that this scaling performs reasonably well given the simplicity of their model. In fact, the best-fit value of the geometric length scale is found to be $\ell_{\text{geo}}^{\text{num}} = 0.0146$, which compares very favorably with the value predicted by the model of Nitz *et al.* (1998), $\ell_{\text{geo}} = 3/2 \cdot \ln(1+\tau)/L_P = 0.0143$. The numerically determined pipette conductance $G_P^{\text{num}} = 0.296$ is about 6% lower than the theoretical value based on the pipette geometry and bulk conductance, which in dimensionless terms is $G_P = \pi/L_P = 0.314$. This is likely due to the non-negligible access resistance present even when the pipette is far from the substrate owing to the relatively small pipette aspect ratio ($L_P = 10$).

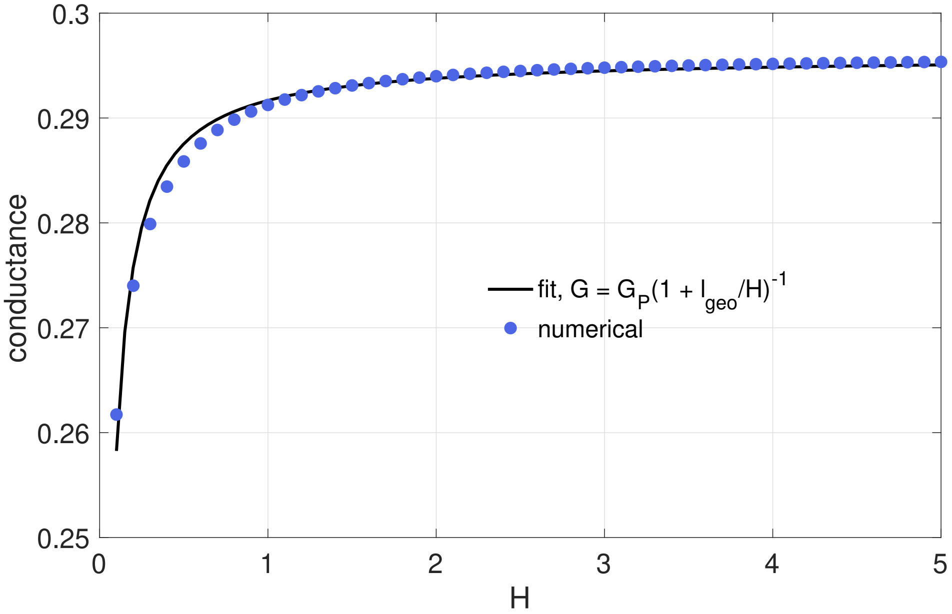

Figure 5.4: Comparison of numerical FEM results (blue dots) for the conductance as a function of separation distance H to the scaling derived by Nitz *et al.* (1998) (solid black curve). The pipette conductance G_P and geometric length scale ℓ_{geo} are calculated via a least-squares best fit. The model parameters are: $\tau = 0.1$, $L_P = 10$, and $\Delta R_{\text{domain}} = 10$, and the best-fit parameters are $\ell_{\text{geo}}^{\text{num}} = 0.0146$ and $G_P^{\text{num}} = 0.296$.

I next examine the modification to the current response induced by the presence of a charged patch. I characterize this modification by the conductance anomaly δG, defined as

$$\delta G(H; \text{Du}) \equiv G(H; \text{Du}) - G(H; \text{Du} = 0). \tag{5.9}$$

Before examining the numerical results, I derive an approximate scaling for this conductance via the Green's function approach. Much of this derivation follows closely that presented in Appendix D. To begin with, we decompose the electrostatic potential as $\phi = \phi^{(0)} + \delta\phi$, where $\phi^{(0)}$ satisfies Eq. 5.6 with $\text{Du} = 0$ ($\partial_z \phi^{(0)}|_{z=0} = 0$), Eq. 5.8, and the remaining boundary conditions given in Fig. 5.3. I then propose to solve the following problem for $\delta\phi$, the perturbation to the potential induced by the charged patch:

$$\nabla^2 \delta\phi = 0, \tag{5.10}$$

$$\delta\phi \xrightarrow[\rho\to\infty]{} 0, \quad \text{and} \tag{5.11}$$

$$\partial_z \delta\phi|_{z=0} = -\mathrm{Du}\frac{\partial_r\left[r\Theta(R_{\text{patch}} - r)\partial_r \phi|_{z=0}\right]}{r}, \tag{5.12}$$

where, in Eq. 5.11, $\rho \equiv \sqrt{r^2 + z^2}$ is the distance from the center of the patch. Note that it is the full potential appearing on the RHS of Eq. 5.12.

I have neglected the geometrically complex no flux boundary conditions induced by the pipette (Fig. 5.3) in Eq. 5.11. This is because including these boundary conditions would render the problem intractable. Strictly speaking, this approximation should only be valid when the Dukhin length and the patch size are smaller than either the height or the internal radius of the pipette; however, we will find that the scaling so obtained is more robust than these limits would suggest. From the development in Appendix D, we learn that $\delta\phi$ may be decomposed in terms of a Green's function $G(\mathbf{r}, \mathbf{r}_0)$ as

$$\delta\phi(\boldsymbol{r}) = -\int \mathrm{d}\boldsymbol{\Sigma}_s G(\boldsymbol{r}, \boldsymbol{r}_s)\partial_{z_0}\delta\phi|_{z_0=0}, \tag{5.13}$$

where $\boldsymbol{r}_s \equiv \boldsymbol{r}_0|_{z_0=0}$ is the source point coordinate confined to the solid-liquid interface, $G(\boldsymbol{r}, \boldsymbol{r}_s)$ is a three dimensional Green's function $G(\boldsymbol{r}, \boldsymbol{r}_0)$ evaluated on the interface, $G(\boldsymbol{r}, \boldsymbol{r}_s) \equiv G(\boldsymbol{r}, \boldsymbol{r}_0)|_{z_0=0}$, and $\mathrm{d}\boldsymbol{\Sigma}_s$ is a surface element on the interface. This decomposition is valid for the Green's function satisfying

$$\nabla^2_{\boldsymbol{r},\boldsymbol{r}_0} G(\boldsymbol{r}, \boldsymbol{r}_0) = -\delta^{(3)}(\boldsymbol{r} - \boldsymbol{r}_0), \tag{5.14}$$

$$G(\boldsymbol{r}, \boldsymbol{r}_0) \xrightarrow[\rho,\rho_0\to\infty]{} 0, \quad \text{and} \tag{5.15}$$

$$\partial_{z,z_0} G(\boldsymbol{r}, \boldsymbol{r}_0)|_{z,z_0=0} = 0. \tag{5.16}$$

Eqs. 5.14 and 5.15 are verified by the fundamental solution to Laplace's equation in three dimensions, $G_1(\boldsymbol{r}, \boldsymbol{r}_0) = 1/4\pi|\boldsymbol{r} - \boldsymbol{r}_0|$; however, in order to satisfy the no flux condition on the $x - y$ plane (Eq. 5.16), we must add to $G_1(\boldsymbol{r}, \boldsymbol{r}_0)$ its reflection about this plane, $G_2(\boldsymbol{r}, \boldsymbol{r}_0) \equiv G_1(\boldsymbol{r}', \boldsymbol{r}_0) \equiv G_1(\boldsymbol{r}, \boldsymbol{r}'_0)$. In the preceding, a prime indicates reflection about the $x - y$ plane–*e.g.*, $\boldsymbol{r}' \equiv (x, y, -z)$. Adding these two contributions to the Green's function and evaluating at $z_0 = 0$ gives

$$G(\boldsymbol{r}, \boldsymbol{r}_s) = \frac{1}{2\pi|\boldsymbol{r} - \boldsymbol{r}_s|}. \tag{5.17}$$

Inserting Eq. 5.17 into Eq. 5.13 and differentiating with respect to the source point coordinate $\boldsymbol{r}$, we obtain

$$\delta\boldsymbol{E}(\boldsymbol{r}) = -\int \mathrm{d}\boldsymbol{\Sigma}_s \frac{\boldsymbol{r} - \boldsymbol{r}_s}{2\pi|\boldsymbol{r} - \boldsymbol{r}_s|^3}\partial_{z_0}\delta\phi|_{z_0=0}, \tag{5.18}$$

where $\delta\boldsymbol{E}$ is the perturbation to $\boldsymbol{E}^{(0)} \equiv -\nabla\phi^{(0)}$ induced by the charged patch. The additional current induced by the surface charge may be evaluated as $\delta I = -2\pi \int_0^1 r\mathrm{d}r \delta E_z(H,r) \propto -\pi\delta E_z(H,0)$. We thus evaluate Eq. 5.18 at $\boldsymbol{r} = H\hat{\boldsymbol{z}}$ to obtain

$$\delta\boldsymbol{E}(H,0) = -\int \mathrm{d}\boldsymbol{\Sigma}_s \frac{H\hat{\boldsymbol{z}} - \boldsymbol{r}_s}{2\pi\left(H^2 + r_s^2\right)^{3/2}} \partial_{z_0}\delta\phi|_{z_0=0}. \tag{5.19}$$

The only angular dependence is contained in $\boldsymbol{r}_s$, and this term is killed by angular integration. Inserting Eq. 5.12 into the remaining term proportional to $\hat{\boldsymbol{z}}$, we obtain

$$\delta E_z(H,0) = \mathrm{Du}\int_0^\infty \mathrm{d}r_s \frac{H}{\left(H^2 + r_s^2\right)^{3/2}} \partial_{r_s}\left[r_s\Theta(R_{\text{patch}} - r_s)\partial_{r_s}\phi|_{z_0=0}\right]. \tag{5.20}$$

Integrating by parts, we obtain

$$\delta E_z(H,0) = -3\mathrm{Du}H \int_0^{R_{\text{patch}}} \mathrm{d}r_s \frac{r_s^2}{\left(H^2 + r_s^2\right)^{5/2}} E_r(r_s,0). \tag{5.21}$$

In order to proceed further, I follow Lee *et al.* (2012) in employing a perturbative approach to Eq. 5.21. I insert the unperturbed field $E_r^{(0)}(r_s,0)$ into the RHS in order to obtain the first order correction to the electric field in Du:

$$\delta E_z^{(1)}(H,0) = -3\mathrm{Du}H \int_0^{R_{\text{patch}}} \mathrm{d}r_s \frac{r_s^2}{\left(H^2 + r_s^2\right)^{5/2}} E_r^{(0)}(r_s,0). \tag{5.22}$$

I next make the *a priori* drastic assumption that we may neglect the geometric dependence of the unperturbed field; this assumption is justified by the success of the scaling so obtained in characterizing the numerical results found below. As the unperturbed field must scale linearly with the applied voltage, this gives for the current anomaly

$$\delta I \propto -\delta E_z^{(1)}(H,0) \propto \mathrm{Du}\Delta V \int_0^{R_{\text{patch}}} \mathrm{d}r_s \frac{3Hr_s^2}{\left(H^2 + r_s^2\right)^{5/2}} = \mathrm{Du}\Delta V \frac{R_{\text{patch}}^3}{H\left(H^2 + R_{\text{patch}}^2\right)^{3/2}}, \tag{5.23}$$

and hence for the conductance anomaly

$$\boxed{\delta G \propto \mathrm{Du}\frac{R_{\text{patch}}^3}{H\left(H^2 + R_{\text{patch}}^2\right)^{3/2}}.} \tag{5.24}$$

Fig. 5.5 shows the numerically calculated conductance anomaly δG (Eq. 5.9) as a function of the separation difference H for several values of Du and $R_{\text{patch}} = 1$. (The remaining model parameters are $\tau = 0.1$, $L_P = 10$, and $\Delta R_{\text{domain}} = 10$.) For reference, the maximum values of the conductance anomalies are between 1 and 10% of the height-dependent conductance obtained when Du = 0 (Eq. 5.5, Fig. 5.4). Typical set points when conducting scanning measurements using SICM are on the order of 0.1 to 1% of the asymptotic current obtained when the pipette is far from the substrate (Korchev *et al.*, 1997; Klenerman *et al.*, 2011). This indicates that the signal calculated here is accessible using current SICM techniques, perhaps after calibration with a neutral substrate or at low Dukhin number.

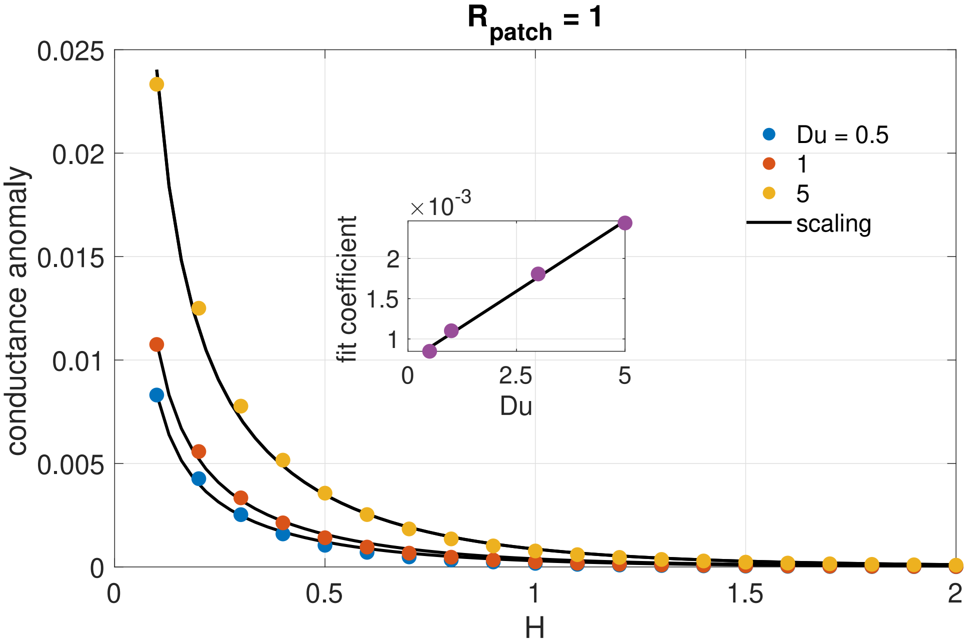

Figure 5.5: Conductance anomaly δG (Eq. 5.9) as a function of separation distance H for several values of the Dukhin number Du (Eq. 5.7), as indicated in the legend. The color-coded dots indicate the numerical values of δG calculated via FEM simulation, and the solid black lines indicate fits to the numerical data based on Eq. 5.25. The inset shows the fit coefficient α (Eq. 5.25) as a function of Du (purple dots) for the three curves shown in the main plot and an additional curve calculated for Du = 3. The solid black line in the inset shows the linear best fit to the fit coefficients. All curves are calculated for $R_{\text{patch}} = 1$, $\tau = 0.1$, $L_P = 10$, and $\Delta R_{\text{domain}} = 10$.

I fit the numerical data presented in Fig. 5.5 to a scaling of the form

$$\delta G = \alpha(\text{Du}) \frac{R_{\text{patch}}^3}{H\left(H^2 + R_{\text{patch}}^2\right)^{3/2}}, \tag{5.25}$$

based on the result given in Eq. 5.24. We see that this scaling characterizes the dependence of δG on the separation distance extremely well. I plot in the inset of Fig. 5.5 the scaling coefficient $\alpha(\text{Du})$ as a function of the Dukhin number. From Eq. 5.24, we anticipate α to be linear in Du, and indeed this is what is observed in the inset. The scaling given in Eq. 5.24 thus appears to adequately describe the dependence of the conductance anomaly on both Dukhin number and separation distance. Furthermore, the observed linear scaling of the signal with Du for a fixed value of $R_{\text{patch}} = 1$ suggests that the disturbance to the bulk electric field indeed scales with the Dukhin length, consistent with our hypothesis.

In Fig. 5.6, I again show δG as a function of H, now with a fixed Dukhin number, $\text{Du} = 5$, and several values of R_{patch}. I fit these curves to a scaling of the form

$$\delta G = \beta(R_{\text{patch}}) \frac{\text{Du}}{H\left(H^2 + R_{\text{patch}}^2\right)^{3/2}}. \tag{5.26}$$

The scaling works reasonably well for each of the values of R_{patch}, though it appears to work best for $R_{\text{patch}} \sim 1$. The inset in Fig. 5.6 shows a cubic fit of the form $\beta(R_{\text{patch}}) = \beta_0 R_{\text{patch}}^3$ to the scaling coefficient in Eq. 5.26. We see that β is indeed cubic in R_{patch} as anticipated from Eq. 5.24. This cubic dependence on the patch size (normalized by the interior pipette radius) means that even for very large Dukhin numbers it will be difficult to resolve charged features much smaller than the interior pipette radius. This partially contradicts our hypothesis, as it reveals that, though the apparent size of the patch does indeed scale with the Dukhin length, as indicated in Eq. 5.24 and Fig. 5.5, the signal is also a function of the ratio of the patch size to the interior pipette radius. Indeed, the (cubic) dependence on patch size is much stronger than the (linear) dependence on Dukhin length (Eq. 5.24, Figs. 5.5 and 5.6), indicating that the pipette radius sets a rough lower limit on the resolution of charge detection based on the method proposed here.

5.2.2 Two-Dimensional Translationally Invariant Model

In order to get a sense of the structure of lateral scanning measurements, in which the pipette is held at a fixed height and moved across the patch, I move from a two-dimensional axisymmetric to a two-dimensional translationally invariant geometry. The configuration of the translationally invariant FEM model is sketched in Fig. 5.7. The charged patch is now a charged strip of half-width R_{patch} centered on the line $x = 0$. Likewise, the pipette is now a channel of half-width $R \equiv 1$. (See the inset in Fig. 5.7.) The centerplane of the pipette is parallel to the centerline of the charged strip and offset a horizontal distance x_c from the center of the strip. As before, the thickness and length of the pipette are τ and L_P, and the tip of the pipette is held at a separation

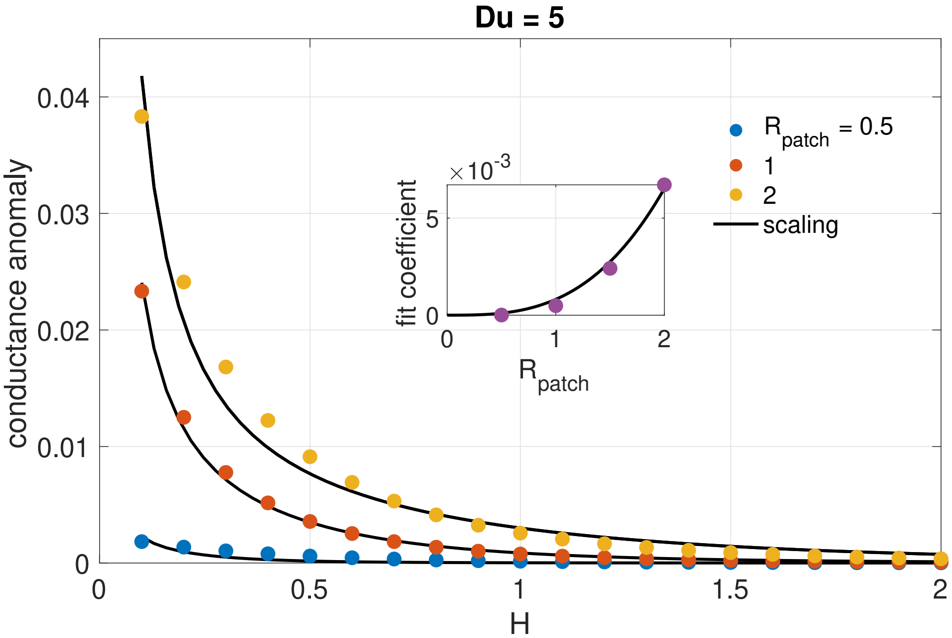

Figure 5.6: Conductance anomaly δG (Eq. 5.9) as a function of separation distance H for several values of the patch size R_{patch}, as indicated in the legend. The color-coded dots indicate the numerical values of δG calculated via FEM simulation, and the solid black lines indicate fits to the numerical data based on Eq. 5.26. The inset shows the fit coefficient β (Eq. 5.26) as a function of R_{patch} (purple dots) for the three curves shown in the main plot and an additional curve calculated for $R_{\text{patch}} = 1.5$. The solid black line in the inset shows a best fit of the form $\beta = \beta_0 R_{\text{patch}}^3$ to the fit coefficients. All curves are calculated for $\text{Du} = 5$, $\tau = 0.1$, $L_P = 10$, and $\Delta R_{\text{domain}} = 10$.

distance H from the substrate. Note that the boundary condition becomes in this configuration

$$\boxed{\partial_y \phi|_{y=0} = -\text{Du}\, \partial_x \left[\Theta\left(R_{\text{patch}} - |x|\right) \partial_x \phi|_{y=0}\right].} \tag{5.27}$$

As before, the electrostatic potential satisfies the Laplace equation (Eq. 5.8) in bulk, and the remaining boundary conditions are indicated in Fig. 5.7 and identical to those imposed in the axisymmetric case (Fig. 5.3).

This configuration is not as physically realistic as the axisymmetric configuration considered above, but it allows me to move the center of the pipette off of the center of the patch without going to a fully three-dimensional model. Given the high computational cost of the three-dimensional model, I use the translationally invariant configuration to simulate scanning measurements in the hope that qualitative features of the results found here carry over to the fully three-dimensional case.

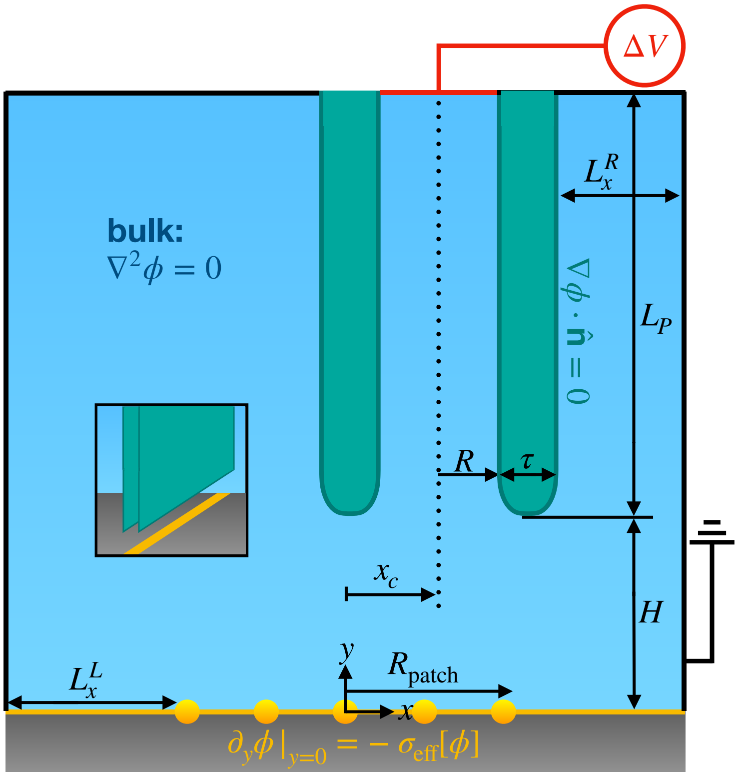

Figure 5.7: Schematic of the two-dimensional translationally invariant model configuration. A pipette of uniform thickness τ, constant interior half-width R, and length L_P is held a distance H above an otherwise uncharged substrate containing an isolated strip of surface charge of half-width R_{patch}. The x coordinate is measured in the plane of the solid-liquid interface from the center of the charged strip and perpendicular to its axis; the y coordinate is measured vertically from the substrate into the electrolyte. The pipette axis (dotted line) is located a horizontal distance x_c from the center of the charged strip. The inset shows a schematic, three-dimensional side view of the pipette, charged strip, substrate, and electrolyte. The total horizontal extent of the domain is $L_x^L + R_{\text{patch}} + x_c + R + \tau + L_x^R$, and the total vertical extent is $H + L_P$. The model boundary conditions are indicated in the schematic.

In Fig. 5.8, I show the conductance anomaly obtained from a lateral scan over a patch of half-width $R_{\text{patch}} = 1$ at several different separation distances $H \in [0.2, 1]$ (in units of the pipette half-width). Fig. 5.8a shows the results for Du $= 0.5$. The signal is roughly $1 - 6\%$ of the background conductance obtained in the absence of any surface charge, indicating that the patch is detectable even when Dukhin length is smaller than both the patch (Du $< R_{\text{patch}}$) and the pipette half-width (Du < 1). The signal shows local maxima in the vicinity of $x_c = \pm R_{\text{patch}}$ and a local minimum at $x_c = 0$; this suggests that the current is more sensitive to the discontinuity than to the uniform charge in the center of the patch for this value of Du and R_{patch}. The location of these maxima could potentially be used to obtain a reasonable estimate of the boundaries of the charged patch. Additionally, there is a sharp break in the slope of the curve in the vicinity of $x_c = \pm(R_{\text{patch}} + R)$, the point where, moving from the center of the patch at $x_c = 0$, the pipette passes entirely off of the patch (Fig. 5.7). The curve obtained for Du = 1 (figure not shown) is structurally identical, though the difference between the peak signal at $x_c \approx \pm R_{\text{patch}}$ and the signal at $x_c = 0$ is smaller. Comparing the panels of Fig. 5.8, it is clear that the peak signal and the signal at $x_c = 0$ both increase monotonically with Du, as anticipated. The results for Du $\lesssim 1$ suggest that information about the magnitude of the surface charge, along with the structure of the patch, may be readily inferred from the lateral structure of the conductance measurements.

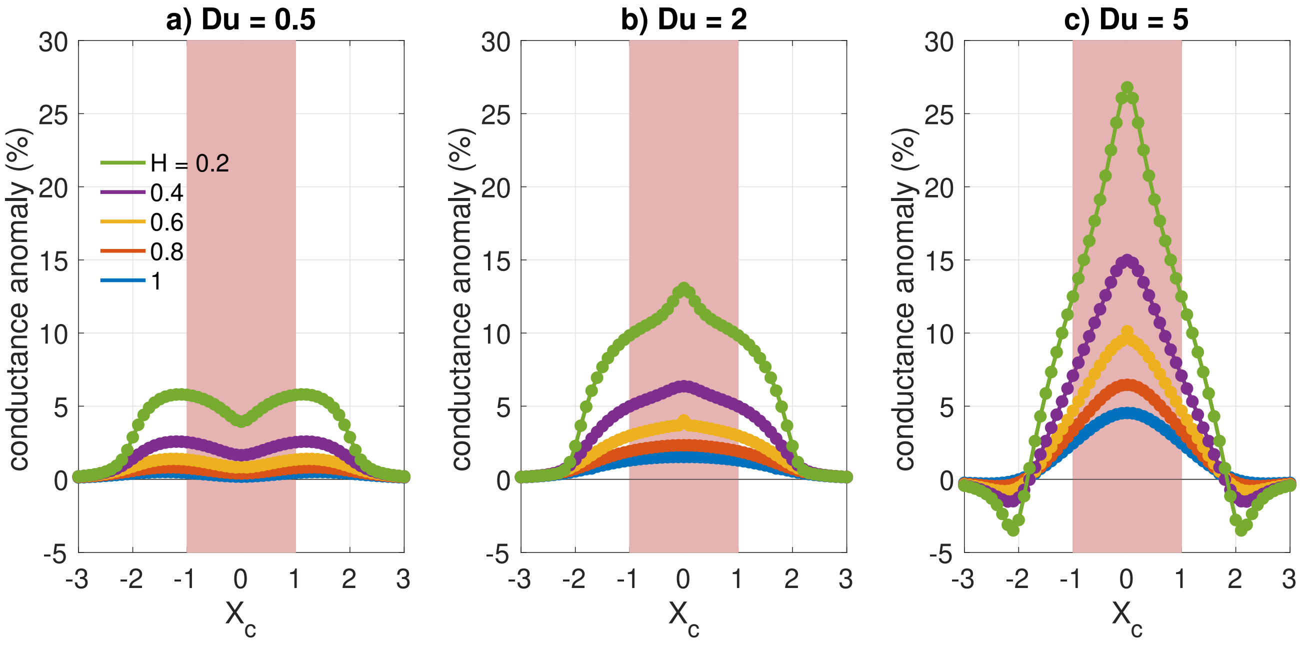

Figure 5.8: Conductance anomaly as a percentage of the unperturbed conductance and as a function of pipette position for a) Du = 0.5, b) Du = 2, and c) Du = 5, and for several different separation distances H, as indicated in the legend in panel a. The color-coded dots are FEM results, and the corresponding curves are guides to the eye. The red shading indicates the location of the charged patch. For all runs, $R_{\text{patch}} = 1$, $\tau = 0.1$, $L_P = 10$, $L_x^L = 10$, and $L_x^R = 10$.

The structure of the signal passes through two inversions as Du is increased. First, for Du = 2 (Fig. 5.8b), we see that the peak signal is now at the center of the patch ($x_c = 0$), and there are no longer local maxima in the vicinity of the patch boundaries at $x_c = \pm R_{\text{patch}}$. As for Du $\lesssim 1$, there is a sharp slope-break in the vicinity of $x_c = \pm(R_{\text{patch}} + R)$. This suggests that the signal may still be sensitive to the boundaries of the patch, even though localized peaks at the discontinuities are no longer present. Increasing the Dukhin number further, we see for Du $= 5$ (Fig. 5.8c) a complete inversion in the structure of the signal compared to those obtained for Du ≤ 1. In addition to the absolute maximum at $x_c = 0$, the slope-breaks have become local minima; indeed, the conductance anomaly actually becomes negative, indicating that the current is weaker than what would be obtained in the absence of a charged patch.

That the locations of the slope-breaks (Du $= 0.5$, 2) or peak negative conductance anomaly (Du $= 5$) roughly coincides with $x_c = \pm(R_{\text{patch}} + R)$ is confirmed in Fig. 5.9, where I plot lateral scans of the conductance anomaly for the same three Dukhin numbers shown in Fig. 5.8 and several patch sizes ($R_{\text{patch}} = 1$, 1.5, 2) for a fixed separation distance $H = 0.2$. The thin vertical lines indicate $x_c = \pm(R_{\text{patch}} + R)$, and it is clear that the substantial breaks or inversions in slope occur very close to this point. This result suggests that information about the patch size may readily be inferred from the lateral structure of the signal even in the absence of localized peaks in the vicinity of the discontinuities. More generally, Fig. 5.9 shows clearly that the shape of the $\delta G(x_c)$ curve is highly dependent on both Dukhin number and patch size. However, even given this substantial variability in the signal structure, the results of this and the preceding section indicate that 1) the lateral structure of the current response over an isolated charged feature may be used to infer the size of the feature, and 2) the scaling of the current with Dukhin number over the center of a charged patch may be used to identify at least relative differences in surface charge density magnitude. Full three-dimensional modeling will be necessary to to verify these results, especially those from the translationally invariant model, and to compare to experiments.

5.3 *Conclusions and Perspectives*

This work was motivated by the hypothesis that small, isolated charged features create disturbances in applied electric fields that scale with the Dukhin length, and that these disturbances may be measured via SICM in order to infer information about both the extent of the charged features and the magnitude of their surface charge. This hypothesis is corroborated by the following results:

- The numerically calculated signal scales with the Dukhin number (Figs. 5.5 and 5.8), at least for small to intermediate Dukhin numbers, in agreement with our analytical prediction

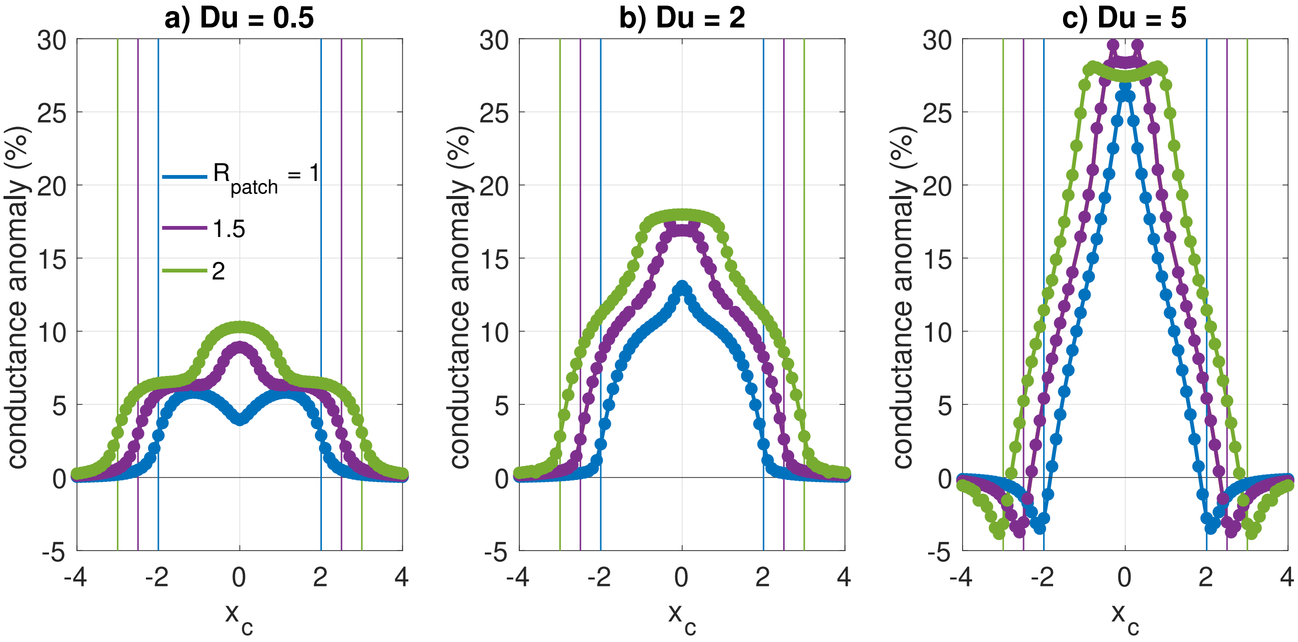

Figure 5.9: Conductance anomaly as a percentage of the unperturbed conductance and as a function of pipette position for a) Du = 0.5, b) Du = 2, and c) Du = 5, and for several different patch half-widths R_{patch}, as indicated in the legend in panel a. The color-coded dots are FEM results, and the corresponding curves are guides to the eye. The color-coded thin vertical lines indicate the corresponding values of $\pm(R_{\text{patch}} + R)$, the point at which the pipette passes from over the patch to adjacent to the patch. For all runs, $H = 0.2$, $\tau = 0.1$, $L_P = 10$, $L_x^L = 10$, and $L_x^R = 10$.

(Eq. 5.24).

- This signal is of the order of $1 - 10\%$ of the background signal obtained in the absence of surface charge, indicating that it may readily be measured via existing SICM techniques (Figs. 5.5, 5.6, 5.8, and 5.9, and associated discussion).

- The boundaries of a charged strip may be inferred from readily apparent features of the lateral profile of the conductance anomaly (Figs. 5.8 and 5.9, and associated discussion).

It should be noted, however, that we have also found that the resolution is limited by the size of the interior pipette radius. Furthermore, I have entirely neglected the solute dynamics in the treatment presented here. This means that I have implicitly neglected the influence of both ionic current rectification (ICR) in the pipette and surface-induced rectification (SIR) on the signal.

These last two points suggest that the technique discussed in this Chapter would be ideal for nanotube-based SICM measurments using individual nanotubes of radii on the order of a single nanometer inserted into nanopipettes (Secchi *et al.*, 2016a,b). This is true both because of the nanometric resolution of charged features that such a nanopipette would provide and because typical Dukhin lengths reach hundreds of nanometers for ionic concentrations on the order of 1 mM. Nanometric pipettes and large Dukhin lengths lead to Dukhin numbers on the order of $10 - 100$, more than sufficient to suppress both ICR and SIR entirely. (See Chapter 2.)

The next steps for this project are confirmation of the above results using a fully three-dimensional FEM model and comparison of these theoretical predictions to experimental results obtained from nanotube SICM measurements.

Chapter 6

CONCLUSIONS, OUTLOOKS, AND FUTURE WORK

The primary contribution of this manuscript is the understanding of the role of Dukhin number in both ion-selectivity and nonlinear transport. It is shown in Chapters 2 and 3 that 1) it is Dukhin, rather than Debye, overlap that determines nanopore selectivity, 2) an asymmetry in selectivity, as determined by an asymmetry in Dukhin number, is a necessary condition for ionic current rectification under an applied voltage, and 3) this nonlinearity extends to other forcings, in particular pressure forcing, when they are coupled with an applied voltage. The results for ion-selectivity may have potentially profound implications for desalination via electrodialysis (ED) and for energy generation via reverse electrodialysis (RED); in both of these technologies, a key limiting factor on their commercial viability is the poor conversion efficiency due to the small pore sizes necessary to achieve Debye overlap and the consequently large nanopore resistances. The results of Chapter 2 indicate that pores an order-of-magnitude larger in radius than typical ion-selective nanopores may readily exhibit significant ion-selectivity if their surface charge is tailored to achieve Dukhin numbers of order one. This would correspond to a reduction in nanopore resistance by two orders-of-magnitude. An immediate next step is therefore the experimental demonstration of substantial selectivity in large nanopores, and the viability of large nanoporous membranes in ED and RED.

Furthermore, this new understanding of nonlinear nanofluidic transport suggests the possibility of designing tailored nanopore and membrane functionalities, perhaps mimicking some of the exotic transport phenomena observed in biological ion transporters. One such functionality is mechanosensitive gating. Though they do not reproduce the full open/closed gating effect, the experimental results of Chapter 3 (and Chapter 4) go a long way in realizing such a phenomenon in the laboratory. In the context of the nonlinear response of ionic flux to coupled forcings, one promising avenue for future investigation is the experimental and theoretical exploration of coupled voltage-concentration forcing. Concentration forcing is particularly relevant in nature; one of the biological functions of mechanosensitive pores is the regulation of osmotic shock, in which the activation of pores is controlled by osmotic pressure differentials induced by concentration anomalies. Indeed, the exploration of coupled concentration-voltage forcing in the nonlinear regime has the potential to be phenomenologically rich, owing to the fact that concentration differentials result in asymmetric Dukhin number, diffusive and diffusio-osmotic forcing, osmotic forcing, and voltage forcing due to the resulting differential in Nernst potential. As such, a combined theoretical and experimental examination of coupled concentration-voltage forcing in the nonlinear regime is a natural continuation of the work presented in Chapter 3.

Chapter 4 is itself a natural continuation of both the work presented in Chapters 2 and 3, and of the project of nanofluidics itself. The goal of systematically exploring fluidic and ionic transport beyond the limits of continuum theory is only now beginning to be realized as technology is being developed to reliably fabricate channels with confinement scales below 1 nm. The experiments presented examining coupled voltage and pressure forcing in such strong confinement does indeed show substantial nonlinearity in the current response, as in Chapter 3, though the phenomenology is much richer, and the origin much different, in this context. The theoretical treatment in Chapter 4 highlights the completele inapplicability of traditional continuum fluid dynamics (*i.e.*, Navier-Stokes) and the severe limitations of even the significantly modified continuum description applied there. For this reason, a molecular dynamics model of the ionic transport in those systems is necessary. Such a model would provide a more detailed and less phenomenological understanding of the fluid and ion dynamics, and would elucidate the role of frictional characteristics and perhaps other factors in the pronounced material-sensitivity of the experimental results.

Chapter 5 is likewise a natural continuation of Chapters 2 and 3. The latter two chapters illustrated the importance of the Dukhin length, an often overlooked parameter, in nanofluidic transport. Chapter 5 goes further, illustrating a context in which the Dukhin length behaves as a physical length scale, setting the effective size of small surface charge features. The work of Chapter 5 is on going; the numerical observations will have to be verified using a fully three-dimensional model. Furthermore, the preliminary results suggest that charge-detection based on the mechanism proposed therein could improve upon the spatial resolution of current techniques by an order-of-magnitude or more. Thus, confirmation of this prediction via nanotube-based scanning ion conductance microscopy is an immediate goal from this work.

The work presented in this thesis offers both fundamental contributions to the theoretical understanding of technological applications and a foundation for future work in more fundamental research. In the context of blue energy generation, for example, RED has been offered as one of only a few potential mechanisms for converting the free energy of salt-and-freshwater mixing into mechanical energy, and it is now understood to be too inefficient to compete with current energy generation techniques (Siria *et al.*, 2017). Along with diffusio-osmotic energy generation (Siria *et al.*, 2013, 2017), large-pore RED as proposed in Chapter 2 suggests a new path forward for the design of low resistance membranes offering power densities that are comparable to current technologies. Likewise, while ED-based desalination is already present in the desalination market, a recent review identified the design of low resistance and high selectivity membranes as a key step in rendering ED a dominant, energy-efficient alternative to, for example, reverse osmosis (Campione *et al.*, 2018). In the domain of fundamental science, on the other hand, not only do Chapters 2 and 3 offer a new understanding of the occurrence of nonlinear transport in 'large' nanopores, but Chapter 4 presents a first step in the experimental and theoretical investigation of truly two-dimensional flows–flows which are no longer amenable to description by the Navier-Stokes equations. This study will remain foundational as this group and other researchers continue to probe two-dimensional hydrodynamics, the break down of continuum mechanics, and the rich taxonomy of phenomena associated therewith.

Appendix A

SOME USEFUL RESULTS FROM THE POISSON-BOLTZMANN EQUILIBRIUM

Abstract In this Appendix I compile some useful results pertaining to the Poisson-Boltzmann (PB) equilibrium that will be used throughout the manuscript. I start with a simple treatment of PB equilibrium in the vicinity of a charged wall in order to derive and illustrate the physical importance of the Debye and Dukhin lengths. I then derive some useful results for the local PB equilibrium on a circular cross-section, relevant for the treatment of ionic transport out of equilibrium discussed in Chapters 2 and 3. Finally, I apply these results to recover the Donnan equilibrium: the equilibrium of a nanopore connecting two reservoirs of equal concentration and electrostatic potential in the limit of strong overlap ($\lambda_D/R \gg 1$).

A.1 PB in the Vicinity of a Charged Wall

I consider the scenario sketched in A.1: a dissolved, monovalent ionic species in a semi-infinite domain is at equilibrium in the vicinity of a charged, infinite, planar wall of surface charge density σ. As is done throughout the manuscript, I adopt here a mean field description of the ions and assume a sufficiently dilute solution that the equilibrium ionic density is proportional to the one-body equilibrium (Boltzmann) distribution. Further, I model the solvent as a uniform dielectric of relative permittivity ϵ_r. In this case, at equilibrium, the mean ionic densities $c_\pm$ must verify the Boltzmann distribution, while the mean electrostatic potential ϕ must satisfy the Poisson equation:

$$c_\pm = \frac{c_\infty}{2} e^{\mp \frac{e\phi}{k_B T}}, \quad \text{and} \tag{A.1}$$

$$\epsilon_r \epsilon_0 \frac{d^2\phi}{dz^2} + n_c = 0, \tag{A.2}$$

where c_∞ is the total ionic concentration far from the wall, and $n_c \equiv e(c_+ - c_-)$ is the ionic charge density. Far from the wall, the ionic concentrations and electrostatic potential return to their undisturbed bulk values:

$$c_{\pm}(z \to \infty) = \frac{c_\infty}{2}, \quad \text{and} \tag{A.3}$$

$$\phi(z \to \infty) = 0. \tag{A.4}$$

Additionally, the electric field is subject to the Gaussian boundary condition at the wall:

$$\left.\frac{d\phi}{dz}\right|_{z=0} = -\frac{\sigma}{\epsilon_r \epsilon_0}, \tag{A.5}$$

where I have assumed that the bounding material is either a conductor or an insulator of sufficient thickness that it sustains no electric field.

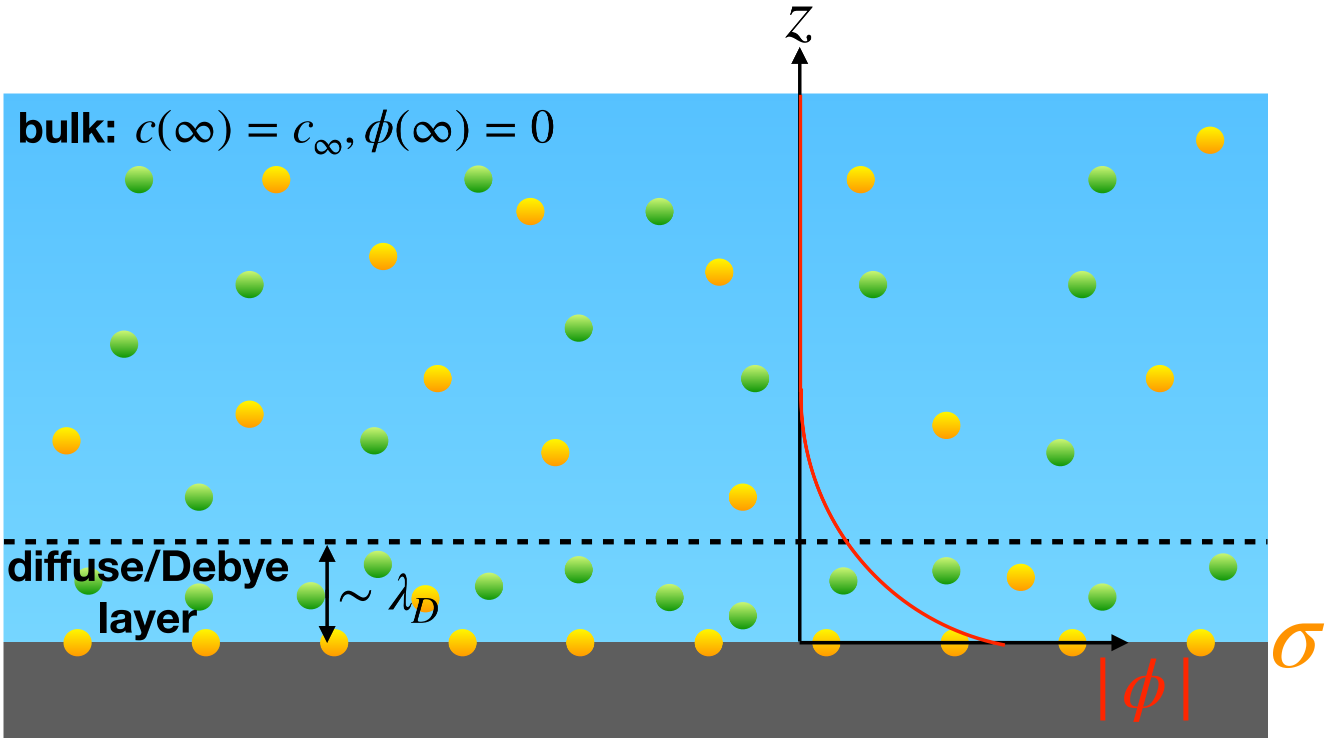

Figure A.1: A sketch of the configuration considered in Sec. A.1. A dissolved, monovalent ionic species at equilibrium in a semi-infinite domain is in contact with a charged planar boundary of surface charge density σ at $z = 0$. Far from the boundary, the total ionic concentration and electrostatic potential take their bulk values, $c(\infty) = c_\infty$ and $\phi(\infty) = 0$, respectively. In the vicinity of the boundary, a net ionic charge is built up via the accumulation of counterions (green) and the exclusion of coions (orange) in order to compensate the charge of the boundary. This accumulation of ionic charge within the so-called diffuse or Debye layer results in a nonzero electrostatic potential, sketched here in red. The characteristic scale of the diffuse layer is the Debye length λ_D, as indicated here and discussed in the text.

A.1.1 PB Equation and the Debye and Dukhin Lengths

We introduce the rescaled potential $\psi \equiv e\phi/k_BT$ and combine Eqs. A.1 and A.2 to find

$$\frac{d^2\psi}{dz^2} - \frac{1}{\lambda_D^2}\mathrm{sinh}\psi = 0. \tag{A.6}$$

This is the Poisson-Boltzmann (PB) equation for the electrostatic potential at equilibrium. I have introduced in Eq. A.6 the Debye length, a key quantity in nanofluidics, defined for a monovalent salt as

$$\boxed{\lambda_D \equiv \sqrt{\frac{k_BT\epsilon_r\epsilon_0}{e^2c_\infty}},} \tag{A.7}$$

or, generalizing to the case that there are several ionic species present, with the j-th ionic species having signed valence z_j and bulk concentration c_j^∞,

$$\boxed{\lambda_D \equiv \sqrt{\frac{k_BT\epsilon_r\epsilon_0}{e^2\sum_j z_j^2c_j^\infty}}.} \tag{A.8}$$

The Debye length is the only length scale appearing in the PB equation. It is thus natural to rescale the normal coordinate by λ_D: $\xi \equiv z/\lambda_D$. With this rescaling, we can rewrite the PB equation, Eq. A.6, and the boundary conditions given in Eqs. A.4 and A.5 as

$$\frac{d^2\psi}{d\xi^2} - \mathrm{sinh}\psi = 0, \tag{A.9}$$

$$\left.\frac{d\psi}{d\xi}\right|_{\xi=0} = -\mathrm{S}\frac{\ell_{\mathrm{Du}}}{\lambda_D}, \quad \text{and} \tag{A.10}$$

$$\psi(\xi \to \infty) = 0, \tag{A.11}$$

where $\mathrm{S} \equiv \mathrm{sign}(\sigma)$ is the sign of the surface charge density, and I have introduced the Dukhin length, defined as

$$\boxed{\ell_{\mathrm{Du}} \equiv \frac{|\sigma|}{ec_\infty}.} \tag{A.12}$$

We note from Eq. A.10 that the ratio of the Dukhin length to the Debye length sets the (rescaled) electric field strength normal to the boundary at the wall.

We multiply Eq. A.9 by $d\psi/d\xi$, recognizing that $(\mathrm{sinh}\psi)d\psi/d\xi = d\mathrm{cosh}\psi/d\xi$, to obtain

$$\frac{1}{2}\frac{d}{d\xi}\left(\frac{d\psi}{d\xi}\right)^2 = \frac{d}{d\xi}\mathrm{cosh}\psi. \tag{A.13}$$

Integration of this equation between ξ and ∞ gives the first integral of the PB equation:

$$\frac{1}{2}\left(\frac{d\psi}{d\xi}\right)^2 = \cosh\psi - 1. \tag{A.14}$$

This result may be related to the total ionic concentration via Eq. A.1:

$$\frac{c}{c_\infty} = 1 + \frac{1}{2}\left(\frac{d\psi}{d\xi}\right)^2. \tag{A.15}$$

This result relates the accumulation of ions within the diffuse layer to the field strength normal to the boundary. In particular, we may insert the Gaussian boundary condition for the normal field at the wall given in Eq. A.10 into Eq. A.15 to determine an expression for the total ionic concentration at the wall $c_w \equiv c(\xi = 0)$:

$$\frac{c_w}{c_0} = 1 + \frac{1}{2}\left(\frac{\ell_{\mathrm{Du}}}{\lambda_D}\right)^2. \tag{A.16}$$

This result suggests that the ratio $\ell_{\mathrm{Du}}/\lambda_D$ determines the ratio of total ionic concentration in the diffuse layer to the total ionic concentration in the bulk. The relationship between the Dukhin length and the accumulation of charge carriers in the diffuse layer will be used below to connect the 'equilibrium' definition of the Dukhin length given in Eq. A.12 to the 'dynamic' definition of the Dukhin length as the ratio of surface to bulk conductivities discussed in Chapters 2 and 5.

A.1.2 Solution of the PB Equation

We solve Eq. A.14 for $d\psi/d\xi$ to obtain

$$\frac{d\psi}{d\xi} = -\mathrm{S}\sqrt{2(\cosh\psi - 1)} = -2\sinh\frac{\psi}{2}, \tag{A.17}$$

where we have made use of the identity $\sqrt{(\cosh x - 1)/2} = \mathrm{sign}(x)\sinh(x/2)$. The factor $-\mathrm{S}$ in the first equality in Eq. A.17 comes from the fact that a positive surface charge induces a positive surface potential and hence a negative value of $d\psi/d\xi$ (and *vice versa*). This equation is readily integrated and solved for ψ to obtain

$$\boxed{\psi = 2\ln\left(\frac{1+\gamma e^{-\xi}}{1-\gamma e^{-\xi}}\right)}, \tag{A.18}$$

where $\gamma \equiv \tanh(\psi_w/4)$, and $\psi_w \equiv \psi(\xi = 0)$ is the potential at the wall. In order to determine ψ_w, we use Eq. A.10 to evaluate Eq. A.14 at $\xi = 0$. We find

$$\cosh\psi_w = 1 + \frac{1}{2}\left(\frac{\ell_{\mathrm{Du}}}{\lambda_D}\right)^2, \tag{A.19}$$

which may be used to relate $\ell_{\mathrm{Du}}/\lambda_D$ to ψ_w and hence to $\gamma \equiv \tanh(\psi_w/4)$.

A.1.3 Diffuse Layer Structure

We may relate the solution for the rescaled electrostatic potential, Eq. A.18, to the ionic concentrations via Eq. A.1. From this equation, we may determine the total ionic concentration c and charge density n_c as

$$c = c_\infty \mathrm{cosh}\psi, \quad \text{and} \tag{A.20}$$

$$n_c = -e c_\infty \mathrm{sinh}\psi, \tag{A.21}$$

respectively. We may also calculate the coion and counterion concentrations c_{co} and c_{count}, respectively, as

$$c_{\mathrm{co/count}} = \frac{c_\infty}{2} e^{\mp \mathrm{S}\psi}. \tag{A.22}$$

From Eq. A.18 (and equally well from Eqs. A.9 and A.10), we see that the rescaled electrostatic potential takes the form $\psi = \mathrm{S}|\psi(\xi, \ell_{\mathrm{Du}}/\lambda_D)|$. In particular, this scaling indicates that 1) the extent of the diffuse layer is $\mathcal{O}(1)$ when rescaled by the Debye length, and 2) the structure of the diffuse layer is determined by the ratio $\ell_{\mathrm{Du}}/\lambda_D$. This is illustrated in Fig. A.2, where I plot ψ and the co- and counterion concentrations as a function of ξ. We indeed observe that, while the structure of the diffuse layer changes significantly with $\ell_{\mathrm{Du}}/\lambda_D$ when $\ell_{\mathrm{Du}}/\lambda_D \gtrsim 1$, the extent of the diffuse layer is $\mathcal{O}(1)$ even for very large values of this parameter. We thus conclude that **the Debye length sets the characteristic size of the charged ionic diffuse layer forming in the vicinity of the charged wall.**

As they will be useful in the developments presented in Appendix B and Chapters 2 and 3, I give here the asymptotic expressions for the electrostatic potential and the coion, counterion, and total ionic concentrations at the wall as $\ell_{\mathrm{Du}}/\lambda_D \to \infty$. From Eq. A.19 we have

$$e^{|\psi_w|} \sim \left(\frac{\ell_{\mathrm{Du}}}{\lambda_D}\right)^2 \Longrightarrow |\psi_w| \sim 2\mathrm{ln}\left(\frac{\ell_{\mathrm{Du}}}{\lambda_D}\right), \quad \frac{\ell_{\mathrm{Du}}}{\lambda_D} \to \infty. \tag{A.23}$$

From Eqs. A.20, A.22, and A.23 we find

$$\frac{c_w}{c_\infty} \sim \frac{c^w_{\mathrm{count}}}{c_\infty} \sim \frac{1}{2}\left(\frac{\ell_{\mathrm{Du}}}{\lambda_D}\right)^2, \quad \text{and} \tag{A.24}$$

$$c^w_{\mathrm{co}} \to 0, \quad \frac{\ell_{\mathrm{Du}}}{\lambda_D} \to \infty. \tag{A.25}$$

These asymptotic expressions are illustrated in the insets in Figs. A.2a and c. In particular, we find that the asymptotic expression for the wall potential, Eq. A.23, is valid for $\ell_{\mathrm{Du}}/\lambda_D \gtrsim 3$.

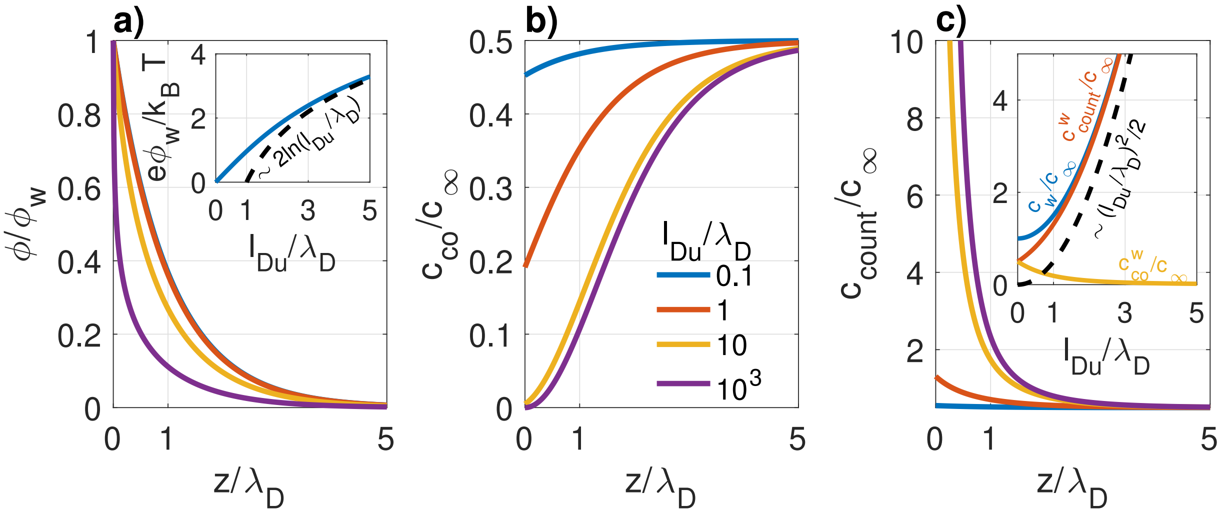

Figure A.2: Structure of the diffuse layer in the vicinity of a charged planar wall. a) Electrostatic potential normalized by the potential at the wall ϕ/ϕ_w versus z/λ_D. b and c) Respectively, the coion and counterion concentrations, normalized by the total ionic concentration in the bulk, c_{co}/c_∞ and $c_{\mathrm{count}}/c_\infty$, versus z/λ_D. In each panel, the curves are colored according to $\ell_{\mathrm{Du}}/\lambda_D$, as indicated in the legend in panel b. The subplot in panel a shows the rescaled wall potential, $e\phi_w/k_BT$, as a function of $\ell_{\mathrm{Du}}/\lambda_D$. The subplot in panel c shows the total, c_w, counter-, c^w_{count}, and coion, c^w_{co}, concentrations at the wall normalized by c_∞ as a function of $\ell_{\mathrm{Du}}/\lambda_D$. The dashed lines in the subplots in panels a and c show, respectively, the asymptotic behavior of the rescaled wall potential, $\psi_w \sim 2\ln(\ell_{\mathrm{Du}}/\lambda_D)$ (Eq. A.23), and the normalized counterion and total ionic concentrations, c^w_{count}, $c_w \sim (\ell_{\mathrm{Du}}/\lambda_D)^2/2$ (Eq. A.24) as $\ell_{\mathrm{Du}}/\lambda_D \to \infty$.

A.1.4 Electroneutrality

Integrating the Poisson equation, Eq. A.2, in z, we find

$$\epsilon_r\epsilon_0 E_z(0) + \int_0^\infty \mathrm{d}z n_c = 0, \tag{A.26}$$

where $E_z \equiv -d\phi/dz$ is the z-component of the electric field. Applying the Gaussian boundary condition, Eq. A.5, we obtain

$$\boxed{\sigma + \int_0^\infty \mathrm{d}z n_c = 0.} \tag{A.27}$$

This result indicates that the ionic charge integrated normal to the charged boundary exactly compensates the surface charge density *at every point along the boundary*. This **condition of local electroneutrality** is a necessary consequence of the Poisson-Boltzmann equilibrium in any configuration, as we will see below. This condition has important consequences even out-of-equilibrium because, in the limit of a strong separation of longitudinal and transverse length scales, an approximate PB equilibrium holds on each cross-section.

A useful form of the electroneutrality condition is obtained by rescaling n_c by ec_∞ and z by λ_D:

$$\boxed{\mathrm{S}\frac{\ell_{\mathrm{Du}}}{\lambda_D} + \int_0^\infty \mathrm{d}\xi \frac{n_c}{ec_\infty} = 0.} \tag{A.28}$$

We see that $\ell_{\mathrm{Du}}/\lambda_D$ is the magnitude of the (rescaled) net charge accumulated in the diffuse layer.

A.1.5 Concentration Accumulation in the Diffuse Layer

I now determine the accumulation of total ionic concentration within the diffuse layer. This result will be applied in the following section examining PB equilibrium on a circular cross-section, and the results therein are used in the derivation of the one-dimensional transport equations in the limit that λ_D is much smaller than the scale of confinement (see Chapters 2 and 3).

We consider the integated excess total ionic concentration $\delta c \equiv c - c_\infty = c_\infty(\cosh\psi - 1)$ (Eq. A.20):

$$\int_0^\infty \mathrm{d}z \frac{\delta c}{c_\infty} = \lambda_D \int_{\psi_w}^0 \mathrm{d}\psi \left(\frac{d\psi}{d\xi}\right)^{-1} \frac{\delta c}{c_\infty} = \lambda_D \int_0^{\psi_w} \mathrm{d}\psi \sinh\frac{\psi}{2} = 2\lambda_D \left(\cosh\frac{\psi_w}{2} - 1\right), \tag{A.29}$$

where in the second equality I have inserted Eq. A.17 and again used the identity $\cosh x - 1 = 2\sinh^2(x/2)$. Finally, we apply the identity $\sqrt{(\cosh x + 1)/2} = \cosh(x/2)$ to Eq. A.19 and insert the result into Eq. A.29 to obtain

$$\boxed{\int_0^\infty \mathrm{d}z \frac{\delta c}{c_\infty} = 2\lambda_D \left[\sqrt{1 + \left(\frac{\ell_{\mathrm{Du}}}{2\lambda_D}\right)^2} - 1\right].} \tag{A.30}$$

We see from Eqs. A.19, A.28, and A.30 that the ratio of the Dukhin length to the Debye length controls both the magnitude of the surface potential and the accumulation of charge and ionic concentration within the diffuse layer. The larger the ratio ℓ_{Du}/λ_D, the stronger the induced potential at the surface and the greater the accumulation within the diffuse layer. Furthermore, we will see in the next section and in Chapters 2 and 3 that the ratio of the Dukhin length to the confinement scale R is the key parameter determining the occurrence of selectivity and nonlinear ionic transport in nanofluidic systems.

A.2 PB on a Circular Cross-Section

I now consider the PB equilibrium of a monovalent electrolytic solution in the interior of a charged annulus of surface charge density σ, as sketched in Fig. A.3. (Note that I am considering a single cross-section in an extended cylindrical or conical geometry such that the surface charge density and ionic concentrations still have dimensions of charge per unit area and number per unit volume, respectively.)

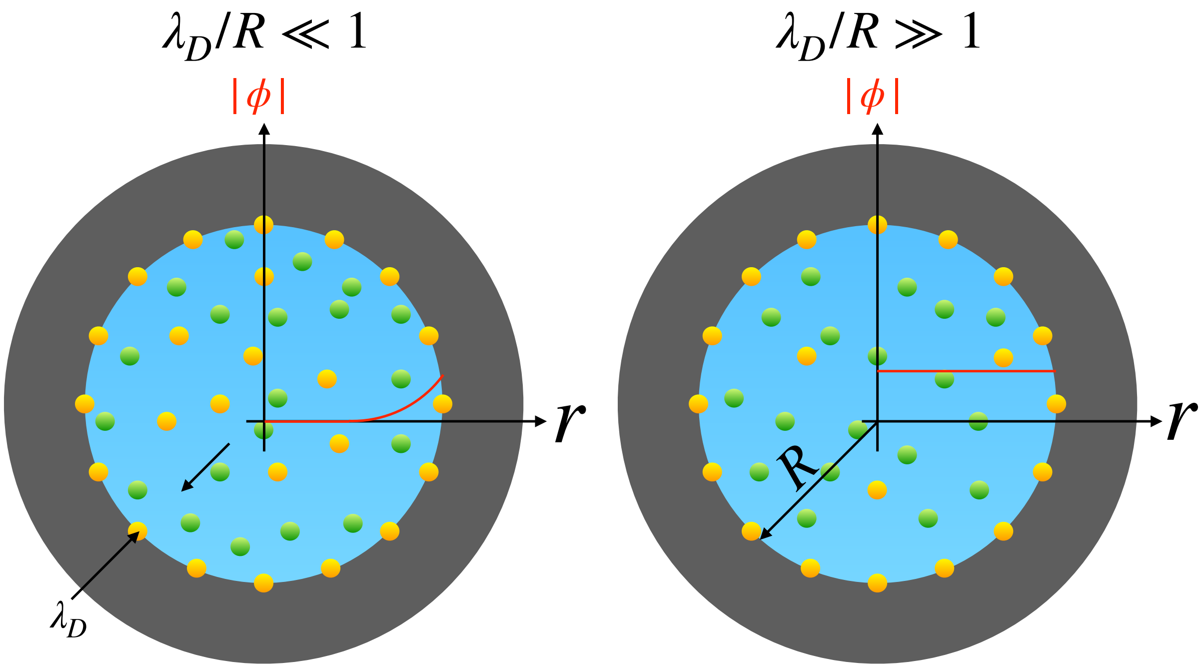

Figure A.3: A sketch of the configuration considered in Sec. A.2. A dissolved, monovalent ionic species at equilibrium in a circular domain is in contact with a ring of surface charge density σ at $r = R$. When $\lambda_D/R \ll 1$, a diffuse layer of thickness $\sim \lambda_D$ forms in the vicinity of the boundary, and the structure of the diffuse layer is similar to the diffuse layer in the vicinity of a charged planar boundary. On the other hand, when $\lambda_D/R \gg 1$, the potential and ionic concentration profiles homogenize on the cross-section, and there is no distinct diffuse layer.

Following Fair & Osterle (1971), we partition the electrostatic potential as

$$\phi(r) = \phi_0 + \delta\phi(r), \tag{A.31}$$

where the radial-dependence is contained only in $\delta\phi(r)$, which is induced by deviations from electroneutrality. Integration of the radial ionic flux equation at equilibrium, $0 = j^r_\pm/D_\pm =$

$(-dc_\pm/dr) \pm c_\pm(-d\delta\psi/dr)$, then gives

$$c_\pm = \frac{c_0}{2} e^{\mp\delta\psi}, \tag{A.32}$$

where $\delta\psi \equiv e\delta\phi/k_BT$ is the rescaled potential deviation and c_0 is the constant of integration. This constant must be the same for both species such that $c_+ = c_-$ and the solution is therefore electroneutral when $\delta\phi = 0$.

Note that, in general, since the diffuse layer forming on the boundary may overlap itself at the center of the cross-section, $\delta\phi(r=0) \neq 0$ and $c_+(0) \neq c_-(0)$. However, in the limit $\lambda_D/R \ll 1$, the solution will be electroneutral at the center and $\delta\phi$ will vanish there. In this case, ϕ_0 and c_0 are the centerline values of the elctrostatic potential and total ionic concentration, respectively.

The potential deviation must verify the radial Poisson equation:

$$\epsilon_r\epsilon_0 \frac{1}{r}\frac{d}{dr}\left(r\frac{d\delta\phi}{dr}\right) + n_c = 0, \tag{A.33}$$

subject to the Gaussian boundary condition at the wall ($r = R$) and the axisymmetry condition at $r = 0$:

$$\left.\frac{d\delta\phi}{dr}\right|_{r=R} = +\frac{\sigma}{\epsilon_r\epsilon_0}, \quad \text{and} \tag{A.34}$$

$$\left.\frac{d\delta\phi}{dr}\right|_{r=0} = 0. \tag{A.35}$$

We obtain the radial PB equation by inserting Eq. A.32 into Eq. A.33, rewriting in terms of $\delta\psi$, and introducing the rescaled coordinate $\rho \equiv r/R$:

$$\frac{1}{\rho}\frac{d}{d\rho}\left(\rho\frac{d\delta\psi}{d\rho}\right) = \left(\frac{R}{\lambda_D}\right)^2 \sinh\delta\psi. \tag{A.36}$$

This equation is subject to the boundary conditions (Eqs. A.34 and A.35)

$$\left.\frac{d\delta\psi}{d\rho}\right|_{\rho=1} = +\mathrm{S}\frac{\mathrm{Du}}{(\lambda_D/R)^2}, \quad \text{and} \tag{A.37}$$

$$\left.\frac{d\delta\psi}{d\rho}\right|_{\rho=0} = 0, \tag{A.38}$$

where I have introduced the Dukhin number, defined as

$$\boxed{\mathrm{Du} \equiv \frac{\ell_{\mathrm{Du}}}{R} \equiv \frac{|\sigma|}{ec_0R}.} \tag{A.39}$$

As shown in Chapters 2 and 3, this is the key parameter controlling selectivity and nonlinear ionic transport in confined geometries. As noted in Chapters 2 and 5, a 'dynamic' definition of the Dukhin number as the ratio of surface to bulk conductivities is sometimes given; the equivalence of these definitions in the case that a local PB equilibrium holds along the length of the nanopore will be demonstrated by considering the accumulation of excess charge carriers in the diffuse layer in Sec. A.2.2 below.

Unlike the case of a single planar boundary discussed above, the radial PB equation (Eq. A.36) has no solution in general. However, useful information may be determined in general (electroneutrality), in the limit $\lambda_D/R \ll 1$ (average excess total ionic concentration), and in the limit $\lambda_D/R \gg 1$ (radial uniformity of concentration and potential profiles). Each of these will be discussed in turn below.

A.2.1 Electroneutrality

We multiply the Poisson equation (Eq. A.33) by $2\pi r$, integrate in r, and apply the Gaussian boundary condition, Eq. A.34, and the axisymmetry condition, Eq. A.35, to obtain

$$2\pi R\sigma + \int_0^R 2\pi r \mathrm{d}r n_c = 0. \tag{A.40}$$

Dividing by the cross-sectional area, πR^2, we find

$$\boxed{\frac{2\sigma}{R} + \langle n_c \rangle = 0,} \tag{A.41}$$

where $\langle\,\rangle \equiv A^{-1}\int_A \mathrm{d}A$ denotes a cross-sectional average. Like Eq. A.27, Eq. A.41 is a statement of the condition of local electroneutrality. We see that the electroneutrality condition is a necessary consequence of the PB equilibrium, irrespective of whether we are in the regime of no overlap ($\lambda_D/R \ll 1$) or overlap ($\lambda_D/R \gtrsim 1$).

A useful form of the electroneutrality condition, Eq. A.41, is obtained by rescaling n_c by ec_{ref}, where c_{ref} is some reference concentration, and the radius $R(x)$ and surface charge density $\sigma(x)$ (which we allow to vary along the length of the nanopore) by some reference radius R_{ref} and surface charge density magnitude $|\sigma|_{\mathrm{ref}}$, respectively:

$$\boxed{\mathrm{S}\frac{2\mathrm{Du}_{\mathrm{ref}}|\sigma'|}{R'} + \langle n_c' \rangle = 0,} \tag{A.42}$$

where $\sigma' \equiv \sigma/|\sigma|_{\text{ref}}$, $R' \equiv R/R_{\text{ref}}$, and $n_c' \equiv n_c/ec_{\text{ref}}$ are the rescaled surface charge density, radial profile, and ionic charge density, respectively, and we have introduced a reference Dukhin number $\text{Du}_{\text{ref}} \equiv |\sigma|_{\text{ref}}/ec_{\text{ref}}R_{\text{ref}}$.

A.2.2 Average Excess Concentration in the Limit of No Overlap ($\lambda_D/R \to 0$)

We begin by expanding the Laplacian in the radial PB equation (Eq. A.36) and examining the scaling of each term in λ_D/R as $\lambda_D/R \to 0$:

$$\underbrace{\frac{d^2\delta\psi}{d\rho^2}}_{\sim(\lambda_D/R)^{-2}} + \underbrace{\frac{1}{\rho}\frac{d\delta\psi}{d\rho}}_{\sim(\lambda_D/R)^{-1}} = \underbrace{\frac{\sinh\delta\psi}{(\lambda_D/R)^2}}_{\sim(\lambda_D/R)^{-2}}. \tag{A.43}$$

The scaling of the gradient terms comes from the fact that significant variation in the potential is confined to the diffuse layer when there is no overlap, and the diffuse layer has a characteristic thickness λ_D/R in rescaled coordinates. We thus anticipate that the second gradient term, induced by the curvature of the boundary, becomes negligible as $\lambda_D/R \to 0$. This is physically intuitive, as we expect the diffuse layer to see only a flat boundary when its extent is much smaller than the radius of curvature.

Thus, defining a new coordinate $\mathcal{Z} \equiv 1 - \rho$, we obtain the planar PB equation in the limit $\lambda_D/R \ll 1$. We may therefore directly transcribe the result given in Eq. A.30 for the integrated excess ionic concentration:

$$\int_0^\infty \mathrm{d}\mathcal{Z}\frac{\delta c}{c_0} = 2\frac{\lambda_D}{R}\left\{\sqrt{1+\left[\frac{\text{Du}}{2(\lambda_D/R)}\right]^2} - 1\right\}. \tag{A.44}$$

The relevant quantity in the derivation of the one-dimensional transport equations in this limit (Chapter 2) is the cross-sectionally averaged excess ionic concentration, $\langle\delta c\rangle = 2\pi\int_0^\infty \mathrm{d}\mathcal{Z}\delta c/\pi$:

$$\boxed{\frac{\langle\delta c\rangle}{c_0} = 4\frac{\lambda_D}{R}\left\{\sqrt{1+\left[\frac{\text{Du}}{2(\lambda_D/R)}\right]^2} - 1\right\}.} \tag{A.45}$$

Note that, in this limit, c_0 is the actual total ionic concentration at the center of the circular domain (*i.e.*, on the nanopore centerline).

In Chapters 2 and 5, a dynamic definition of the Dukhin length is given as the ratio of the surface to the bulk conductivities, κ_{surf} and κ_{bulk}, respectively. This can be connected to the equilibrium definition of the Dukhin length in terms of the surface charge density and bulk concentration given in Eq. A.12 via Eq. A.45, which gives the total excess charge carriers $\pi R^2\langle\delta c\rangle$ accumulated within the diffuse layer. The surface and bulk conductivities are defined by the relations $I_{\text{surf}} = 2\pi R \times \kappa_{\text{surf}} \times E$ and $I_{\text{bulk}} = \pi R^2 \times \kappa_{\text{bulk}} \times E$, respectively, with E the applied electric field. Assuming the currents are dominated by the electrophoretic contributions, we therefore have $\kappa_{\text{bulk}} \propto c_0$ and $\kappa_{\text{surf}} \propto \pi R^2\langle\delta c\rangle/2\pi R = R\langle\delta c\rangle/2$. We consider the case of a large nanopore, taking the limit $\ell_{\text{Du}}/\lambda_D \to \infty$ in Eq. A.45 to find that $\langle\delta c\rangle \to 2\text{Du}c_0$. Thus, $\kappa_{\text{surf}} \propto (R/2) \times 2\text{Du}c_0 = \ell_{\text{Du}}c_0 \Longrightarrow \kappa_{\text{surf}} = \ell_{\text{Du}}\kappa_{\text{bulk}}$, and we have

$$\boxed{\ell_{\text{Du}} = \frac{\kappa_{\text{surf}}}{\kappa_{\text{bulk}}}.} \tag{A.46}$$

Furthermore, the ratio of the surface to the bulk conductances, G_{surf} and G_{bulk}, respectively, is given by $G_{\text{surf}}/G_{\text{bulk}} = 2\pi R\kappa_{\text{surf}}/\pi R^2\kappa_{\text{bulk}} = 2\ell_{\text{Du}}/R$, such that

$$\boxed{2\text{Du} = \frac{G_{\text{surf}}}{G_{\text{bulk}}}.} \tag{A.47}$$

A.2.3 Homogenization of the Concentration and Potential Profiles in the Limit of Strong Overlap ($\lambda_D/R \to \infty$)

In the opposing limit, $\lambda_D/R \to \infty$, the gradient terms in Eq. A.43 no longer vary with λ_D/R as the scale of variation of the gradient saturates at the radius (unity in rescaled coordinates) as λ_D/R increases. On the other hand, the source term on the RHS becomes negligibly small in comparison. Thus, we anticipate that the rescaled potential deviation verifies $(1/\rho)d[\rho(d\delta\psi/d\rho)] \approx 0$. Furthermore, for any fixed finite value of the Dukhin number, the Gaussian boundary condition, Eq. A.37, reduces to $d\psi/d\rho|_{\rho=1} = 0$ as $\lambda_D/R \to \infty$. Thus, $\delta\psi$, and therefore ψ and ϕ, approaches a constant value in this limit. From Eqs. A.32, we see that the ionic concentration profiles are likewise uniform in the limit of strong overlap. Furthermore, Eq. A.41 determines the value of $n_c = \langle n_c\rangle = -2\sigma/R$. Thus, the solution in this limit takes the form

$$\boxed{\frac{d\phi}{dr} = \frac{dc}{dr} = 0, \quad \text{and}} \tag{A.48}$$

$$\boxed{n_c = -\frac{2\sigma}{R}.} \tag{A.49}$$

We conclude that **in the limit of strong overlap ($\boldsymbol{\lambda_D/R \gg 1}$) the profiles of electrostatic potential and ionic concentration are radially uniform.** This will continue to be approximately valid in a nanopore out-of-equilibrium, though the radially uniform potentials and ionic concentrations will in this case vary along the length of the nanopore.

A.3 Donnan Equilibrium

Finally, I consider the equilibrium of a nanopore of uniform radius $R \gg \lambda_D$ and surface charge density σ connecting two reservoirs of equal concentration c_{res} and electrostatic potential V_{res}. (It is useful to take $V_{\text{res}} \neq 0$ for the developments in the main text, even if it is equal in both reservoirs here.) The configuration considered here is sketched in Fig. A.4.

In general, the equilibrium condition reduces to equality of the chemical potential. In the case of a dilute solution that I consider throughout the manuscript, the chemical potential is composed of an electrostatic and an entropic ideal gas term (Barrat & Hansen, 2003):

$$\mu_\pm = k_B T \ln(c_\pm \Lambda^3) \pm e\phi, \tag{A.50}$$

where $1/\Lambda^3$ is an arbitrary reference concentration. In a quantum statistical derivation of the chemical potential, the length scale Λ emerges naturally as the thermal de Broglie wavelength.

Our equilibrium conditions are the spatial homogeneity of the chemical potential and electroneutrality in both the reservoirs and the nanopore (see Eq. A.41). In the reservoirs, electroneutrality requires $c_+ = c_- = c_{\text{res}}/2$, and the reservoir chemical potentials are therefore

$$\mu_\pm^{\text{res}} = k_B T \ln\left(\frac{c_{\text{res}}\Lambda^3}{2}\right) \pm eV_{\text{res}}. \tag{A.51}$$

In the nanopore, we first note that, since we are in the regime of strong overlap, the ionic concentrations and electrostatic potential will be radially uniform (Eqs. A.48 and A.49). Furthermore, the accumulation of a net ionic charge within the pore to balance the surface charge will result in a shift in the electrostatic potential in the pore relative to the reservoir. I denote the pore potential and ionic concentrations as V_{pore} and $c_\pm^{\text{pore}}$. The chemical potential and electroneutrality condition in the pore are thus

$$\mu_\pm^{\text{pore}} = k_B T \ln\left(c_\pm \Lambda^3\right) \pm eV_{\text{pore}}, \quad \text{and} \tag{A.52}$$

$$\frac{2\sigma}{R} + n_c = 0, \tag{A.53}$$

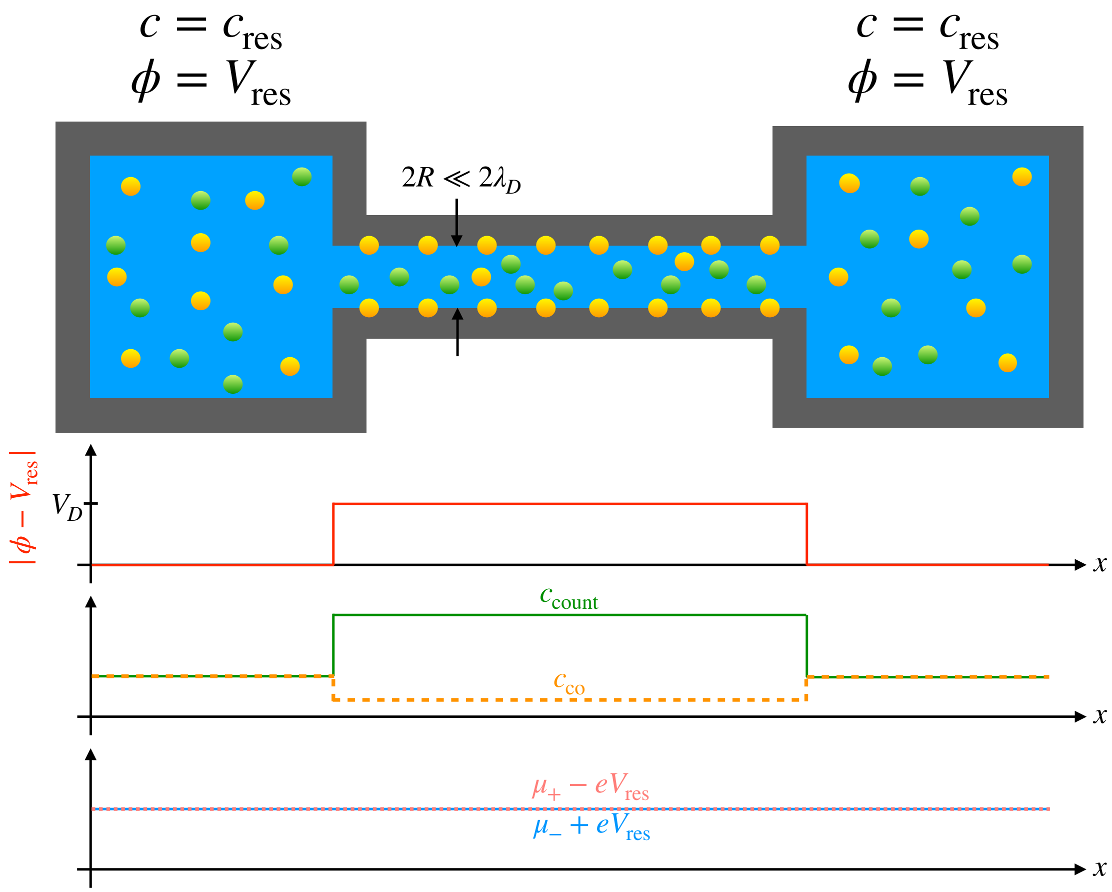

Figure A.4: A sketch of the configuration considered in Sec. A.3. A cylindrical nanopore of uniform radius $R \ll \lambda_D$ and surface charge density σ connects two reservoirs of equal concentration c_res and electrostatic potential V_res. The surface charge induces an accumulation of counterions and an exclusion of coions in the pore, and this results in the build up of a Donnan potential V_D in the pore interior. The ionic concentrations and electrostatic potential vary rapidly at the ends of the nanopore, but at equilibrium the adjustments must be such that the cation and anion chemical potentials are spatially uniform.

respectively.

We equate the chemical potentials in the reservoirs (Eq. A.51) and in the pore (Eq. A.52) and solve for the ionic concentrations in the pore:

$$c_\pm^\mathrm{pore} = \frac{c_\mathrm{res}}{2} e^{\mp \frac{e(V_\mathrm{pore} - V_\mathrm{res})}{k_B T}}. \tag{A.54}$$

Taking the product of the cation and anion concentrations in the pore, we find

$$\boxed{c_+^\mathrm{pore} c_-^\mathrm{pore} = \frac{c_\mathrm{res}^2}{4}.} \tag{A.55}$$

Taking the ratio of the anion to the cation concentration in the pore and solving for the shift in the electrostatic potential, $V_D \equiv V_{\text{pore}} - V_{\text{res}}$, we find

$$\boxed{V_D = \frac{1}{2}\frac{k_B T}{e}\ln\left(\frac{c_-^{\text{res}}}{c_+^{\text{res}}}\right).} \tag{A.56}$$

The potential shift V_D is termed the Donnan potential.

We may solve Eqs. A.53 and A.55 for the ionic concentrations in the pore. The result is

$$\boxed{c_\pm^{\text{pore}} = \frac{c_{\text{res}}}{2}\left[\sqrt{1+(2\text{Du})^2} \mp \text{S}2\text{Du}\right],} \tag{A.57}$$

where I have introduced a Dukhin number $\text{Du} = |\sigma|/ec_{\text{res}}R$. From this, we determine the total ionic concentration to be

$$\boxed{c_{\text{pore}} = c_{\text{res}}\sqrt{1+(2\text{Du})^2}.} \tag{A.58}$$

We insert the result given in Eq. A.57 into Eq. A.56 to obtain another useful expression for the Donnan potential:

$$\boxed{V_D = \text{S}\frac{1}{2}\frac{k_B T}{e}\ln\left[\frac{\sqrt{1+(2\text{Du})^2}+2\text{Du}}{\sqrt{1+(2\text{Du})^2}-2\text{Du}}\right].} \tag{A.59}$$

These results will be applied in Chapter 2 when I consider ionic transport in nanopores having radii much smaller than the Debye length. Though in this case we will be out-of-equilibrium, continuity of the chemical potential at both ends of the nanopore will result in the formation of a local Donnan equilibrium.

Appendix B

DERIVATION OF THE ELECTRO-OSMOTIC, DIFFUSIO-OSMOTIC, AND STREAMING SOLVENT AND ION FLUXES

Abstract In this Appendix, I derive the expressions for the solvent and ion fluxes induced by the Hagen-Poiseuille, electro-osmotic, and diffusio-osmotic flows in the limits $\lambda_D/R \to 0$ and $(\lambda_D/R)/\mathrm{Du} \to 0$. These results are applied in the derivation of the one-dimensional transport equations in Chapter 3.

B.1 Governing Equations and Boundary Conditions

Our starting point in this Appendix will be the rescaled longitudinal momentum equation derived in Chapter 3 (Eq. 3.20),

$$\underbrace{\frac{dP_0}{dx} + \delta n_c \frac{d\phi_0}{dx}}_{\mathrm{Hagen-Poiseuille}} + \underbrace{n_c^{\mathrm{PB}} \frac{d\phi_0}{dx}}_{\mathrm{electro-osmosis}} + \underbrace{\delta c \frac{d \mathrm{ln} c_0}{dx}}_{\mathrm{diffusio-osmosis}} = \frac{1}{\mathrm{Pe}_{\mathrm{osm}}} \frac{\partial_r \left(r \partial_r u_x \right)}{r}, \tag{B.1}$$

along with the local Poisson equation (Chapter 3, Eq. 3.13),

$$\left(\frac{\lambda_D^{\mathrm{ref}}}{R_{\mathrm{min}}} \right)^2 \partial_Z^2 \delta\phi + n_c^{\mathrm{PB}} = 0, \tag{B.2}$$

where I have made the approximation $\partial_r(r\partial_r\delta\phi)/r \approx \partial_Z^2\delta\phi$, valid in the limit of no overlap $(\lambda_D/R \ll 1)$ (Appendix A). In the preceding, $Z \equiv R - r$, where $R(x)$ is the local nanopore radius. Additionally, assuming a local PB equilibrium, we will apply the Boltzmann distributions for the radial deviation in the total ionic concentration δc and the ionic charge density n_c^{PB}:

$$\delta c = c_0 \left(\mathrm{cosh} \delta\phi - 1 \right), \quad \text{and} \tag{B.3}$$

$$n_c^{\mathrm{PB}} = -c_0 \mathrm{sinh} \delta\phi. \tag{B.4}$$

Finally, we will frequently use the first integral of the PB equation (Appendix A, Eq. A.17),

$$\partial_Z \delta\phi = -2 \frac{R_{\mathrm{min}}\sqrt{c_0}}{\lambda_D^{\mathrm{ref}}} \mathrm{sinh} \delta\phi, \tag{B.5}$$

in changing the variable of integration from Z to $\delta\phi$ when calculating the cross-sectionally integrated transport coefficients. Note that the prefactor $R_{\min}\sqrt{c_0}/\lambda_D^{\mathrm{ref}}$ appears in Eq. B.5 but not A.17 because we have rescaled Z by the minimum radius $R_{\min}$ rather than the local Debye length $\lambda_D^{\mathrm{ref}}/\sqrt{c_0}$.

The definitions of the terms appearing in Eqs. B.1 through B.5 are given in Chapter 3. Note that variables are rescaled as in Chapter 3 (Table 3.1).

The forcing terms on the LHS of Eq. B.1 have been segregated into those resulting in the parabolic Hagen-Poiseuille (HP) flow u_{HP} and the plug-like electro-osmotic (EO) and diffusio-osmotic (DO) flows, u_{EO} and u_{DO}, respectively. Owing to the linearity of the Stokes (low Reynolds number) momentum equation, we may solve for each of these flows individually and obtain the total flow as $u_x = u_{\mathrm{HP}} + u_{\mathrm{EO}} + u_{\mathrm{DO}}$.

We neglect hydrodynamic slip such that each of the flows is subject to the no-slip condition:

$$u_{\mathrm{HP}}(x, r = R) = u_{\mathrm{EO}}(x, r = R) = u_{\mathrm{DO}}(x, r = R) = 0. \tag{B.6}$$

Furthermore, axisymmetry requires the shear to vanish at the nanopore centerline:

$$\partial_r u_{\mathrm{HP}}(x, r = 0) = \partial_r u_{\mathrm{EO}}(x, r = 0) = \partial_r u_{\mathrm{DO}}(x, r = 0) = 0. \tag{B.7}$$

B.2 Hagen-Poiseuille and Streaming Fluxes

B.2.1 Flow Profile and Solvent Flux

We begin with the HP flow, satisfying

$$\frac{dP_0}{dx} + \delta n_c \frac{d\phi_0}{dx} = \frac{1}{\mathrm{Pe}_{\mathrm{osm}}} \frac{\partial_r (r \partial_r u_{\mathrm{HP}})}{r}. \tag{B.8}$$

Radial integration of Eq. B.8, subject to the no-slip and axisymmetry conditions given in Eqs. B.6 and B.7, respectively, is straight forward, as the forcing terms on the LHS are radially uniform. The results for the velocity profile u_{HP} and volumetric flux Q_{HP} are

$$\boxed{u_{\mathrm{HP}} = -2\mathcal{L}(R)\left[1 - \left(\frac{r}{R}\right)^2\right]\left(\frac{dP_0}{dx} + \delta n_c \frac{d\phi_0}{dx}\right), \quad \text{and}} \tag{B.9}$$

$$\boxed{\frac{Q_{\mathrm{HP}}}{\pi R^2} = -\mathcal{L}(R)\left(\frac{dP_0}{dx} + \delta n_c \frac{d\phi_0}{dx}\right),} \tag{B.10}$$

where I have introduced the HP hydraulic conductivity $\mathcal{L}(R)$, given by

$$\boxed{\mathcal{L}(R) \equiv \frac{\mathrm{Pe}_{\mathrm{osm}} R^2}{8}.} \tag{B.11}$$

B.2.2 Current and Ion Number Flux

The streaming current is defined as

$$I_{\mathrm{stm}} \equiv \int_0^R 2\pi r \mathrm{d}r u_{\mathrm{HP}} n_c^{\mathrm{PB}}. \tag{B.12}$$

Note that, in order to be consistent with the definition of the streaming current in the literature, I do not include the deviation from electroneutrality δn_c in Eq. B.12; however, this contribution to the current is accounted for in the expression for the total advective current (Eq. B.55).

On the assumption of no overlap ($\lambda_D/R \ll 1$), we may write the cross-sectional integral as $\int_0^R 2\pi r \mathrm{d}r \approx 2\pi R \int_0^\infty dZ$. Furthermore, since the PB ionic charge density is significantly different from zero only within the diffuse layer, we may linearize the HP velocity (Eq. B.9) as

$$u_{\mathrm{HP}} = -4\mathcal{L}\frac{Z}{R}\left(\frac{dP_0}{dx} + \delta n_c \frac{d\phi_0}{dx}\right) + \mathcal{O}\left(\frac{Z}{R}\right)^2. \tag{B.13}$$

From the local Poisson equation (Eq. B.2), we may write the PB ionic charge distribution as $n_c^{\mathrm{PB}} = -(\lambda_D^{\mathrm{ref}}/R_{\min})^2 \partial_Z^2 \delta\phi$. Thus, inserting these results into Eq. B.12, we find

$$\begin{aligned} I_{\mathrm{stm}} &= 2\pi R \times \left(\frac{\lambda_D^{\mathrm{ref}}}{R_{\min}}\right)^2 \times \left[\frac{4\mathcal{L}}{R}\left(\frac{dP_0}{dx} + \delta n_c \frac{d\phi_0}{dx}\right)\right] \times \int_0^\infty \mathrm{d}Z\, Z \partial_Z^2 \delta\phi \\ &= \pi R^2 \mathrm{Pe}_{\mathrm{osm}} \left(\frac{\lambda_D^{\mathrm{ref}}}{R_{\min}}\right)^2 \left(\frac{dP_0}{dx} + \delta n_c \frac{d\phi_0}{dx}\right)\left(Z\partial_Z \delta\phi|_0^\infty - \int_0^\infty \mathrm{d}Z \partial_Z \delta\phi\right) \\ &= \pi R^2 \mathrm{Pe}_{\mathrm{osm}} \left(\frac{\lambda_D^{\mathrm{ref}}}{R_{\min}}\right)^2 \delta\phi_w \left(\frac{dP_0}{dx} + \delta n_c \frac{d\phi_0}{dx}\right). \end{aligned}$$

In the second line I have inserted the definition of the HP hydraulic conductivity (Eq. B.11) and integrated by parts. We thus write for the streaming current

$$\boxed{I_{\mathrm{stm}} = +\mathrm{S}\pi R^2 |\mu_{\mathrm{EO}}| \left(\frac{dP_0}{dx} + \delta n_c \frac{d\phi_0}{dx}\right),} \tag{B.14}$$

where I have anticipated the result for the EO mobility given in Eq. B.23. In Eq. B.14, $\mathrm{S} \equiv \mathrm{sign}(\sigma)$ is the sign of the surface charge density.

The streaming ion number flux is defined as

$$J_{\text{stm}} = \int_0^R 2\pi r \mathrm{d}r u_{\text{HP}} \delta c. \tag{B.15}$$

As in the case of the streaming current, the bulk advective transport $Q_{\text{HP}} c_0$ is segregated from J_{stm} but included in the total advective ion number flux (Eq. B.53). We insert the linearized HP velocity (Eq. B.13) into Eq. B.15 and evaluate the integral in the no overlap limit ($\lambda_D/R \ll 1$):

$$J_{\text{stm}} = \pi R^2 \text{Pe}_{\text{osm}} \left(\frac{dP_0}{dx} + \delta n_c \frac{d\phi_0}{dx} \right) \int_0^\infty \mathrm{d}Z \delta c Z. \tag{B.16}$$

Evaluating the integral by parts, we find

$$J_{\text{stm}} = -\pi R^2 \text{Pe}_{\text{osm}} \left(\frac{dP_0}{dx} + \delta n_c \frac{d\phi_0}{dx} \right) \int_0^\infty \mathrm{d}Z \int_Z^\infty \mathrm{d}Z' \delta c. \tag{B.17}$$

In order to evaluate the integral in Eq. B.17, we apply the Boltzmann distribution for the deviation in the total ionic concentration (B.3) and the first integral of the PB equation (B.5):

$$\int_Z^\infty \mathrm{d}Z' \delta c = \frac{1}{2} \frac{\lambda_D^{\text{ref}} \sqrt{c_0}}{R_{\min}} \int_0^{|\delta\phi|} \mathrm{d}|\delta\phi| \frac{\cosh|\delta\phi| - 1}{\sinh(|\delta\phi|/2)} = 2 \frac{\lambda_D^{\text{ref}} \sqrt{c_0}}{R_{\min}} \left[\cosh\left(\frac{|\delta\phi|}{2} \right) - 1 \right]$$

$$\begin{aligned} \Longrightarrow \int_0^\infty \mathrm{d}Z \int_Z^\infty \mathrm{d}Z' \delta c &= 2 \frac{\lambda_D^{\text{ref}} \sqrt{c_0}}{R_{\min}} \int_0^\infty \mathrm{d}Z \left[\cosh\left(\frac{|\delta\phi|}{2} \right) - 1 \right] \\ &= \left(\frac{\lambda_D^{\text{ref}}}{R_{\min}} \right)^2 \int_0^{|\delta\phi_w|} \mathrm{d}|\delta\phi| \frac{\cosh(|\delta\phi|/2) - 1}{\sinh(|\delta\phi|/2)} \\ &= \left(\frac{\lambda_D^{\text{ref}}}{R_{\min}} \right)^2 4\ln\left[\cosh\left(\frac{|\delta\phi_w|}{4} \right) \right]. \end{aligned}$$

Inserting this result into Eq. B.17 and anticipating the expression for the DO mobility μ_{DO} given in Eq. B.38, we find

$$\boxed{J_{\text{stm}} = -\pi R^2 \mu_{\text{DO}} \left(\frac{dP_0}{dx} + \delta n_c \frac{d\phi_0}{dx} \right).} \tag{B.18}$$

B.3 Electro-osmosis

B.3.1 Flow Profile and Solvent Flux

We next consider the EO flow, which verifies

$$n_c^{\text{PB}} \frac{d\phi_0}{dx} = \frac{\partial_r (r \partial_r u_{\text{EO}})}{r}, \tag{B.19}$$

along with the no-slip and axisymmetry conditions given in Eqs. B.6 and B.7, respectively. We first use Eq. B.2 to recast Eq. B.19 in a form that is easily integrated radially by eliminating the PB ionic charge density n_c^{PB} in favor of the radial deviation in the electrostatic potential $\delta\phi$:

$$\partial_r \left[r\partial_r \left(u_{\mathrm{EO}} + \frac{1}{2}\kappa \frac{d\phi_0}{dx}\delta\phi \right) \right] = 0. \tag{B.20}$$

where we have defined

$$\boxed{\kappa \equiv 2\mathrm{Pe}_{\mathrm{osm}} \left(\frac{\lambda_D^{\mathrm{ref}}}{R_{\min}} \right)^2 \equiv 2\frac{\epsilon_r \epsilon_0}{\eta D} \left(\frac{k_B T}{e} \right)^2 .} \tag{B.21}$$

In the second equivalence I have applied the definitions of $\mathrm{Pe}_{\mathrm{osm}}$ and λ_D^{ref} given in Chapter 3 (Eq. 3.16 and the text following Eq. 3.13). We note that κ is a material property of the solvent and solute and approximately 0.45 for potassium chloride (KCl) in water at room temperature. The transport equations derived in Chapter 3 (Eqs. 3.24 and 3.25) indicate that κ is the ratio of the electro-osmotic/diffusio-osmotic current to the surface electrophoretic/diffusive current. Radial integration of Eq. B.21 is trivial and gives

$$\boxed{u_{\mathrm{EO}} = +\mathrm{S}|\mu_{\mathrm{EO}}| \left(1 - \frac{|\delta\phi|}{|\delta\phi_w|} \right) \frac{d\phi_0}{dx},} \tag{B.22}$$

where I have introduced the EO mobility μ_{EO}, rescaled by the electrophoretic mobility $\mu_{\mathrm{EP}} \equiv eD/k_BT$ and given by

$$\mu_{\mathrm{EO}} \equiv -\mathrm{S}\frac{\kappa}{2}|\delta\phi_w| \equiv \frac{1}{\mu_{\mathrm{EP}}} \frac{\epsilon_r \epsilon_0}{\eta} \left(-\frac{k_B T}{e}\delta\phi_w \right) = -\mathrm{S}\kappa \ln \left[\frac{\mathrm{Du}_{\mathrm{ref}}}{(\lambda_D^{\mathrm{ref}}/R_{\min})\sqrt{c_0}} \right]. \tag{B.23}$$

In the third equality I have applied the asymptotic expression for $|\delta\phi_w|$ valid in the limit $(\lambda_D/R)/\mathrm{Du} \to 0$ (Appendix A, Eq. A.23). The factor $-\mathrm{S}$ corresponds to the fact that a negative surface charge results in the accumulation of an excess of positive counterions in the diffuse layer, and the motion of these ions under an applied electric field induces a flow in the same direction and along the direction of the electric field (and *vice versa*). The contribution of $\sqrt{c_0}$ in $\ln[\mathrm{Du}^{\mathrm{ref}}/(\lambda_D^{\mathrm{ref}}/R_{\min})\sqrt{c_0}]$ $= \ln[\mathrm{Du}^{\mathrm{ref}}/(\lambda_D^{\mathrm{ref}}/R_{\min})] - \ln(c_0)/2$ is typically negligible in the limit we are considering, and so I will approximate μ_{EO} as a constant. This is consistent with what is typically done in the literature.

In the limit of no overlap ($\lambda_D/R \ll 1$), $\delta\phi = 0$ outside of the (thin) diffuse layer and thus over the bulk of the cross-section. From Eq. B.22, we see that this corresponds to a uniform EO velocity denoted u_{EO}^{∞} and given by

$$\boxed{u_{\mathrm{EO}}^{\infty} = +\mathrm{S}|\mu_{\mathrm{EO}}| \frac{d\phi_0}{dx}.} \tag{B.24}$$

This result, along with the expression given in Eq. B.23 for the EO mobility in terms of the wall potential, is known as the Smoluchowski equation. Overall, we see that the nonzero ionic charge in the diffuse layer results in a hydrodynamic body force that is balanced by shear in this region. The result is a uniform plug flow over the bulk of the cross-section with a velocity given by Eq. B.24.

Radial integration of Eq. B.22 gives

$$Q_{\mathrm{EO}} = \pi R^2 u_{\mathrm{EO}}^{\infty} - \mathrm{S}|\mu_{\mathrm{EO}}| \frac{d\phi_0}{dx} \int_0^R 2\pi r \mathrm{d}r \frac{\delta\phi}{\delta\phi_w}, \tag{B.25}$$

and in the limit of no overlap ($\lambda_D/R \ll 1$), the integral of $\delta\phi$ may be evaluated as

$$\int_0^R 2\pi r \mathrm{d}r \delta\phi = 2\pi R \int_0^{\infty} dZ \delta\phi. \tag{B.26}$$

Inserting Eq. B.5 into Eq. B.26, we obtain

$$\begin{aligned} \int_0^R 2\pi r \mathrm{d}r \delta\phi &= 2\pi R \times 2 \frac{\lambda_D^{\mathrm{ref}}}{R_{\mathrm{min}}\sqrt{c_0}} \int_0^{\delta\phi_w/2} \mathrm{d}u\, u \,\mathrm{csch} u \\ &\xrightarrow[\frac{\lambda_D/R}{\mathrm{Du}} \to 0]{} 4\pi R \frac{\lambda_D^{\mathrm{ref}}}{R_{\mathrm{min}}\sqrt{c_0}} \int_0^{\mathrm{S}\infty} \mathrm{d}u\, u \,\mathrm{csch} u = \mathrm{S}\pi^3 R \frac{\lambda_D^{\mathrm{ref}}}{R_{\mathrm{min}}\sqrt{c_0}}. \end{aligned}$$

Dividing by the asymptotic value of $\delta\phi_w$ (Appendix A, Eq. A.23), we find

$$\int_0^R 2\pi r \mathrm{d}r \frac{\delta\phi}{\delta\phi_w} = -\frac{\pi^3 R}{2} \mathrm{Du}_{\mathrm{ref}} \frac{\frac{(\lambda_D^{\mathrm{ref}}/R_{\mathrm{min}})\sqrt{c_0}}{\mathrm{Du}_{\mathrm{ref}}}}{\ln\left[\frac{(\lambda_D^{\mathrm{ref}}/R_{\mathrm{min}})\sqrt{c_0}}{\mathrm{Du}_{\mathrm{ref}}}\right]} \xrightarrow[\frac{\lambda_D/R}{\mathrm{Du}} \to 0]{} 0.$$

Thus, inserting this result into Eq. B.25, we find

$$\boxed{\frac{Q_{\mathrm{EO}}}{\pi R^2} = u_{\mathrm{EO}}^{\infty} = +\mathrm{S}|\mu_{\mathrm{EO}}| \frac{d\phi_0}{dx},} \tag{B.27}$$

consistent with the fact that $u_{\mathrm{EO}} = u_{\mathrm{EO}}^{\infty}$ everywhere on the cross-section except in the negligibly thin diffuse layer.

B.3.2 Current and Ion Number Flux

I define the EO current as

$$I_{\mathrm{EO}} \equiv \int_0^R 2\pi r \mathrm{d}r u_{\mathrm{EO}} n_c^{\mathrm{PB}}. \tag{B.28}$$

Inserting Eq. B.22 and the Boltzmann distribution for the ionic charge (Eq. B.4) into Eq. B.28, we have

$$I_{\mathrm{EO}} = -\mu_{\mathrm{EO}} \frac{d\phi_0}{dx} \int_0^R 2\pi r \mathrm{d}r \left(1 - \frac{|\delta\phi|}{|\delta\phi_w|}\right) n_c^{\mathrm{PB}} = -|\mu_{\mathrm{EO}}| \frac{d\phi_0}{dx} 2\pi R c_0 \int_0^\infty \mathrm{d}Z \left(1 - \frac{|\delta\phi|}{|\delta\phi_w|}\right) \mathrm{sinh}|\delta\phi|, \tag{B.29}$$

where in the second equality we have recognized that the signs of the EO mobility and the PB ionic charge density cancel each other and made use of the no overlap limit $\lambda_D/R \ll 1$ to simplify the integral. We insert Eq. B.5 to find

$$\begin{aligned} I_{\mathrm{EO}} &= -|\mu_{\mathrm{EO}}| \frac{d\phi_0}{dx} \pi R \frac{\lambda_D^{\mathrm{ref}} \sqrt{c_0}}{R_{\mathrm{min}}} \int_0^{|\delta\phi_w|} \mathrm{d}|\delta\phi_w| \left(1 - \frac{|\delta\phi|}{|\delta\phi_w|}\right) \frac{\mathrm{sinh}|\delta\phi|}{\mathrm{sinh}(|\delta\phi_w|/2)} \\ &= -2\pi R \times \kappa \times \left[4 \frac{\lambda_D^{\mathrm{ref}} \sqrt{c_0}}{R_{\mathrm{min}}} \mathrm{sinh}^2 \left(\frac{|\delta\phi_w|}{4}\right)\right] \times \frac{d\phi_0}{dx}. \end{aligned} \tag{B.30}$$

The term in square brackets may be evaluated asymptotically using the fact that

$$|\delta\phi_w| \sim 2 \mathrm{ln} \left[\frac{\mathrm{Du}_{\mathrm{ref}} |\sigma|}{(\lambda_D^{\mathrm{ref}}/R_{\mathrm{min}}) \sqrt{c_0}}\right]$$

in the limit $\mathrm{Du}/(\lambda_D/R) \to \infty$ (Appendix A, Eq. A.23):

$$\mathrm{sinh}^2 \left(\frac{|\delta\phi_w|}{4}\right) \sim \frac{e^{|\delta\phi_w|/2}}{4} \sim \frac{1}{4} \frac{\mathrm{Du}_{\mathrm{ref}} |\sigma|}{(\lambda_D^{\mathrm{ref}}/R_{\mathrm{min}}) \sqrt{c_0}}$$

$$\Longrightarrow 4 \frac{\lambda_D^{\mathrm{ref}} \sqrt{c_0}}{R_{\mathrm{min}}} \mathrm{sinh}^2 \left(\frac{|\delta\phi_w|}{4}\right) \sim \mathrm{Du}_{\mathrm{ref}} |\sigma|.$$

With Eq. B.23, we thus find for the EO current

$$\boxed{I_{\mathrm{EO}} = -2\pi R \mathrm{Du}_{\mathrm{ref}} |\sigma| \kappa \frac{d\phi_0}{dx}.} \tag{B.31}$$

The EO ionic number flux is defined as

$$J_{\mathrm{EO}} \equiv \int_0^R 2\pi r \mathrm{d}r u_{\mathrm{EO}} \delta c. \tag{B.32}$$

Following the same procedure as above for the EO current, we insert the expression for the EO velocity (Eq. B.22), the Boltzmann distribution for the deviation in the total ionic concentration (Eq. B.3), and the first integral of the PB equation (Eq. B.5) and apply the no overlap limit to obtain

$$\begin{aligned} J_{\mathrm{EO}} &= +\mathrm{S} |\mu_{\mathrm{EO}}| \frac{d\phi_0}{dx} \pi R c_0 \frac{\lambda_D^{\mathrm{ref}} \sqrt{c_0}}{R_{\mathrm{min}}} \int_0^{|\delta\phi_w|} \mathrm{d}|\delta\phi| \left(1 - \frac{|\delta\phi|}{|\delta\phi_w|}\right) \frac{\mathrm{cosh}|\delta\phi| - 1}{\mathrm{sinh}(|\delta\phi|/2)} \\ &= +\mathrm{S} 2\pi R \times \kappa \times \left\{\frac{\lambda_D^{\mathrm{ref}} \sqrt{c_0}}{R_{\mathrm{min}}} \left[2 \mathrm{sinh}(|\delta\phi_w|/2) - |\delta\phi_w|\right]\right\} \times \frac{d\phi_0}{dx}. \end{aligned} \tag{B.33}$$

The term in curly brackets may be evaluated in the limit $\mathrm{Du}/(\lambda_D/R) \to \infty$ using the fact that (Appendix A, Eq. A.23)

$$|\delta\phi_w| \sim 2\mathrm{ln}\left[\frac{\mathrm{Du}_{\mathrm{ref}}|\sigma|}{(\lambda_D^{\mathrm{ref}}/R_{\mathrm{min}})\sqrt{c_0}}\right]$$

$$\Longrightarrow 2\mathrm{sinh}\left(\frac{|\delta\phi_w|}{2}\right) \sim \exp\left(\frac{|\delta\phi_w|}{2}\right),$$

which indicates that this term tends to $\mathrm{Du}_{\mathrm{ref}}|\sigma|$. Thus,

$$\boxed{J_{\mathrm{EO}} = +\mathrm{S}2\pi R\mathrm{Du}_{\mathrm{ref}}|\sigma|\kappa\frac{d\phi_0}{dx}.} \tag{B.34}$$

B.4 Diffusio-osmosis

B.4.1 Flow Profile and Solvent Flux

Finally, we consider the DO flow, which satisfies

$$\delta c\frac{d\mathrm{ln}c_0}{dx} = \frac{1}{\mathrm{Pe}_{\mathrm{osm}}}\frac{\partial_r(r\partial_r u_{\mathrm{DO}})}{r} = \frac{1}{\mathrm{Pe}_{\mathrm{osm}}}\partial_Z^2 u_{\mathrm{DO}}, \tag{B.35}$$

subject to the no-slip and axisymmetry conditions given in Eqs. B.6 and B.7. In the second equality in Eq. B.35 we have neglected the portion of the Laplacian associated with the curvature of the nanopore wall. This is justified because the region of nonzero shear is confined to the diffuse layer, and I assume $\lambda_D/R \ll 1$.

We integrate Eq. B.35 twice to obtain

$$u_{\mathrm{DO}} = -\mathrm{Pe}_{\mathrm{osm}}\frac{d\mathrm{ln}c_0}{dx}\int_0^Z \mathrm{d}Z'\int_{Z'}^{\infty}\mathrm{d}Z''\delta c. \tag{B.36}$$

The indefinite integral on the RHS may be evaluated in the same manner as the corresponding definite integral appearing in Eq. B.17. The result is

$$\int_0^Z \mathrm{d}Z'\int_{Z'}^{\infty}\mathrm{d}Z''\delta c = 4\left(\frac{\lambda_D^{\mathrm{ref}}}{R_{\mathrm{min}}}\right)^2\left\{\ln\left[\cosh\left(\frac{\delta\phi_w}{4}\right)\right] - \ln\left[\cosh\left(\frac{\delta\phi}{4}\right)\right]\right\}.$$

Thus, inserting this result into Eq. B.36, we obtain

$$\boxed{u_{\mathrm{DO}} = -\mu_{\mathrm{DO}}\left\{1 - \frac{\ln\left[\cosh(|\delta\phi|/4)\right]}{\ln\left[\cosh(|\delta\phi_w|/4)\right]}\right\}\frac{d\mathrm{ln}c_0}{dx},} \tag{B.37}$$

where I have introduced μ_{DO}, the DO mobility normalized by the diffusion coefficient:

$$\begin{aligned}\mu_{\mathrm{DO}} &\equiv \frac{\kappa}{2} 4\ln\left[\cosh\left(\frac{|\delta\phi_w|}{4}\right)\right] \equiv \frac{1}{D}\frac{\epsilon_r\epsilon_0}{\eta}\left(\frac{k_BT}{e}\right)^2 4\ln\left[\cosh\left(\frac{|\delta\phi_w|}{4}\right)\right] \\ &\xrightarrow[\frac{\lambda_D/R}{\mathrm{Du}}\to 0]{} \frac{1}{D}\frac{\epsilon_r\epsilon_0}{\eta}\frac{k_BT}{e}\left(\frac{k_BT}{e}|\delta\phi_w|\right).\end{aligned} \tag{B.38}$$

The uniform DO velocity far outside of the diffuse layer is given by

$$\boxed{u_{\mathrm{DO}}^{\infty} = -\mu_{\mathrm{DO}}\frac{d\ln c_0}{dx}.} \tag{B.39}$$

The excess concentration in the diffuse layer induces an excess osmotic pressure, and this pressure varies along the length of the nanopore in the presence of an applied concentration differential (or a locally variable centerline concentration). This additional pressure gradient is balanced by a shear. As for the EO flow, outside of the diffuse layer the velocity is uniform, and the result in the limit of no overlap ($\lambda_D/R \ll 1$) is a plug-like flow with a uniform value over the cross-section given by Eq. B.39.

Radial integration of Eq. B.37 gives

$$Q_{\mathrm{DO}} = \pi R^2 u_{\mathrm{DO}}^{\infty} + \mu_{\mathrm{DO}}\frac{d\ln c_0}{dx}\int_0^R 2\pi r\mathrm{d}r\frac{\ln\left[\cosh(\delta\phi/4)\right]}{\ln\left[\cosh(\delta\phi_w/4)\right]}. \tag{B.40}$$

The denominator of the integral in Eq. B.40 diverges as $\ln[\mathrm{Du}_{\mathrm{ref}}|\sigma|/(\lambda_D^{\mathrm{ref}}/R_{\min})\sqrt{c_0}]$ as $\mathrm{Du}/(\lambda_D/R) \to \infty$, while the integral of the numerator can be evaluated as

$$\begin{aligned}\int_0^R 2\pi r\mathrm{d}r\ln\left[\cosh\left(\frac{\delta\phi}{4}\right)\right] &= 2\pi R\int_0^\infty \mathrm{d}Z\ln\left[\cosh\left(\frac{\delta\phi}{4}\right)\right] \\ &= \pi R\frac{\lambda_D^{\mathrm{ref}}}{R_{\min}\sqrt{c_0}}\int_0^{|\delta\phi_w|}\mathrm{d}\delta\phi\frac{\ln\left[\cosh\left(\delta\phi/R\right)\right]}{\sinh(\delta\phi/2)} \xrightarrow[\frac{\lambda_D/R}{\mathrm{Du}}\to 0]{} 4\pi R\frac{\lambda_D^{\mathrm{ref}}}{R_{\min}\sqrt{c_0}}\int_0^\infty \mathrm{d}u\frac{\ln(\cosh u)}{\sinh(2u)} \\ &= \frac{\pi^3 R}{12}\frac{\lambda_D^{\mathrm{ref}}}{R_{\min}\sqrt{c_0}}.\end{aligned}$$

We thus find

$$\int_0^R 2\pi r\mathrm{d}r\frac{\ln\left[\cosh(\delta\phi/4)\right]}{\ln\left[\cosh(\delta\phi_w/4)\right]} = -\frac{\pi^3 R}{6}\mathrm{Du}_{\mathrm{ref}}\frac{\frac{(\lambda_D^{\mathrm{ref}}/R_{\min})\sqrt{c_0}}{\mathrm{Du}_{\mathrm{ref}}}}{\ln\left[\frac{(\lambda_D^{\mathrm{ref}}/R_{\min})\sqrt{c_0}}{\mathrm{Du}_{\mathrm{ref}}}\right]} \xrightarrow[\frac{\lambda_D/R}{\mathrm{Du}}\to 0]{} 0.$$

Inserting this result into Eq. B.40, we obtain

$$\boxed{\frac{Q_{\mathrm{DO}}}{\pi R^2} = u_{\mathrm{DO}}^{\infty} = -\mu_{\mathrm{DO}}\frac{d\ln c_0}{dx}.} \tag{B.41}$$

B.4.2 Current and Ion Number Flux

The DO current is defined as

$$I_{\mathrm{DO}} \equiv \int_0^R 2\pi r \mathrm{d}r u_{\mathrm{DO}} n_c^{\mathrm{PB}}. \tag{B.42}$$

We note from Eqs. B.21, B.37, and B.38 that the DO velocity may be written as

$$u_{\mathrm{DO}} = -2\kappa \ln \left[\frac{\cosh(|\delta\phi_w|/4)}{\cosh(|\delta\phi|/4)} \right] \frac{d\ln c_0}{dx}. \tag{B.43}$$

Inserting this expression for u_{DO} and the Boltzmann distribution for the ionic charge density (Eq. B.3) into Eq. B.42 and evaluating the integral in the limit of no overlap ($\lambda_D/R \ll 1$), we find (with Eq. B.5)

$$I_{\mathrm{DO}} = \mathrm{S} 2\pi R\kappa \frac{d\ln c_0}{dx} \frac{\lambda_D^{\mathrm{ref}} \sqrt{c_0}}{R_{\min}} \int_0^{|\delta\phi_w|} \mathrm{d}|\delta\phi| \ln \left[\frac{\cosh(|\delta\phi_w|/4)}{\cosh(|\delta\phi|/4)} \right] \frac{\sinh|\delta\phi|}{\sinh(|\delta\phi|/2)}. \tag{B.44}$$

Evaluating the integral, we find, in the limit $(\lambda_D/R)/\mathrm{Du} \to 0$,

$$\boxed{I_{\mathrm{DO}} = +\mathrm{S} 2\pi R \mathrm{Du}_{\mathrm{ref}} |\sigma| \kappa \frac{d\ln c_0}{dx}.} \tag{B.45}$$

Adding this result to Eq. B.31, we find

$$\boxed{\frac{I_{\mathrm{DO}} + I_{\mathrm{EO}}}{\pi R^2} = \mathrm{S} \frac{2\mathrm{Du}_{\mathrm{ref}} |\sigma|}{R} \kappa \frac{d\mu_{\mathrm{count}}}{dx}.} \tag{B.46}$$

The DO ion number flux is defined as

$$J_{\mathrm{DO}} \equiv \int_0^R 2\pi r \mathrm{d}r u_{\mathrm{DO}} \delta c. \tag{B.47}$$

Application of the same procedure used above results in

$$J_{\mathrm{DO}} = -2\pi R\kappa \frac{d\ln c_0}{dx} \frac{\lambda_D^{\mathrm{ref}} \sqrt{c_0}}{R_{\min}} \int_0^{|\delta\phi_w|} \mathrm{d}|\delta\phi| \ln \left[\frac{\cosh(|\delta\phi_w|/4)}{\cosh(|\delta\phi|/4)} \right] \frac{\cosh|\delta\phi| - 1}{\sinh(|\delta\phi|/2)}. \tag{B.48}$$

Evaluation of the integral in the limit $(\lambda_D/R)/\mathrm{Du} \to 0$ gives

$$\boxed{J_{\mathrm{DO}} = -2\pi R \mathrm{Du}_{\mathrm{ref}} |\sigma| \kappa \frac{d\ln c_0}{dx}.} \tag{B.49}$$

The sum of Eqs. B.34 and B.49 is

$$\boxed{\frac{J_{\mathrm{DO}} + J_{\mathrm{EO}}}{\pi R^2} = -\frac{2\mathrm{Du}_{\mathrm{ref}} |\sigma|}{R} \kappa \frac{d\mu_{\mathrm{count}}}{dx}.} \tag{B.50}$$

B.5 Summary of Results

I compile the key results of this Appendix. Summing Eqs. B.10, B.27, and B.41, we find for the total volumetric solvent flux

$$\boxed{\frac{Q}{\pi R^2} = -\mathcal{L}\left(\frac{dP_0}{dx} + \delta n_c \frac{d\phi_0}{dx}\right) - \mu_{\mathrm{DO}} \frac{d\mathrm{ln}c_0}{dx} + \mathrm{S}|\mu_{\mathrm{EO}}| \frac{d\phi_0}{dx},} \tag{B.51}$$

where the HP hydraulic conductivity $\mathcal{L}$ is given by

$$\boxed{\mathcal{L}(R) \equiv \frac{\mathrm{Pe}_{\mathrm{osm}} R^2}{8}.} \tag{B.52}$$

Similarly, we sum Eqs. B.18 and B.50, including the additional contribution of bulk advection Qc_0, to find for the total advective ion number flux

$$\boxed{\frac{J_{\mathrm{adv}}}{\pi R^2} = -\frac{2\mathrm{Du}_{\mathrm{ref}}|\sigma|}{R} \kappa \frac{d\mu_{\mathrm{count}}}{dx} - \mu_{\mathrm{DO}} \left(\frac{dP_0}{dx} + \delta n_c \frac{d\phi_0}{dx}\right) + \frac{Q}{\pi R^2} c_0,} \tag{B.53}$$

where κ is the ratio of the electro-/diffusio-osmotic ion transport to the electrophoretic/diffusive transport and is given by

$$\boxed{\kappa \equiv 2 \frac{\epsilon_r \epsilon_0}{\eta D} \left(\frac{k_B T}{e}\right)^2 \approx 0.45 \quad (\mathrm{KCl\,in\,water,}\ 293\,\mathrm{K}).} \tag{B.54}$$

Finally, we sum Eqs. B.14 and B.46 and the additional advective flux associated with the deviation from electroneutrality $Q\delta n_c$ to find for the total advective current

$$\boxed{\frac{I_{\mathrm{adv}}}{\pi R^2} = \mathrm{S} \frac{2\mathrm{Du}_{\mathrm{ref}}|\sigma|}{R} \kappa \frac{d\mu_{\mathrm{count}}}{dx} + \mathrm{S}|\mu_{\mathrm{EO}}| \left(\frac{dP_0}{dx} + \delta n_c \frac{d\phi_0}{dx}\right) + \frac{Q}{\pi R^2} \delta n_c.} \tag{B.55}$$

Appendix C

SUPPLEMENTARY MATERIAL FOR CHAPTER 4: MOLECULAR STREAMING AND ITS VOLTAGE CONTROL IN ÅNGSTRÖM-SCALE CHANNELS

Abstract In this Appendix, I present supplementary material pertaining to the experiments and theory presented in Chapter 4: Molecular Streaming and its Voltage Control in Ångström-Scale Channels.

C.1 Experiments

C.1.1 Streaming current measurements

Figs. C.2a-c show the streaming current measurements as a function of the applied pressure for a sample containing no channels (varying from 0 to 250 mbar). The pressure is applied via a pressure pump (AF1, Elveflow), and ΔV is controlled via a patch-clamp amplifier (Axopatch 200B, Molecular Devices) with the ground electrode on the top side. Note that a positive value of ΔP corresponds to a pressure applied through the hole in the SiN substrate, and a positive ΔV corresponds to an electric field directed into this hole. For a sample containing no channels, we did not detect any significant current. Figs. C.1d-f compare the streaming current measured for the control sample and a graphite device containing 200 channels. In the case of graphite channels, the streaming current is four orders-of-magnitude larger than the noise measured in the control sample.

To investigate the pressure dependence of the streaming current, we performed streaming current measurements applying the pressure in successive increments on each side of the membrane. The inversion of the pressure gradient fully reverts the streaming current sign as presented in Extended Data Fig. C.2; this confirms the linear dependence of the streaming current on the mechanical forcing.

The molecular streaming current I_{str} as a function of the pressure gradient $\Delta P/L$ is shown

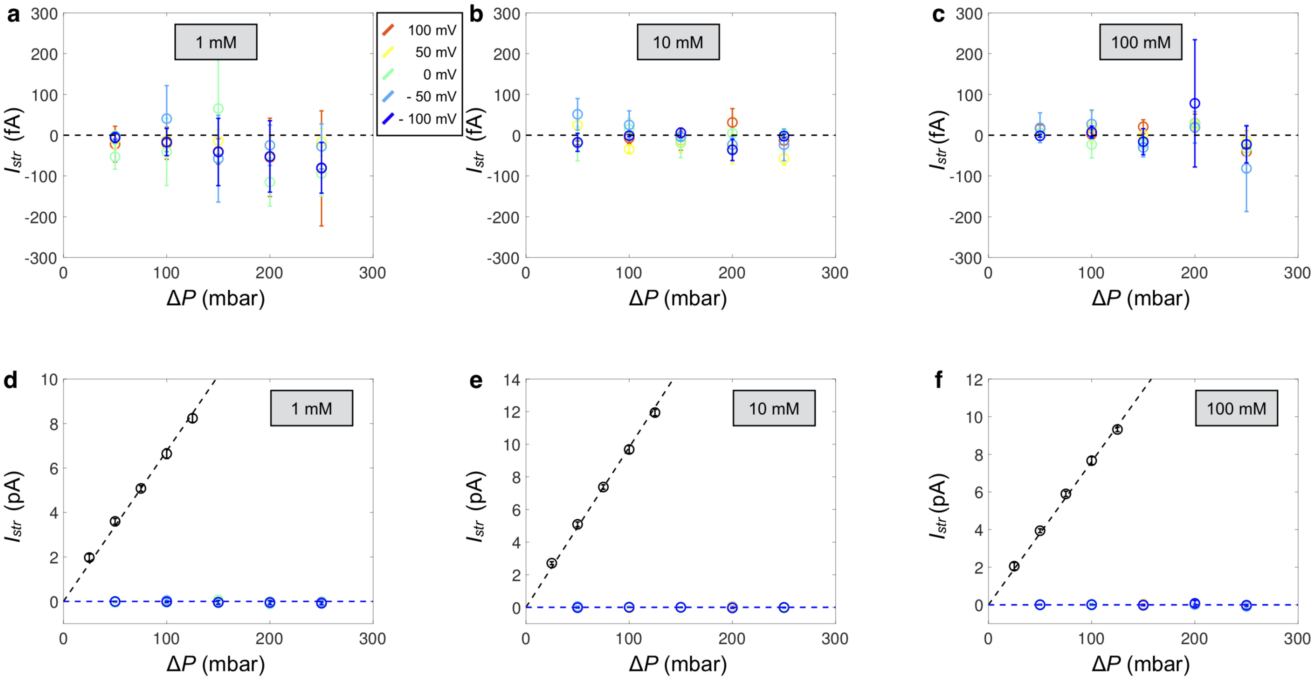

Figure C.1: Control sample test. a-c) Streaming current measured in a control sample without any channels as a function of the pressure. We varied the applied voltage from −100 to +100 mV (color coded from blue to red). d-f) Same measurements as for panels a-c (colored symbols) but compared with the streaming current measured with 200 graphite channels (black symbols). The streaming current is around 4 orders-of-magnitude larger, which confirms that channels remain mechanically stable and are not delaminated under pressure.

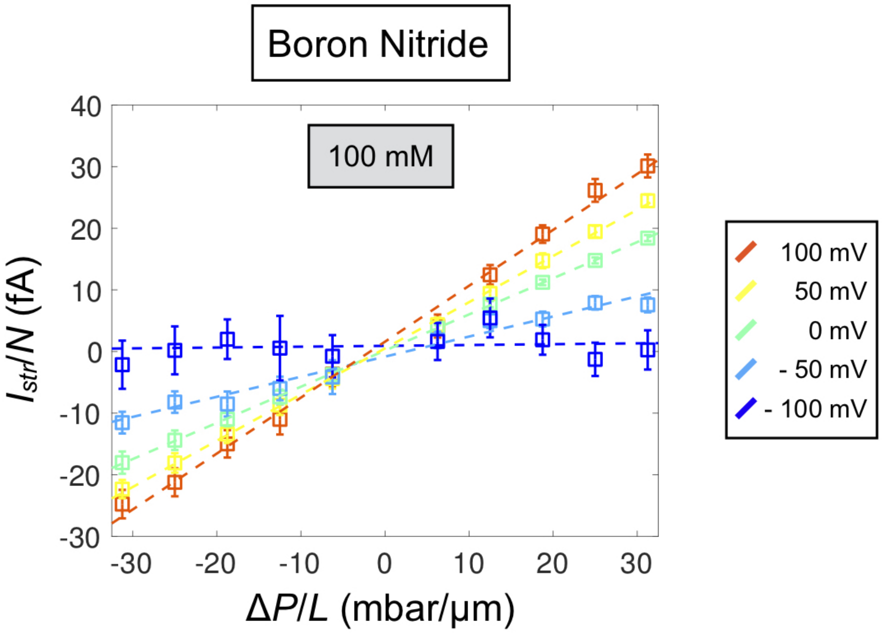

Figure C.2: Gated pressure-driven current. Streaming current per channel plotted as a function of $\Delta P/L$ with ΔV ranging between -100 and $+100$ mV (color coded from blue to red with increasing voltage difference), KCl concentration of 100 mM and hBN channels of length $L = 16 \pm 0.1$ μm.

in Fig. C.3 for both graphite and hBN devices and for different KCl concentrations and applied voltages. The streaming current varies linearly with the driving force $\Delta P/L$.

C.2 Theory

C.2.1 Geometric Sensitivity

The effect of the reservoir geometry on the numerical model predictions is illustrated in Fig. C.4. In this plot I show the influence of both the relative and absolute magnitudes of Γ_ℓ and Γ_r on the predicted $\mu(\Delta V)$ responses for both the low-friction (graphite-like) and high-friction (hBN-like) configurations. Between the blue and yellow curves, I vary the absolute magnitudes of Γ_ℓ and Γ_r by an order of magnitude while keeping the ratio Γ_ℓ/Γ_r fixed. We see that the magnitudes of Γ_ℓ and Γ_r have no influence on the qualitative (linear or quadratic) behavior of the mobility curves and have only a slight quantitative influence on the graphite configuration. I also vary the ratio Γ_ℓ/Γ_r (red and purple versus blue and yellow curves). In the graphite response, we see that the minima in the red and purple ($\Gamma_\ell/\Gamma_r = 1/8$) and the blue and yellow ($\Gamma_\ell/\Gamma_r = 1/4$) curves are

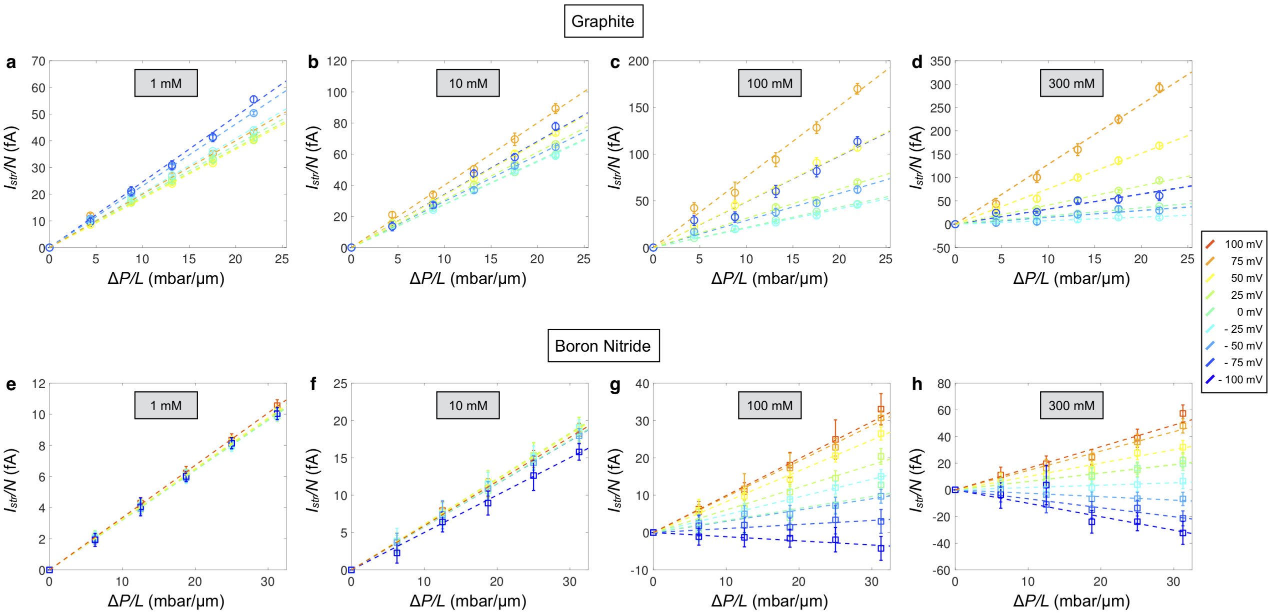

Figure C.3: Gated pressure-driven current and material dependency. Streaming current per channel plotted as a function of $\Delta P/L$ for a KCl concentration varying from 1 to 300 mM and with ΔV ranging between -100 and $+100$ mV (color coded from blue to red with increasing voltage difference). a-d) The channel length L for graphite is 5.7 ± 0.1 μm. e-h) For hBN, $L = 16 \pm 0.1$ μm.

coincident, even as we vary the absolute magnitudes of Γ_ℓ and Γ_r by an order of magnitude. This indicates that in the model, for fixed values of the friction coefficients, the asymmetry determines the location of the minimum mobility in graphite. Likewise, in the hBN curves, we see that the asymmetry is the only geometric characteristic that determines the slope of the $\mu(\Delta V)$ curve.

As a final note on the model geometry, a one-dimensional model of the type that I have applied here is strictly valid only if the slope verifies $|dh/dx| \ll 1$. Formally, this condition is not satisfied deep in the reservoirs. However, variations of the various profiles in the reservoir occur over length scales that are found to be at most of the order of the channel length L so that $|dh/dx| < \Gamma h_0/L$, which remains very small. Note furthermore that reservoirs are included merely to qualitatively capture the influence of (1) the device asymmetry and (2) the entrance/exit effects associated with the abrupt change in anion mobility at the entrance and exit of the slit. Previous work using this approach to include the reservoirs within a one-dimensional PNPS model was successful in capturing the nontrivial qualitative behavior of the ionic current under applied pressures and voltages (Chapter 3).

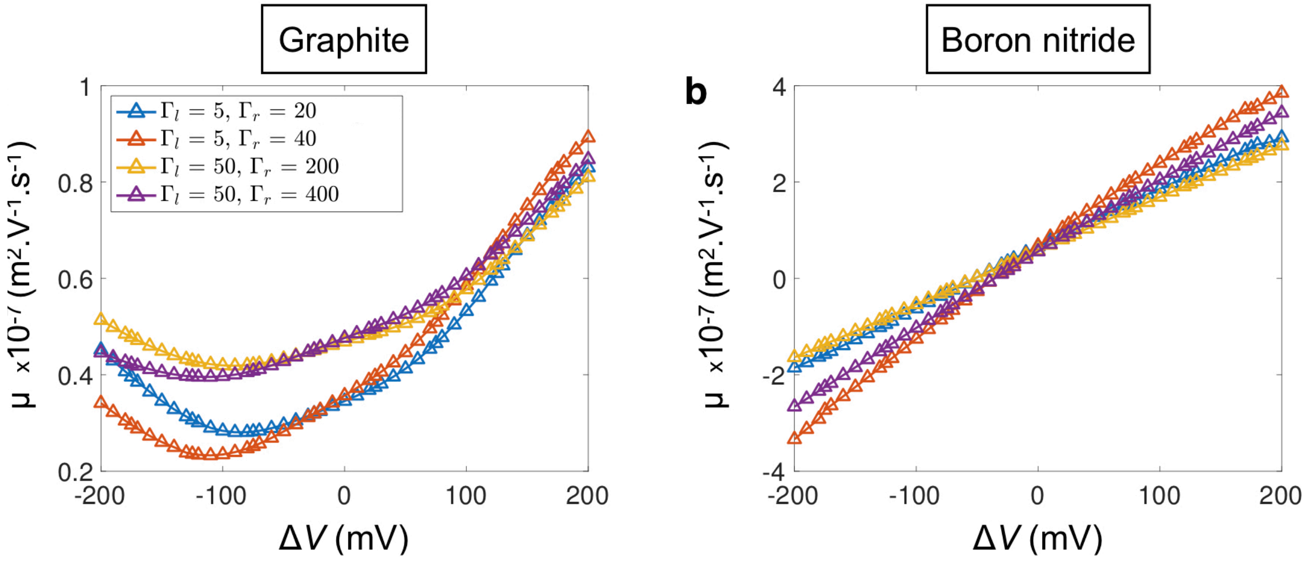

Figure C.4: Effect of the asymmetry of the system. The plots show $\mu(\Delta V)$ versus ΔV as a function of asymmetry. a) Low-friction (graphite-like) behavior. In this plot, we take $c = 100$ mM, $\alpha_+ = 1$, $\alpha_- = 0.7$, $\mu_+ = \mu_+^{\text{bulk}}$, $\mu_- = 0.5\mu_-^{\text{bulk}}$, and $\lambda_0/h_0 = 10^{11}$ kg m^{-3} s^{-1}, as in the main text, while varying the geometric parameters Γ_ℓ and Γ_r, as indicated in the legend. b) High-friction (hBN-like) behavior, $c = 100$ mM, $\alpha_+ = 0.01$, $\alpha_- = 0.01$, $\mu_+ = \mu_+^{\text{bulk}}$, $\mu_- = 0.5\mu_-^{\text{bulk}}$, and $\lambda_0/h_0 = 10^{13}$ kg m^{-3} s^{-1}

C.2.2 Transition Behavior

In Figs. C.5a-c, I show the influence of the friction parameters for high, low, and intermediate friction on the gated mobilities, and in Figs. C.5d-f I show the relative pressure dependence of the normalized potential $e\Delta\phi/k_BT$ along the channel axis. Here, $\Delta\phi$ is defined as the potential variation with an applied pressure $\Delta\phi \equiv \phi\,(\Delta V,\, \Delta P = 30\,\text{mbar}\,\mu\text{m}^{-1}) - \phi\,(\Delta V, \Delta P = 0)$. The modification of the electrostatic potential, and hence the electric field, under coupled pressure-voltage forcing contributes–along with the modification of the concentration field (Fig. 4.8)–to the modification of the electrophoretic current under an applied pressure. Figs. 4.8 and C.5 illustrate the complex interplay of competing interactions that contribute to the surprisingly simple linear streaming response observed in the model.

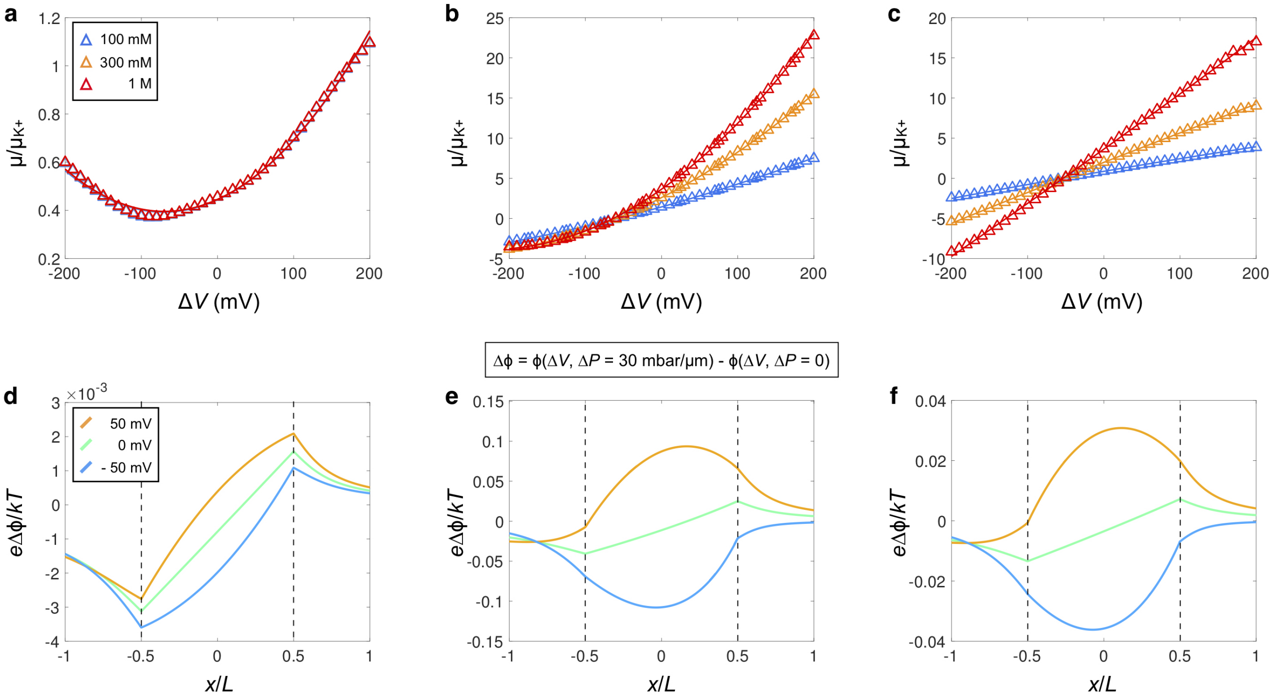

g

	a, d - Low friction (C) c = (100, 300, 1000)mM	**b, e - Intermediate friction** c = (100, 300, 1000)mM	**c, f - High friction (BN)** c = (100, 300, 1000)mM
α_+	1	0.02	0.01
α_-	0.7	0.01	0.01
μ_+/μ_{K+}	1	1	1
μ_-/μ_{K+}	0.5	0.5	0.5
λ_0/h_0 (kg m^{-3} s^{-1})	10^{11}	5.10^{12}	10^{13}
$\kappa_+\rho_+$ (kg m^{-3} s^{-1})	0	(0.25, 0.75, 2.48) 10^{13}	(0.13, 0.38, 1.25) 10^{13}
$\kappa_-\rho_-$ (kg m^{-3} s^{-1})	(0.53, 1.60, 5.32) 10^{14}	(0.25, 0.75, 2.51) 10^{13}	(0.25, 0.75, 2.51) 10^{13}
λ_w/h_0 (kg m^{-3} s^{-1})	(0.53, 1.60, 5.32) 10^{14}	(1.00, 2.00, 5.49) 10^{13}	(1.38, 2.13, 4.76) 10^{13}

Figure C.5: Influence of the friction parameters on the model predictions. a-c) Plots show $\mu(\Delta V)$ versus ΔV for different concentrations (c = 100 mM, 300 mM, and 1 M) and friction parameters. a) Low-friction (graphite-like) behavior. In this plot, we take $\alpha_+ = 1$, $\alpha_- = 0.7$, $\mu_+ = \mu_+^{\text{bulk}}$, $\mu_- = 0.5\mu_-^{\text{bulk}}$, and $\lambda_0/h_0 = 10^{11}$ kg m^{-3} s^{-1}. b) Intermediate-friction behavior, $\alpha_+ = 0.02$, $\alpha_- = 0.01$, $\mu_+ = \mu_+^{\text{bulk}}$, $\mu_- = 0.5\mu_-^{\text{bulk}}$, and $\lambda_0/h_0 = 5 \times 10^{12}$ kg m^{-3} s^{-1}. c) High-friction (hBN-like) behavior, $\alpha_+ = 0.01$, $\alpha_- = 0.01$, $\mu_+ = \mu_+^{\text{bulk}}$, $\mu_- = 0.5\mu_-^{\text{bulk}}$, and $\lambda_0/h_0 = 10^{13}$ kg m^{-3} s^{-1}. d-f) Pressure-induced variation of the normalized electric potential $\Delta\phi \equiv \phi\,(\Delta V,\, \Delta P = 30\,\text{mbar}\,\mu\text{m}^{-1}) - \phi\,(\Delta V,\, \Delta P = 0)$ plotted as a function of the normalized channel coordinate x/L for $\Delta V = -50$, 0, and +50 mV. The dashed vertical lines segregate the channel interior, $x/L \in (-0.5, +0.5)$, from the left ($x/L < -0.5$) and right ($x/L > +0.5$) reservoirs. The curves are colored according to the applied voltage from -50 (blue) to +50 mV (orange). Panels d-f correspond to the parameters of panels a-c, respectively. g) Table of friction parameters corresponding to the data shown in a-c. The table also shows the decomposition of $\lambda_w(c)$ into its three main components for the concentrations considered here.

Appendix D

DUKHIN LENGTH AS ELECTROSTATIC HEALING LENGTH: SOME RESULTS FROM KHAIR & SQUIRES (2008)

Abstract In this Appendix, I rederive some of the results presented in Khair & Squires (2008) for the perturbation to an applied electric field induced by a discontinuity in surface charge–and hence surface conductivity. These authors consider only the uniform electrolyte outside of the diffuse layer on the assumption that the 'healing length' characterizing the spatial scale of the perturbation to the applied field is much larger than the Debye length λ_D, which characterizes the extent of the diffuse layer. Furthermore, they show that this healing length is given by the Dukhin length, defined dynamically as the ratio of the surface conductivity κ_s to the bulk conductivity κ_b: $\ell_{\mathrm{Du}} \equiv \kappa_s/\kappa_b$. Altogether, this suggests that surface charge discontinuities should have an 'effective extent' into the bulk given by the Dukhin length, and that the influence of these discontinuities may therefore be detectable well outside the diffuse layer. The treatment presented here differs from that presented in Khair & Squires (2008) in that I begin directly with a more formal Green's function approach for developing an implicit integral solution, afterwards making a connection to the development presented in Khair & Squires (2008) in terms of an 'effective surface charge distribution'. The Green's function approach will lay the foundation for the scaling calculations presented in Chapter 5, in which the ideas developed in Khair & Squires (2008) are applied in the context of scanning ion conductance microscopy.

D.1 Problem Statement

The configuration considered in Khair & Squires (2008) is shown schematically in Fig. D.1. Electrolyte is in contact with a solid substrate, forming a solid-liquid interface on the $x-z$ plane, and an external electric field $\mathbf{E}_\infty = E_\infty\hat{\boldsymbol{x}}$ is applied along the interface. Khair & Squires (2008) consider a discontinuity in surface charge along the line $x=0$ such that the surface charge is zero for $x<0$ and nonzero for $x>0$. The surface charge density is independent of z, making the problem translationally invariant and hence effectively two-dimensional.

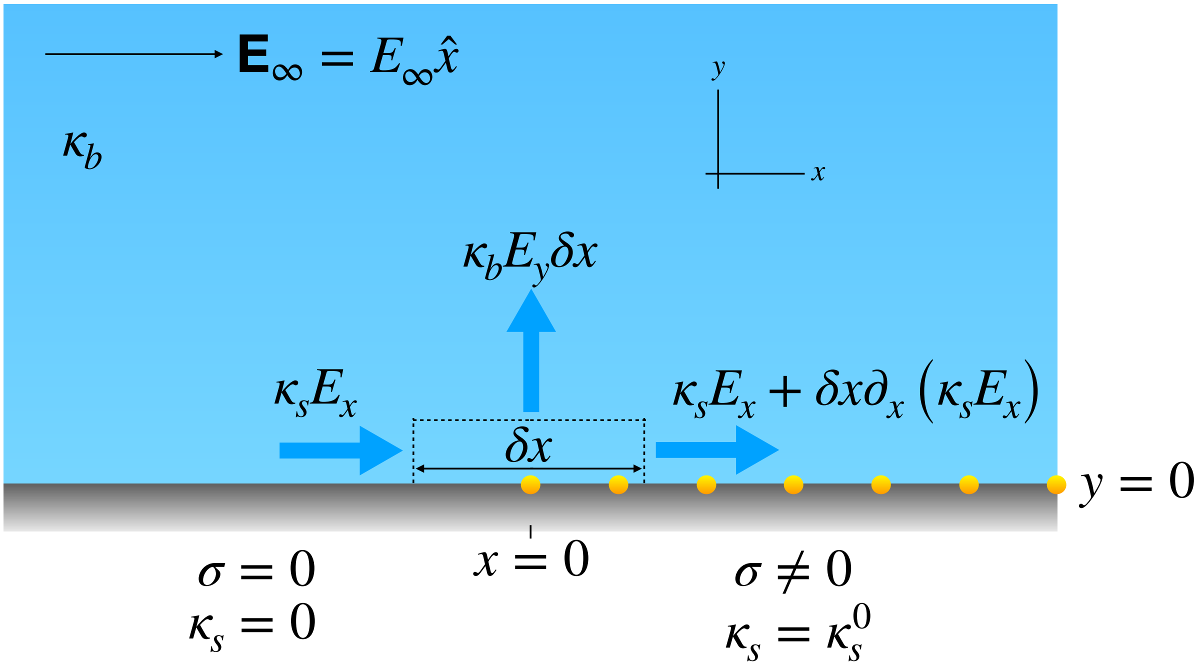

[h]

Figure D.1: Schematic showing the configuration considered in Khair & Squires (2008). An electrolyte is in contact with a solid substrate, forming a solid-liquid interface on the $x - z$ plane. There is a discontinuity in the surface charge density, and hence in the surface conductivity, along the line $x = 0$, with zero surface charge for $x < 0$ and nonzero surface charge for $x > 0$, and an external field $\mathbf{E}_\infty = E_\infty \hat{\boldsymbol{x}}$ is applied along the interface. The blue arrows indicate currents entering and leaving a control volume of infinitesimal length δx and height h much smaller than the healing (Dukhin) length ℓ_{Du} and larger than the characteristic extent of the diffuse layer, the Debye length λ_D: $\lambda_D < h \ll \ell_{\mathrm{Du}}$.

In the treatment of Khair & Squires (2008), it is assumed that the perturbation to the applied electric field induced by a discontinuity in surface charge occurs over a healing length ℓ_H that is much larger than the characteristic extent of the diffuse layer, the Debye length λ_D: $\ell_H \gg \lambda_D$. In this case, we need not resolve the detailed structure of the diffuse layer, instead treating the enhanced electrophoretic conductivity therein as a surface conductance. As a diffuse layer forms only when the surface charge is nonzero, the surface conductivity is nonzero only for $x > 0$. Denoting this nonzero value as κ_s^0, the surface conductivity distribution considered in Khair & Squires (2008) is given by

$$\kappa_s(x) = \kappa_s^0 \Theta(x), \tag{D.1}$$

where $\Theta(x)$ is the Heaviside theta function. Furthermore, as we do not resolve the diffuse layer, we may assume that the salt concentration, and hence the bulk conductivity κ_b, is uniform.

In order to understand the influence of the variable surface conductivity on the field structure, we consider the expression of charge conservation at steady state along the solid-liquid interface. We must have that the negative divergence of current along the surface is balanced by vertical current leaving the surface (and *vice versa*). This may be understood intuitively by summing the currents leaving the control volume illustrated in Fig. D.1 and setting the result to zero at steady state. The result is

$$E_y|_{y=0} + \ell_{\text{Du}} \frac{d}{dx} \left[K_{\lambda \ell_{\text{Du}}}(x) E_x|_{y=0} \right] = 0, \tag{D.2}$$

where I have introduced the normalized surface conductivity distribution $K_{\lambda \ell_{\text{Du}}}(x) \equiv \kappa_s(x)/\kappa_s^0$, taken $\kappa_s^0 \equiv \kappa_s(x \to \infty)$ to be the maximum, asymptotic value of $\kappa_s(x)$ far from the discontinuity, and applied the *dynamic* definition of the Dukhin length discussed in Appendix A (Eq. A.46): $\ell_{\text{Du}} \equiv \kappa_s^0/\kappa_b$. As demonstrated in Appendix A, this definition is equivalent to the definition in terms of the surface charge density magnitude $|\sigma|$, $\ell_{\text{Du}} \equiv |\sigma|/ec$, so long as Poisson-Boltzmann equilibrium theory is adequate in describing the structure of the diffuse layer. The subscript $\lambda \ell_{\text{Du}}$ on the normalized surface conductivity distribution $K_{\lambda \ell_{\text{Du}}}(x)$ refers to the spatial extent of the region of surface charge variation; the surface charge variation becomes an apparent discontinuity in the limit $\lambda \to 0$, and we have $K_0(x) = \Theta(x)$, corresponding to the case considered in Khair & Squires (2008).

We must impose steady state continuity of the current density $\mathbf{i} = \kappa_b \mathbf{E}$ in the bulk: $\nabla \cdot \mathbf{i} = 0$. As we neglect the electrolyte dynamics in the bulk, assuming a constant bulk conductivity κ_b, this reduces to the condition that the electric field be solenoidal:

$$\nabla \cdot \mathbf{E} = 0. \tag{D.3}$$

Furthermore, the field must return to its imposed value far from the discontinuity:

$$\mathbf{E} \xrightarrow[r\to\infty]{} \mathbf{E}_\infty, \tag{D.4}$$

where $r \equiv \sqrt{x^2 + y^2}$ is the distance from the discontinuity.

Eqs. D.2 through D.4 fully characterize the problem; however, before continuing, we nondimensionalize the problem by introducing the following rescalings: $\mathbf{r} \to \ell_{\mathrm{Du}}\mathbf{r}$; $\mathbf{E} \to E_\infty \mathbf{E}$; $\phi \to \ell_{\mathrm{Du}} E_\infty \phi$. In the preceding, ϕ is the electrostatic potential. Furthermore, it will be convenient in developing the Green's function solution to partition the electrostatic potential into a portion due to the applied field and an additional portion ϕ' representing the perturbation to the applied field induced by the surface charge discontinuity. With these modifications our governing equations become

$$\boxed{\nabla^2 \phi' = 0,} \tag{D.5}$$

$$\boxed{\phi' \xrightarrow[r\to\infty]{} 0,} \tag{D.6}$$

$$\boxed{\partial_y \phi'|_{y=0} + \frac{d}{dx}\left[K_\lambda(x)\partial_x \phi|_{y=0}\right] = 0, \quad \text{and}} \tag{D.7}$$

$$\boxed{\phi = \phi' - x + \mathrm{f}(x, y).} \tag{D.8}$$

Note, in Eq. D.7, that the perturbed field ϕ' appears in the first term on the LHS, while the total field ϕ appears in the second. In Eq. D.8, $\mathrm{f}(x, y)$ is a harmonic function verifying the conditions $\nabla \mathrm{f} \to 0$ as $r \to \infty$ and, from Eq. D.7, $\partial_y \mathrm{f}(x, y)|_{y=0} = 0$. As we will see below, it is necessary to include this term because of the logarithmic divergence of the fundamental solution (Green's function) to the Laplace equation in two dimensions, and its presence will have no influence on the solution.

Before proceeding to the Green's function solution of Eqs. D.5 through D.8, we note that this system of equations becomes scale invariant when the spatial coordinate is rescaled by the Dukhin length only in the limit $\lambda \to 0$. This indicates that ℓ_{Du} is the characteristic scale of the perturbation to the applied field, and hence equal to the healing length ℓ_H introduced above, when the extent of the discontinuity is much smaller than ℓ_{Du} ($\lambda \ll 1$). As the Dukhin length sets the lower limit on the magnitude of the healing length, we learn first of all that our description is valid in the limit $\ell_{\mathrm{Du}}/\lambda_D \gg 1$. More importantly, we learn that a rapid variation in surface charge over a length scale much smaller than the Dukhin length (an apparent surface charge discontinuity) is expressed by a disturbance in the bulk that is of the order of ℓ_{Du}. This immediately suggests the possibility of resolving small scale surface charge features on substrates submerged in electrolytes, and the applications to surface charge microscopy are discussed in detail in Chapter 5.

D.2 Green's Function Solution

D.2.1 Green's Theorem and Formal Inversion

We begin with Green's theorem for the Laplacian operator:

$$\int_{\Omega} \mathrm{d}^d\mathbf{r} \left(f\nabla^2 g - g\nabla^2 f\right) = \oint_{\partial\Omega} \mathrm{d}\mathbf{\Sigma} \cdot \left(f\nabla g - g\nabla f\right), \tag{D.9}$$

where f and g are arbitrary functions of the spatial coordinates, Ω is the spatial domain, here the upper half plane, $\partial\Omega$ is the domain boundary, and $\mathrm{d}\mathbf{\Sigma}$ is a surface element with direction given by the outward normal. We define a Green's function G' satisfying

$$\nabla^2_{\mathbf{r}} G'(\mathbf{r}, \mathbf{r}_0) = \nabla^2_{\mathbf{r}_0} G'(\mathbf{r}, \mathbf{r}_0) = -\delta^{(3)}(\mathbf{r} - \mathbf{r}_0). \tag{D.10}$$

We will choose convenient boundary conditions for the Green's function in what follows. We insert the Green's function and the perturbation ϕ' into Green's theorem, Eq. D.9, making use of Eqs. D.5 and D.10, and change the variable of integration to $\mathbf{r}_0$ to obtain

$$\phi'(\mathbf{r}) = \oint_{\partial\Omega} \mathrm{d}\mathbf{\Sigma}_0 \cdot \left(G'\nabla\phi' - \phi'\nabla G'\right). \tag{D.11}$$

From boundary condition D.6, the second term on the RHS vanishes on the boundary at infinity, and we can similarly eliminate the first term by requiring that $G'(\mathbf{r}, \mathbf{r}_0) \to 0$ as $|\mathbf{r}_0| \to \infty$ or $|\mathbf{r}| \to \infty$. We then find

$$\phi'(\mathbf{r}) = \int_{-\infty}^{+\infty} \mathrm{d}x_0 \left[\phi'(x_0, 0)\partial_{y_0} G'|_{y_0=0} - G'|_{y_0=0}\partial_{y_0}\phi'|_{y_0=0}\right]. \tag{D.12}$$

In order to connect with the boundary condition at $y = 0$ (Eq. D.7), which contains $\partial_y\phi'$ directly, we would like to eliminate the first term on the RHS of Eq. D.12 by setting $\partial_y G'|_{y=0} = 0$. However, in imposing Neumann conditions on the Green's function, we must be careful not to violate the divergence theorem, which, from Eq. D.10, requires

$$-1 = -\lim_{L\to\infty}\langle\partial_y G'|_{y=0}\rangle_L \times 2L + \lim_{R\to\infty}\int_0^{\pi} R\mathrm{d}\theta\partial_r G'|_{r=R}, \tag{D.13}$$

where $\langle\,\rangle_L$ indicates an average over $x - x_0 \in (-L, +L)$. We anticipate that the Green's function will be proportional to the logarithm such that the second term on the RHS will be a constant, independent of R. This constant may be set to -1 by proper choice of the proportionality constant. The first term on the LHS will remain finite as $L \to \infty$ only if $\langle\partial_y G'|_{y=0}\rangle = 0$. Thus, we may impose a uniform value of zero for the y-derivative of the Green's function on the x-axis. The solution may therefore be decomposed as

$$\boxed{\phi(\mathbf{r}) = -x - \int_{-\infty}^{+\infty}\mathrm{d}x_0 G(x, y; x_0, 0)\partial_{y_0}\phi|_{y_0=0},} \tag{D.14}$$

where we have introduced a shifted Green's function

$$G(x, y; x_0, y_0) \equiv G'(x, y; x_0, y_0) - \frac{\mathrm{f}(x, y)}{\int_{-\infty}^{+\infty}\mathrm{d}x_0\partial_{y_0}\phi|_{y_0=0}}. \tag{D.15}$$

As f is a harmonic function, this Green's function still satisfies Eq. D.10. However, this Green's function no longer must vanish as $r \to \infty$. Instead, we need only require that the gradient vanish at infinity to ensure that we match the applied electric field. In summary, we must solve for the Green's function satisfying

$$\boxed{\nabla^2_{\mathbf{r},\mathbf{r}_0} G(\mathbf{r}, \mathbf{r}_0) = -\delta^{(3)}(\mathbf{r} - \mathbf{r}_0),} \tag{D.16}$$

$$\boxed{\nabla_{\mathbf{r},\,\mathbf{r}_0} G(\mathbf{r}, \mathbf{r}_0) \xrightarrow[r,\,r_0\to\infty]{} 0, \quad \text{and}} \tag{D.17}$$

$$\boxed{\partial_{y,\,y_0} G(\mathbf{r}, \mathbf{r}_0)|_{y,\,y_0=0} = 0.} \tag{D.18}$$

D.2.2 Green's Function and the Effective Surface Charge Density

The fundamental solution to the Laplace equation in two dimensions is

$$G_1(\mathbf{r}, \mathbf{r}_0) = -\frac{\ln\left[(x - x_0)^2 + (y - y_0)^2\right]}{4\pi}. \tag{D.19}$$

That this verifies Eq. D.16 is readily verified by direct calculation of $\nabla^2 G_1$ for $|\mathbf{r} - \mathbf{r}_0| \neq 0$, along with application of the divergence theorem. Furthermore, its verification of Eq. D.17 is readily apparent as the gradient of the logarithm decays as $1/|\mathbf{r}-\mathbf{r}_0|$. However, this Green's function does not satisfy the boundary condition given in Eq. D.18. Applying the method of images, we add to the Green's function given in Eq. D.19 its reflection about the x-axis:

$$G_2(\mathbf{r},\mathbf{r}_0) \equiv G_1(\mathbf{r}',\mathbf{r}_0) \equiv G_1(\mathbf{r},\mathbf{r}_0') \equiv -\frac{\ln\left[(x-x_0)^2+(y+y_0)^2\right]}{4\pi}, \tag{D.20}$$

where $\mathbf{r}' \equiv (x,-y)$ and $\mathbf{r}_0' \equiv (x_0,-y_0)$. The full Green's function is thus given by

$$G(\mathbf{r},\mathbf{r}_0) = -\frac{\ln\left[(x-x_0)^2+(y-y_0)^2\right]+\ln\left[(x-x_0)^2+(y+y_0)^2\right]}{4\pi}, \tag{D.21}$$

which, by direct calculation, can be shown to satisfy the boundary conditions given in Eqs. D.17 and D.18. Furthermore, as $\mathbf{r}',\mathbf{r}_0' \notin \Omega$, this Green's function still verifies Eq. D.16 on the upper half plane.

Finally, we evaluate Eq. D.21 along $y_0 = 0$, insert the result into Eq. D.14, and apply the boundary condition given in Eq. D.7 to obtain

$$\boxed{\phi(\mathbf{r}) = -x - \int_{-\infty}^{+\infty} \mathrm{d}x_0 \frac{\ln\left[(x-x_0)^2+y^2\right]}{2\pi}\frac{d}{dx_0}\left[K_\lambda(x_0)\partial_{x_0}\phi|_{y_0=0}\right].} \tag{D.22}$$

We make the connection to the treatment of Khair & Squires (2008) by noting that Eq. D.7 may be combined with the Gaussian boundary condition for the normal electric field in the vicinity of the charged surface of a conducting or thick insulating material, $\mathbf{E}\cdot\hat{\boldsymbol{n}} = \sigma/\epsilon$, to reinterpret the problem in terms of an effective surface charge density:

$$\sigma_{\text{eff}}(x) \equiv \frac{d}{dx}\left[K_\lambda(x)\partial_x\phi|_{y=0}\right]. \tag{D.23}$$

We may then obtain an integral equation for this effective surface density by inserting Eq. D.23 into Eq. D.22 and then inserting this decomposition for the electrostatic potential back into Eq. D.23. The result is

$$\boxed{\sigma_{\text{eff}}(x) + \frac{1}{\pi}\int_{-\infty}^{+\infty} \mathrm{d}x_0 \left[\frac{K_\lambda'(x)}{x-x_0} - \frac{K_\lambda(x)}{(x-x_0)^2}\right]\sigma_{\text{eff}}(x_0) + K'(x) = 0,} \tag{D.24}$$

where here a prime indicates differentiation with respect to x. The effective surface charge density is of course related to the electrostatic potential via, from Eqs. D.22 and D.23,

$$\boxed{\phi(\mathbf{r}) = -x - \int_{-\infty}^{+\infty} \mathrm{d}x_0 \frac{\ln\left[(x-x_0)^2+y^2\right]}{2\pi}\sigma_{\text{eff}}(x_0).} \tag{D.25}$$

We see from Eq. D.22 why it was necessary to include $\mathrm{f}(x, y)$ in Eq. D.25. As $r \to \infty$, $\phi \to \infty$ owing to the divergence of the logarithmic Green's function in two dimensions; however, $\mathbf{E} \equiv -\nabla\phi \to \hat{\boldsymbol{x}} = \mathbf{E}_\infty$, which is all that is required from a physical point of view.

Finally, we note that, whereas Khair & Squires (2008) compute the solution for the electrostatic potential by discretizing Eqs. D.24 and D.25, we find it easier to numerically solve the PDE statement of the problem (Eqs. D.5 through D.8) directly via the finite element method (FEM). In Chapter 5 we explore the applications of the results of Khair & Squires (2008) to surface charge microscopy; in this case, the Green's function method is used to develop quasi-analytical scalings for the dependence of the electric field on the setup geometry and the Dukhin number.

D.3 Khair & Squires (2008) Solution

Finally, I present for completeness the FEM solution of the Khair & Squires (2008) problem for a diffuse transition from zero to nonzero surface conductance given by

$$K_\lambda(x) = \frac{1 + \tanh(2x/\lambda)}{2}, \tag{D.26}$$

where λ is the transition length in units of ℓ_{Du}. Note that this is the same functional dependence used to model the transition in Khair & Squires (2008), where they take $\lambda = 2/15 \approx 0.133$.

Figs. D.2a-c show the structure of the electrostatic potential (colored equipotential lines) and electric field (solid black field lines) in the vicinity of the 'discontinuity' at $x = 0$ for $\lambda = 2$ (Fig. D.2a), $\lambda = 0.5$ (Fig. D.2b), and $\lambda = 0.1$ (Fig. D.2c). The corresponding normalized surface conductance distributions are shown in Figs. D.2d-f. We see that a value of $\lambda > 1$ leads to a diffuse perturbation to the applied electric field, with a healing length likewise larger than unity (Fig. D.2a), whereas the structure of the perturbation appears to become independent of λ as $\lambda \to 0$ (Figs. D.2b and c). This is consistent with our above inference, that the 'apparent size' of a transition much smaller than the Dukhin length scales with the Dukhin length in the bulk.

Finally, we note that the magnitude of the perturbation to the applied field becomes stronger as $\lambda \to 0$. This is indicated by the increased density of the field lines in the vicinity of $x = 0$ in Figs. D.2b and c.

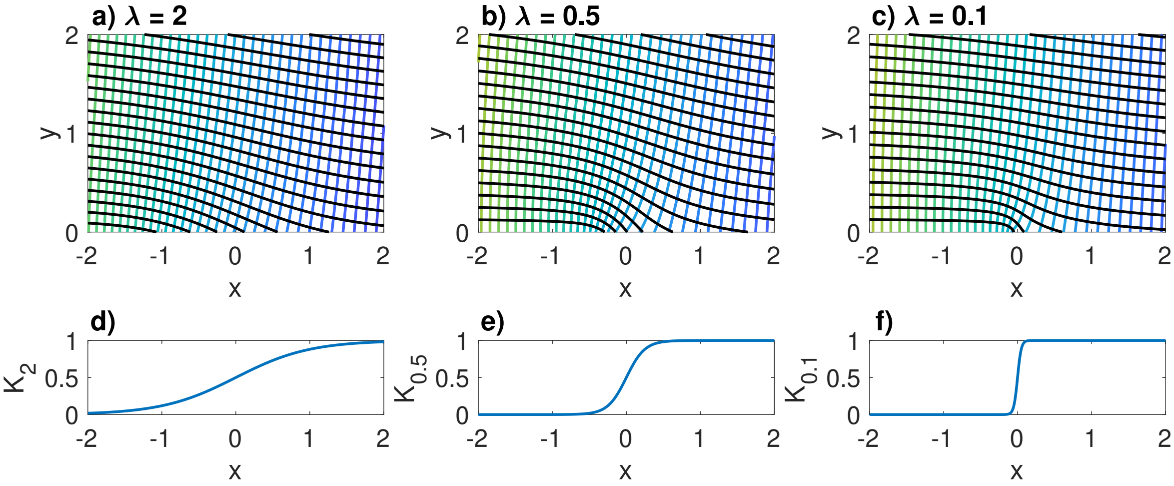

[h]

Figure D.2: Structure of electrostatic potential and electric field in the presence of an applied electric field and in the vicinity of an increasingly confined (from left to right) transition from zero to nonzero surface conductance. Panels a-c) show the equipotential (colored) and field (solid black) lines in the vicinity of a transition from zero to nonzero surface conductance centered at $x = 0$ for a transition length $\lambda = 2$ (panel a), $\lambda = 0.5$ (panel b), and $\lambda = 0.1$ (panel c). Panels d through f show the corresponding normalized surface conductance profiles $K_\lambda(x)$, plotted according to Eq. D.26.

BIBLIOGRAPHY

Abraham, J., Vasu, K. S., Williams, C. D., Gopinadhan, K., Su, Y., Cherian, C. T., Dix, J., Prestat, E., , Haigh, S. J., Grigorieva, I. V., Carbone, P., & Geim, A. K. 2017. Tunable sieving of ions using graphene oxide membranes. *Nat. Nanotechnol.*, **12**, 546–550.

Ai, Y., Zhang, M., Joo, S. W., Cheney, M. A., & Qian, S. 2010. Effects of electroosmotic flow on ionic current rectification in conical nanopores. *J. Phys. Chem. C*, **114**, 3883–3890.

Ajdari, A., & Bocquet, L. 2006. Giant amplification of interfacially driven transport by hydrodynamic slip: Diffusio-osmosis and beyond. *Phys. Rev. Lett.*, **96**.

Algara-Siller, G., Lehtinen, O., Wang, F. C., Nair, R. R., Kaiser, U., Wu, H. A., Geim, A. K., & Grigorieva, I. V. 2015. Square ice in graphene nanocapillaries. *Nature*, **519**, 443–445.

Barrat, J. L., & Hansen, J. P. 2003. *Basic Concepts for Simple and Complex Liquids*. 1 edn. Cambridge.

Behrens, S. H., & Grier, D. G. 2001. The charge of glass and silica surfaces. *J. Chem. Phys.*, **115**, 6716–6721.

Bocquet, L., & Charlaix, E. 2010. Nanofluidics, from bulk to interfaces. *Chem. Soc. Rev.*, **39**, 1073–1095.

Bonthuis, D. J., & Golestanian, R. 2014. Mechanosensitive channel activation by diffusio-osmotic force. *Phys. Rev. Lett.*, **113**, 148101.

Campione, A., Gurreri, L., Ciofalo, M., Micale, G., Tamburini, A., & Cipollina, A. 2018. Electrodialysis for water desalination: A critical assessment of recent developments on process fundamentals, models and applications. *Desalination*, **434**, 121–160.

Cervera, J., Schiedt, B., Neumann, R., Mafé, S., & Ramírez, P. 2006. Ionic conduction, rectification, and selectivity in single conical nanopores. *J. Chem. Phys.*, **124**, 104706.

Cheng, L. J., & Guo, L. J. 2007. Rectified ion transport through concentration gradient in homogeneous silica nanochannels. *Nano Lett.*, **7**, 3165–3171.

Cheng, L. J., & Guo, L. J. 2010. Nanofluidic diodes. *Chem. Soc. Rev.*, **39**, 923–938.

Chua, L. 2013. Memristor, Hodgkin-Huxley, and edge of chaos. *Nanotechnology*, **24**, 383001.

Chun, H., & Chung, T. D. 2015. Iontronics. *Annu. Rev. Anal. Chem.*, **8**, 441–462.

Constantin, D., & Siwy, Z. S. 2007. Poisson-Nernst-Planck model of ion current rectification through a nanofluidic diode. *Phys. Rev. E*, **76**, 041202.

Coste, B., Xiao, B., Santos, J. S., Syeda, R., Grandl, J., Spencer, K. S., Kim, S. E., Schmidt, M., Mathur, J., Dubin, A. E., Montal, M., & Patapoutian, A. 2012. Piezo proteins are pore-forming subunits of mechanically activated channels. *Nature*, **483**, 176–181.

Dal Cengio, S., & Pagonabarraga, I. 2019. Confinement-controlled rectification in a geometric nanofluidic diode. *J. Chem. Phys.*, **151**, 044707.

Delgado, A. V., Gonzàlez-Caballero, F., Hunter, R. J., Koopal, L. K., & Lyklema, J. 2005. Measurement and Interpretation of Electrokinetic Phenomena. *Pure Appl. Chem.*, **77**, 1753–1805.

Dorwling-Carter, L., Aramesh, M., Han, H., Zambelli, T., & Momotenko, D. 2018. Combined ion conductance and atomic force microscope for fast simultaneous topographical and surface charge imaging. *Anal. Chem.*, **90**, 11453–11460.

Eijkel, J. C. T., & van den Berg, A. 2005. Nanofluidics: what is it and what can we expect from it? *Microfluid. Nanofluid.*, **1**, 249–267.

Esfandiar, A., Radha, B., Wang, F. C., Yang, Q., Hu, S., Garaj, S., Nair, R. R., Geim, A. K., & Gopinadhan, K. 2017. Size effect in ion transport through angstrom-scale slits. *Nature*, **358**, 511–513.

Fair, J. C., & Osterle, J. F. 1971. Reverse electrodialysis in charged capillary membranes. *J. Chem. Phys.*, **54**, 3307–3316.

Feng, J., Graf, M., Liu, K., Ovchinnikov, D., Dumcenco, D., Heiranian, M., Nandigana, V., Aluru, N. R., Kis, A., & Radenovic, A. 2016. Single-layer MoS_2 nanopores as nanopower generators. *Nature*, **536**, 197–200.

Fornasiero, F., Park, H. G., Holt, J. K., Stadermann, M., Grigoropoulos, C. P., Noy, A., & Bakajin, O. 2008. Ion exclusion by sub-2-nm carbon nanotube pores. *Proc. Natl. Acad. Sci. U.S.A.*, **105**, 17250–17255.

Frament, C. M., & Dwyer, J. R. 2012. Conductance-based determination of solid-state nanopore size and shape: An exploration of performance limits. *J. Phys. Chem. C*, **116**, 23315–23321.

Fu, Y. M., Wan, C. J., Zhu, L. Q., Xiao, H., Chen, X. D., & Wan, Q. 2017. Hodgkin-Huxley artificial synaptic membrane based on protonic/electronic hybrid neuromorphic transistors. *Adv. Biosyst.*, **2**, 1700198.

Fumagalli, L., Esfandiar, A., Fabregas, R., Hu, S., ares, P., Janardanan, A., Yang, Q., Radha, B., Taniguchi, T., Watanabe, K., Gomila, G., Novoselov, K. S., & Geim, A. K. 2018. Anomalously low dielectric constant of confined water. *Science*, **360**, 1339–1342.

Garaj, S., Hubbard, W., Reina, A., Kong, J., Branton, D., & Golovchenko, J. A. 2010. Graphene as subnanometre trans-electrode membrane. *Nature*, **467**.

Geim, A. K., & Grigorieva, I. V. 2013. Van der Waals heterostructures. *Nature*, **499**, 419–425.

Geismann, C., Yaroshchuk, A., & Ulbricht, M. 2007. Permeability and electrokinetic characterization of poly(ethylene terephthalate) capillary pore membranes with grafted temperature-responsive polymers. *Langmuir*, **23**, 76–83.

Graf, M., Lihter, M., Unuchek, D., Sarathy, A., Leburton, J.-P., Kis, A., & Radenovic, A. 2019. Light-enhanced blue energy generation using MoS_2 Nanopores. *Joule*, **3**, 1549–1564.

Hansma, P. K., Drake, B., Marti, O., Gould, S. A., & Prater, C. B. 1989. The scanning ion-conductance microscope. *Science*, **243**, 641–643.

He, X., Zhang, K., Li, T., Jiang, Y., Yu, P., & Mao, L. 2017. Micrometer-scale ion current rectification at polyelectrolyte brush-modified micropipets. *J. Am. Chem. Soc.*, **139**, 1396–1399.

Hong, S., , Constans, C., Martins, M. V. S., Seow, Y. C., Carriò, J. A. G., & Garaj, S. 2017. Scalable graphene-based membranes for ionic sieving with ultrahigh charge selectivity. *Nano Lett.*, **17**, 728–732.

Howorka, S., & Siwy, Z. 2009. Nanopore analytics: sensing of single molecules. *Chem. Soc. Rev.*, **38**, 2360–2384.

Iler, R. K. 1979. *The Chemistry of Silica: Solubility, Polymerization, Colloid and Surface Properties, and Biochemistry.* 1 edn. Wiley.

Jain, T., Rasera, B. C., Boutilier, R. J. S. Guerrero M. S. H., O'Hern, S. C., Idrobo, J.-C., & Karnik, R. 2015. Heterogeneous sub-continuum ionic transport in statistically isolated graphene nanopores. *Nat. Nanotechnol.*, **10**, 1053–1057.

Jiang, Z., & Stein, D. 2011. Charge regulation in nanopore ionic field-effect transistors. *Phys. Rev. E*, **83**, 031203.

Joshi, R. K., Carbone, P., Wang, F. C., Kravets, V. G., Su, Y., Grigorieva, I. V., Wu, H. A., Geim, A. K., & Nair, R. R. 2014. Precise and ultrafast molecular sieving through graphene oxide membranes. *Science*, **343**, 752–754.

Jubin, L., Poggioli, A. R., Siria, A., & Bocquet, L. 2018. Dramatic pressure-sensitive ion conduction in conical nanopores. *Proc. Natl. Acad. Sci. U.S.A.*, **115**, 4063–4068.

Karnik, R., & Castelino, K. 2006. Field-effect control of protein transport in a nanofluidic transistor circuit. *Appl. Phys. Lett.*, **88**, 123114.

Karnik, R., Castelino, K., Fan, R., Yang, P., & Majumdar, A. 2005. Effects of biological reactions and modifications on conductance of nanofluidic channels. *Nano Lett.*, **5**, 1638–1642.

Karnik, R., Duan, C., Castelino, K., Daiguji, H., & Majumdar, A. 2007. Rectification of ionic current in a nanofluidic diode. *Nano Lett.*, **7**, 547–551.

Keerthi, A., Geim, A. K., Janardanan, A., Rooney, A. P., Esfandiar, A., Hu, S., Dar, S. A., Grigorieva, I. V., Haigh, S. J., Wang, F. C., & Radha, B. 2018. Ballistic molecular transport through two-dimensional channels. *Nature*, **558**, 420–424.

Khair, A. S., & Squires, T. M. 2008. Surprising consequences of ion conservation in electro-osmosis over a surface charge discontinuity. *J. Fluid Mech.*, **615**, 323–334.

Kim, S. J., Li, L. D., & Han, J. 2009. Amplified electrokinetic response by concentration polarization near nanofluidic channel. *Langmuir*, **25**, 7759–7765.

Klenerman, D., Korchev, Y. E., & Davis, S. J. 2011. Imaging and characterisation of the surface of live cells. *Curr. Opin. Chem. Biol.*, **15**, 696–703.

Korchev, Y. E., Bashford, C. L., Milovanovic, M., Vodyanoy, I., & Lab, M. J. 1997. Scanning ion conductance microscopy of living cells. *Biophys. J.*, **73**, 653–658.

Kovarik, M. L., Zhou, K., & Jacobson, S. C. 2009. Effect of conical nanopore diameter on ion current rectification. *J. Phys. Chem. B*, **113**, 15960–15966.

Kubeil, C., & Bund, A. 2011. The role of nanopore geometry for the rectification of ionic currents. *J. Phys. Chem. C*, **115**, 7866–7873.

Lan, W. J., Holden, D. A., & White, H. S. 2011. Pressure-dependent ion current rectification in conical-shaped glass nanopores. *J. Am. Chem. Soc.*, **133**, 13300–13303.

Laohakunakorn, N., & Keyser, U. F. 2015. Electroosmotic flow rectification in conical nanopores. *Nanotechnology*, **26**, 275202.

Lee, C., Joly, L., Siria, A., Biance, A.-L., Fulcrand, R., & Bocquet, L. 2012. Large Apparent Electric Size of Solid-State Nanopores Due to Spatially Extended Surface Conduction. *Nano Lett.*, **12**, 4037–4044.

Li, C.-Y., Ma, F.-X., Wu, Z.-Q., Gao, H.-L., Shao, W.-T., Wang, K., & Xia, X.-H. 2013. Solution-pH-modulated rectification of ionic current in highly ordered nanochannel arrays patterned with chemical functional groups at designed positions. *Adv. Funct. Mat.*, **23**, 3836–3844.

Lin, C.-Y., Yeh, L.-H., & Siwy, Z. S. 2018. Voltage-induced modulation of ionic concentrations and ion current rectification in mesopores with highly charged pore walls. *J. Phys. Chem. Lett.*, **9**, 393–398.

Liu, Q., Wang, Y., Guo, W., Ji, H., Xue, J., & Ouyang, Q. 2007. Asymmetric properties of ion transport in a charged conical nanopore. *Phys. Rev. E*, **75**, 051201.

Macha, M., Marion, S., Nandigana, V. V. R., & Radenovic, A. 2019. 2D materials as emerging platform for nanopore-based power generation. *Nat. Rev. Mater.*, **4**.

Maddar, F. M., Perry, D., Brooks, R., Page, A., & Unwin, P. R. 2019. Nanoscale surface charge visualization of human hair. *Anal. Chem.*, **91**, 4632–4639.

Malgaretti, P., Pagonabarraga, I., & Rubi, J. M. 2015. Geometrically tuned channel permeability. *Macromol. Symp.*, **357**, 178–188.

Malgaretti, P., Pagonabarraga, I., & Rubi, J. M. 2016. Entropically induced asymmetric passage times of charged tracers across corrugated channels. *J. Chem. Phys.*, **144**, 034901.

McKelvey, K., Kinnear, S. L., Perry, D., Momotenko, D., & Unwin, P. R. 2014. Surface Charge Mapping with a Nanopipette. *J. Am. Chem. Soc.*, **136**, 13735–13744.

Misakian, M., & Kasianowicz, J. J. 2003. Electrostatic influence on ion transport through the αHL channel. *J. Membrane Biol.*, **195**, 137–146.

Mouterde, T., Keerthi, A., Poggioli, A. R., Dar, S. A., Siria, A., Geim, A. K., Bocquet, L., & Radha, B. 2019. Molecular streaming and its voltage control in ångström-scale channels. *Nature*, **567**, 87–90.

Nguyen, G., Vlassiouk, I., & Siwy, Z. S. 2010. Comparison of bipolar and unipolar ionic diodes. *Nanotechnology*, **21**, 265301.

Nitz, H., Kamp, J., & Fuchs, H. 1998. A Combined Scanning Ion-Conductance and Shear-Force Microscope. *Probe Microscopy*, **1**, 187–200.

Pang, P., He, J., Park, J. H., Krstiȅ, P. S., & Lindsay, S. 2011. Origin of giant ionic currents in carbon nanotube channels. *ACS Nano*, **5**, 7277–7283.

Perozo, E., Cortes, D. M., Sompornpisut, P., Kloda, A., & Martinac, B. 2002. Open channel structure of MscL and the gating mechanism of mechanosensitive channels. *Nature*, **418**, 942–948.

Perry, J. M., Zhou, K., Harms, Z. D., & Jacobson, S. C. 2010. Ion transport in nanofluidic funnels. *ACS Nano*, **4**, 3897–3902.

Picallo, C. B., Gravelle, S., Joly, L., Charlaix, E., & Bocquet, L. 2013. Nanofluidic osmotic diodes: Theory and molecular dynamics simulations. *Phys. Rev. Lett.*, **111**, 244501.

Plecis, A., Schoch, R. B., & Renaud, P. 2005. Ionic transport phenomena in nanofluidics: Experimental and theoretical study of the exclusion-enrichment effect on a chip. *Nano Lett.*, **5**, 1147–1155.

Poggioli, A. R., Siria, A., & Bocquet, L. 2019. Beyond the tradeoff: Dynamic selectivity in ionic transport and current selectivity. *J. Phys. Chem. B*, **123**, 1171–1185.

Posner, J. D. 2009. Properties and electrokinetic behavior of non-dilute colloidal suspension. *Mech. Res. Commun.*, **36**, 22–32.

Radha, B., Esfandiar, A., Wang, F. C., Rooney, A. P., Gopinadhan, K., Keerthi, A., Mishchenko, A., Janardanan, A., Blake, P., Fumagalli, L., Lozada-Hidalgo, M., Garaj, S., Haigh, S. J., Grigorieva, I. V., Wu, H. A., & Geim, A. K. 2016. Molecular transport through capillaries made with atomic-scale precision. *Nature*, **538**, 222–225.

Rankin, D. J., & Huang, D. M. 2016. The effect of hydrodynamic slip on membrane-based salinity-gradient-driven energy harvesting. *Langmuir*, **32**, 3420–3432.

Ren, Y., & Stein, D. 2008. Slip-enhanced electrokinetic energy conversion in nanofluidic channels. *Nanotechnology*, **19**, 195707.

Sa, N., Lan, W.-J., Shi, W., & Baker, L. A. 2013. Rectification of ion current in nanopipettes by external substrates. *ACS Nano*, **7**, 11273–11282.

Schasfoort, R. B. M., Schlautmann, S., Hendrikse, J., & van den Berg, A. 1999. Field-effect flow control for microfabricated fluidic networks. *Science*, **286**, 942–945.

Schiedt, B., Healy, K., Morrison, A. P., Neumann, R., & Siwy, Z. 2005. Transport of ions and biomolecules through single asymmetric nanopores in polymer films. *Nucl. Instr. Meth. Phys. Res. B*, **236**, 109–116.

Schlaich, A., Knapp, E. W., & Netz, R. R. 2016. Water dielectric effects in planar confinement. *Phys. Rev. Lett.*, **117**, 048001.

Schoch, R. B., Han, J., & Renaud, P. 2008. Transport phenomena in nanofluidics. *Rev. Mod. Phys.*, **80**, 839–883.

Secchi, E., Marbach, S., Niguès, A., Stein, D., Siria, A., & Bocquet, L. 2016a. Massive radius-dependent flow slippage in carbon nanotubes. *Nature*, **537**, 210–213.

Secchi, E., Niguès, A., Jubin, L., Siria, A., & Bocquet, L. 2016b. Scaling behavior for ionic transport and its fluctuations in individual carbon nanotubes. *Phys. Rev. Lett.*, **116**, 154501.

Shockley, W. 1949. The theory of p-n junctions in semiconductors and p-n junction transistors. *Bell Labs Tech. J.*, **28**, 435–489.

Siria, A., Poncharal, P., Biance, A. L., Fulcrand, R., Blase, X., Purcell, S. T., & Bocquet, L. 2013. Giant osmotic energy conversion measured in a single transmembrane boron nitride nanotube. *Nature*, **494**, 455–458.

Siria, A., Bocquet, L., & Bocquet, M.-L. 2017. New avenues for the large-scale harvesting of blue energy. *Nat. Rev. Chem.*, **1**, 0091.

Siwy, Z., & Fuliński, A. 2002. Fabrication of a synthetic nanopore ion pump. *Phys. Rev. Lett.*, **89**, 198103.

Stein, D., Kruithof, M., & Dekker, C. 2004. Surface-charge-governed ion transport in nanofluidic channels. *Phys. Rev. Lett.*, **93**, 035901.

Sze, A., Erickson, D., Ren, L., & Li, D. 2003. Zeta-potential measurement using the Smoluchowski equation and the slope of the current-time relationship in electroosmotic flow. *J. Colloid Interface Sci.*, **261**, 402–410.

Takasaki, R. Futamura T. Iiyama Y., Gogotsi, Y., Biggs, M. J., Salanne, M., Ségalini, J., Simon, P., & Kaneko, K. 2017. Partial breaking of the Coulombic ordering of ionic liquids confined in carbon nanopores. *Nat. Mater.*, **16**, 1225–1232.

Tocci, G., Joly, L., & Michaelides, A. 2014. Friction of water on graphene and hexagonal boron nitride from *ab inition* methods: very different slippage despite very similar interface structures. *Nano Lett.*, **14**, 6872–6877.

Tunuguntla, R. H., Henley, R. Y., Yao, Y.-C., Pham, T. A., Wanunu, M., & Noy, A. 2017. Enhanced water permeability and tunable ion selectivity in subnanometer carbon nanotube porins. *Science*, **357**.

Tybrandt, K. 2017. Exploring the potential of ionic bipolar diodes for chemical neural interfaces. *Soft Matter*, **13**, 8171–8177.

van der Heyden, F. H. J., Bonthuis, D. J., Stein, D., Meyer, C., & Dekker, C. 2006. Electrokinetic energy conversion efficiency in nanofluidic channels. *Nano Lett.*, **6**, 2232–2237.

Vásquez, V., Sotomayor, M., Cordero-Morales, J., Schulten, K., & Perozo, E. 2008. A structural mechanism for MscS gating in lipid bilayers. *Science*, **321**, 1210–1214.

Vlassiouk, I., & Siwy, Z. S. 2007. Nanofluidic diode. *Nano Lett.*, **7**, 552–556.

Vlassiouk, I., Smirnov, S., & Siwy, Z. 2008a. Ionic selectivity of single nanochannels. *Nano Lett.*, **8**, 1978–1985.

Vlassiouk, I., Smirnov, S., & Siwy, Z. 2008b. Nanofluidic ionic diodes. Comparison of analytical and numerical solutions. *ACS Nano*, **2**, 1589–1602.

Vlassiouk, I., Kozel, T. R., & Siwy, Z. S. 2009. Biosensing with nanofluidic diodes. *J. Am. Chem. Soc.*, **131**, 8211–8220.

Wang, X., Xue, J., Wang, L., Guo, W., Zhang, W., Wang, Y., Liu, Q., Ji, H., & Ouyang, Q. 2007. How the geometric configuration and the surface charge distribution influence the ionic current rectification in nanopores. *J. Phys. D: Appl. Phys.*, **40**, 7077–7084.

White, H. S., & Bund, A. 2008. Ion current rectification at nanopores in glass membranes. *Langmuir*, **24**, 2212–2218.

White, R. J., Zhang, B., Daniel, S., Tang, J. M., Ervin, E. N., Cremer, P. S., & White, H. S. 2006. Ionic conductivity of the aqueous layer separating a lipid bilayer membrane and a glass support. *Langmuir*, **22**, 10777–10783.

Woermann, D. 2003. Electrochemical transport properties of a cone-shaped nanopore: high and low electrical conductivity states depending on the sign of an applied electrical potential difference. *Phys. Chem. Chem. Phys.*, **5**, 1853–1858.

Wu, J., Lewis, A. H., & Grandl, J. 2017. Touch, tension, and transduction–The function and regulation of piezo ion channels. *Trends Biochem. Sci.*, **42**, 57–71.

Xie, Q., Alibakhshi, M. A., Jiao, S., Xu, Z., Hempel, M., Kong, J., Park, H. G., & Duan, C. 2018. Fast water transport in graphene nanofluidic channels. *Nat. Nanotechnol.*, **13**, 238–245.

Zhao, Y., Janot, J.-M., Balanzat, E., & Balme, S. 2017. Mimicking pH-gated ionic channels by polyelectrolyte complex confinement inside a single nanopore. *Langmuir*, **33**, 3484–3490.

Zhou, K., Perry, J. M., & Jacobson, S. C. 2011. Transport and sensing in nanofluidic devices. *Annu. Rev. Anal. Chem.*, **4**, 321–341.

RÉSUMÉ

La recherche en nanofluidique est motivée par l'intérêt intrinsèque des nouveaux phénomènes de transport observables uniquement à cette échelle, et par les applications qui en résultent comme la production d'énergie, le dessalement, l'analyse macromoléculaire et la microscopie. Deux points clés pour le développement de telles technologies sont : 1) le contrôle du transport ionique non-linéaire et 2) la caractérisation des propriétés électrostatiques, frictionnelles et autres des interfaces solide-liquide avec des solutions électrolytiques. Dans ce manuscript, je m'intéresse à la sélectivité ionique ainsi qu'au transport non-linéaire des ions dans les nanopores. Je développe une théorie cohérente qui permet de rationaliser les travaux expérimentaux précédents et ouvre des nouvelles voies pour le dessalement et la génération d'énergie. J'explore ensuite chacun des deux points clés cites précédemment. D'abord, j'étudie les limites de l'approche en milieu continu à travers l'exemple du couplage non-linéaire observé pour le transport dans des canaux qui font quelques ångström d'épaisseur. Dans ce cadre, je montre que l'équation de Navier-Stokes ne permet plus de décrire correctement la dynamique des fluides (à cette échelle), et je mets en évidence l'importance des propriétés de friction du matériau qui confine le liquide. Enfin, j'explore l'effet des propriétés de surface sur le champ électrique appliqué en Microscopie à conductance ionique à balayage (Scanning Ion Conductance Microscopy). Je propose une nouvelle approche pour l'imagerie de la charge de surface qui pourrait améliorer considérablement la résolution spatiale des techniques actuelles.

MOTS CLÉS

nanofluidique, ångströfluidique, non-linéaire, transport, hydrodynamique, microscopie

ABSTRACT

Nanofluidics research is motivated both by intrinsic interest in the novel transport phenomena observable only at the (sub-)nanometric scale, and by applications including energy generation, desalination, macromolecular analysis, and microscopy. Two key considerations in the development of such technologies are 1) the control of nonlinear ionic transport and 2) the characterization of electrostatic, frictional, and other interactions of solid-liquid interfaces with bulk electrolyte solutions. In this manuscript, I develop a coherent theory of ion-selectivity and nonlinear ionic transport in nanopores $\gtrsim 1$ nm in diameter, rationalizing previous experimental work and offering new routes in the development of desalination, energy generation, and other exotic functionalities. I then explore each of the above considerations separately. First, I explore the limits of continuum theory in rationalizing nonlinear coupled transport observed experimentally in ångströmetric channels, revealing the irrelevance of the Navier-Stokes description of the fluid dynamics at this scale and highlighting the role of the frictional characteristics of the confining material. Finally, I examine the surface-controlled modification of applied electric fields in scanning ion conductance microscopy, proposing a new approach for the imaging of surface charge that may substantially improve on the spatial resolution of current techniques.

KEYWORDS

nanofluidics, ångströfluidics, nonlinear, transport, hydrodynamics, microscopy